THE EFFECT OF MICROSTRUCTURE IN ALUMINUM OXIDE CERAMICS ON ACOUSTIC LOSS MECHANISMS

by

STEPHEN BOTTIGLIERI

A Dissertation submitted to the

Graduate School-New Brunswick

Rutgers, The State University of New Jersey

in partial fulfillment of the requirements

for the degree of

Doctor of Philosophy

Graduate Program in Materials Science and Engineering

written under the direction of

Professor Richard Haber

and approved by

_____

_____

_____

_____

New Brunswick, New Jersey

January 2012

ABSTRACT OF THE DISSERTATION

The Effect of Microstructure in Alumina Oxide Ceramics on Acoustic Loss Mechanisms

By STEPHEN BOTTIGLIERI

Dissertation Director:
Professor Richard Haber

Ultrasound nondestructive testing was chosen as the method for characterizing the microstructures of dense, polycrystalline, high hardness aluminum oxide materials. The acoustic waves interact with all aspects of a material's microstructure through frequency dependent mechanisms. These interactions include those with grains, secondary phases, solid inclusions, and porosity. Ultrasonic nondestructive testing is performed over large sample areas such that C-Scan maps of elastic properties, sonic velocities, or the degree of acoustic energy loss may be obtained.

The work performed in this thesis involves deconvoluting temporal sample surface reflections seen in an oscilloscope to obtain frequency-based attenuation coefficient spectra. These spectra contain all microstructural information relating to the size scale in which the acoustic wave is capable of directly interacting with. Within the overarching loss mechanisms of acoustic scattering and absorption lie specific types of loss mechanisms related to each. For scattering there are three regimes, Rayleigh, stochastic, and diffuse, which describe how acoustic energy is lost depending on wavelength and scatterer size. Absorption is generally defined as the conversion of sound energy into heat. The primary loss mechanisms seen in the alumina-based

materials studied in this thesis were intraparticle thermoelastic absorption, Rayleigh scattering, and stochastic scattering.

An analytical solution relating the amount of acoustic energy lost due to thermoelastic absorption was derived along with a functional form to predict secondary phase grain size distributions. Determination of material constants, used to relate attenuation-based measurements to grain size based on acoustic scattering, allowed for the prediction of average alumina grain sizes. Four custom engineered alumina-based sample series were created with the intention of testing and validating the absorption and scattering concepts behind acoustic spectroscopy. Acoustic techniques were developed and applied to single points and large sample areas to obtain microstructural information relating to secondary phase size distributions as well as Al_2O_3 average grain sizes. Comparisons to results obtained through the use of conventional microstructural testing, including Field Emission Scanning Electron Microscopy (FESEM) imaging and X-ray Diffraction (XRD), showed strong correlations between measured and predicted results.

ACKNOWLEDGEMENTS

There were a great deal of people who have given me support, advice, and friendship throughout my experience in graduate school; without it, this dissertation would not have been possible. Many thanks go to my thesis advisor, Dr. Richard Haber, for giving me the opportunity and motivation to perform my graduate studies and thesis work under his tutelage. Although the direction in which Dr. Haber tried to push my research was unclear to me at times, I am grateful for having someone there in the beginning to guide me. As time progressed, I became capable of directing my own research, gained fortitude in myself, and grasped confidence in the ability to deliver presentations to a wide host of different audiences. For this, I will be grateful throughout my career. I would also like to thank the illustrious members of my thesis committee; Dr. Dale E. Niesz, Dr. M. John Matthewson, and Dr. Raymond E. Brennan. Without any of you, I could not have accomplished this dissertation which will lay the foundation for the rest of my life.

I am extremely thankful to the United States Army Research Laboratory's Materials Center of Excellence in Lightweight Materials for Vehicular Protection and the Ceramic, Composite, and Optical Materials Center for providing me with the funding necessary to perform the research in this thesis. The experience and professional development I acquired by working closely with both Centers has proved to be invaluable and I hope my future endeavors match the quality of work which is born out of such institutions.

The distinguished professors who comprise the Department of Materials Science and Engineering at Rutgers University greatly helped in not only educating me in the

content of materials science but also how to teach myself new topics as they develop. Such professors include Dr. Lisa Klein, Dr. Victor Greenhut, Dr. George Sigel, Dr. M. John Matthewson, Dr. Richard Lehman, Dr. Armen Khachaturyan, Dr. Dunbar Birnie, Dr. Thomas Tsakalakos, and Dr. John Wenzel - I am honored to join this field and the likes of you. I would additionally like to thank Phyllis Cassell, Claudia Kuchinow, and John Yaniero, without whom this department would not function properly. A very special thanks goes to Michelle Sole, who ensures that our research group does not fall apart, gives excellent advice to the graduate students, and deals with Dr. Haber regarding the tough issues on behalf of the graduate students.

Throughout my extended experience with the MCOE and CCOMC I have had the tremendous opportunity to acquaint myself with researchers from many backgrounds including industry, government, and academia. The close association with such people showed me how the real world works by giving me the chance to study a wide range of different topics. From the Army Research Laboratory I would like to thank Dr. Jim McCauley, Dr. Todd Jessen, Dr. Ernie Chin, Dr. Jerry LaSalvia, Dr. Jeff Swab, Dr. Matt Bratcher, Dr. Jim Campbell, Dr. Raymond Brennan, and Bill Green. My sincere appreciation goes to Alberto Arcaro and Dr. Ricardo Rovai from Industrie Bitossi for providing me with as many different samples as I could have asked for. From Greenleaf, I extend my gratitude to Dr. Timothy Neumann and Dr. Jason Goldsmith for also providing me with a sample set used extensively in this thesis. I would also like to thank the various CCOMC members whom I have had the chance to collaborate with by providing me with materials of many types to perform my testing on. Such people include: Dr. Rich Palicka from BAE, Dr. Bryan Harlan and Dr. Fred Kimock from

Morgan Advanced Ceramics, Dr. Frank Anderson from CoorsTek, Dr. Russ Yeckley from Kennametal, and Dr. Doug Mrotek from Saint Gobain.

Thank you the undergraduate assistants who helped me during my time as a graduate student. Your assistance in performing the tedious and mind-numbing tasks necessary for my project will not be forgotten. Without your dedication of sorting through thousands of data files, watching a scan go back and forth, or sitting in front of an automated polisher for hours I could not have completed this thesis. Such undergraduates include: Yao, Vinesh, Katy, Justin, Marco, TJ, Matt, Chirag, Kristin, Sarah, Chris, Logan, Charlie, Josh, and Dave.

My appreciation goes out to all of the members who have been in my research group over the years. Thank you for teaching me when I was new to the group and becoming my friends as time passed. Such people include Volkan, Navin, Cari, Steve, Doug, Rob, Fatih, Nick, Vlad, Sarah, Minh, and Bob. Special thanks go to Dan and Steve for showing me how to use pretty much everything in the department - thanks for your patience. To Paul, this thesis would certainly not have been possible without your assistance. Thank you to Vince; I wish you the best of luck in continuing to build upon the project you are left with. The biggest thanks and appreciation I owe is to Dr. Andrew Portune and Dr. Raymond Brennan. Without your contributions I could not have made mine. To all of the friendships I've made throughout my time as a graduate student, I am grateful. I'd like to extend my thanks to Joe, Jesse, Ben, Brian, Andrew, Larry, JD, Jen, Wojtek, Vishnu, Glenn, Bob, Stuart, and Carlos.

Thank you to my good friends who always supported me-Billy, Jay, Tina, Jared, Dan, Hurley, Kyle, Marco, Joey, Lisa, Jeff, and Lindsay.

To Nikki, the love of my life, my gratitude is undying for your constant support and belief in me. Thank you for being alongside me during my career as a graduate student. The life choices I've made, you had to live with and I greatly appreciate your patience during these past few years. Completion of this thesis marks the beginning of the next chapter of our lives together. Love you lots.

To all of my many aunts, uncles, and cousins-I greatly appreciate your encouragement and words of advice. Thank you to my grandfather and grandmother who always told me to choose my company wisely-I hope to always make you proud. To my brothers, Mike and Joe, I always enjoy our academic arguments, debates, and level of conversations we typically find ourselves in, even though they usually result in loud yelling. A very special thank you is given to my parents, for without you I would not have had the opportunity to achieve anything. Thank you for the wonderful life you've given me along with the encouragement and praise which has made me the person I am today-I love you both.

For everyone who has helped me in completing this dissertation, your influences have had profound effects which will not be forgotten.

TABLE OF CONTENTS

TABLE LISTING

FIGURE LISTING

EQUATION LISTING

1. Introduction

Aluminum oxide (Al_2O_3) is used in a broad range of applications due to its favorable mechanical, electrical, and thermal properties. Catalysts, electronic substrates, gas purification, furnace lining, abrasives for grinding and milling, and armor are just a few of the many places where one may find aluminum oxide being employed. Its low areal density, high elastic properties, and high hardness make it an excellent candidate for high strain-rate situations [1]. From a manufacturing standpoint, the production of high density alumina versus other widely used high hardness ceramic materials (such as silicon carbide) can be less expensive due to lower powder costs and lower sintering temperatures [1, 2]. Production methods for high density alumina tiles can vary as with any type of ceramic material, but common methods for processing alumina include sintering, injection molding, slip casting, hot pressing, and novel techniques such as spark plasma sintering [1, 3, 4].

The typical temperature for conventional sintering of commercial alumina is approximately 1500-1550°C [5]. Depending on the type and concentration of the additives introduced into the Al_2O_3 starting powders, the optimal sintering temperature will vary. Poor mixing or thermal fluctuations in a sintering furnace can cause the additives in Al_2O_3 (i.e. CaO, SiO_2, or MgO) to agglomerate or distribute nonuniformly throughout an alumina body [6]. Glassy grain boundaries, rich with SiO_2, CaO, and MgO, are commonly found in many commercial alumina tiles. While these additives form a liquid at grain boundaries that enables a high-diffusivity path which enhances densification, glass formation will have a degenerative effect on the overall mechanical properties of the sample [7]. The agglomeration of sintering additives and degradation of

properties due to glass formation from these additives may very well become the performance-limiting features within an alumina microstructure.

A well-defined limiting property of high density alumina used for high strain rate applications does not exist. Properties such as sonic velocity, elastic modulus, hardness, toughness, strength, etc. have been used as metrics to gauge how alumina tiles will perform during high stress environments [2, 8]. Manufacturers of ceramic materials use an enormous amount of resources for the elimination of property-degrading macro and microscopic flaws. It is coming to the point where microstructural variations are an important factor to consider for the improvement of all types of ceramics. Advancements in ceramic processing can eliminate macroscopic bulk flaws, but room for improvement may lie in targeting smaller scale features such as grains and solid inclusions [9, 10]. This necessitates the need for enhancing and innovating new characterization techniques which can be used for efficiently testing changes in aluminum oxide.

Nondestructive evaluation (NDE) methods are viewed as a panacea to traditional destructive testing for determination of certain material properties or bulk inspection [11, 12]. The vast majority of material testing is destructive and is only performed on small sample areas. A pitfall of quality control testing for large sample lots is the assumption that all samples will show similar behavior compared to the few that are actually tested [11, 13]. Nondestructive testing allows for full sample flaw detection and may be implemented as part of a product assembly line [14]. Common nondestructive testing types used to analyze ceramic armor components include radiography, acoustic emission, ultrasound, X-ray computed tomography and thermal

imaging [15]. Each type of NDE technique shares the commonality of being a cost effective way of testing large sample areas in a pass or fail manner.

Ultrasonic testing is arguably the most versatile of these NDE types [16, 17]. It has been widely studied for use with many material systems such as colloidal suspensions, metals, and ceramics. Ultrasonic NDE is a commonly used method for particle sizing in suspensions using acoustic spectroscopy [18]. Studies have been performed in metals which attempt to explain how high frequency acoustic waves interact with microstructural variations by measuring the frequency dependence loss of the acoustic energy [19]. Acoustic spectroscopy is not a currently used characterization technique for fully dense, high hardness, ceramic materials. Ultrasound NDE in ceramic materials has been solely limited to measuring elastic properties and spatially locating large flaws [14]. By understanding the different mechanisms by which ultrasound energy can be attenuated at specific frequencies, acoustic spectroscopy can be used as a way to determine microstructural causes of material property differences in ceramics [20].

A transmitted ultrasonic beam will interact with all microstructural features such as grains, grain boundaries, pores, and secondary phases. The loss of acoustic energy as the beam interacts with the microstructure will be dependent on the frequency of the interrogating wave and the size, thermal properties, and elastic properties of the microstructural features [21, 22]. Advanced signal processing and wave deconvolution is the basis of understanding measured acoustic attenuation spectra and how they relate to the microstructure of ceramic materials [20, 22].

This dissertation will explore the relationship between the attenuation coefficient spectra and the microstructure of dense aluminum oxide. Scanning acoustic spectroscopy

will be utilized to spatially measure the attenuation coefficient spectra over large sample areas. Results will show correlations between microstructural variations such as grain size differences and additive concentration. Acoustic spectroscopy will support the use of this technique as a viable characterization tool for high density alumina. The ability to collect acoustic data over large sample areas leads to the ability of performing spectroscopic analysis to obtain microstructural information about every point in a sample. This information would be invaluable to finite element modeling as it would limit the assumptions that need to be made regarding grain and inclusion size, and their distributions.

First, a background on alumina, applications involving the use of alumina, ultrasound, ultrasound NDE, and acoustic spectroscopy will be presented at length. The method of attack will cover how the objectives of this thesis will be met. The experimental method will explain the specifics of the sample sets and exact detail of testing that was performed to achieve the goals of the objectives. The results and discussion section will explain the use and comparison of necessary curve fitting algorithms, the enhancement of the acoustic hardware, and connections between microstructural variations in alumina and acoustic spectra. A discussion of the outcomes of this research and considerations for future study will conclude this thesis.

This dissertation studies the effect of different alumina microstructures on acoustic loss mechanisms. Specifically, the two acoustic loss mechanisms studied are intraparticle thermoelastic absorption and Rayleigh and stochastic scattering. Two sample sets which contain incremental concentrations of separate secondary phases, mullite and titanium carbide, will be used to study the effects of acoustic absorption. An

alumina sample series which contains samples having different grain sizes will be used to determine a correlation between grain size and the degree of scattering attenuation. The results of this thesis will allow for the ultrasonic nondestructive prediction of microstructural parameters within dense aluminum oxide.

2. Background/ Literature Review

The background and literature review section of this dissertation provides an explanation of the concepts and topics necessary to understand the work performed in this thesis. As the focus of this thesis is on aluminum oxide, a principal consideration is given to the discussion of the fundamentals of Al_2O_3. This includes a focus on material properties, applications, and fabrication of high density alumina. The principles of acoustics, ultrasonic NDE, and the behavior of acoustic waves within dense ceramic materials are discussed. More detailed consideration is given to the phenomena of frequency-based acoustic attenuation in dense polycrystalline materials through the means of acoustic absorption and scattering. The implications of understanding the absorption and scattering mechanisms in aluminum oxide are explained. This will delineate from an explanation of previous acoustic attenuation measurements performed in material systems other than ceramics. Ultrasound NDE testing methods and the individual components which comprise a test setup are also explained.

2.1. Aluminum Oxide

Aluminum oxide is one of the most widely studied and used materials in the world. Otherwise known as alumina, its chemical formula is Al_2O_3; having four aluminum atoms to six oxygen atoms per rhombohedral primitive unit cell [23]. The Al_2O_3 unit cell has a hexagonal crystal symmetry, where a single alumina grain has an

appreciable degree of anisotropy, approximately 5.5% between the a and c crystal directions [24]. Aluminum oxide comes in several forms with corundum (or alpha alumina) being the most common and the only alumina phase stable at all temperatures [25, 26]. Alpha alumina was once thought of as being the only form of crystalline alumina that existed, but that is no longer the case. Other forms of emerging metastable aluminas are known as γ, δ, η, θ, κ, χ polymorphs [25]. Different forms of alumina occur due to differences in crystal structures. For instance, alpha alumina has a trigonal crystal structure while gamma alumina has a cubic structure [27].

This section of the literature review will examine details related to aluminum oxide and its uses as a high performance ceramic material. For the sake of this thesis, aluminum oxide, alumina, or Al_2O_3, refers to the as-manufactured polycrystalline dense ceramic used for laboratory, industrial, or structural applications. This alumina is produced commercially, has trace impurities and additives in it, and bears little resemblance to the precious gemstones in its family. A discussion of the properties which make alumina a favorable material for many applications is presented. The specific properties of interest for structural alumina used in high strain-rate environments are briefly explained. This section ends with a review of synthesis methods used for creating high density aluminum oxide. The use of sintering additives and their effects during sintering are examined.

2.1.1. Aluminum Oxide Material Properties

In 1887, Karl Bayer created a process which was used to refine bauxite and manufacture aluminum oxide. Bauxite is an aluminum ore which contains up to approximately 50% Al_2O_3 with the rest being water, iron oxide, silica and titanium

dioxide. The process involves the leaching of bauxite with NaOH, crystallization of aluminum trihydrate and subsequent calcining to produce alumina [28]. Other refining processes may be necessary to remove trace impurities resulting in different purity grades of aluminum oxide. The purity, or difference in phase percent of bulk alumina powder required, is dictated by the end application. Fully dense commercially manufactured alumina has a theoretical density of $3.97 g/cm^3$ [29]. Fully dense products may have a range of color, but typical dense polycrystalline alumina used for structural applications is either white or ivory depending on where the base alumina powder originated from and how large the grains are [26].

Aluminum oxide is one of the most readily available, economical, and widely used of the engineering ceramics [26, 30]. This is due to the versatility and superior combination of its material properties. High hardness and strength, good thermal conductivity, strong chemical resistance, and outstanding dielectric properties are some of the available properties alumina has to offer. From a production standpoint, alumina is a relatively routine material to produce when compared to other high hardness ceramics. The ability to cast alumina and form it into a variety of shapes and geometries is another reason why it is preferential for a multitude of uses. Applications and production methods of aluminum oxide are discussed in length after an examination of the material properties which make alumina the suitable choice for such applications.

The material properties of alumina are discussed to give a foundation regarding the testing performed on the materials used in this thesis. The ability to perform electron microscopy on the alumina samples studied relies on an understanding of their mechanical properties and electrical properties such that they can be properly prepared

for the microscope. Good ceramographic preparation of high hardness, brittle materials requires knowledge of their mechanical properties. Knowing if the material is a strong electrical insulator or conductor is important as it dictates whether charging will occur once the samples are interrogated with an electron beam. An understanding of the thermal properties of alumina is required for this thesis, as one of the two primary loss mechanisms studied is based on coupling of the thermal and elastic fields produced by propagating acoustic waves.

All of the mechanical properties described in the following section are directly related to grain size. This thesis outlines a method to acoustically predict grain size in aluminum oxide. As with some metallic materials, a metric which ranks mechanical properties (such as hardness, toughness, and strength) can be created using the grain size information collected via nondestructive means. A review of this is discussed in section 2.3.2.

2.1.1.1. Electrical Properties

Choosing a material for its electrical properties is dictated by what the material will be used for and if it even has suitable properties for the application. Knowing the specifics about all the electrical properties of the material of choice will lead to a better understanding of how it can be used. With regards to electrical properties materials are usually first classified as electrical insulators or conductors with special classes being semiconductors and superconductors. In simple terms, electrical conductivity is a measure of how well a material supports the movement of an electric charge [31]. Although it has been shown that certain surfaces of alumina can be strongly conductive

(such as the $(\bar{1}10)$ surface), alumina is generally a strong electrical insulator with a very wide band gap [23].

High volume resistivity and dielectric strength are what make alumina an excellent electrical insulator [30, 32]. Volume resistivity is the inverse of electrical conductivity and increases with an increase of a materials electric bandgap [33]. Dielectric strength is a property of an insulating material which dictates the amount of electric field strength the material can withstand before experiencing a breakdown of its insulating properties [32]. The strong electrical insulation behavior of alumina makes it a difficult material to examine using electron microscopy on, as the electron charge tends to build up on the surface. To alleviate this problem, a thin layer of a metal coating can be put on alumina samples to prepare them for microscopy. An accelerating voltage which matches the zero point of charge (~2kV) of alumina may also be used.

2.1.1.2. Thermal Properties

The high negative free energy of formation of aluminum oxide makes it a chemically stable and refractory material. Its excellent thermal properties allow alumina to be used in harsh or high temperature environments. Understanding the thermal properties of alumina will aid in a later discussion on acoustic energy dissipation and acoustic spectroscopy. The thermal conductivity of a material is its ability to conduct heat. Having units of watts per meter Kelvin (W/m·K), thermal conductivity determines the rate at which thermal energy is transported through a material [34]. Al_2O_3 has a relatively high thermal conductivity making it useful as a high temperature material [26].

The tendency for a material to change its volume in response to changes in temperature is known as thermal expansion. A quantification of this phenomenon is

known as a materials thermal expansion coefficient (TEC) [34]. TEC will generally vary as temperatures change and is an extremely important thermal property to understand when choosing a material for applications which involve cyclic temperature changes. Materials with microstructures that exhibit large thermal expansion anisotropy are prone to temperature induced failure. This is caused by the random orientation of the microstructure expanding and contracting by different amounts in different directions. Local stresses in the microstructure will begin to nucleate cracks if high TEC materials undergo rapid and large changes in temperature (thermal shock). Aluminum oxide has a relatively low thermal expansion coefficient which makes it suitable for use with high temperature systems. These thermal properties become important when studying the effects of acoustic thermoelastic absorption in dense aluminum oxide and will be discussed in a later section when describing this type of acoustic absorption in alumina.

2.1.1.3. Mechanical Properties

The work presented in this dissertation focuses on high density, polycrystalline alumina used for structural applications and the relationship between microstructure, mechanical properties, and acoustic response. To facilitate an understanding of these relationships, this section gives a more detailed discussion with regard to mechanical properties of interest, what they are, and why aluminum oxide exhibits desired mechanical behavior. Structural alumina is an attractive ceramic used for engineering purposes due to its low areal density, and high properties such as strength, toughness, and hardness [1, 35]. The ability of increasing or changing these properties is obtained through modification of the microstructure [10, 35]. This can be done by changing composition through the use of different formulations or by using different processing

methods. The need and ability of obtaining specific mechanical properties of a structural ceramic is limited by a variety of factors including cost, feasibility of mass production, and type of ceramic to be used [1, 2]. A table containing strength, toughness, and hardness values for commercially available alumina is shown at the end of this section.

2.1.1.3.1. Mechanical Strength

Mechanical strength is the maximum stress a material is capable of withstanding before undergoing an irreversible change in its structure [36]. There are several definitions of strength which describe the material during different states of stress: yield strength, tensile strength, compressive strength, and shear strength [37]. Under loading, materials undergo elastic deformation, or a strain, where the structure returns to its initial state after the stress is applied. For the stresses exerted on the material which only lend to elastic deformation a plot of stress versus strain will produce approximately a straight line; this is shown in Figure 1 as the elastic region. As the loading stress on a material increases this straight line begins to deviate at a stress (point σ_Y in Figure 1) referred to as the yield stress. After the yield stress is reached irreversible deformation (plastic deformation) continues to a maximum point known as the materials tensile strength (point σ_T in Figure 1). This is the final maximum stress a material can withstand in tension before fracture and failure occurs (point F) [36, 37]. It is important to clarify that this type of behavior occurs primarily with ductile materials such as metals and not ceramics, such as aluminum oxide. This is due to the strength of metallic bonds and the propensity of dislocation slipping [36].

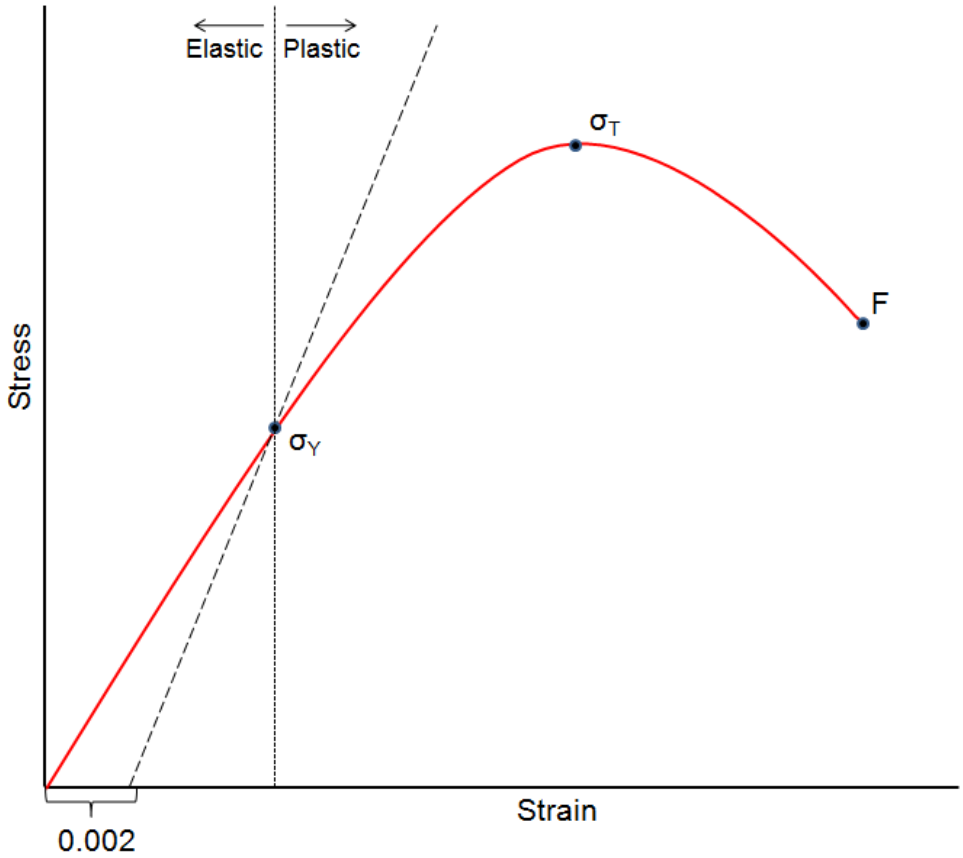

Figure 1. Stress-strain behavior exhibiting points of yield stress, tensile stress, and failure.

Brittle materials such as ceramics are characterized as being either ionically and/ or covalently bonded materials [38]. These bonds are stronger than what is seen in metals where dislocation movement and slip occur. As a result, many brittle ceramic materials undergo cracking and failure before a yield stress is reached. Typically, ceramic materials will fail while still behaving elastically and do not have a well defined yield point [39].

Compressive and shear strength are similar to their tensile counterpart as they relate to stress-strain behavior into the permanently deformed plastic regime. However, the stress directions are different from tensile testing, being either compressive or torsional. Compression strength for a ceramic is the minimum compressive stress the

ceramic can withstand before crack propagation or slip across a weak atomic plane occurs [38]. Compressive strength is important for alumina used in structural applications as it provides resistance to static, quasi-static, or dynamic loading [40].

Grain size and defects are microstructural factors which play a role in a material's strength [41]. Material strength is determined by the types of bonds it has and the ability of those bonds to stretch or move. Under loading, atomic planes within grains with bonds that are already broken and reoriented (dislocations) are the easiest to strain [37]. As the stress is increased, these partially broken atomic planes will move to the grain boundary where they are pinned. At this point even a metal becomes brittle and will fracture. Ductile materials, such as metals, have a comparably higher amount of dislocations compared to brittle ceramics due to their differences in bonding and bond strength (metallic bonding versus ionic and/ or covalent). In a metal or ceramics, the larger a grain is, the more dislocations. An increase in the number of dislocations will lead to a greater ability of a stress to cause more strain and therefore decreases strength. This phenomenon can be expressed through the Hall-Petch equation (equation1) [38].

$$\sigma_y = \sigma_0 + k_y d^{-\frac{1}{2}} \qquad \text{Eq. 1}$$

where σ_y is the yield strength, d is the average grain diameter, and σ_0 and k_y are material constants.

Defects within a material matrix act as stress concentrators where stress near the tip of a defect will change upon loading [36]. Griffith developed a sufficient and necessary condition to answer the question of the plane stress required to disrupt bonds at the tip of a defect, such as a microcrack (equation 2) [42]. The Griffith equations are

based on energy conservation to account for stored elastic energy, surface energy, and the work done by the system on its surroundings [43].

$$\sigma_f = \left(2E\gamma/\pi c\right)^{\frac{1}{2}} \quad \text{Eq. 2}$$

where σ_f is the fracture stress, E is Young's modulus, γ is surface energy per unit area, and c is half crack length. Essentially as the crack length increases the stress a material can withstand before fracture decreases. High mechanical strength is but one of many important physical properties alumina must have to be a good engineering ceramic. One single parameter for relating the quality of a material does not exist; all parameters must be taken into account.

2.1.1.3.2. Fracture Toughness

Toughness is defined as the ability of a material to absorb energy up until the point of full catastrophic fracture of a crack [38]. Toughness, denoted as K_{IC}, depends on the specimen geometry, the applied load, and the flaws present in the bulk microstructure or at the surface [43]. A higher toughness value usually indicates that there are microstructural mechanisms which are capable of dispersing energy without the need for forming cracks. Metals tend to exhibit higher fracture toughness values when compared to ceramics because they are able to dissipate energy during loading through plastic deformation; brittle ceramics tend to break before that point [38].

Toughness can be delineated into three modes, $K_{I,}$ K_{II}, and K_{III}, which completely dictate the stress interaction for all types of loading [36]. These modes relate to the method of fracture that is occurring due to the type of stress which is applied. Mode I is indicative of fracture occurring in an opening direction, and modes II and II indicate

either in-plane shearing or anti-shearing, respectively [36]. It is assumed that fracture mode I completely dominates the other two types of modes in polycrystalline ceramics as failure occurs at the largest flaw normal to the greatest tensile stress [36]. As a result modes II and III are usually ignored and a single critical value, K_{IC}, has been defined to be the point where an open crack is in equilibrium and further loading will cause rapid and uncontrolled failure. This is expressed in the following equation:

$$K_{IC} = Y\sigma_f\sqrt{\pi a} \quad \text{Eq. 3}$$

where Y is a dimensionless factor dependent on flaw shape and loading geometry, σ_f is the fracture stress, and a is the flaw diameter [36].

2.1.1.3.3. Hardness

Hardness is a measure of material resistance to localized plastic deformation [38]. Hardness testing is one of the most common types of mechanical measurement performed on materials as it is fast, inexpensive, simple to execute, and only require a small amount of material. The desirability of alumina for high strain rate applications is due to its high hardness. Aluminum oxide, second only to diamond (of the naturally occurring materials), has an approximate hardness of approximately 14GPa (Knoop at 50N) [44, 45]. Hardness is fundamentally reliant upon material bond strength. Materials which exhibit high ionic and covalent character are usually attributed to also having high hardness [46].

Hardness is a relative measure with many different scales. The Mohs scale was the first hardness scale to be used where materials were qualitatively organized according to which material could scratch the other [37]. Systematic and quantitative methods were created through the development of standardized indentation testing. This type of testing

is useful for categorizing brittle ceramics which fall in the Mohs range of 8-10 [37]. In these tests, a small diamond tipped indenter is pressed into the surface of a material with a predefined load and rate. The resulting indent size is measured and related back to a hardness number predefined through specified equations [47]. Depending on which scale is used (Knoop, Vickers, etc.), the resistance to indent penetration is expressed in direct units, rather than the Mohs ranking system [38].

Different types of indentation testing require different indenter shape geometries. In the ceramic industry, Knoop or Vickers indentation testing are the most commonly used methods for determining hardness [44]. These two hardness scales are not directly comparable due to their differences in determining stress imparted to the material from the indenter. The Knoop calculation uses the projected area of the indenter while a Vickers calculation relies on the contact area of the indenter [44, 48]. Figure 2 shows Vickers versus Knoop indents for fully dense Al_2O_3. Vickers indentation imparts a pyramidal square shape to the material while a Knoop indent leaves an elongated pyramidal square shape.

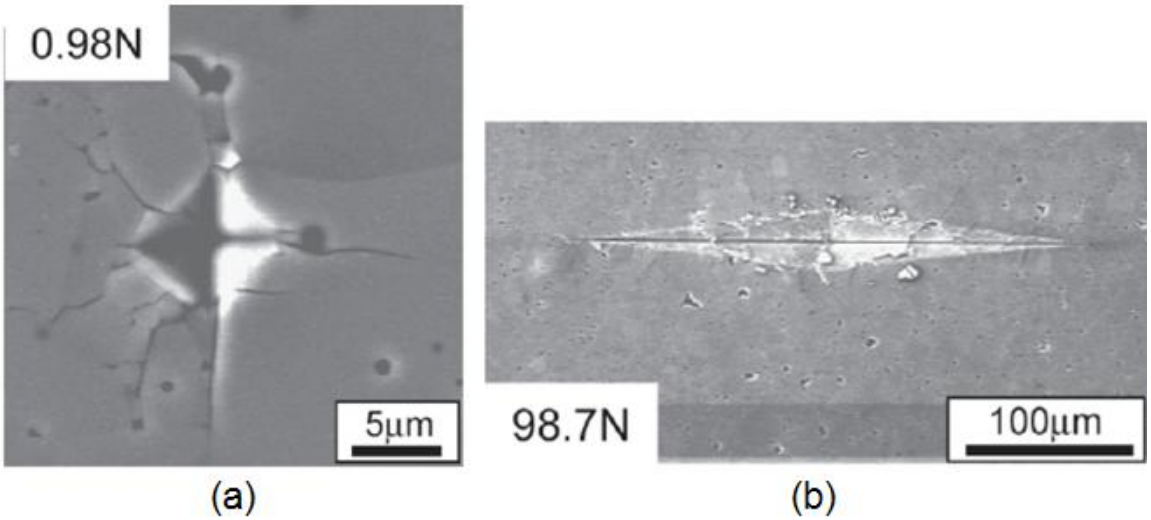

Figure 2. Vickers (a) versus Knoop (b) indents for Al_2O_3 [44].

Load's that are too high for brittle ceramics will result in massive cracking and spalling of the material. These types of indents are not recommended to be used when making a hardness measurement [48]. It is well known that hardness of ceramics will, in fact, decrease with increasing load. This is known as the indentation size effect (ISE) where very low loads will give very high hardness values, and as load increases, hardness values will decrease and become independent of load [44]. A clear reason for this effect is yet to be determined, but it is suspected that testing procedure, strain rate effects, frictional forces, material dislocation, material elastic recovery, and material cracking all play a role in the ISE [49-52] . Hardness versus load curves which exhibit the ISE for several high hardness ceramics are shown below in Figure 3.

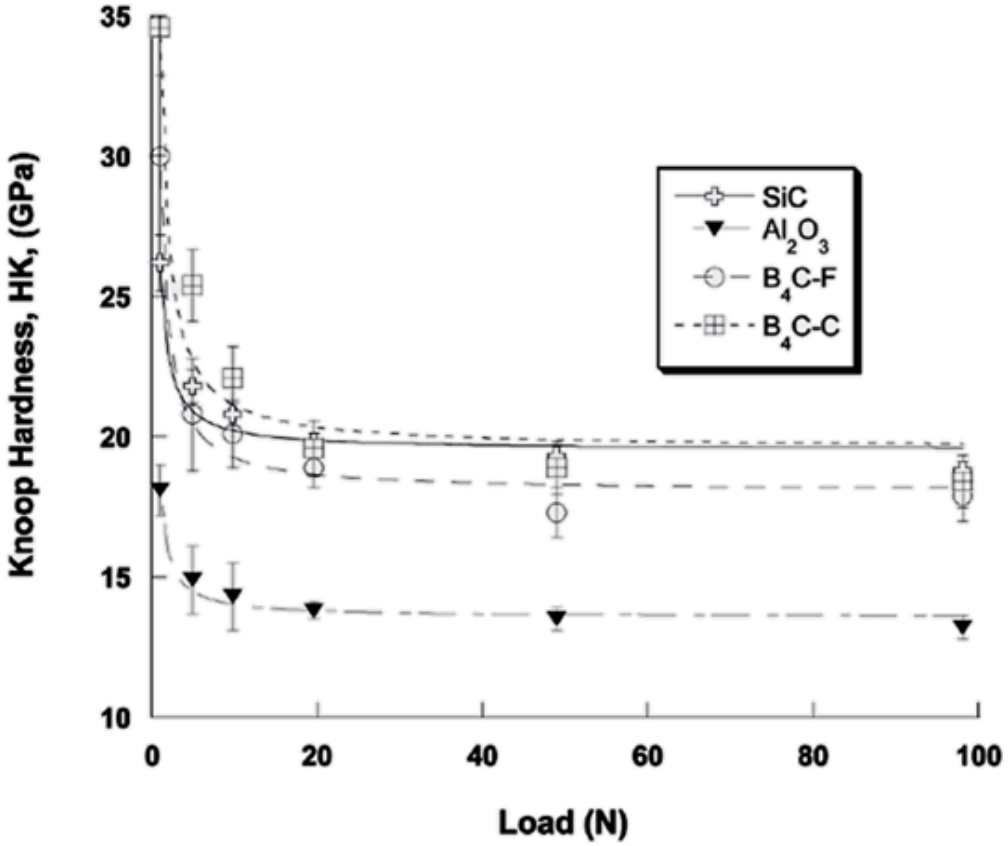

Figure 3. Load versus hardness curves for several high hardness ceramics. Shows indentation size effect [44].

As with strength and toughness, changing a material's grain size will alter its hardness [36, 38]. Decreases in grain size decrease the statistical amount of inherent dislocations within a grain [36]. With fewer dislocations, slip does not occur as readily and the material will exhibit high resistance to indentation. As grain size increases, ceramics will contain a higher amount of dislocations which do not aid in opposition to indentation. This effect is analogous to the Hall-Petch effect, and it should be noted that there exists a lower critical grain size where the opposite takes place [38]. As grain size decreases the overall surface area of the grains increase. This causes an increase in grain boundary volume percent about the entire material. When the grain boundary percentage rivals that of the actual material, an indent will be sampling much of the weaker grain boundary rather than the material grains themselves [36, 38]. This leads to a reversal of what is expected from the Hall-Petch effect.

Table I. Various Mechanical Properties of Al_2O_3 [26, 44, 53]

Property	**99.9% Al_2O_3**
Tensile Strength (MPa)	
At 25°C	310
At 1000°C	220
Compressive Strength (MPa)	
At 25°C	3790
At 1000°C	1929
Toughness K_{IC} (MPa·m$^{1/2}$)	4.9 (+/- 0.9)
Hardness (Gpa)	
Knoop at 1N	17.5 (+/- 1.5)
Vickers at 1N	17.5 (+/- 1.5)

2.1.2. Applications of Aluminum Oxide

This section of the dissertation describes some of the applications where aluminum oxide is used. These applications are categorized according to the material property being exploited. Its combination of excellent properties has enabled Al_2O_3 to

become one of the most commonly used materials in the world. Being abundant, inexpensive, and easily manufactured markets for alumina extend from electronic substrates to furnace liners to armor [30, 54]. There are quite a number of uses for alumina; this section describes at most three per category of application.

2.1.2.1. Al_2O_3 Applications: Electronic

A large portion of electrotechnical ceramics are based on aluminum oxide. For example, the high volume resistivity and high dielectric strength of alumina has been exploited by the automotive industry to be used as insulators for spark plugs. The ability to reduce sintering temperature of alumina through the addition of sintering aides facilitates the production of spark plug insulators without degrading necessary electrical properties. Cost of production is decreased by using lower temperatures and maintaining the integrity of the insulating alumina [55]. Today, more than 3 million high-purity alumina spark plugs are produced each year by the automotive industry [56].

The electronics industry also benefits from using alumina as the material of choice for electronic substrates. The role of the substrate is to form an electric circuit by creating interconnections. Aluminum oxide is a widely used substrate mainly due to its low cost and high voltage insulation [57]. Alumina substrates consisting of arrays of pores can be used in the manufacturing of ultra-high-density magnetic recording and storage media. Alumina substrates are an attractive choice for this application due to the ability of creating excellent uniformity and spacing of nano-pores [58]. As an example, the high density and ordering of the alumina nano-pores allows separate but densely packed nickel arrays to be grown and ultimately achieve a gain in electronic storage capacity [58].

2.1.2.2. Al_2O_3 Applications: Thermal

A refractory material is one that retains its shape and composition despite exposure to extreme temperatures. Certain high temperature furnaces use alumina refractory bricks to line the walls. The need for refractory furnace lining is to contain radiant heat within the furnace and allow it to dissipate at a safe rate. These materials also need to resist the attack of molten glasses and metals [26]. Alumina-based refractories are capable of withstanding high temperatures without undergoing thermal shock or phase changes. Aside from this, alumina refractories offer good chemical attack resistance at high temperatures [59].

The stability of Al_2O_3 at high temperatures, its resistance to chemical attack, and its low cost make it the preferential choice for laboratory ware. Alumina lab ware such as crucibles, ignition dishes, boats, and lids, find use in laboratories for molten metal and glass processing, rapid thermal cycling, and gemstone purification [60]. Alumina used for furnace ware has found a very useful application for thermocouple protection tubes. Thermocouple protection tubes need to be capable of withstanding high temperatures and pressures along with resistance to chemical aggression. Alumina-based protection tubes meet the requirements for protecting thermocouples in harsh environments where other coverings (such as Teflon) would fail [61].

2.1.2.3. Al_2O_3 Applications: Mechanical

Aluminum oxide finds tremendous use as industrial milling media, grinding material, and polishing abrasive. Its low cost, high hardness, and high strength make it an excellent substitute compared to the more costly industrial diamond [62]. Abrasive alumina is made in a multitude of ways to address all cutting, grinding, and polishing

needs. The different types of alumina abrasives are classified according to their manufacturing process, hardness, purity, and classification process [63]. The main types of alumina produced for industrial abrasives are either monocrystalline, calcined, or polycrystalline alumina with different sub-characterizations depending on grain shape and purity [63]. There is a difference in performance of each type of alumina abrasive depending on the crystal structure of the alumina used; either the harder alpha alumina or the softer gamma alumina. Reduction of particle sizes can be done through milling methods using alumina as the contact media [26]. For materials which require fine polishing and lapping, such as electronic substrates, alumina can be used in suspension as submicron particulates. Different types of alumina abrasive media are shown in Figure 4. Aside from industrial polishing, Al_2O_3 has found its way into another widely used item, toothpaste. Toothpaste gets its power from the added abrasives such as alumina, calcium phosphate, or silica [64].

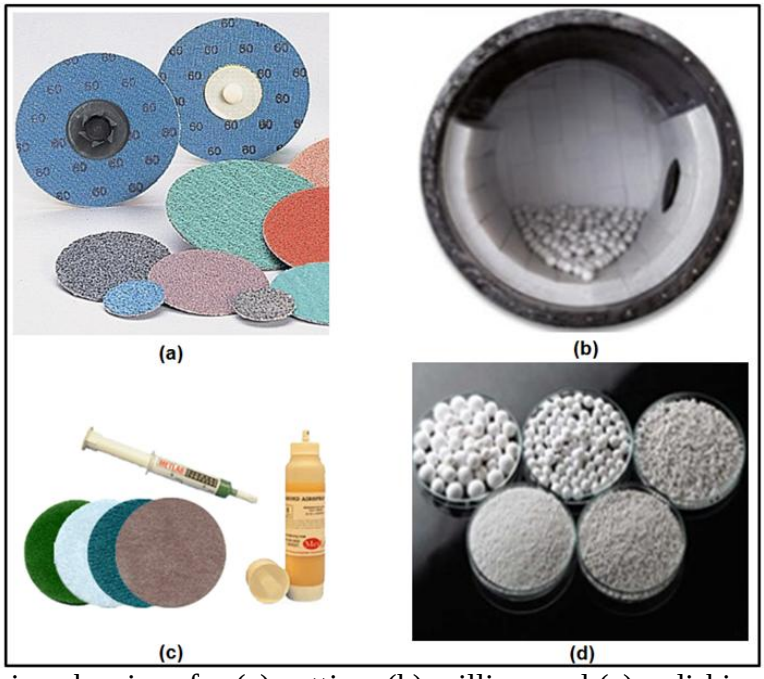

Figure 4. Alumina abrasives for (a) cutting, (b) milling, and (c) polishing. (d) Different sized Al_2O_3 milling media [54, 65].

Ceramics have been used in armor systems for at least half a century [66]. Their low density, high hardness, and high Young's modulus make them attractive candidates for armor applications [1]. Although ceramics generally have lower tensile strength compared to their metallic counterparts, the high compressive strength of ceramic materials is exploited by integrating them into multi-layer armor packages for personnel or vehicular use [66]. Alumina armor ceramic small arms protective insert (SAPI) plates and monolithic tiles can be seen in Figure 5.

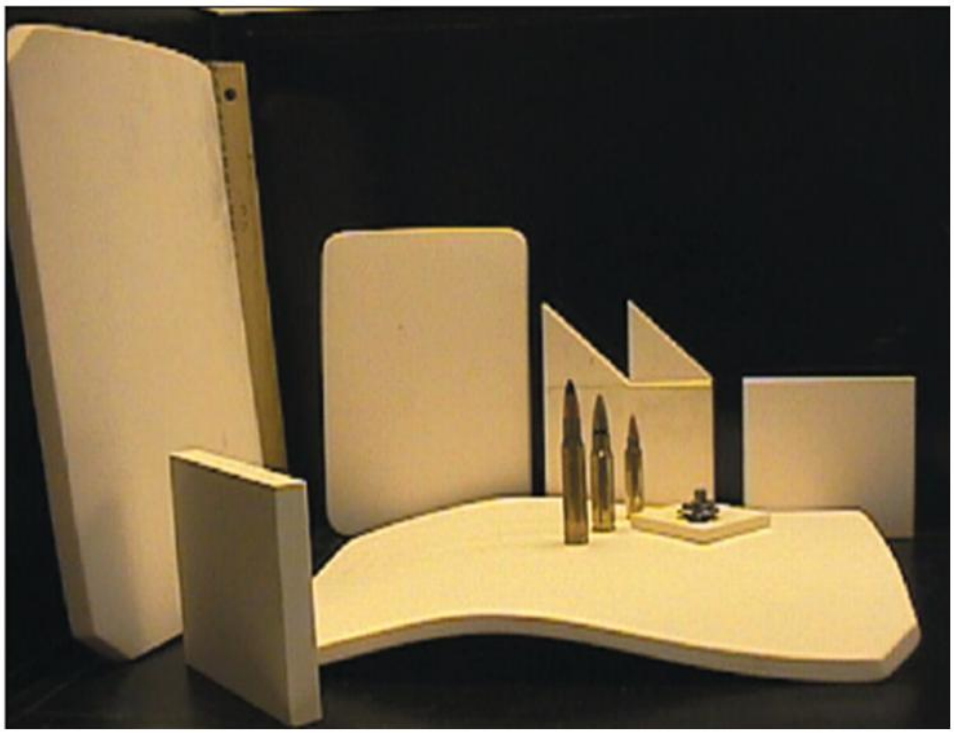

Figure 5. Al_2O_3 monolithic tiles used in armor applications [1].

Alumina armor systems are usually based on different compositions such as Al_2O_3-SiO_2-CaO-MgO, Al_2O_3-MgO, or Al_2O_3-ZrO_2. These additives all play different roles in either production or performance processes and will be discussed in the next section of this dissertation. Alumina-based armor ceramics have a high level of physical properties, can be manufactured using a variety of methods, and low costs make them suitable candidates for ballistic protection [1]. Although there is no single parameter

which is used as a metric to predict ballistic performance, higher properties such as hardness, elastic modulus, and sonic velocities above 10,000 m/s have been correlated with better performing materials [1, 2]. Alumina meets these requirements with having hardness values of 17.5 GPa (Knoop), Young's modulus as high as 450 GPa, and longitudinal velocity of approximately 10,500 m/s [2, 44].

2.1.3. Evolution of Dense Microstructures

This section focuses on the complete cycle of manufacturing a dense alumina-based body. The use of sintering additives to improved densification is discussed. Common sintering aids used to lower sintering temperature include SiO_2, CaO, and MgO. Other additives can be introduced into an alumina microstructure to provide reinforcement of particles. This will lead to an improvement in mechanical properties of alumina-based materials used for high stress applications.

2.1.3.1. Sintering Additives

The driving force for sintering is the reduction in the total free energy of the system, including the volume, boundaries and surfaces of the grains [10]. During sintering one looks to facilitate mass transport mechanisms to aid in densification. Transport mechanisms which lead to densification include lattice diffusion and grain boundary diffusion [10, 67]. Additives can be used to control sintering behavior and obtain different material properties from the final product. The types of sintering additives discussed in this section are contained in the alumina-based sample sets studied in this thesis. Their effects on sintering and mechanical properties are outlined.

Glassy grain boundaries rich with SiO_2, CaO, and MgO are commonly found in many commercial aluminas. These are common additives which are introduced to Al_2O_3

during sintering include a mix of CaO-MgO-SiO_2. The use of these additives allows one to lower sintering temperatures, control grain growth rates, and reach full density [68]. Using a mix of these sintering additives with alumina has an effect on liquid phase sintering which can be described in three stages: particle rearrangement, solution-reprecipitation, and coalescence. Particle rearrangement is the rearrangement of the solid particles due to the capillary forces of the formed liquid. This leads to the initial densification of the alumina compact. The different solubilities of the solid in the liquid allow transport of Al_2O_3 material from points of solid-solid contact to free surfaces of the alumina particles. Finally, permanent solid-solid contact between particles form and the liquid phase sintering job of the CaO-MgO-SiO_2 is complete [69].

The phase diagram of the CaO-MgO-SiO_2 can be seen in Figure 6 with the eutectic highlighted. Using these additives and forming liquid at grain boundaries is critical as it facilitates densification with a high diffusivity path of material during sintering [7]. The use of a mix of additives such as CaO-MgO-SiO_2 is chosen not only to form a liquid at the grain boundaries but to also control crystallization and abnormal grain growth [70]. Without the mix of these three additives one may find difficulty with forming a lower temperature liquid without reacting with the Al_2O_3 [69]. The eutectic from the CaO-MgO-SiO_2 system has a low melting temperature of 1320°C which forms a liquid phase at sintering temperatures but does not necessarily enter into chemical reactions with the alumina [69, 70].

Problems with using sintering additives in alumina arise if they are improperly or nonuniformly mixed. These additives may agglomerate and form large glassy inclusions which can degrade the properties of a manufactured alumina tile. Aside from large

agglomerations, even uniformly distributed additives will play a role in controlling the final properties of a produced alumina product. Lower strength grain boundaries will decrease elastic properties, hardness, and strength in an alumina sample. Consideration must be given to the new interfaces and phases created when using sintering additives in alumina [68]. One of the several alumina sample sets which are studied in this thesis has had a CaO-MgO-SiO_2 mix introduced as sintering aids.

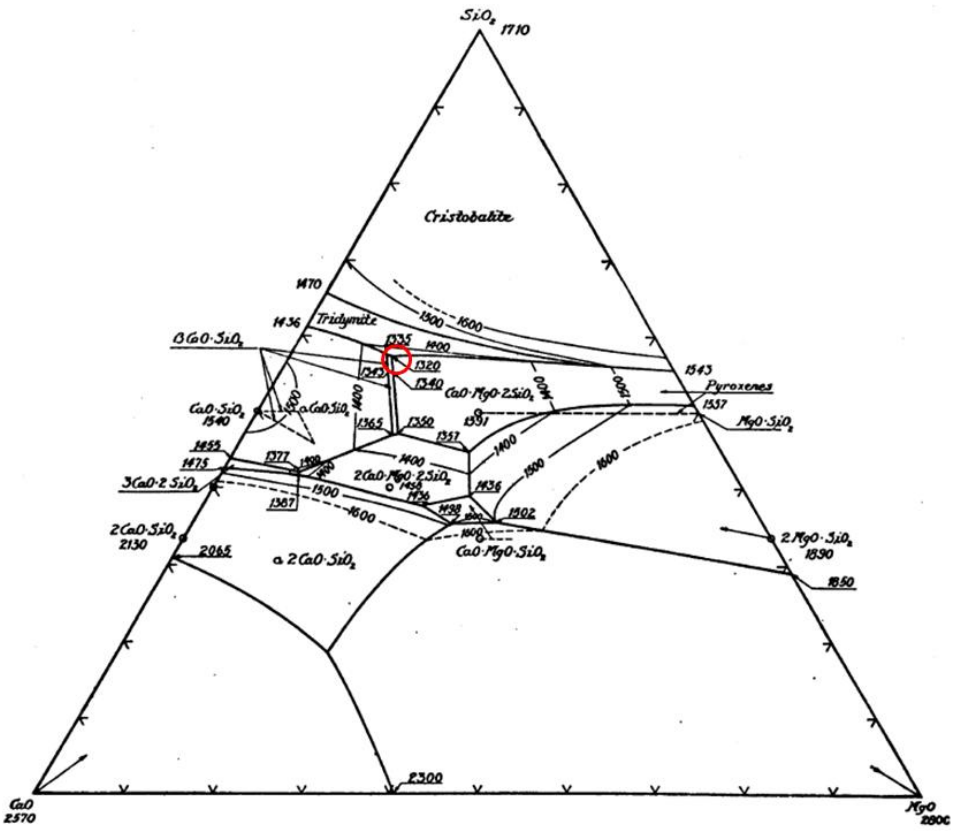

Figure 6. CaO-MgO-SiO_2 phase diagram. Eutectic at 1320°C highlighted in red [70].

Mullite within alumina and aluminosilicate ceramics are among the most used ceramic materials for refractories [71]. Creating the secondary phase of mullite (3:2 or 2:1 Al_2O_3:SiO_2) within an alumina host requires additions of SiO_2. A phase diagram of Al_2O_3-SiO_2 is shown in Figure 7. Pure mullite is formed with SiO_2 additions in the range of approximately 37-41wt%. SiO_2 additions less than this will result in a high alumina

and mullite solid solution. This secondary phase can enhance the thermal properties and the mechanical properties of the alumina host. For example, materials with two crystalline phases can have increased fracture toughness and strength compared to their singular phase counterparts.

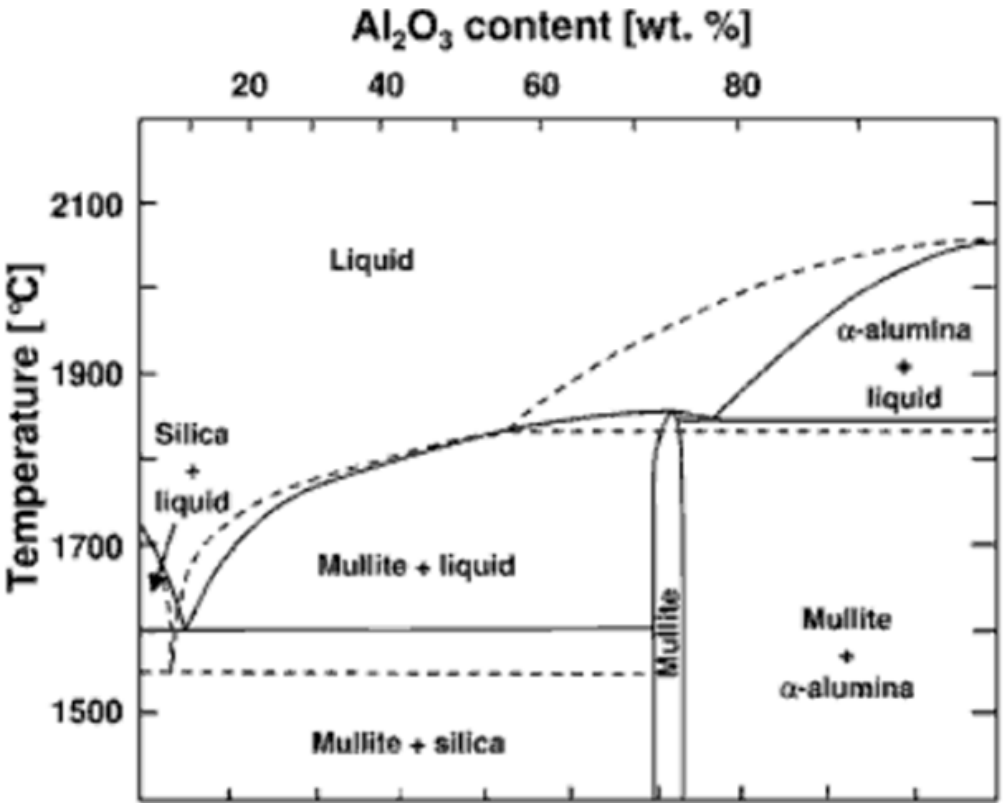

Figure 7. Al_2O_3-SiO_2 phase diagram [72].

Reinforcing alumina-based microstructures through the use of secondary phase additions leads to an increase in hardness, toughness, and strength. Typical additions to alumina microstructures to achieve this reinforcement behavior include ZrO_2, mullite, and TiC. Two of the sample sets studied in this thesis includes the latter of the two types of additions. These sample sets include different concentrations of mullite and titanium carbide were used to create a causal relationship between acoustic absorption and grain size distributions of secondary phases present in a dense alumina body.

Crystalline mullite in aluminum oxide has been studied for structural applications due to having a lower areal density; 3.2g/cm^3 for alumina-mullite compared to 3.95g/cm^3 for standard alumina [73]. Increasing the toughness and strength of alumina by addition of SiO_2 to create a secondary mullite phase is due to the structure of the mullite. Mullite can grow as long needle-like crystals which create longer fracture paths and ultimately give an increase in toughness [74]. A micrograph image of mullite crystals is shown in Figure 8. Creation of compressive residual stress at the surface of alumina grains and crack blunting are two mechanisms by which mullite increases strength of an alumina-based body [73, 74]. Remarkably high flexural strengths of alumina-mullite ceramics have been reported up to 350MPa [75]. Interest in alumina containing a secondary mullite phase comes from work done in this thesis testing an alumina-mullite sample set.

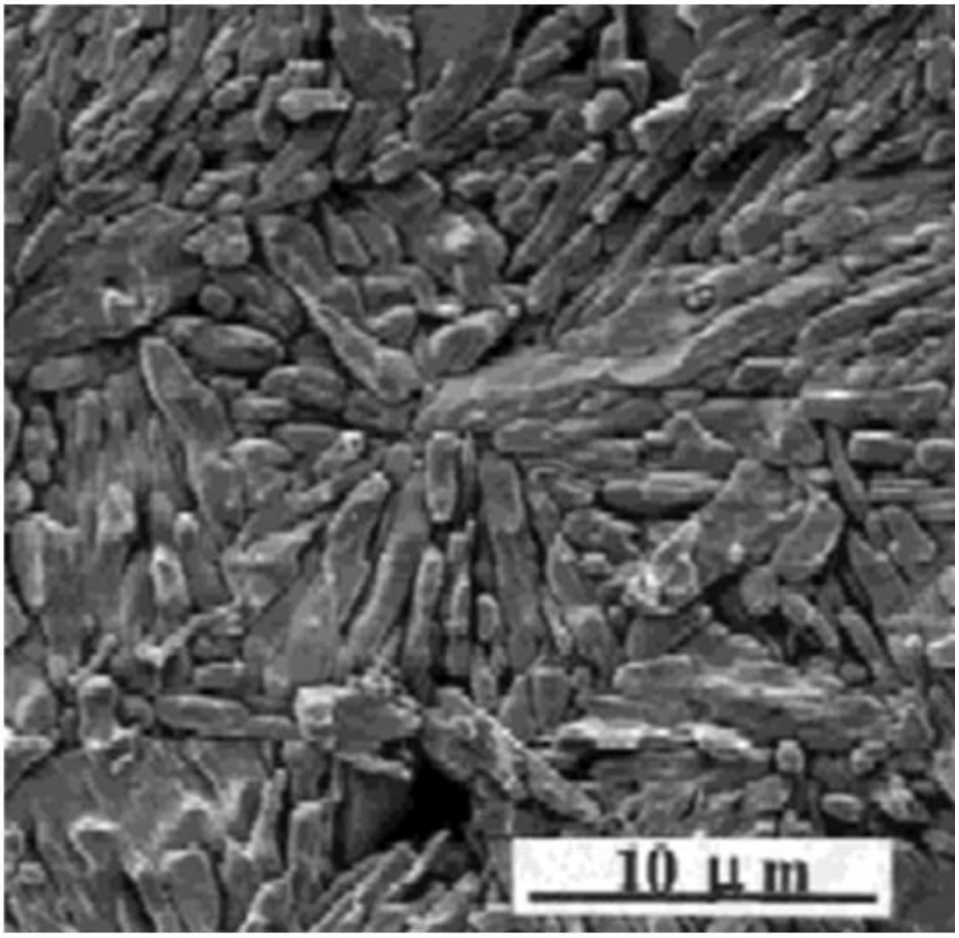

Figure 8. Micrograph image showing mullite grains [74].

Ceramic cutting tools based on aluminum oxide are desired for a number of applications including the aerospace, automotive, and steel industries [76]. Their refractory nature along with high compressive strength and wear resistance has necessitated their use at high speeds [76]. Titanium carbide (TiC) is a common cemented carbide which is added to Al_2O_3 which increases toughness and decreases unpredictable tool performance and brittle failure [77]. Alumina-TiC composites provide an improvement in hardness, fracture toughness, and strength when compared to alumina alone. These factors can be tuned by changing the initial titanium carbide parameters such as particle size distribution [77]. A micrograph image of an Al_2O_3-TiC composite can be seen in Figure 9.

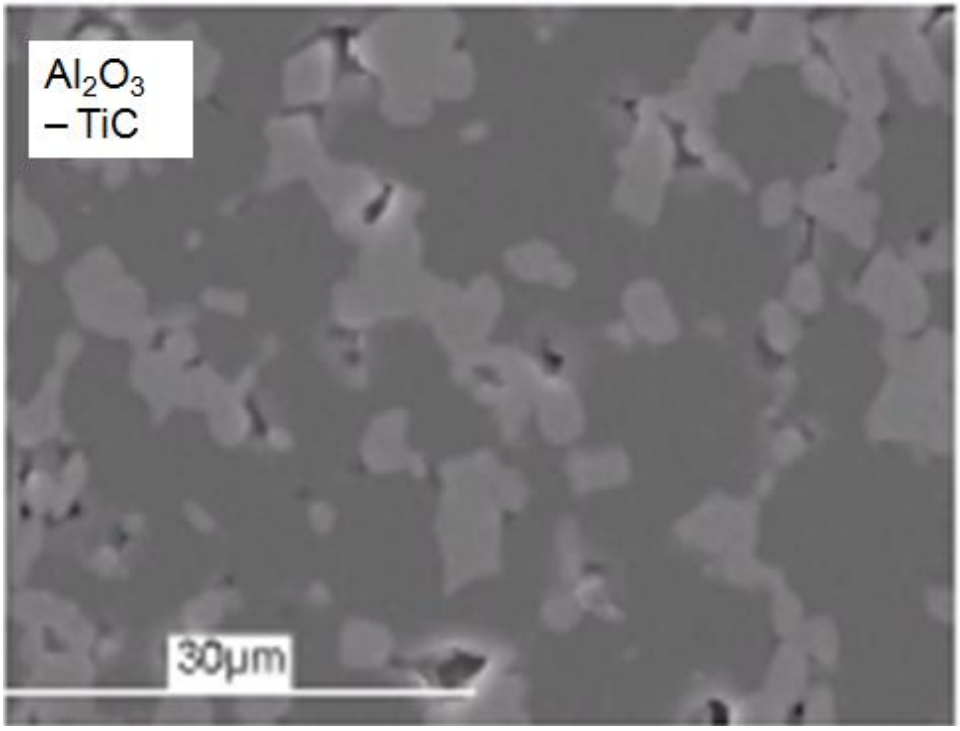

Figure 9. Al_2O_3–TiC microstructure. Dark areas are Al_2O_3; light areas are TiC [77].

2.1.3.2. Densification of Aluminum Oxide

Sintering additives are chosen to lower densification temperatures and to have the final product exhibit a change in material properties. Once these additives are properly mixed with the base powder, a densification method must be chosen. High hardness materials such as aluminum oxide can require high firing temperatures, high pressures, sintering additives, or combinations of the three [35]. The typical temperature for conventional sintering of Al_2O_3 is approximately 1500-1550°C [5]. Depending on the type and concentration of the sintering additives used, the optimal sintering temperature will vary.

Brittle ceramic materials which exhibit high hardness typically have some ionic or covalent character [38]. Alumina has approximately two-thirds ionic nature and one-third covalent nature [38]. Sintering kinetics of ceramics materials must be understood when densifying alumina. Compared to high-hardness carbides and borides, alumina has

relatively good sintering kinetics which are controlled by lattice or grainboundary diffusion [78-80]. Comparably lower sintering temperatures due to predominantly ionic bonding, good sintering kinetics, and the possibility of incorporating many sintering additives allows for many densification methods of alumina [5]. Sintering of Al_2O_3 to near theoretical densities has been achieved through techniques such as pressureless sintering, hot pressing, and novel sintering methods such as spark plasma sintering (SPS) [4, 10, 35]. While there are many production methods used to create high density alumina, they usually require four basic steps: preparing the body, molding, sintering, and finishing [35].

2.1.3.2.1. Pressureless Sintering

Pressureless sintering is the densification of a powder compact without the use of externally applied pressure. An advantage of sintering ceramics without pressure is that the ceramic compact can be slip cast into a variety of shapes and geometries. Alumina is a relatively easy ceramic to sinter due to its predominantly ionic bonding and lower working temperatures [26, 38]. It should be noted that pressureless solid-state sintering of alumina requires higher temperatures and result in slightly lower densities than alumina manufactured using pressure [10]. Figure 10 shows comparisons of the solid-state densification behavior between pressureless sintering and hot pressing. Micrograph images of pressureless solid-state sintered alumina are shown in Figure 11.

Pressureless sintering of alumina does not necessarily require the use of additives, but using them will result in faster sintering times, lower temperatures, and a more easily densified material [10, 35]. This is due to a liquid phase which is able to form due to the lower temperature additives. The liquid phase provides for faster atomic diffusion than

solid-state processes [10, 68]. Ceramic materials which are harder to sinter, such as silicon carbide, usually require sintering aids to reduce firing temperatures and create the high diffusivity liquid phase [10, 68].

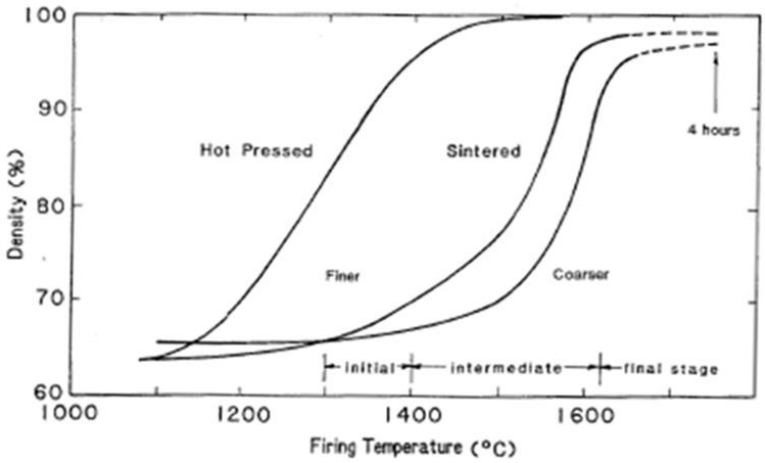

Figure 10. Comparison of solid-state densification behavior between pressureless sintering and hot pressing [10].

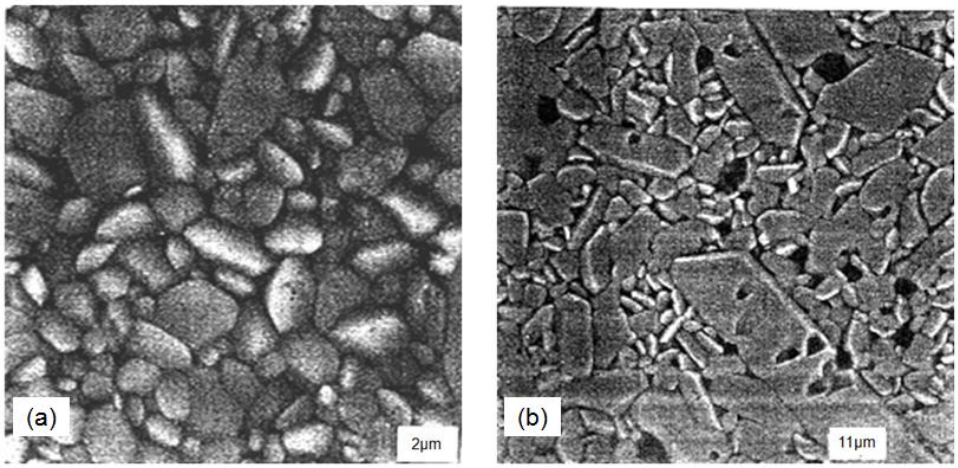

Figure 11. Micrograph images of pressureless solid-state sintered alumina [10].

2.1.3.2.2. Hot Pressing

Sintering with the application of heat and externally applied pressure is known as hot pressing. External pressure can increase the driving force for densification of a compact by acting against internal pore pressure without increasing the driving force for coarsening [10]. This can lead to the production of fine grained ceramics with higher

densities compared to those produced without the use of mechanically applied pressure. As shown in Figure 9, hot pressing allows for densification to occur more rapidly and at lower temperatures when compared to pressureless sintering.

Uniaxial hot pressing consists of pressing and sintering material within a die. When hot pressing high hardness ceramics such as Al_2O_3 one may typically use graphite dies to endure the necessary high sintering temperatures. This causes the industrial use of uniaxial hot pressing to be limited due to high cost, low productivity, die maintenance, and poor shaping possibilities. Aside from these disadvantages, hot pressing has great practical value as it provides a method for the densification of materials which show inherently poor sinterability such as SiC and B_4C [81].

The thesis work done by Peelen provides a comparison of dense hot pressed alumina with dense pressureless sintered alumina and that each showed a number of different characteristics. The much lower sintering temperatures used while hot pressing (~1400°C), compared with pressureless sintering (~1800°C), gives a smaller average grain size [82]. Pore size and position vary as well when performing hot pressing versus pressureless sintering of alumina. On average, the pore size one may expect to find with pressureless sintered alumina is 1µm while the average pore size found in hot pressed alumina is approximately five times less than this at 0.2 µm [82]. The lower grain boundary mobility during hot pressing leads to the majority of pores lying at the grain boundaries while pores in pressureless sintered alumina are usually found within the grains [82]. A comparison of hot pressed and pressureless sintered alumina is given in Table II.

Table II. Preparation and microstructural conditions of hot pressed and pressureless sintered Al_2O_3 [82].

	Hot Pressed Al_2O_3	Pressureless Sintered Al_2O_3
Temperature (°C)	1400	1850
Time (hours)	0.5	10
Pressure (MN/m^2)	125	0.1
Atmosphere	not critical	H_2
Additive	…	MgO
Mean Grain Size (μm)	1.5	25
Mean Pore Size (μm)	0.2	1
Density (g/cm^3)	3.982	3.982
Position of Pores	intergranular	intragranular

2.1.3.2.3. Spark Plasma Sintering

Spark plasma sintering (SPS) is a novel sintering technique which is thought to rely on plasma and Joule heating as the mechanisms for densification and grain growth [83]. Plasma heating occurs when the electrical discharge between particles results in a local and momentary heating at particle surfaces to reach several thousands of degrees Celsius [84]. The particle surfaces then melt, fuse together, and form necks between the particles. Joule heating generated by the pulsed direct current increases diffusion of the atoms in the necks enhancing their growth [84]. A diagram showing plasma and Joule heating is shown in Figure 12. The process is similar to conventional hot pressing in that the precursor powders are loaded into a die and uniaxial pressure is applied during sintering [85].

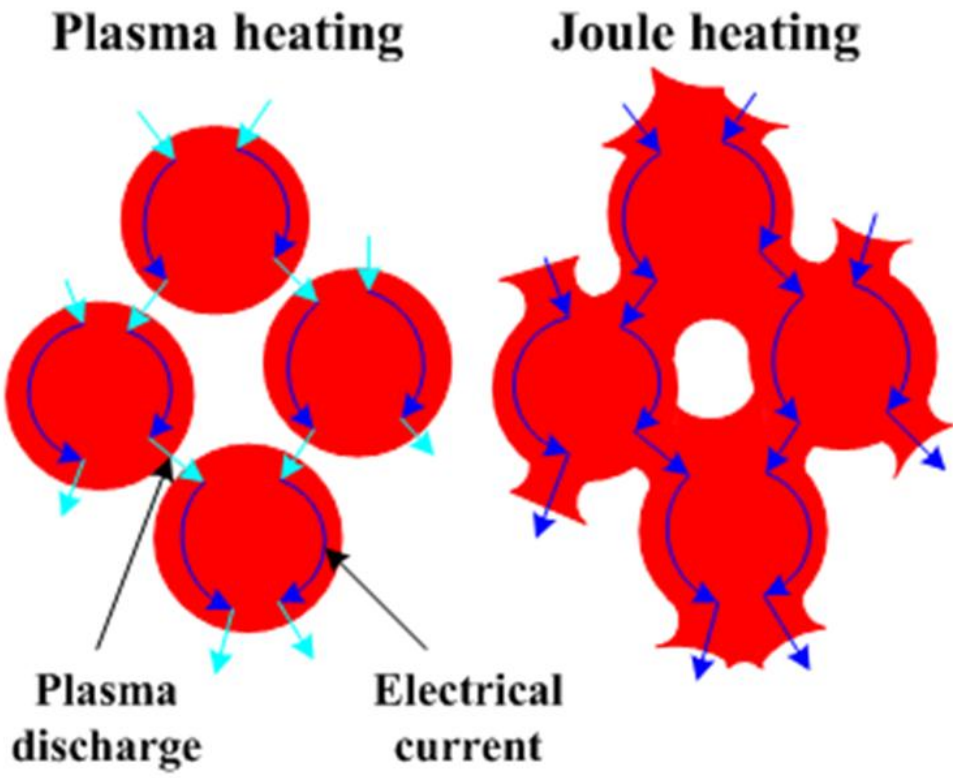

Figure 12. Illustration of plasma and Joule heating effects during SPS [84].

Rather than an external heating source (as with hot pressings conduction heating) a pulsed direct current is passed through the conductive die and the powder material. This allows for the material to be heated from within while the heated surrounding die heats from the outside [85]. A schematic illustration of this is shown in Figure 13. Shen discerned three factors which contribute to the unique ability of an SPS to densify a sample using short holding times. The first is the application of mechanical pressure, the second is the ability to use very rapid heating rates, and the third is the use of direct current the introduces material to an electric field [85].

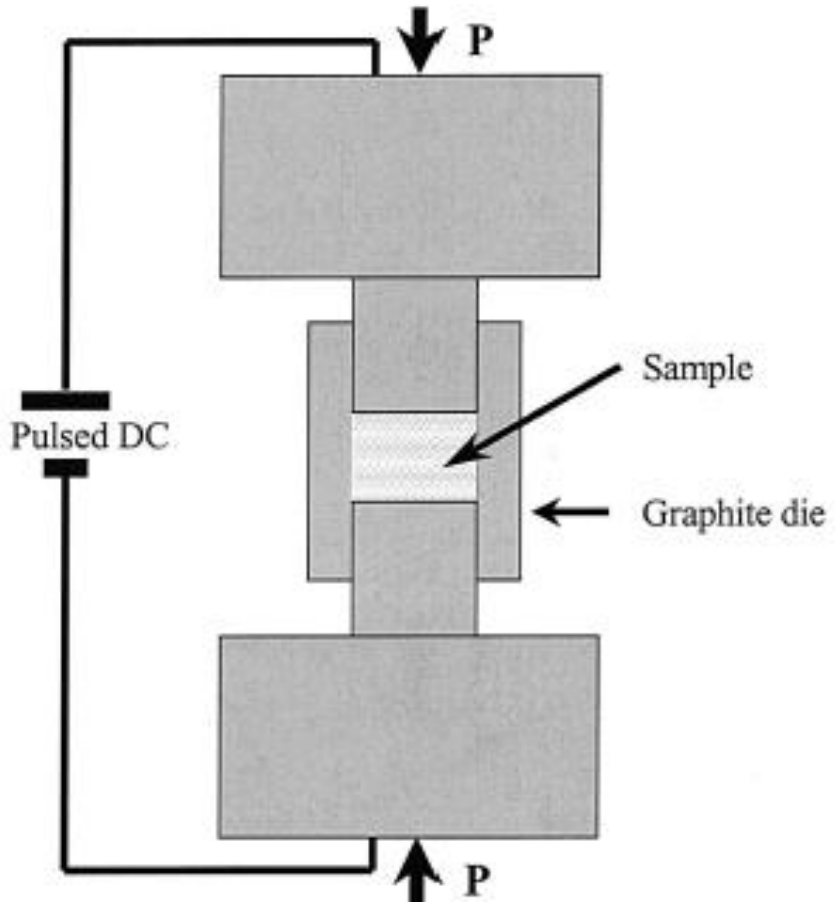

Figure 13. Schematic illustration of SPS setup. Shows current (DC), pressure (P), die, and sample [84].

The SPS technique holds advantages in that it is capable of producing uniform fine-grained ceramics with improved mechanical properties at lower temperatures at significantly lower times [83, 86]. The various sintering conditions used during an SPS treatment of alumina powder will have drastic effects on the final product. The use of rapid densification does not always guarantee the avoidance of extensive or abnormal grain growth [85, 86]. As spark plasma sintering is a relatively new technique, systematic studies of each material must be conducted to determine the correct sintering parameters when using an SPS system [83, 85, 87]. An Al_2O_3 sample set studied in this thesis was fabricated using the spark plasma sintering technique. Details regarding this sample set will be discussed in the Experimental Procedure section.

2.2. Ultrasound

Ultrasound is defined as any acoustic wave consisting of frequencies greater than 20,000Hz, above the threshold of audible hearing for humans [88]. Acoustic waves find analogous behavior to that of electromagnetic waves and can be understood through principles of optic physics [33]. Differences between acoustic and electromagnetic waves lie primarily on the fact that acoustic waves require a medium to travel within [33]. Due to this fact, the governing principles of acoustic waves are reliant upon material properties such as density, elastic moduli, and the differences of these properties at surfaces. The possibility of measuring material properties and acoustic response within dense materials is made possible through an understanding of acoustic physics and the use of modern technology to control all aspects of an ultrasonic wave [9, 89].

This portion of the literature review section starts with giving an understanding of the fundamentals of acoustic waves, material properties which control acoustic interaction in materials, and acoustic behavior at surfaces. Definitions of sound propagation modes and their reliance on acoustic impedance, reflection, and mode conversion will be given. Special attention is given to material mechanisms which cause ultrasound energy loss as the acoustic wave passes through the material. A distinction between absorption and scattering mechanisms will be explained. The operable loss, or attenuation, mechanisms active within full dense, polycrystalline, aluminum oxide are detailed.

2.2.1. Fundamentals of Acoustic Waves

A governing property of waves in general is that they have the ability to transport energy and information through a medium where material is not also transported [90].

As a wave propagates, a physical disturbance is passed along from point to point within the medium. For electromagnetic waves, this disturbance occurs as a change in electrical and magnetic fields, while acoustic waves cause disturbances in pressure and density [91]. All types of waves have certain things in common; such as they carry energy and can be reflected, refracted, and diffracted. The major difference between acoustic and electromagnetic waves is that electromagnetic waves are capable of travelling through vacuums where acoustic waves require a physical medium to traverse [92]. Acoustic waves are hereafter defined as waves which exist as ordered particle motion within an elastic medium emanating from a source of creation [91].

The equation which describes the behavior of elastic sound propagation is given as [33]:

$$y(x,t) = y_o \sin\left(\frac{2\pi x}{\lambda} - \omega t\right) \quad \text{Eq. 4}$$

where y is the displacement of the propagating sound wave with respect to distance, x, and time, t, y_o is the amplitude of the wave, λ is wavelength, and ω is the angular wave frequency. It should be noted that equation 4 is the solution to the wave equation for both longitudinal and transverse waves. Wavelength and angular frequency are constants defined by the medium in which the sound is travelling. They are also defined as [33]:

$$c = f \cdot \lambda \quad \text{Eq. 5}$$

$$\omega = 2\pi f \quad \text{Eq. 6}$$

where c is the speed of sound within an elastic medium and f is the frequency.

In many dense materials the speed of sound can be approximated as constant with frequency [89]. This is in contrast to electromagnetic waves where significant dispersion

can be seen. This lack of dispersion in dense ceramic materials allows for the simplification of acoustic measurements. The ramifications of a lack of dispersion coupled with Equation 5 become extremely important for ultrasonic testing. For a constant material acoustic velocity, increasing frequency causes wavelength to decrease proportionally. With regards to ultrasonic testing in ceramic materials, one may choose the frequency of sound to be introduced such that the acoustic wavelength is commensurate with microstructural feature size and cause a direct interaction. For high density, high hardness ceramics, previous ultrasonic testing showed that frequencies in the megahertz regime were necessary to generate wavelengths as small as the microstructural features [14, 93].

The velocity of sound and its propagation mode are directly dependent on the physical composition of the transmitting medium. Furthermore, the speed of sound, c, may also be expressed in terms of the elastic modulus and density of a material [94]. Distinctions are made regarding the degree of anisotropy of the material and the relation of speed of sound and elastic modulus delineates into two terms; one for assuming an elastically isotropic material and another if assuming anisotropic mediums [14, 91, 95].

The speed of sound in an elastically isotropic medium is defined as [91]:

$$c = \sqrt{\frac{M}{\rho}} \qquad \text{Eq. 7}$$

where ρ is the material density and M is the applicable elastic modulus; Young's or shear, relating to either longitudinal or transverse waves, respectively. Equation 7 may be modified by use of the Poisson ratio, ν. Although single crystals of alumina exhibit some degree of elastic anisotropy, the ultrasound beam interacts with many differently oriented

single grains and it can be assumed that, overall, isotropic conditions can be applied and Poisson's ratio can be used. This is shown in equation 8 [95].

$$c = \sqrt{\frac{M}{\rho}\,\frac{(1-\nu)}{(1+\nu)(1-2\nu)}} \qquad \text{Eq. 8}$$

Materials which do not have a shear modulus are incapable of propagating shear waves. Such materials include air and water; only longitudinal acoustic waves are capable of existing in these types of media [91].

While there are many types of propagation modes of ultrasound only two of interest are discussed here; longitudinal and shear modes. Longitudinal waves are characterized as having amplitude displacements which are parallel to the direction of travel. Longitudinal waves can also be thought of as compressional waves [91]. Shear, or transverse, waves are distinguished as having an amplitude displacement which is perpendicular to the direction of which the wave is travelling. Figure 14 shows a schematic diagram illustrating both of these types of propagation modes.

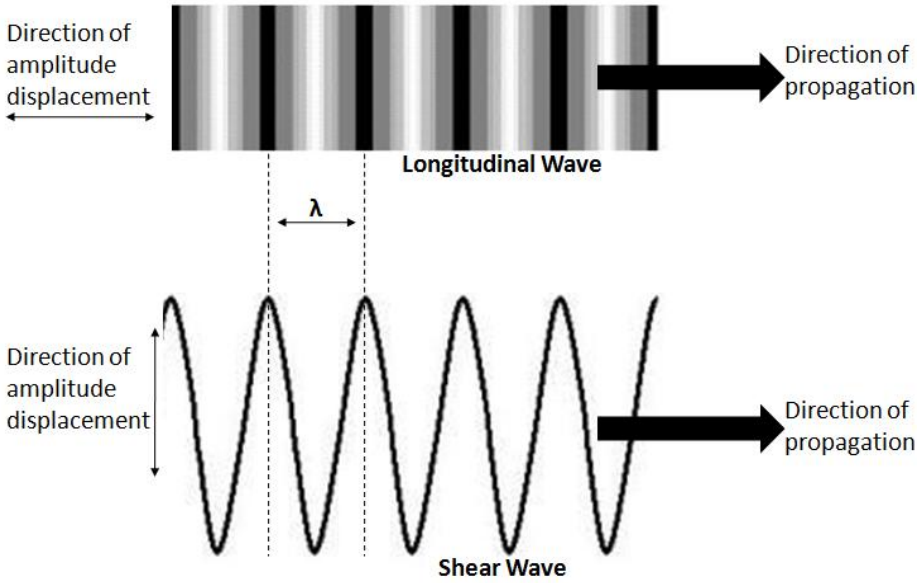

Figure 14. Pictorial illustration of longitudinal and shear wave modes. Λ is the wavelength between crests [90].

Materials which exhibit higher elastic modulus typically result in higher sonic velocities due to the nature of how an acoustic wave travels through a medium. Acoustic waves exist as the ordered motion of elastic oscillations of adjacent atoms [92]. The stronger the bond between such atoms allows for faster elastic oscillations and ultimately a higher sonic velocity [33, 96]. Gases are comprised of physically separated molecules and particles and therefore exhibit low sonic velocities. Liquids have higher bond strength when compared with gases which allow for higher velocities. When looking at solids, materials with ionic or covalent bonding such as ceramics typically tend to have higher acoustic velocities when compared to metals, with metallic bonding [91].

The intensity of energy carried by an acoustic wave is directly proportional to the square of its amplitude [33].

$$I = \frac{1}{2}\rho c(\omega y_o)^2 \qquad \text{Eq. 9}$$

where I is intensity measured in W/m^2. As the amplitude of the acoustic wave decreases, the intensity of energy contained within the propagating acoustic wave decreases as well. Correction for acoustic energy lost due to reflection and diffraction rely upon this proportion and is shown in a future section.

2.2.2. Acoustic Properties of Materials

It is a material's properties which define the properties of propagating acoustic waves. Parameters such as density, elastic modulus, and crystallographic isotropy determine the sonic velocity of a material which defines what the acoustic wavelength is at any frequency present [97]. As stated earlier, materials with strong ionic or covalent

bonds tend to exhibit higher acoustic velocities than those with weaker bonds. This has a direct effect on another vital material acoustic property; the acoustic impedance (Z) [89]:

$$Z = C_L \rho \qquad \text{Eq. 10}$$

where C_L is longitudinal velocity and ρ is density. Acoustic impedance is measured in Rayls (Pa·s/m). Acoustic impedance can also be described as the ratio of sound pressure to sound velocity but is more conveniently noted as equation 10.

Impedance is typically used in electrical, thermal, and mechanical applications to describe different types of energy loss mechanisms at surfaces and a materials resistance to energy flow [16]. Similarly, acoustic impedance is the quantification of the resistance of sound propagation in a medium [89]. Acoustic impedance is akin to the index of refraction described by optical physics. Both index of refraction and acoustic impedance dictate the behavior of electromagnetic and acoustic waves at an interface [98]. While index of refraction is inversely proportional to the speed of light, acoustic impedance is directly proportional to sonic velocity [89].

The strong bonding nature of ceramic materials lend to their high sonic velocities and ultimately high acoustic impedance values. Metals show comparable acoustic impedance values to that of dense ceramics due to their higher densities. Plastics, having weak bonds and low densities, are lower than ceramics and metals on the acoustic impedance scale. Fluid media such as liquids and gases on average exhibit much lower acoustic impedance values not only due to weak bonding but also because of the physical separation and disorder of their molecules [16, 89]. A compilation of acoustic impedance values along with density and sonic velocity are shown in Table III.

Some of the earliest attempts at measurements of acoustic impedance were done by Kennelly and Siskind [99, 100]. In Kennelly's method he made electrical measurements of the motional impedance of a telephone receiver with and without an attached acoustic impedance causing device. However, this experiment was not entirely accurate due to mechanical impedance which convoluted with the acoustic impedance [99]. Since these early attempts to measure acoustic impedance large strides have been made to not only create better acoustic impedance measurement devices, but to implement them for practical use.

Acoustic impedance measurements are commonly made for medical purposes as they offer a direct method of examination of middle ear functionality and disorder [101]. Ground penetrating acoustic waves are used by geophysicists to map subterranean structures such as reservoirs, water tables, caves, and mineral deposits. At its heart the science behind this relies upon acoustic impedance measurement and advanced signal processing [102-104].

Table III. Density, longitudinal velocity, and acoustic impedance values for common materials [20, 105, 106].

Material	**Density (kg/m^3)**	**Longitudinal Velocity (m/s)**	**Acoustic Impedance (MRayls)**
Ceramics			
SiC (sintered)	3160	11820	37.35
SiC (hot pressed)	3210	12100	38.84
Al_2O_3	3970	10600	42.08
AlN	3260	10700	34.88
B_4C	2510	14090	35.37
TiB_2	4500	11400	51.30
WC	1580	9500	15.01
Si_3N_4	3050	11000	33.55
TiC	5150	8270	42.59

Glass (crown)	2500	5300	13.25
Quartz	2650	5800	15.37
Ice	917	4000	3.67
Metals			
Iron	7690	5900	45.37
Steel (stainless)	7800	5800	45.24
Aluminum	2700	6300	17.01
Copper	8920	4700	41.92
Gold	19300	3200	61.76
Lead	11342	2200	24.95
Platinum	21460	3300	70.82
Tungsten	19250	5200	100.10
Titanium	4506	6100	27.49
Zinc	7140	4200	29.99
Plastics			
Neoprene	1230	1600	1.97
Nylon	1150	2600	2.99
PMMA	1180	2700	3.19
Polyethelene (HDPE)	941	1900	1.79
Polystyrene	1050	2400	2.52
Butyl Rubber	920	1800	1.66
Fluids			
Air	…	330	0.0004
Glycerin	1260	1900	2.394
Mercury	13534	1400	18.9476
Water	1000	1480	1.48
Oil	880	1700	1.496

2.2.3. Interfacial Behavior of Acoustic Waves

When an acoustic wave encounters an interface several interesting and critical phenomena occur which are necessary for ultrasonic testing. The types of surfaces which an ultrasonic wave may come in contact with are liquid-liquid, liquid-solid, and solid-solid. Both the angle of incidence of the acoustic wave and the magnitude of difference in acoustic impedance between the two surfaces dictate what happens to the wave after

the interaction. Reflection, transmission, refraction, and mode conversion are the phenomena of interest in which ultrasonic testing relies upon [14, 92]. Other inherent outcomes of wave interaction which may occur are interference, superposition, and resonance [17, 90].

2.2.3.1. Reflection and Transmission

Acoustic waves are reflected at boundaries where there exists a difference between the acoustic impedance values of the materials on either side of the boundary [107]. This difference in acoustic impedance is ordinarily referred to as the acoustic impedance mismatch. Considering waves which are normal to an interface, the degree of reflection and transmission of an acoustic wave can be calculated as [108]:

$$R = \frac{(Z_2 - Z_1)^2}{(Z_2 + Z_1)^2} \quad \text{Eq. 11}$$

$$T = \frac{4Z_1Z_2}{(Z_2 + Z_1)^2} \quad \text{Eq. 12}$$

where the subscripts on Z represent two media with different acoustic impedance values. A greater acoustic impedance mismatch causes a larger amount of energy to be reflected at an interface. The same amount of energy is reflected and transmitted independent of the direction of wave propagation; low to high impedance media or high to low impedance media. This is represented mathematically in equation 11 where the acoustic impedance mismatch is squared. The reflection and transmission coefficients represent the percentage of acoustic energy which is either reflected or transmitted at a boundary. As such, the two parameters are compliments of each other where the addition of both

will return unity. Table IV shows typical interfaces an ultrasonic wave will encounter when testing alumina and the resulting reflection coefficient for each.

Table IV. Reflection coefficient and percentage of energy reflected at common interfaces found in dense aluminum oxide.

Boundary	Reflection Coefficient	Percent Reflected (%)
Al2O3 - Water	0.868	86.8
Al2O3 - Air	0.999	99.9
Al2O3 - MgO	0.105	10.5
Al2O3 - CaO	0.329	32.9
Al2O3 - SiO2	0.216	21.6
Al2O3 - Al2O3 (anisotropy)	0.0007	0.07

2.2.3.2. Refraction and Mode Conversion

The above discussion on reflection and transmission was for the idealized case of when the incident acoustic wave is normal to an interface. Two very important phenomena for ultrasonic testing occur when the acoustic wave is at an oblique angle to a surface [9]. When this is the case, reflection still occurs but transmission takes the form of refraction. Acoustic refraction is exactly analogous to what can be seen with optics; a straw in a glass of water appears to be bent due to a difference in the speed of light in air and water. However, the straw is not bent and what actually occurs is the bending, or refracting, of the light as it passes from air into the water. The same effect happens when an oblique sound wave passes between two media with different acoustic impedance values. The governing equation for this event can be described by Snell's Law [92]. A schematic illustration of this effect can be seen in Figure 15.

$$\frac{\sin(\theta_1)}{C_1} = \frac{\sin(\theta_2)}{C_2} \qquad \text{Eq. 13}$$

where θ_1 and θ_2 are the angles of incidence and refraction, respectively, and C_1 and C_2 are the longitudinal speeds of sound for two materials at an interface.

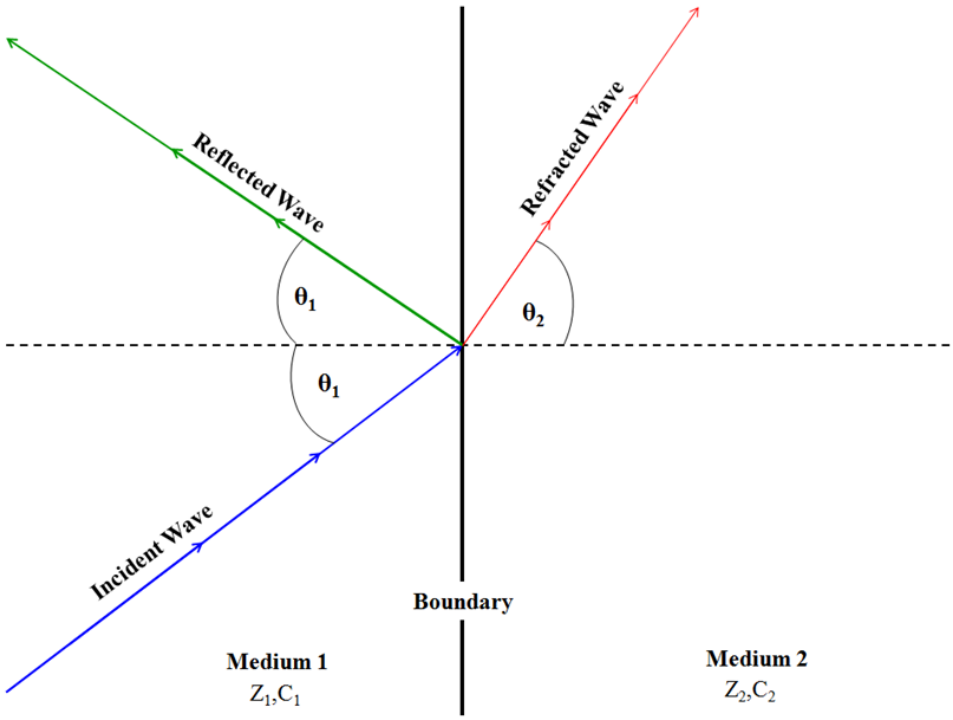

Figure 15. Schematic illustration of the reflection and refraction of an incident oblique acoustic wave.

The alteration and conversion of part of the energy contained in an incident longitudinal wave occurs when such a longitudinal wave encounters a boundary at an angle. The generation of shear waves in solids by this method is known as mode conversion [109]. Mode conversion of longitudinal to shear waves holds an advantage when the direct introduction of a shear wave is not possible. An example of this (and the basis of testing performed in this thesis) is when one is performing immersion-based, non-contact, ultrasound NDE. This method of ultrasound NDE uses longitudinal transducers which require a fluid as the propagating medium for the ultrasonic wave. Longitudinal wave transducers are used for this method due to the fact that shear waves do not propagate in low viscosity fluids, such as water [110]. When the longitudinal

wave encounters the liquid-solid interface part of that energy generates a shear wave in the solid material.

The introduction of shear waves into a solid has practical use as it allows for the measurement of elastic properties in solid materials using only a single longitudinal wave transducer [89]. This conversion of longitudinal to shear waves occurs at each interface with which the longitudinal wave comes in contact. The opposite effect has also been observed where a generated shear wave mode converts part of its energy back to a longitudinal wave [16, 89, 111]. Other than relying on mode conversion for the introduction and use of shear waves in solid media, one may choose to use a contact shear wave transducer. These types of transducers are specifically designed to only generate shear waves. A disadvantage of this method is that one will have to use both a longitudinal wave transducer and shear wave transducer in contact to measure a solid materials elastic properties [110].

2.2.3.3. Superposition and Interference

An interesting property of waves is that two of them travelling towards each other in opposite directions can pass right through each other and emerge with their original identities [33, 90]. This is known as the principle of linear superposition. At the point where the two waves intersect, two situations occur: constructive or destructive interference. Interference is the addition or subtraction of these waves at their point of contact. The addition or subtraction of two waves is called constructive or destructive interference, respectively. An illustration of this is shown in Figure 16.

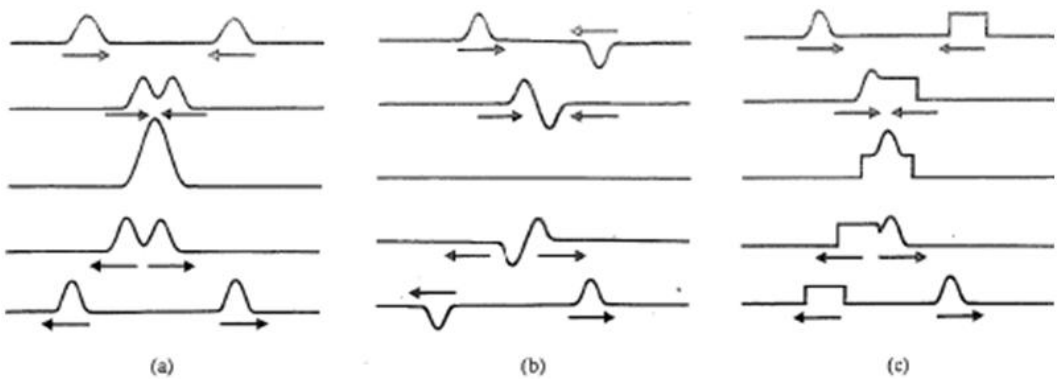

Figure 16. Superposition of wave pulses travelling in opposite directions. (a) Pulses in phase; (b) pulses out of phase; (c) pulses with different shapes [90].

For continuously pulsed waves consisting of many frequencies the principles of superposition and interference have the effect of producing well defined peaks consisting of multiple frequencies. Discussed in detail as part of a later section, ultrasonic transducers simultaneously emit acoustic waves over a range of frequencies. The result of this emission can be viewed on an oscilloscope as the superposition of each acoustic wave of different frequency. Figure 17 shows a simplistic example of this with the superposition of only three frequencies.

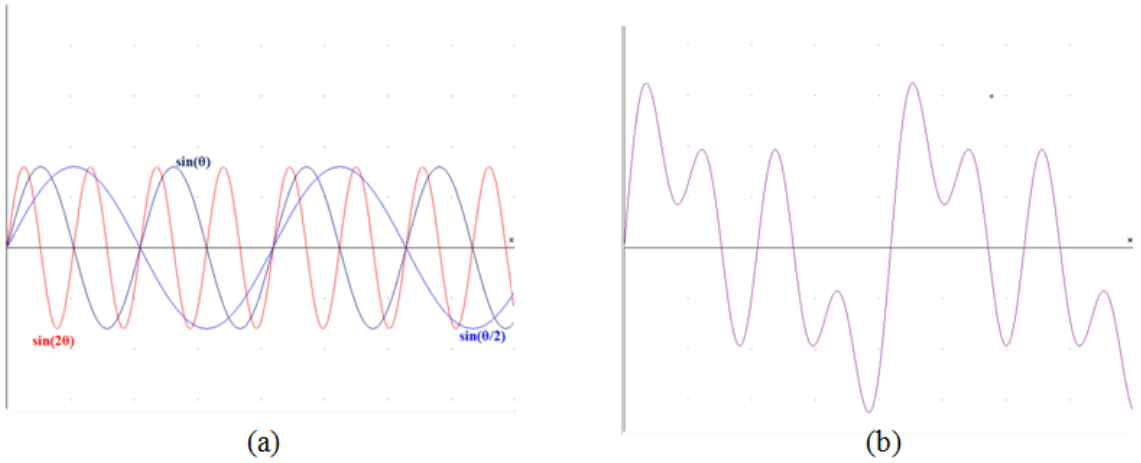

Figure 16. Superposition of continuously pulsed waves. (a) Three sine waves of arbitrary frequencies; (b) Resulting superposition three sine waves of arbitrary frequencies.

2.2.3.4. Resonance

In the work done by Uberall, and others, it was shown that a feature of the correct size and sonic velocity embedded within a dense material will resonate in the presence of an acoustic wave [112, 113]. Resonance is the gradual increase in amplitude of an oscillator as it is driven by an external harmonic force. An expression for the amplitude of a damped, driven, harmonic oscillator is given as Equation 14 [90].

$$|x_o| = \frac{\left(F/m\right)}{\left(\left(\omega^2 - \omega_o^2\right) + \gamma^2\omega^2\right)^{1/2}} \qquad \text{Eq. 14}$$

where x_o is the amplitude of oscillation, F is the driving force, m is the mass of the oscillator, ω is angular frequency, ω_o is resonant frequency, and γ is a damping constant.

In the case of small features embedded within a dense material, a feature acts as an oscillator and the driving force is the periodic force of the ultrasonic pulse emitted by a transducer. If the above conditions are met, the embedded feature will emit low amplitude acoustic waves. If the acoustic waves emitted by the embedded oscillator are of a frequency readily accepted by the transducer used, lateral distortion across an ultrasonic C-scan image can be seen [114]. This distortion is an example of an acoustically created artifact due to the constructive and destructive interference of the emitted ultrasonic transducer waves and those created by an oscillating embedded feature [114]. An example of this is shown in Figure 17.

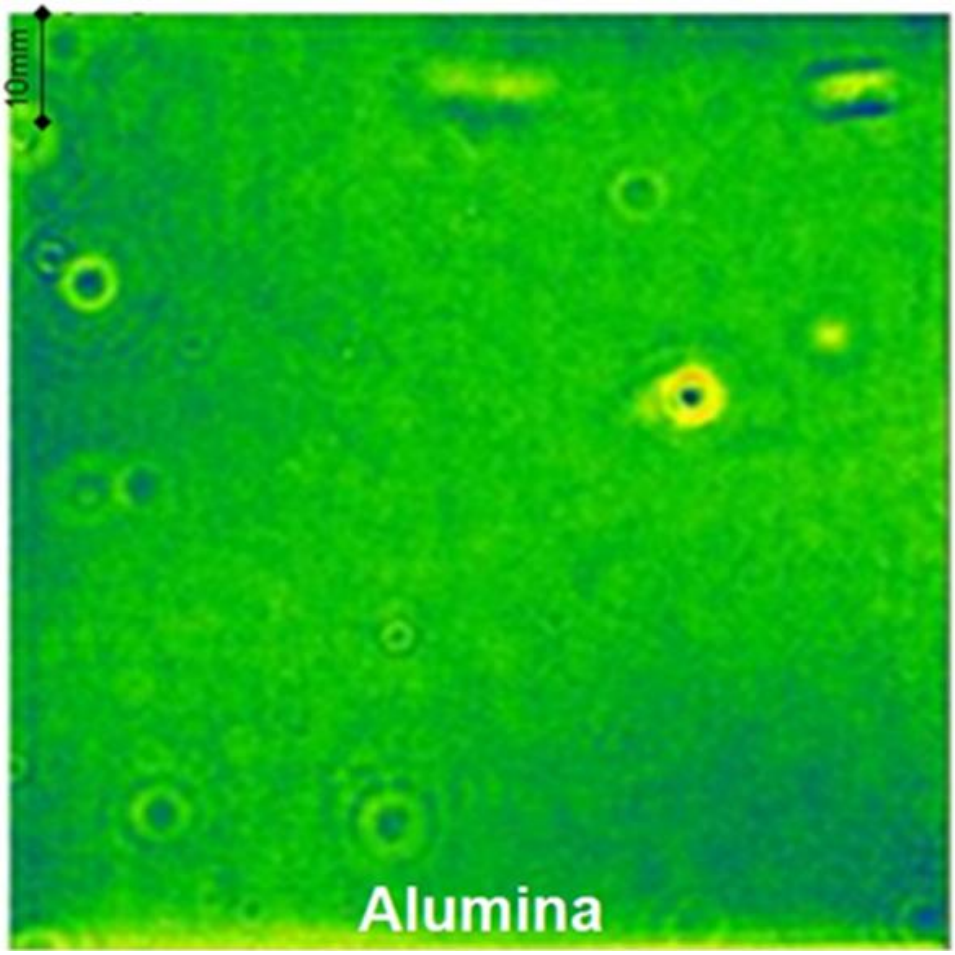

Figure 17. Ultrasonic C-scan image showing acoustic distortion caused by resonance-based interference. The center of each set of concentric rings is the origin of where a small embedded feature is oscillating [6].

2.2.4. Acoustic Attenuation

As an ultrasonic wave propagates through a material it loses a portion of its acoustic energy [19]. Materials attenuate acoustic waves through a variety of different mechanisms which can be directly measured as a reduction in wave amplitude [115-118]. Everything within a material; grains, grain boundaries, inclusions, pores, etc. will cause acoustic attenuation [119]. This attenuation is not only dependent on features throughout the material microstructure, but also the size and frequency of the interrogating ultrasonic beam [19]. A pristine, ideal material is one which does not cause acoustic attenuation. In this situation, signal attenuation is only caused by geometric factors such as reflection

and beam spreading losses [120]. This dissertation takes account for these loss mechanisms and is discussed in a future section. For real materials, an increase in attenuation is brought about by changes of everything within the bulk material microstructure and is viewed as a decrease in signal amplitude. A pictorial representation of this is shown in Figure 18.

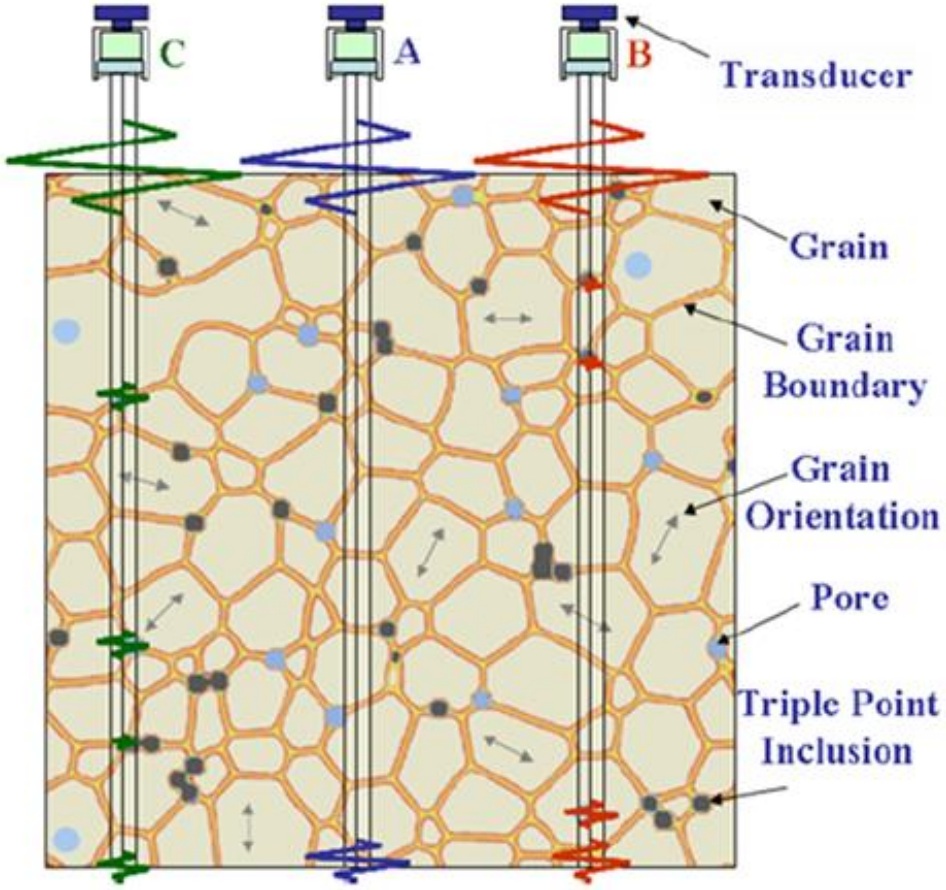

Figure 18. Schematic of acoustic signal loss. (A) Minimal acoustic attenuation; (B) and (C) Attenuation caused by interactions with grains, pores, inclusions, etc. [14].

Amplitude-based attenuation measurements are extremely sensitive to frequency [19]. This is due to the large dependence on frequency of the scattering and absorption mechanisms. Scattering and absorption are the two constitutive mechanisms by which ultrasonic energy is lost as an acoustic wave travels through a material [19]. For many materials, attenuation typically monotonically increases with frequency but may undergo

peak-like behavior in certain frequency ranges [121, 122]. Based on microstructural characteristics such as size distribution and composition there exists frequency regimes where acoustic attenuation effectively does not occur or is negligible [19, 122-124]. These regimes of acoustic transparency differ from material to material.

Scattering is the redirection of an acoustic wave such that the wave never gets measured [125]. Absorption is the conversion of energy contained in the ordered particle motion of the wave into disordered heat energy [126]. A general summation for the total attenuation coefficient over all frequencies can be written as equation 15 [19].

$$\alpha_{Total} = \alpha_{GS} + \alpha_{GA} + \alpha_{HS} + \alpha_{HA} + \ldots \quad \text{Eq.15}$$

$$\ldots + \alpha_{Reflection} + \alpha_{Diffraction}$$

where α is attenuation, 'G' refers to grains, 'H' refers to heterogeneities within a microstructure, 'S' refers to scattering and 'A' to absorption. Reflection and diffraction attenuation are not dependent on the size of microstructural features and can be taken into account by other means [111]. Within these two fundamentally different attenuation mechanisms exists sub categories further defining the type of scattering or absorption based on frequency and material characteristics. A discussion of specific types of scattering and absorption follows this section. This thesis makes great use of understanding each applicable loss mechanism which arises in Al_2O_3 such that microstructural information can be gleaned by a deconstruction of equation 17.

2.2.5. Ultrasonic Scattering

Scattering is the redirection of an energy wave when such a wave encounters an obstacle or interference. The degree of scattering is dependent on frequency, size of the obstacle, and the difference between acoustic impedance of the feature and preceding

medium [127]. Upon each scattering interaction the intensity of each redirected wave lessens until the total intensity of the original wave becomes completely dispersed or attenuated. An illustration of this can be seen in Figure 19. The dispersed waves which never reach a measurement device are considered to be a loss of acoustic energy. In dense polycrystalline alumina typical obstacles or scatterers an acoustic wave may encounter include grain boundaries, pores, solid inclusions, and a grain-grain interface where two grains are oriented such that there exists an elastic modulus mismatch between the two in the direction of the wave.

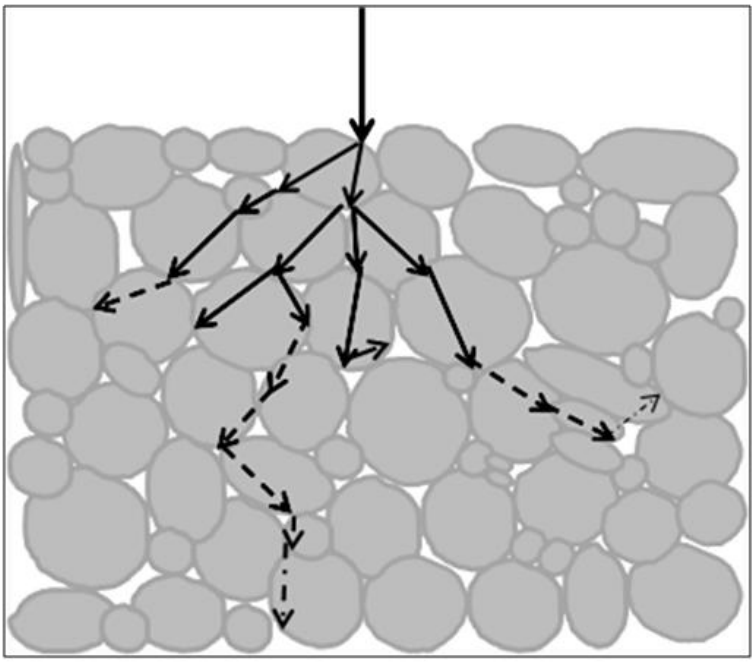

Figure 19. Illustration of acoustic wave dispersion and attenuation. Dashed arrows indicate lower intensity waves.

When a travelling acoustic wave impinges on an obstacle there are in general three subsequent waves which are produced: the unimpeded incident wave which is transmitted, the wave scattered in a different direction, and a possible wave excited from within the obstacle [128]. The third type of wave was discussed prior to this section as

that being created from a feature resonating [112, 128]. Scattering usually accounts for the greatest portion of losses in polycrystalline aggregates [19]. In ceramic materials, such as aluminum oxide, this is only true for a certain frequency range. On an increasing frequency scale, absorption attenuation mechanisms account for the majority of lower frequency losses where scattering doesn't become dominant until higher frequencies [121].

Ultrasonic attenuation due to scattering losses is dictated by the size of the scatterer and the wavelength of the interrogating sound beam. The ratio of the wavelength to scatterer size plays a critical role in the overall amount of sound energy which is lost. Classically three scattering regimes have been defined based on this ratio [129]. The first regime is known as the Rayleigh scattering region. This is frequency region such that the size of the scatterer is much smaller than the size of the wavelength of sound. The stochastic region is where the scatterer size and wavelength are commensurate with each other. The third and last regime is the diffuse region where the size of the scatterer is greater than that of the wavelength. A phenomenon which occurs with diffuse scattering is the presence of Mie resonances. This is oscillatory behavior which averages to be constant with frequency [130]. A distinct difference in size between the scatterer and wavelength to analytically separate each regime is not defined, but it has been shown that Rayleigh scattering dominates when the scatterer is approximately an order of magnitude less in size than that of the wavelength [19, 119, 126]. As frequency increases and the wavelength approaches the size of the scatterer overlapping of Rayleigh and stochastic scattering occurs [19].

A simple way of defining these three regimes is to compare the acoustic wavenumber, k, multiplied by scatterer size, a, to unity (Table V).

$$ka = \frac{2\pi}{\lambda}a = \frac{2\pi f}{c}a \qquad \text{Eq.16}$$

The diameter of a single scatterer is represented by 'a'. Nicoletti, and others, defined relationships for each scattering regime between the attenuation coefficient and frequency [131]. It can be seen in Table V that acoustic scattering attenuation behaves as a power law which has been verified for liquids, metals, plastics and ceramics [18, 122, 123].

Table V. Scattering regime, wavenumber to size relationship, and attenuation coefficient to frequency relationship [131].

Scattering Regime	**ka Relationship**	**α to frequency Relationship**
Rayleigh	ka << 1	$\alpha_R = C_R a^3 f^4$
Stochastic	ka ≈ 1	$\alpha_S = C_S a f^2$
Diffuse	ka >> 1	$\alpha_D = \frac{C_D f^0}{a}$

For the attenuation coefficient-to-frequency relationships 'a' represents the mean diameter of all scatterers within a medium. These relationships do not make the assumption that the scatterers are equiaxed or spherical. The prefactors, C_S, C_R, and C_D, are material dependent and take into account geometric factors, density, impedance mismatch, and elastic anisotropy [129, 132, 133].

When examining attenuation coefficient curves of not only dense alumina but metals and liquids as well, it is evident there is a clear superposition of a multitude of different loss mechanism. All absorption mechanisms have shown trends such that they dominate a different frequency range of the attenuation coefficient spectrum compared to that of the scattering mechanisms [134]. Looking at extreme ends of the frequency scale (really low or really high frequencies) will ensure that there is no convolution between scattering and absorption. This thesis takes advantage of the distinctly different frequency ranges where each loss mechanism is operable to study both scattering and absorption separately. An idealized attenuation coefficient spectrum showing frequency regimes where either scattering or absorption is dominant can be seen in Figure 20.

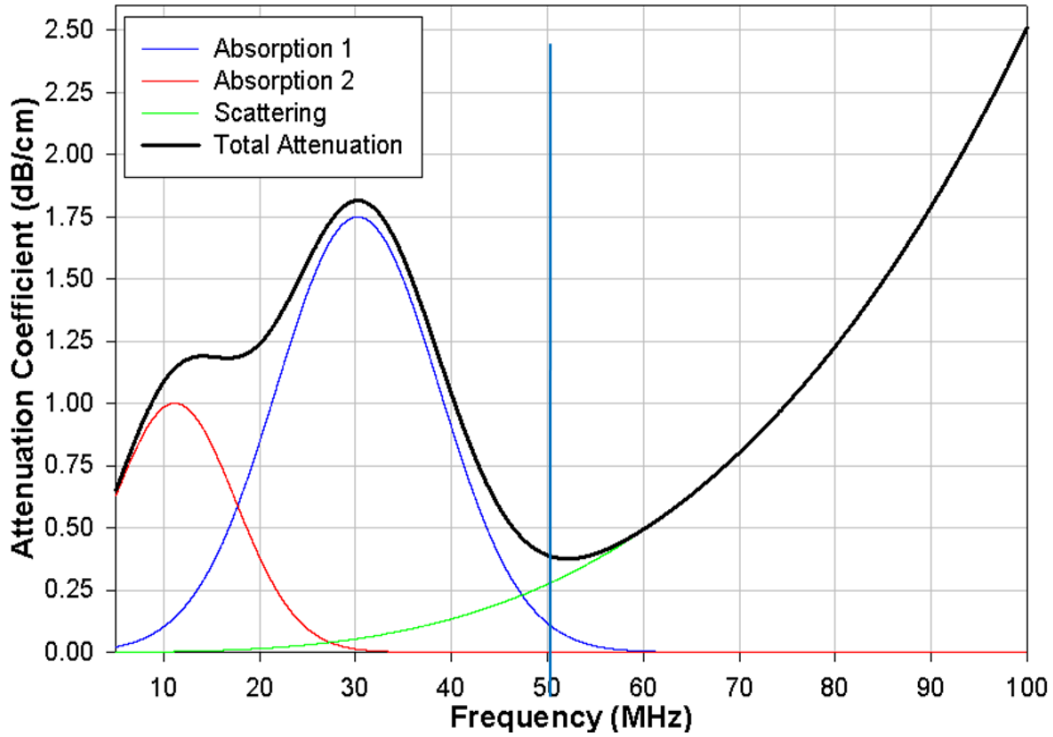

Figure 20. Idealized attenuation coefficient spectrum showing distinct regimes of absorption and scattering.

The sizes of the scatterers which would be expected in dense alumina do not reach scales where diffuse scattering would occur which allows for diffuse scattering losses to

be neglected. Focused attempts to derive analytical expressions which model Rayleigh, stochastic, and diffuse scattering have been made by leaders in the field of acoustics [135-138]. John William Strutt, better known as Lord Rayleigh, worked on modeling scattering cross sections based on the elastic properties of the scatterer and its host material [136]. A scattering cross-section shows a proportion of the amount of acoustic energy lost due to the scatterer. Scattering cross section values are an analog to attenuation coefficient. Rayleigh came to two conclusions in his attempts to mathematically explain acoustic scattering. The first relationship assumes the elastic mismatch between the scatterer and host medium is negligible and allows variation of scatterer morphology. The second relationship makes the opposite assumption: scatterer morphology is constant and the elastic mismatch may vary [136, 139]. Both solutions restrict the scatterer to being much smaller than that of the wavelength and therefore make them only valid for the Rayleigh regime (for which it is named) as seen in Table V.

The limitation to particular frequencies or particle sizes led to an attempt by others to account for not only the Rayleigh scattering regime but also the stochastic scattering region. There is a continuity inconsistency in attempting to combine the expressions for Rayleigh and stochastic scattering. As ultrasonic frequency increases, the fourth power term for Rayleigh scattering becomes less dominant and the stochastic mechanism begins to take over. Papadakis dealt with this discontinuity by making scattering behavior into a piecewise function and applying a logarithmic smoothing function [88]. This method worked well but does not give a generalized function for scattering at all frequencies. Maisel overcame this problem by using an analog from an electrical network equation to combine Rayleigh and stochastic scattering [138]:

$$\alpha_{RS} = C_{RS} \frac{4a^3k^4}{1+4a^2k^2} \quad \text{Eq.17}$$

where α_{RS} is the attenuation coefficient due to either Rayleigh, stochastic, or both types of scattering and C_{RS} is a scattering prefactor account for scatterer geometry, and elastic mismatch with the host material. Rayleigh, Papadakis, Maisel, and many others fell short with their attempts when it came to also accounting for diffuse scattering at very high frequencies. All of the aforementioned attempts at solving acoustic scattering theory rely heavily on assuming sizes for the scattering and ultrasonic wavelength.

Gustav Mie, a German mathematician and physicists, developed a theory which calculates scattering cross sections and does not rely on assumptions such as scatterer size, frequency limits, or elastic mismatch limits [140]. This solution does, however, still assume that the scattering particles are spherical. Mie theory was created as an interpretive solution of Maxwell's equations for the scattering of electromagnetic radiation [141]. Maxwell's equations are used to derive a wave equation in spherical coordinates which is a separable partial differential equation. Drawing from the likeness of electromagnetic waves, Mie theory also applies to acoustic waves [18].

The most integral part of Mie theory is its solution for the scattering cross section [141]:

$$\alpha_M = \frac{2\pi}{k^2}\sum_{n=1}^{\infty}[(2n+1)(|a_n|^2 + |b_n|^2)] \quad \text{Eq.18}$$

Where α_M is the Mie scattering cross section, k is wavenumber, and a_n and b_n are known as the Mie coefficients, as shown in the following equations.

$$a_n = \frac{\Psi_n'(mrk)\cdot\Psi_n(rk) - m\cdot\Psi_n(mrk)\cdot\Psi_n'(rk)}{\Psi_n'(mrk)\cdot\zeta_n(rk) - m\cdot\Psi_n(mrk)\cdot\zeta_n'(rk)} \quad \text{Eq.19}$$

$$b_n = \frac{m \cdot \Psi_n'(mrk) \cdot \Psi_n(rk) - \Psi_n(mrk) \cdot \Psi_n'(rk)}{m \cdot \Psi_n'(mrk) \cdot \zeta_n(rk) - \Psi_n(mrk) \cdot \zeta_n'(rk)} \quad \text{Eq.20}$$

Where m is the acoustic impedance ratio of scatterer to medium, r is scatterer radius, and k is wavenumber. Ψ is the spherical Bessel function of the first kind and ζ is the spherical Bessel function of the second kind, both of the n^{th} order. Primes represent the first derivative with respect to r. Due to symmetry the Ψ and ζ of the spherical Bessel functions are negated. Explicit equations for the first and second spherical Bessel functions as a function of radius are given as [141]:

$$\Psi_n(r) = (-r)^n \left(\frac{1}{r}\frac{d}{dr}\right)^n \frac{\sin(r)}{r} \quad \text{Eq.21}$$

$$\zeta_n(r) = -(-r)^n \left(\frac{1}{r}\frac{d}{dr}\right)^n \frac{\cos(r)}{r} \quad \text{Eq.22}$$

Even after eliminating two of the three coordinates from the spherical Mie scattering solution (θ and φ), calculating the Mie coefficient is still a very time intensive process as it is the summation of an infinite convergent series. Chronologically, Mie theory came before many of the attempts at deriving an analytical solution which encompasses all frequency ranges. Due to a lack of computing power and deficiencies in signal and data processing, either the Mie solution was not a practical one or it was approximated as its first few terms through perturbation theory [128]. As of today, even with state-of-the-art processing power, the time it takes to compute the Mie scattering cross section must be shortened by limiting the number of summations taken in equation 20. This has not been seen as detrimental and does give results which make physical sense matching by with experimental data.

An example showing the scattering cross sections solved using the Mie equation in MATLAB can be seen in Figure 21. This example shows the relative increase of attenuation that would be expected if one were to increase grain size in aluminum oxide from 0.5μm to 100μm (diameter). Size steps of 1μm give approximately 100 curves. The curve representing the largest grain sizes can be seen to have wavelength independent diffuse scattering occurring at the highest frequencies. Actual sample scattering spectra may show localized peak-like behavior at ultra high frequencies which superimpose on the scattering power law-type curves. This is due to the relative difference in the amount of energy scattered between Rayleigh, stochastic and diffuse mechanisms. Stochastic mechanisms scatter as much as $1x10^5$ more energy than that of Rayleigh scattering and diffuse scattering scatters even more than stochastic scattering [141]. This means that for an acoustic wave passing through billions of grains, ppm and less really large grains will cause noticeable stochastic and diffuse scattering effects [142]. Acoustic scattering losses in ceramic materials have been shown to be more strongly dependent on grain size rather than possible solid inclusions, pores, or secondary phases present [143].

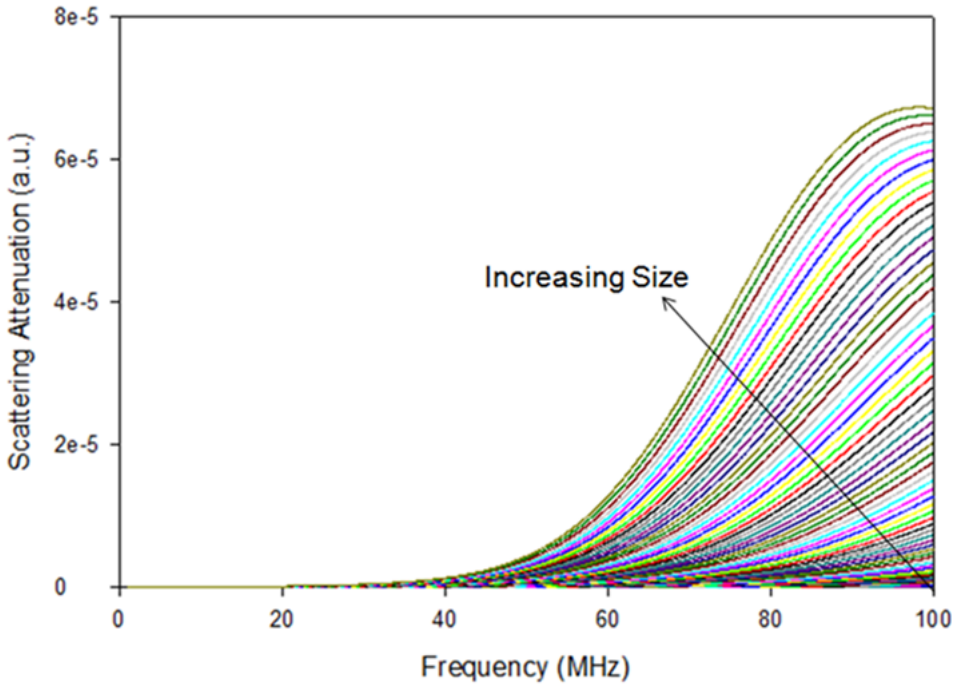

Figure 21. Generated scattering cross sections for alumina with different grain sizes. Calculated using Mie scattering solution in MATLAB [142].

2.2.6. Ultrasonic Absorption

The conversion of energy from ordered particle motion to disordered chaotic motion, or heat, can be described by absorption effects. Ultrasonic absorption is the overarching mechanism by which sound energy is turned into heat energy. Under absorption as one of the two primary loss mechanisms, exist a variety of sub types listing the specific method by which energy is absorbed. These sub types include absorption by viscous drag, ferromagnetic, chemical relaxation, hysteresis, dislocation damping, thermal conduction, and thermoelasticity. Different types of acoustic absorption losses will be operable depending on the propagating medium, wavelength, elastic properties, and temperature. This section discusses each type of absorption mechanism and places special emphasis on the type of absorption mechanism present with ultrasonic testing of dense polycrystalline aluminum oxide.

2.2.6.1. Viscous Absorption

An absorption mechanism that is operable in liquids, colloidal suspensions, and viscous fluids is known as viscous drag attenuation. This mechanism has been well studied starting in the early 1900's by Sewell with work done on fogs of varying densities [144]. This work made the assumptions that secondary particles of higher density within the host fluid medium were static which was later deemed to be unrealistic. Viscous drag attenuation occurs from a velocity mismatch between higher density suspended particles in a lower density host fluid. A heat loss at the surface of the particles occurs as an acoustic wave passes through [145]. This is due to the slight movement of the particles (which is contradictory to Sewell's initial assumptions) and the resulting frictive heating between the suspended particles and fluid medium [146]. Even without suspended particles there are still visco-inertial drag losses due to localized movement of viscous fluid medium [147]. The rise of acoustic spectroscopy as a means of characterizing particulate sizes in colloidal suspensions resulted from the theory of viscous absorption of ultrasound in heterogeneous suspensions created by Epstein, Carhart, Allegra, and Hawley (ECAH theory) [18, 145, 147]. ECAH theory is the term coined for the work done in solving for the attenuation mechanisms present in fluid suspensions. For small particles and frequencies less than 1MHz viscous losses account for all ultrasonic attenuation in suspensions [146].

Prior to the finalized ECAH theory Epstein and Carhart developed an analytical equation to predict the degree of attenuation due to viscous drag:

$$\alpha_{\eta} = 4\pi nkR^2(1-\delta)Re(i\frac{\lambda}{D}) \qquad \text{Eq.23}$$

where α_η is the attenuation caused by viscous absorption, n is the concentration of the particulates in suspension, k is the wavenumber, R is the radius of the particulates, δ is the ratio of the densities between the viscous medium and suspended particulates, and D is a term used to maintain field continuity between host media and suspended particles [145]. Allegra and Hawley added contributions which generalized the results of Epstein and Carhart by removing restrictive assumptions on acoustic wavelength [147]. The work done by Allegra and Hawley in suspensions noted that attenuation would undergo peak-like behavior through frequency as there is negligible attenuation at low or high frequencies. This is due to the fact that viscous drag attenuation reaches a maximum when the suspended particles have greatest motion [147].

Acoustic spectroscopy for characterizing concentrated dispersions has a big advantage over modern backlight scattering techniques [148]. This is due to the work done by Dukhin on the development of acoustic and electroacoustic spectroscopy in concentrated dispersions which refined ECAH theory to account for particle-particle interactions [149]. Aside from being able to account for particle interactions, acoustic spectroscopy does not require calibrations with a known colloid. Light scattering techniques are more sensitive to larger particles thereby resulting in an overestimate of the amount of larger particles and an underestimate of smaller ones [134]. A simplified expression for viscous attenuation in colloidal suspensions is given by Dukhin to be [18]:

$$\frac{\alpha}{\varepsilon} = \frac{1}{9}\omega^2 r^2 \frac{\rho}{c\eta}\left(\frac{\rho'}{\rho} - 1\right)^2 \qquad \text{Eq.24}$$

where ε is the concentration of the suspended particulates, ω is waveneumber, r is radius, ρ' is the density of the particulate, ρ is the density of the host fluid, and η is the viscosity

of the fluid medium. Dukhin noted that acoustic scattering in colloidal suspensions becomes important for larger particles and high frequencies (> 3μm and >10MHz). Viscous losses dominate absorption attenuation in suspensions at low frequencies before the effects of scattering can be seen [134]. Therefore lower frequencies are where viscous absorption attenuation measurements are made. Specific examples and applications of acoustic spectroscopy and viscous losses in colloidal suspensions are shown in a later section. Viscous losses are not expected to be operable in dense polycrystalline aluminum oxide.

2.2.6.2. Hysteresis, Dislocation, and Chemical Relaxation Absorption

Hysteresis absorption occurs in single crystals, amorphous solids, biological tissue, and most strongly in polymers [150, 151]. It is defined as a physical relaxation activated by the movement of an acoustic wave. Hysteresis occurs in materials prone to having metastable structures when small pressures are applied [151]. The degree of ultrasonic energy absorbed due to this mechanism is dependent on the acoustic wavelength and temperature of the propagating medium. The movement of physical structures in a medium caused by acoustic pressure is an irreversible process causing an increase in entropy and ultimately gives rise to a measureable quantity of absorbed acoustic energy [151].

Hysteresis absorption in polymers is caused by the trapping of a mer in one of its many metastable potential energy minima [151]. Hysteresis in polymers brought on by relaxation processes has been shown to exhibit attenuations proportional to the square of frequency [151]. A distribution in the relaxation times of the polymers to a metastable state is what brings on hysteresis absorption. In fact, almost any experimental result regarding acoustic absorption for polymers can be expressed as a distribution of

relaxation times [152]. Hysteresis absorption is not expected to be active in dense polycrystalline alumina as it does not meet the criteria as a type of material prone to hysteresis absorption effects.

The dislocation nonlinearity of single crystals is affected by the amplitude of pressure of a passing acoustic wave [153]. The parameters of the dislocations themselves: effective mass, stiffness, and damping coefficients, become functions of the amplitude of the acoustic pressure oscillations. These dislocations can be forced to move if the pressure wave is strong enough to overcome the dislocation parameters. This movement of dislocations gives rise to absorption caused by hysteresis in solids [153]. Burlak developed a numerical solution of the effective ultrasonic absorption coefficient caused by hysteresis effects:

$$\Gamma(U_0) = -\frac{1}{L} ln(\frac{U_0(L,t+L/C_g)}{U_0(0,t)}) \qquad \text{Eq.25}$$

where U represents displacements as a function of distance and time, L is length of the crystal, and C_g is the group velocity.

The activation of dislocation-based absorption is dependent on the presence of dislocations with enough mobility such that an imposed pressure wave can cause dislocation slipping [154]. The interaction of dislocations with acoustic waves is caused by phonon-phonon collisions [19]. A phonon is a quantification of the energy contained in a periodic elastic arrangement of atoms or molecules; as in an acoustic wave travelling through a solid material. If a weakly bonded crystallographic plane or dislocation band is oriented normal to an acoustic wave the pressure associated with the wave can cause the plane or dislocation to glide [129]. The mechanical energy contained within the acoustic

wave is transferred to the dislocations in the form of kinetic translational energy providing them the required energy to slip. Some of this energy is also converted to heat due to friction between atomic planes [92, 155].

Chemical relaxation absorption is brought on when the pressure of a propagating acoustic wave causes a temperature variation large enough to override equilibrium of a chemical state [156]. This absorption mechanism is associated mostly with gases and viscous liquids and is strongly dependent on temperature, wavelength, pressure, and concentration of absorbing particles [157]. These dependencies are described through the work done by Barthel, Lieberman, and Tamm as given by Verma [157]. An encompassing equation which describes the effect of hysteresis absorption in fluid media has been given by Bauer and follows the commonly seen 3-parameter Lorentzian function which has been known to describe many types of absorptive mechanisms [21, 126, 158].

Chemical relaxation losses in solids do occur when the acoustic wavelength is very long compared to the thermal phonon mean free path [126]. An acoustic wave passing through a medium produces phonons as the oscillatory vibration of the lattice. When the oscillations are not mechanically caused but by temperature fluctuations caused by a propagating acoustic wave the resulting phonons are thermal in nature. Sehgal defined acoustic absorption in solids due to chemical relaxation through the following equation [159]:

$$\alpha = \frac{2\omega}{c} sin\left(\frac{\omega \Gamma ln\,(\gamma)}{2\sqrt{1+\omega^2\Gamma^2}}\right) \qquad \text{Eq.26}$$

where Γ is the relaxation time, c is speed of sound, and ω is the wavenumber. It should be noted that attenuation due to chemical relaxation in solids will oscillate between being

either linear or squared due to the sine function. If the term ωΓ approaches unity attenuation becomes parabolic with frequency [159]. The excellent chemical stability of aluminum oxide (and many other dense polycrystalline ceramic materials) ensures that chemical relaxation effects will not occur during ultrasonic testing and this type of absorption mechanism may be neglected.

2.2.6.3. Thermal Conduction Absorption

Absorption losses are generalized as the conversion of ordered particle wave motion into heat. The thermal conductivity of a material strongly dictates the ability of heat generation and thermal flow within a material. Bhatia determined that acoustic losses due to thermal conduction are caused by differences in a materials Young's modulus between adiabatic or isothermal conditions [21]. The absorption caused by such a mechanism is also dependent on the materials thermal conductivity and acoustic wavelength. The greater the mismatch in elastic properties between isothermal and adiabatic conditions, and a greater thermal conductivity of the material will produce higher attenuation. Bhatia defined a governing term for the attenuation caused by thermal conduction which is reminiscent of many attenuation models dealing with thermal effects [21].

$$\alpha = \pi \left(\frac{V}{V_o}\right)^2 \left(\frac{E_A - E_I}{E_I}\right)\left(\frac{f f_o}{f^2 + f_o^2}\right) \qquad \text{Eq.27}$$

where v is the longitudinal sonic velocity of the material, v_o is the velocity of the material at null frequency which is defined by the density and stiffness of the material, E_A and E_I are the elastic moduli under adiabatic and isothermal conditions, f is frequency, and f_o is the frequency of maximum attenuation. Equation 27 follows a three-parameter

Lorentzian distribution function which arises when one is dealing with acoustic losses related to thermal effects [21, 90]. Bhatia also stated that for plane waves this type of absorption is generally negligible except in metals at frequencies higher than 1000MHz. However, for transverse vibrations in a one dimensional case, the damping due to thermal conductivity and heat flow can be quite paramount at considerably lower frequencies [21]. Materials which exhibit different sonic velocities at different frequencies tend to be prone to having thermal conduction absorptive losses [21]. This means that for dense polycrystalline ceramics, where acoustic dispersion is near non-existent, attenuative losses caused by thermal conduction do not contribute to the overall acoustic attenuation.

2.2.6.4. Thermoelastic Absorption

The role of heat conduction is much more significant in certain types of vibrations, which solids can be made to execute, than in sound-wave propagation. This is primarily due to the fact that specimens will vibrate either adiabatically or isothermally at specific frequencies [21]. The work done by Zener in 1941 paved the way for the understanding of whether or not local fluctuations in temperature of a vibrating solid are important in the damping of acoustic energy [160]. In his work he defined an acoustic loss mechanism based on thermoelasticity which is a coupling of the thermal and elastic fields created by a propagating acoustic wave. Stress inhomogeneities in a vibrating body will give rise to fluctuations in temperature and ultimately local heat currents. These currents will cause an increase in the entropy of the vibrating solid and give a source of internal friction leading to acoustic absorption [161]. The degree of local heating in polycrystalline solids is dictated by the extent of pressure changes in the medium caused by the acoustic wave, the coefficient of thermal expansion of the solid

crystals, and the orientation of the crystals with respect to the incident acoustic wave [21].

Thermal and elastic waves travelling across adjacent grains, solid inclusions, or within either are continuous [96, 162]. This leads to two types of absorption mechanisms based on thermoelasticity: interparticle thermoelastic absorption and intraparticle thermoelastic absorption [21, 160]. Particles are defined as features within a sample which can have a coupling of their thermal and elastic fields and can describe solids inclusions, pores, amorphous solids, and grains. The seminal work performed by Portune showed that thermoelastic absorption is the dominating absorptive loss mechanism active in dense polycrystalline ceramics [20]. The two types of thermoelastic absorption are discussed in greater detail below.

2.2.6.4.1. Interparticle Thermoelastic Absorption

There are many cases where dissimilar, thermoelastic solids come in contact. Dissimilar solids interfaces may refer to solid inclusion-grain, solid inclusion-solid inclusion, or grain-grain boundaries. For the case where two solids of the same type contact each other it is implied that there exists a difference in crystal orientation and thermal and elastic isotropy at such interfaces. With nonzero thermal conductivities between adjacent particles thermal currents exists which give rise to a continuous temperature distribution and result in mechanical energy absorption [163]. As elastic anisotropy between two adjacent particles increases interparticle thermoelastic absorption increases as well. This is due to the creation of a large temperature gradient between particles and therefore requires more energy to seek thermal equilibrium. The work done

by Lessen and Bhatia furthered the understanding of thermoelastic absorption as previous studies were focused on thermoelastic affects within singular particles [21, 160, 163].

Bhatia determined that it is irreversible heat flow which leads to absorption [163]. Acoustic waves propagate in a single distinct direction passing through a multitude of randomly oriented anisotropic particles. The different particles are heated to different temperatures depending on their orientation and degree of anisotropy. The degree of heat flow between particles is dictated by the amount each grain is heated to depending on its orientation [21]. A term derived for the attenuation caused by interparticle thermoelastic absorption is given as [21]:

$$\alpha = \kappa_a \left(\frac{C_P - C_V}{C_V}\right)\left(\frac{f f_o}{f^2 + f_o^2}\right) \qquad \text{Eq.28}$$

Where κ_a is an anisotropy factor, C_P and C_V are the specific heats at constant pressure and volume, f is the frequency of the acoustic wave, and f_o is the frequency at which the greatest difference in temperature mismatch gives a maximum in attenuation. Equation 28 follows the behavior of a 3-parameter Lorentzian distribution. The parameter f_o is defined through the thermal properties of the absorbing particles as well as their diameters, according to the equation:

$$f_o = \frac{3\pi}{2}\frac{\chi}{C_V a^2} \qquad \text{Eq.29}$$

where χ is thermal conductivity (W/mK) and 'a' is the diameter of the absorbing particle.

Interparticle thermoelastic absorption undergoes a maximum with respect to frequency. This is due to small and large wavelength conditions related to causing either adiabatic or isothermal conditions which result in a lack of heat flow [164]. If the

acoustic wave has sufficiently small wavelengths, compared to the size of the particles, the particles heat at an even rate and create adiabatic conditions [160]. When the propagating acoustic wave has a large enough wavelength, vibrations of singular particles do not occur where heat flow between adjacent particles can result. This leads to isothermal conditions [164]. The maximum frequency of attenuation between these two extreme scenarios is defined by equation 31.

2.2.6.4.2. Intraparticle Thermoelastic Absorption

The work done by Zener was concerned with thermoelastic absorption of singular particles. As a simplification he considered a one dimensional reed to be the oscillating particle [160, 161]. The thickness of the reed, a, was considered to be significantly thinner than that of the interrogating wavelength. The reed was then subjected to transverse vibration where the amplitude of the vibration was noted as the reed bent up and down according to the cycle time (Figure 22). One half of the vibrating reed went into compression as the other half was in tension. This occurs in two states depending on the cycle of the wavelength; ¼ λ and ¾ λ [21]. The side which was in compression heated up due to thermodynamic effects and the side in tension cooled. The resultant heat flow traveled along the transverse direction of the reed [21]. The same conditions, as stated above, of interparticle heat flow applied whether the system was isothermal or adiabatic according to the wavelength and did not cause thermoelastic absorption [21]. At very small wavelengths the particle was able to oscillate very fast allowing for thermal equilibrium to be attained without the need for thermal flow. This resulted in the adiabatic condition. When the wavelength of the acoustic wave was extremely long the amount of stress on the entire particle was equal causing equal heating and resulting in

isothermal conditions [21]. Both cases caused a negligible amount of acoustic energy absorption (Figure 23).

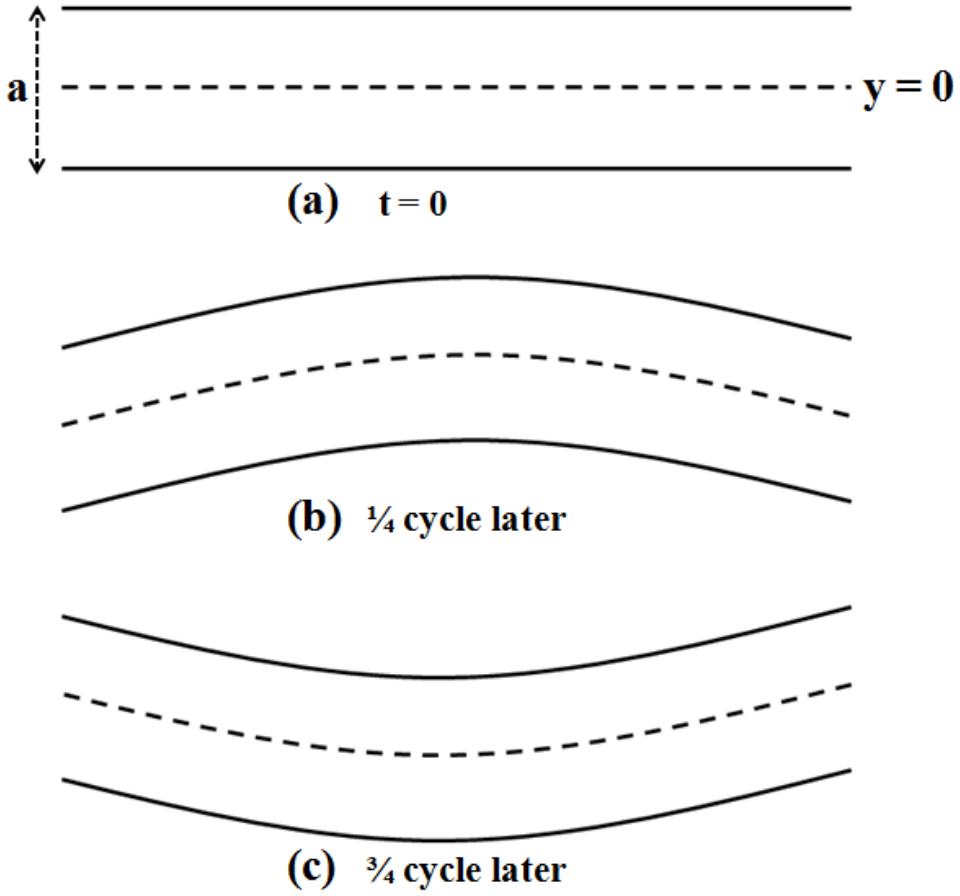

Figure 22. Transverse vibrations of a one dimensional particle subject to an acoustic wave. (a) Initial state, (b) 1/4 λ later, and (c) 3/4 λ from initial state [21].

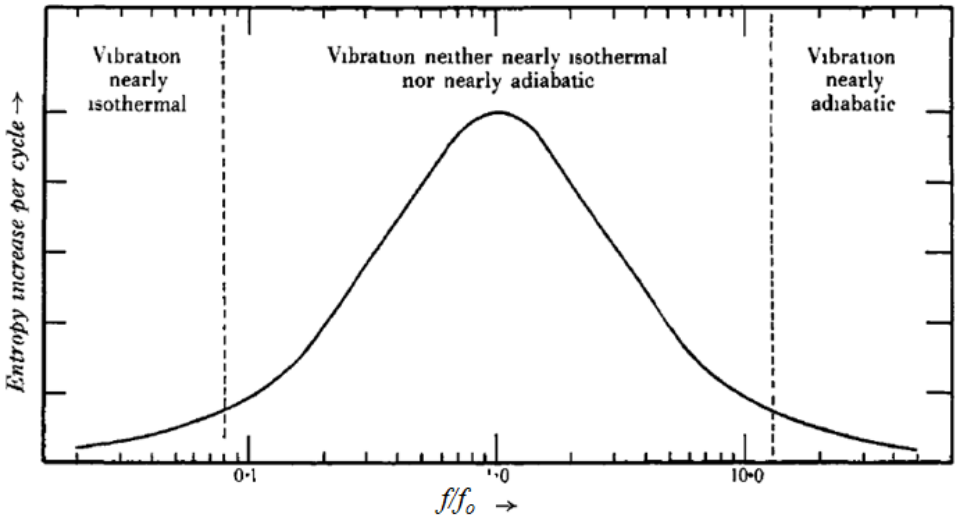

Figure 23. Degree of thermoelastic absorption at relative wavelengths [164].

The governing equation for intraparticle thermoelastic absorption is the same as seen in equation 29, but the frequency at where attenuation reaches a maximum is defined to be three times less than what is seen in equation 30 [21].

$$f_o = \frac{\pi}{2}\frac{\chi}{C_V a^2} \qquad \text{Eq.30}$$

Equation 30 becomes invaluable for the work done is this thesis as it is the heart of modeling thermoelastic absorption in dense polycrystalline ceramics.

Extending from a one dimensional particle to that of a real life three dimensional one is trivial as the same behavior occurs [21]. Rather than a vibrating reed pinned at both ends the analogous scenario is a vibrating drum head which is pinned about its circumference. The oscillations of three dimensional particles occur about their great diameters as an acoustic wave passes through [20]. Measurements of attenuation caused by intraparticle thermoelastic absorption have been made primarily in metals or glass and more recently in ceramic materials [20, 21, 165]. It should be noted that thermoelastic damping occurs at significantly lower frequencies in metals compared to ceramics due to

their generally larger grain sizes and overall differences in density and thermal properties [154]. Lucke showed that intraparticle thermoelastic absorption is dominant in zinc up to approximately 1MHz after which adiabatic conditions take over and scattering dominates the loss spectrum [154]. Bennewitz and Rotger showed that this loss mechanism peaks before the kHz regime for many metals and glasses [165]. Portune showed the same effect operating in the MHz regime for dense polycrystalline silicon carbide ceramics [20].

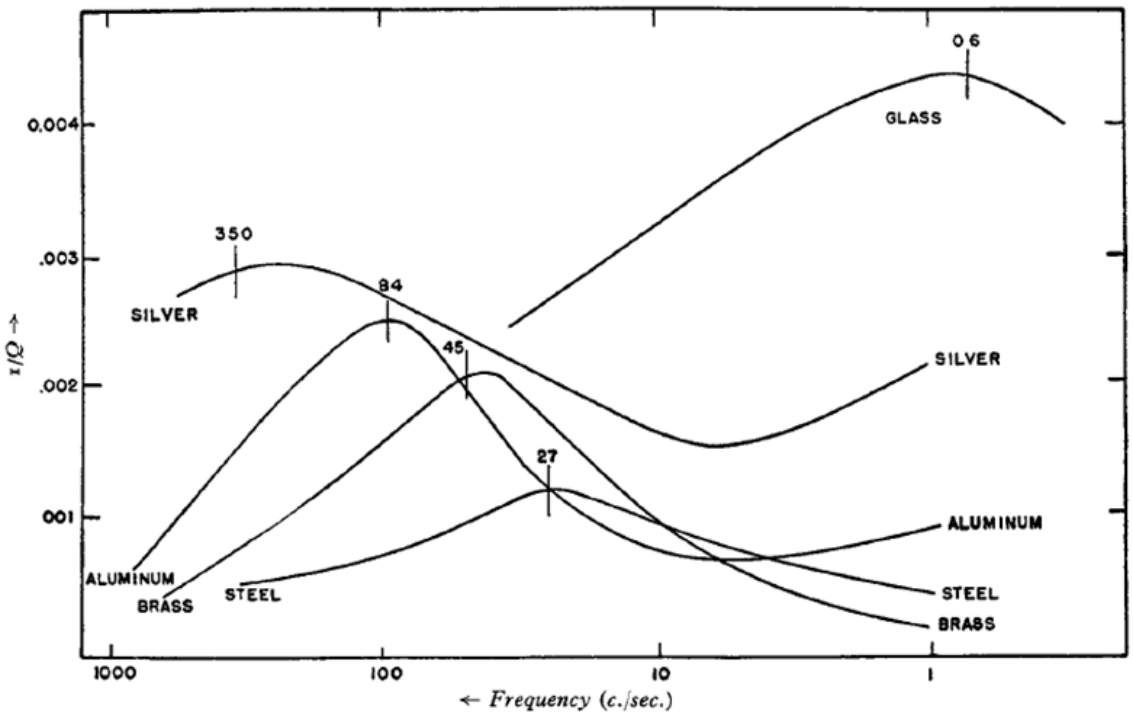

Figure 24. Intraparticle thermoelastic attenuation of glass and metals. The numbers above vertical bars represent the predicted frequency of maximum attenuation [165].

It was shown that intraparticle absorption is the dominant thermoelastic absorption mechanism in polycrystalline ceramics [20]. The time consideration for thermal flow between adjacent particles for an acoustic wave in the MHz regime is such that interparticle absorption cannot occur. Thermal diffusion between adjacent grains in a ceramic material is on the order of 10^{-6} seconds while the cycle of a propagating

acoustic wave in the MHz regime is of an even smaller time [166]. This results in the adiabatic condition as stated above. The dominant absorption mechanism in dense polycrystalline alumina is intraparticle thermoelastic absorption. The attenuation due to absorption is hereafter referring to intraparticle thermoelastic absorption.

2.2.7. Attenuation Mechanisms Applicable to Dense Al_2O_3

The ultrasonic waves emitted by an ultrasonic transducer will experience a general decay of intensity as they pass through aluminum oxide. Everything in an alumina sample lends to this loss in ultrasonic energy: grains, grain boundaries, pores, secondary phases, solid inclusions, and etcetera. It is expected that scattering attenuation will be mainly of the Rayleigh and stochastic types. The practical size of a scatterer in high density, polycrystalline aluminum oxide used for structural applications is as large as approximately 20μm [167]. Large agglomerations due to poor mixing of sintering additives could possibly reach up to 100 μm [167]. The frequencies used for ultrasonic testing in this thesis reach up to approximately 110MHz. The occurrence of diffuse scattering implies that there are features approximately 100μm within the alumina matrix. The occurrence of alumina grains this large is unlikely but is still a statistical possibility. If diffuse scattering occurs in polycrystalline alumina Mie resonances will be noticeable at high frequencies.

Ultrasonic absorption in aluminum oxide is dominated by intraparticle thermoelasticity. This attenuation will be operable mainly at lower frequencies (up to approximately 40MHz) after which scattering will become the dominant mechanism. Thermoelastic absorption results in peak-like behavior possibly in the measureable frequency range used in this thesis. The work done by others in glasses, metals, and

ceramics provide reason as to why intraparticle absorption will be operable while interparticle absorption may be neglected [20, 21, 164, 165].

2.3. Acoustic Spectroscopy

Nature provided a significant advantage of ultrasound over light, and that is related to its wavelength dependence. Acoustic spectroscopy refers to the study of frequency-based energy loss of acoustic waves as they propagate through a medium [18]. Over the past century the field of ultrasonics has grown tremendously; acoustic spectroscopy techniques provide us with insight into problems of basic physics and has found a large number of industrial and biological-medical applications [168]. Acoustic spectroscopy is an ever-changing field with regards to understanding physical mechanisms behind energy loss in various media and finding new applications for its use. More than 300 years ago Isaac Newton illustrated the importance of thermodynamic considerations to adequately describe ultrasonic phenomena [139]. Since then scientists such as Laplace, Stokes, Sewell and others have been refining the theory of sound and sound attenuation in heterogeneous media [18].

The earliest treatment (circa 1910) of acoustic attenuation was given by Sewell for the study of sound absorption in fogs [144]. Dilute and concentrated liquid suspensions have been examined since then, but the work done in creating ECAH theory paved the way for modern acoustic spectroscopy [121]. A few decades after the investigation of acoustic spectroscopy in fluid media began the study of sound attenuation in solid materials was undertaken by Mason, Bhatia, Herzfeld, Litovitz, Lucke, and others [21, 124, 154, 162]. This section chronologically describes the study and evolution of acoustic spectroscopy in different media. Special attention is given to

the work done in heterogeneous solids and the attempts at linking acoustic attenuation with microstructure.

2.3.1. Acoustic Spectroscopy of Fluid Media

In the early 1950's Epstein and Carhart refined the theory of sound absorption in fogs by Sewell [145]. They considered conditions which were closer to reality where fog particles in air were attributed to the properties either of viscous fluids or elastic solids. Thermal conductivity was a property neglected by Sewell but accounted for by Epstein. Epstein and Carhart divided acoustic attenuation in fluid media into two parts: viscous absorption and thermal attenuation. The mechanisms behind these absorption types are described above.

Some twenty years later Allegra and Hawley added contributions to the theory of acoustic absorption in fluid suspensions [147]. The work done by Allegra and Hawley demonstrated that the theory provides a reasonable description of ultrasonic damping in water emulsions. Quantitative tests at the time were limited due to imprecise measurement and knowledge about particle sizes of particulates in suspensions. An initial test which was not limited was using aqueous suspensions of polystyrene spheres as their radii were accurately measureable at the time. Figure 25 shows an example of measured and predicted attenuation of polystyrene spheres in suspension [147].

The advantages of modern computing power and advanced signal processing were still in their beginnings for this type of work. The use of signal filtering and high frequency Fourier transforms were unable to be performed in the complexity required to cut back on experimental and theoretical error. As a result multiple transducers were

used to cover just a few points of frequency without the ability to take advantage of their inherent bandwidth capabilities [91].

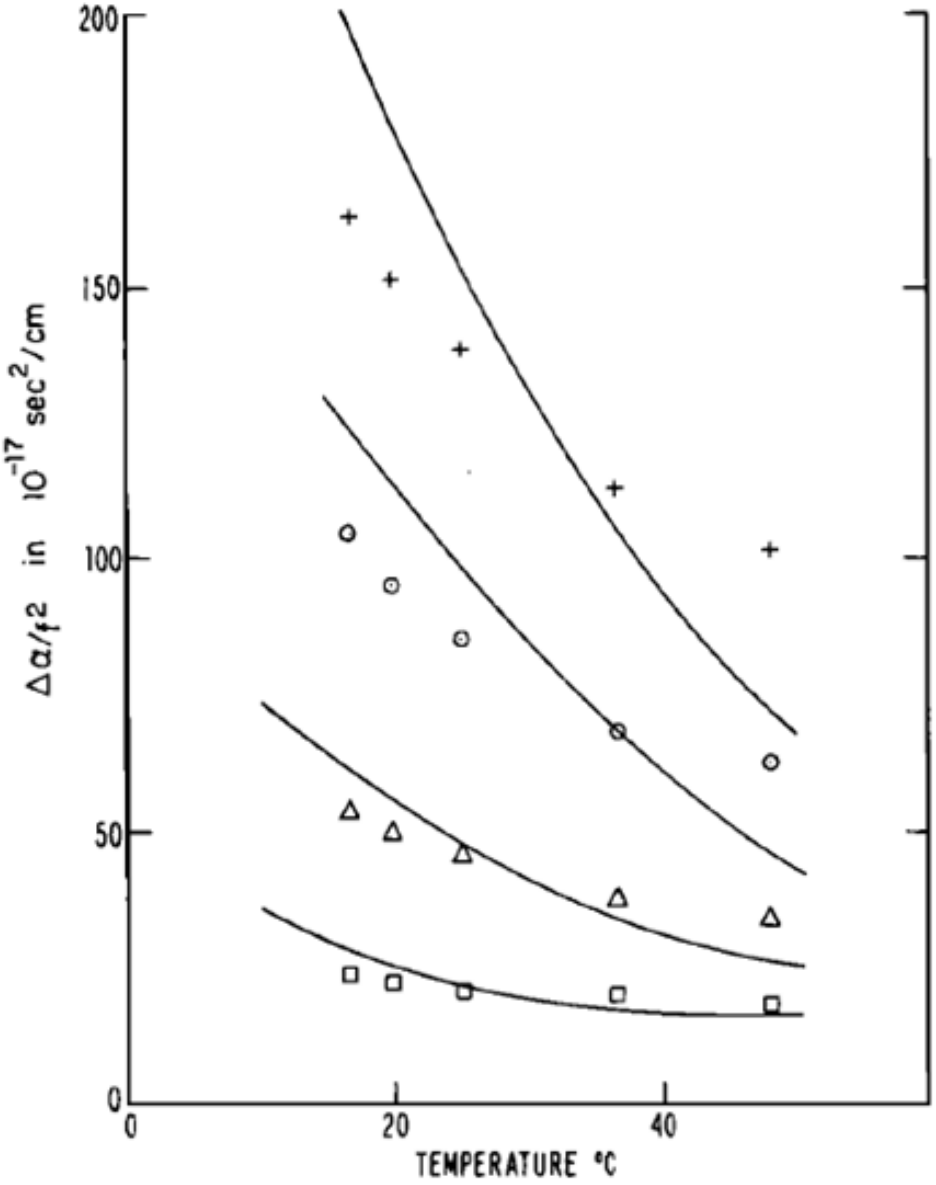

Figure 25. Attenuation as a function of frequency and temperature for an aqueous suspension of polystyrene spheres. Radii = 0.11µm. Frequencies (+): 9MHz; (○): 15MHz; (Δ): 27MHz; (□): 51MHz; (—): theoretical curves [147].

Dukhin deemed the absorption of ultrasound in colloids "easy to calculate" [134]. He studied several methods for using acoustic spectroscopy to determine microscopic

characteristics of heterogeneous systems such as composition, structure, particle size distribution, and zeta potential [18]. In doing this, ECAH theory was widely used along with some simplifying assumptions; namely that sub-micron particles do not cause scattering losses in frequency ranges under 100MHz. The theory of superposition for multiple loss mechanisms (as seen in equation 17) allowed for particle-particle interactions to be taken into account more easily. Dukhin demonstrated the high sensitivity of acoustic spectroscopy for obtaining particulate size distributions of liquid emulsions, plastic suspensions, and ceramic slurries [121]. An example of this can be seen in Figure 26. This example shows measured attenuation coefficient matching almost perfectly with predicted data.

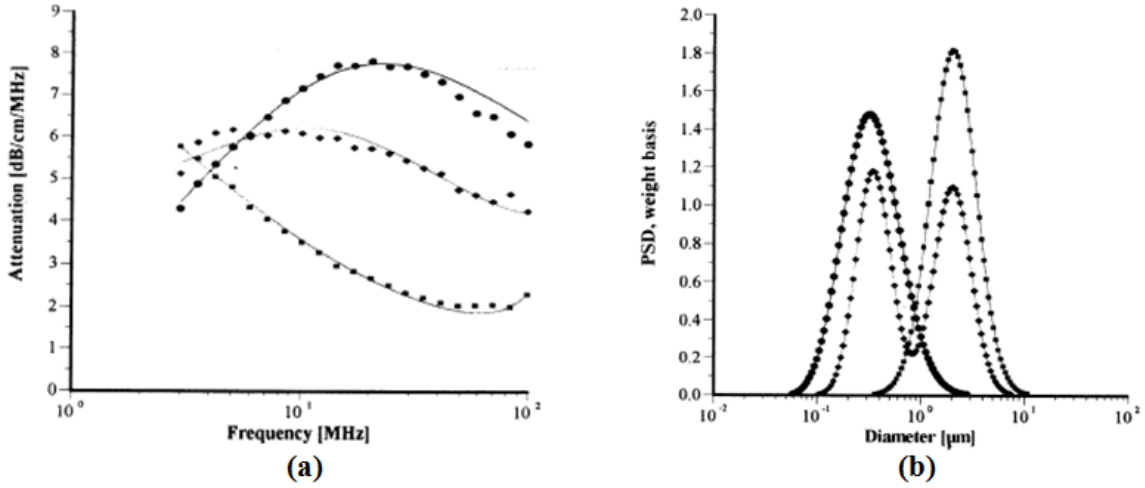

Figure 26. (a) Measured attenuation coefficient curves of different alumina slurries along with theoretical predicted lines; (b) predicted particle size distributions of alumina slurries [121].

Today acoustic spectroscopy finds its main use in testing liquid suspensions and slurries. It is widely used in the food science industry for determining particulate sizes in liquids such as milk and oils [169-171]. This type of testing has been shown to be accurate with up to 5% error, when compared to laser diffractometry [169].

2.3.2. Acoustic Spectroscopy of Solid Systems: Metals

The jump to using acoustic spectroscopy in solid media came several decades after it was first performed in fluids. Metal-based materials were among the first solid materials to be studied using ultrasound characterization methods. During the sixties ultrasonic spectroscopy was proclaimed as the panacea for the problems of nondestructive testing where the size, shape, and grain size of metals could be easily measured [172]. However, this type of testing had little recognition in industrial use as it was unlikely that an inspection engineer would be found on site with equipment capable of performing this type of testing [172]. The research and testing provided by those in the past and the advent of modern computing power makes the concept of using acoustic spectroscopy for industrial use today a real possibility.

The sensitivity of acoustic attenuation to grain size makes it a feasible property to be used in measuring any mechanical property related to grain size, approximate bulk porosity, or estimate average grain size [143]. The fundamental theory set forth by Zener, Mason, and McSkimin in the 1940's paved the way for reliable characterization using acoustic spectroscopy. This work showed that acoustic scattering caused by grains dominates attenuation coefficient spectra in the megahertz regime for metals [124, 143]. The first attempt for modeling frequency based acoustic attenuation as a superposition of multiple loss mechanisms took the form of [124]:

$$\alpha(f) = B_1 f + B_2 f^4 \qquad \text{Eq.31}$$

where the first term on the right side of the equation is indicative of an absorptive hysteresis mechanism only occurring at exceptionally low frequencies (kilohertz regime)

and the second term is caused by Rayleigh scattering. The B coefficients with the subscripts 1 and 2 represent constants dependent on the material scrutinized.

A commonly seen and used graph in the field of ultrasonics created by Mason demonstrates the first time theoretical and experimental data were compared. This was done in aluminum rods where Mason used the anisotropy of the elastic properties of aluminum and followed only Rayleigh scattering behavior, as can be seen by equation 31.

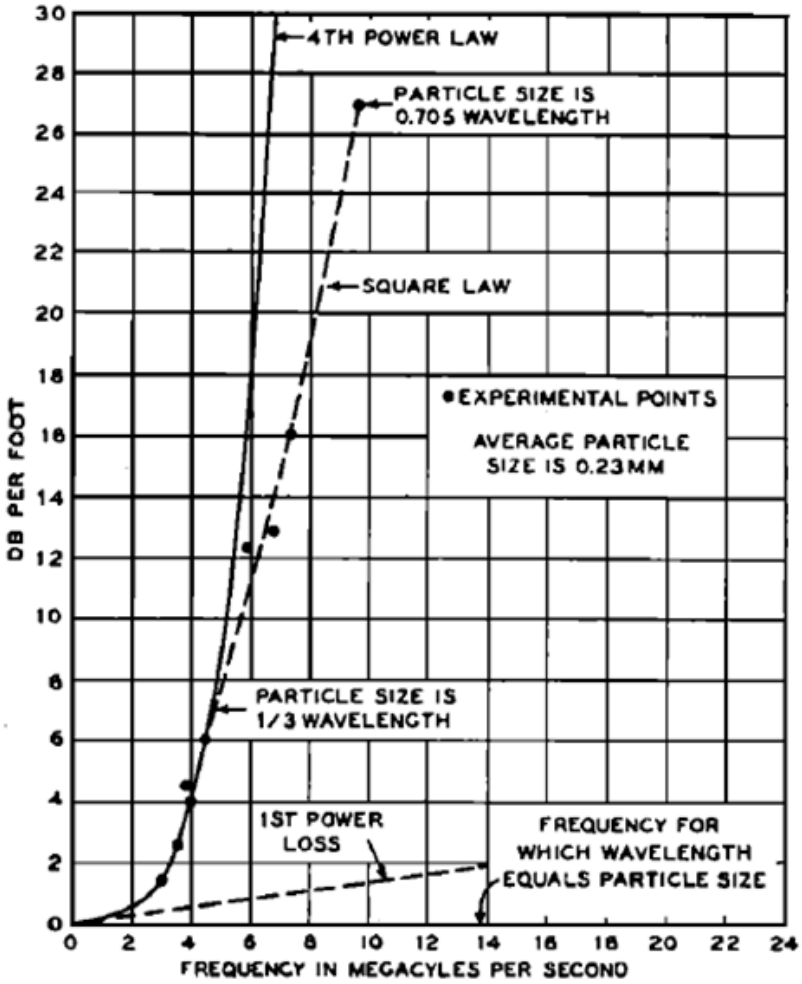

Figure 27. Scattering losses for an aluminum rod when particle size approaches wavelength [124].

The results from the work done by Mason and McSkimin showed the transition from Rayleigh to stochastic scattering approximately when the mean particle size is one third

the size of the interrogating wavelength. The black dots shown in Figure 27 display the experimental data taken from several transducers with different average frequency outputs.

Papadakis noted that the acoustic measurement of mean grain size in metals has some inaccuracies; namely that many metals in fact contain a distribution of grain sizes [173]. His contributions include an equation to estimate grain size distributions in different types of metals. Although, there exists as much as 20% error and much a priori information is required for use as constants in his equation [173].

$$N(R_i) = A(R_i - R_o)^m e^{-aR_i} \quad \text{Eq.32}$$

Where N is number of grains of size R, R_O is the radius between the i^{th} and i^{th}+1 radius, and 'A', 'a', and 'm' are constants dependent on the elastic anisotropy and morphology of the grains. Papadakis found the parameters R_O, A, a, and m experimentally for iron and an iron-nickel alloy [173]. Equation 32 takes into account on grains which are small enough to cause Rayleigh scattering behavior. An overarching equation (the Mie scattering equation as seen in section 2.2.5.) to account for any wavelength to scatterer size ratio would not be accessible for practical use for some time due to computing limitations [128, 140].

More modern testing using acoustic spectroscopy in metals was performed by Roderick, Rosen, Thompson, Vary, and others where they noted that only empirical relationships under controlled conditions have been observed [174]. Vary stated, "Ultrasonic measurements give indirect indications of mechanical property variations and morphological conditions. Empirical correlations and calibrations must be established for each material even where theoretical bases exist [168]." This reasoning holds true

today with performing acoustic spectroscopy in dense ceramic solids as will be shown in future sections of this thesis.

Roderick and Vary reported on correlations between fracture toughness, hardness, and ultrasonic attenuation coefficient for a variety of metals. It was concluded that this correlation only works well when the hardness or fracture toughness is strictly controlled by microstructural features such as grain diameter or the sizes of various phases, which interact with the ultrasonic waves via scattering mechanisms [174, 175].

Analysis of attenuation coefficient data took the form of using the average drop in intensity from one sample surface reflection to the next [175]. At the time this average frequency attenuation coefficient value was used to correlate with mechanical properties of metals (Figure 28). A method created by Vary shows good correlation between the slope of scattering curves and the degree of plane strain fracture toughness of several steel specimens (Figure 29) [176]. Researchers like Vary, Thompson, Klima, and Adler pioneered the analysis of frequency-based attenuation coefficient by taking advantage of the broadband abilities of piezoelectric transducers [120, 174, 176, 177].

The use of signal deconvolution through Fourier transforms started to become popular in the second half of the 20^{th} century allowing for one single broadband ultrasonic transducer to collect a wide range frequency-based attenuation coefficient values [19]. The ability to use fewer transducers and obtain data from larger frequency regimes cuts back on the error introduced by discontinuities in attenuation coefficient spectra caused by the transducers limited bandwidths.

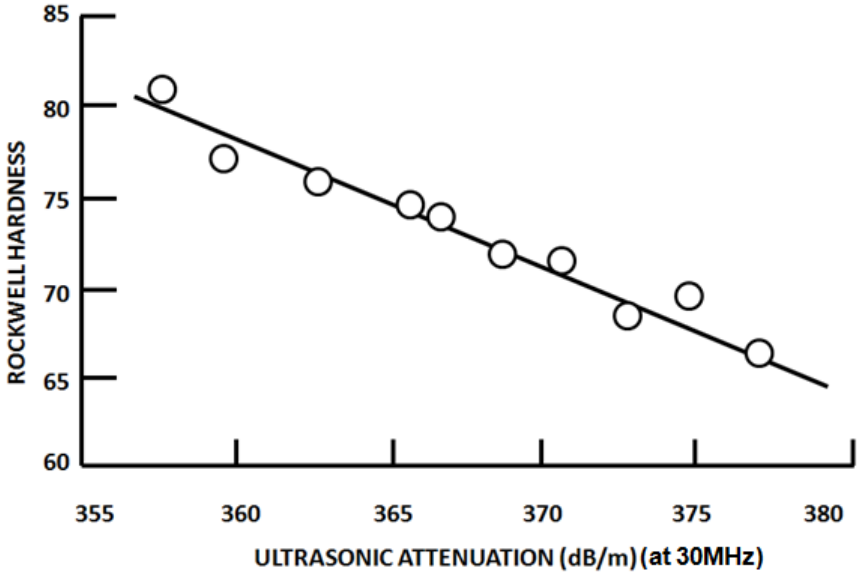

Figure 28. Ultrasonic attenuation measured at 30MHz versus Rockwell hardness for an age hardened aluminum alloy [174].

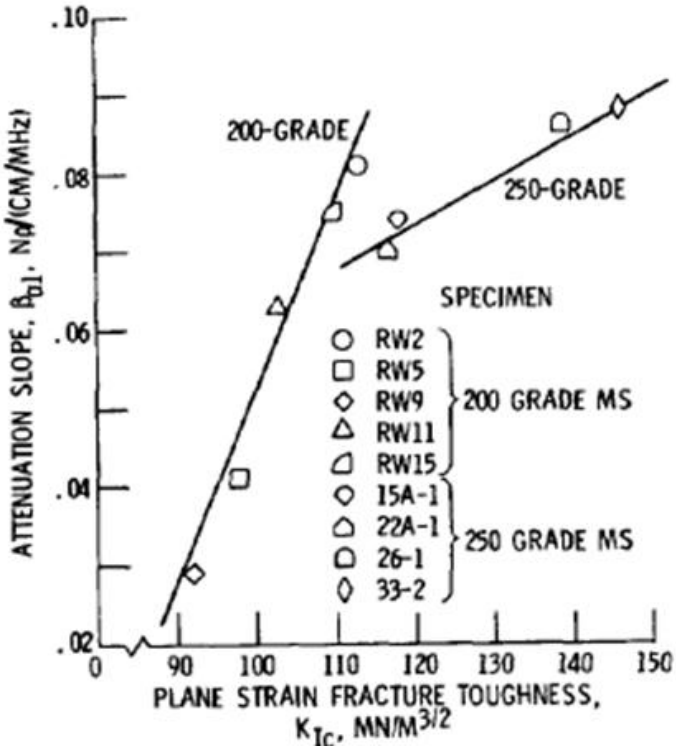

Figure 29. Correlation of scattering attenuation slope with fracture toughness for maraging steels [176].

The theoretical development of the relationship between attenuation coefficient and grain size distributions in metals climaxed in the early 1990's through the work done

by Nicoletti [178]. This work sought to establish not only a basis for the ultrasonic scattering at grain boundaries, but to also improve on previous models derived by those who came before her [178]. The work done by Mason, Lifshitz, and Roney between 1947 and 1950 assumed that the grain sizes within metals are constant and neglected the real life scenario of grain size distributions [124, 132, 179]. Building upon the Roney model for grain scattering by single grains, Nicoletti derived equations which assumed that the total measured attenuation is the summation of scattering attenuation caused by each individual grain (equation 33). This analysis only holds true where scattering is the dominant acoustic energy loss mechanism [178].

$$\alpha(\lambda) = \int_0^\infty N(D) \cdot \alpha(D, \lambda) \qquad \text{Eq.33}$$

where N(D) is a function for the distribution of grains sizes, D is grain diameter, and α(D, λ) is the equation derived by Roney to model the attenuation of single sized grains in metals:

$$\alpha(D, \lambda) = \frac{2}{D^2} \left(\frac{\Delta k}{k}\right)^2 \sum_0^\infty [(2m+1) \cdot sin_m^2(\delta)] \qquad \text{Eq.34}$$

where μ = πD/λ, k is the bulk modulus, and δ is a kroenecker delta related to the spherical Bessel function of order m [179].

A power law function for N(D) was assumed by Nicoletti and given the functional form of [131]:

$$N(D) = KD^{-\gamma} \qquad \text{Eq.35}$$

where K and γ are parameters relating to an assumed single mode grain size distribution. One may obtain these two important parameters, K and γ, by obtaining the attenuation

coefficient from equation 33 by performing acoustic spectroscopy and having some information regarding approximate bounds for the sizes of the distribution. The work done by Nicoletti is influential for this thesis as it explored the basis of obtaining grain size information in dense polycrystalline materials.

2.3.3. Acoustic Spectroscopy of Solid Systems: Ceramics

The comparably more complex microstructures of polycrystalline ceramics to that of metals or particulate suspensions is the greatest limiting cause of the lack of study for acoustic spectroscopy in ceramic materials. Previous attempts at quantitative analysis of attenuation in metals have been devoted to the scattering caused by grains. The work done by Mason, Papadakis, Vary, and others easily separated frequency regimes of attenuation mechanisms such that Rayleigh scattering behavior was primarily studied. The study of acoustic attenuation in dense polycrystalline ceramics does not offer such a benefit. Overlap of Rayleigh and stochastic scattering along with possible absorption mechanisms can occur across wide frequency ranges caused by the presence of solid inclusions, pores, secondary phases, and large grain size distributions. For the sake of this thesis attempts have been made to study controlled alumina microstructures and their effect on attenuation. Fully dense alumina ceramics for structural applications are the focus of this work; therefore, only the effect of fully dense ceramic microstructures will be discussed in this section.

Some of the earliest research performed on linking ceramic microstructure to measured attenuation was done by Evans in 1977 [115]. The approach taken by Evans is based on numerical analyses of the cross sections and size distributions of the predominant scatterers (grains) within polycrystalline ceramics [115]. Several fully

dense ceramic materials were selected for a detailed study: MgO, ZnS, Si_3N_4, SiC, and PZT. The analysis performed by Evans on these ceramic materials is extremely mathematically intensive and required a priori knowledge of the ceramic materials. Spherical grains were assumed where their sizes where estimated using extreme-value bounding conditions; i.e. very large and very small grains were neglected [115].

It was found that using an extreme-value approach to attenuation was tenable for estimating the size of scatterers in these materials and should be applicable to most ceramic systems [115]. The end result of this research allowed for an analytical solution for the prediction of attenuation at each frequency given a certain size distribution of grains and the appropriate elastic properties of the ceramic. This approach built upon earlier theory that scattering follows a power-law dependency. Similar to the Mie scattering equation the solution for scattering cross section derived by Evans and others, does not infer an inverse to solve for grain diameter given a frequency-based attenuation coefficient measurement [115, 140]. In essence all possible solutions for scattering cross section would need to be calculated for each type of polycrystalline ceramic material and a data mining process could limit the total number of possible grain size distributions which would cause such scattering. Even with modern computing power the time considerations for undertaking such a task do not make this approach a feasible one.

The work done by Kulkarni with the aid of Bhardwaj at Ultran Labs focused on using ultrasonic time-of-flight based measurements for the goal of determining the feasibility of using acoustic testing as a method to determine sample density [180]. This work did not rely on spectral-based analyses but provides a good parallel as a different type of ultrasonic microstructural characterization technique. High purity α-alumina

powder of density 3.98g/cm^3 was used to created slip cast green samples from alumina suspensions having different zeta potentials. These green samples were sintered between 1200°C and 1500°C to promote different degrees of density. The result of this study shows the veracity of using time-of-flight based measurements such as sonic velocity and elastic modulus as useful measurements to estimate bulk material density [180]. Figure 30 shows the relative density of each green sample versus either longitudinal velocity or Young's modulus. The result of the work performed by Kulkarni and Bhardwaj gives the possibility of using ultrasonic testing methods as a method of determining only the bulk density and not the average pore size or pore size distribution.

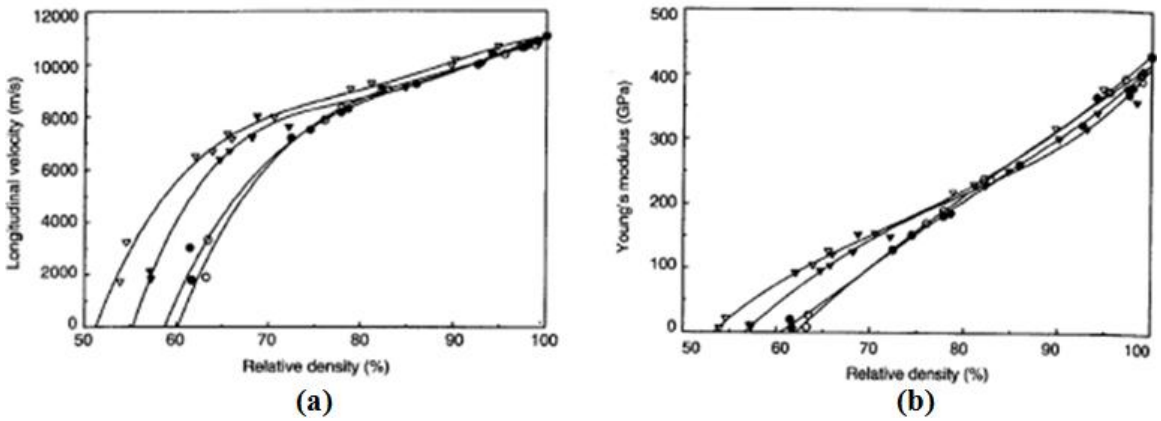

Figure 30. Relative density versus (a) longitudinal velocity and (b) Young's modulus for alumina bodies of varying density and zeta potential. ○: pH 4.0, 62.9% green density; ●: pH 4.5, 61.7% green density; v: pH 10.5, 53.9% green density; ▼: pH 11.0, 57.3% green density [180].

A frequency-based attenuation analysis will have to be performed to obtain any semblance of this kind of information. Further work on the same alpha alumina samples created by Kulkarni and Bhardwaj was to do exactly this. Attenuation coefficient measurements were made in the frequency range of 5-30MHz. The conclusion of this testing showed that the relative attenuation measurements were sensitive to the microstructures of the partially sintered samples containing lower densities [181]. Their

final conclusion was that accounting for the attenuation behavior of the complex range of microstructures present in their samples was too difficult such that any quantitative information could be gleaned [181]. Commonly seen scattering trends were qualitatively observed but a more detailed investigation was required due to the different types of scattering mechanisms present.

Empirical correlations between ceramic microstructure and attenuation coefficient have been made by Klima and Baaklini in the late 1980's [119, 177]. These studies showed that a positive correlation exists between the density and average pore size of silicon carbides with different microstructures and varying densities. Figure 31 shows some of the earliest recorded qualitative attenuation data as a function of variable ceramic microstructure.

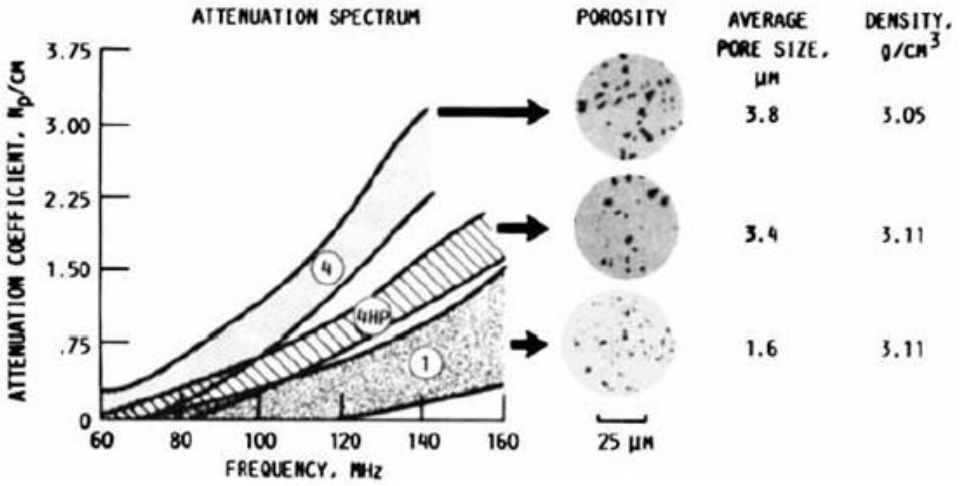

Figure 31. Attenuation coefficient for various silicon carbides. 1 and 4: sintered and 4HP: hot isostatic pressed. Bounds for each spectrum represent measured range of each SiC set [119].

Baaklini's postulate that scattering is controlled by porosity (when present) at exceptionally high frequencies and fine grains for ceramic materials is validated by the work done by himself, Klima, and Tittmann and summarized in Figure 30 [115, 119, 177]. The implications of these results provide a means for creating quantitative analyses

of attenuation coefficient spectra with regards to obtaining pore size information in structural ceramic materials [119]. With regards to the samples studied in this thesis, scattering due to porosity is considered to be negligible as the samples can be approximated as being fully dense.

In 1993 the first attempt to perform frequency-based attenuation measurements about multiple points in any material was done by Roth and others, in Si_3N_4 ceramics. This technique made use of traditional ultrasonic nondestructive testing methods in what was referred to as an "Ultrasonic Contact Scan Technique" [182]. Essentially, frequency-based attenuation coefficient data were collected by using a single contact transducer while manually positioning the transducer at different points about the sample. The data were collected at each point and manually processed using a FFT. Attenuation coefficient values were plotted as a function of spatial location every 10MHz [182]. The resultant plots can be viewed in a flipbook style format to visualize how attenuation changes with frequency and location. The goal of this study was to spatially and spectrally locate six defect regions of the silicon nitride ceramic which contained a significantly higher degree of porosity compared with the rest of that sample. The attenuation coefficient images revealed the known pore fraction nonuniformity across the sample but were unable to quantify the amount of or size distribution of the pores [182]. Figure 32 shows the frequency-based attenuation coefficient maps created over the entire area of the Si_3N_4 sample.

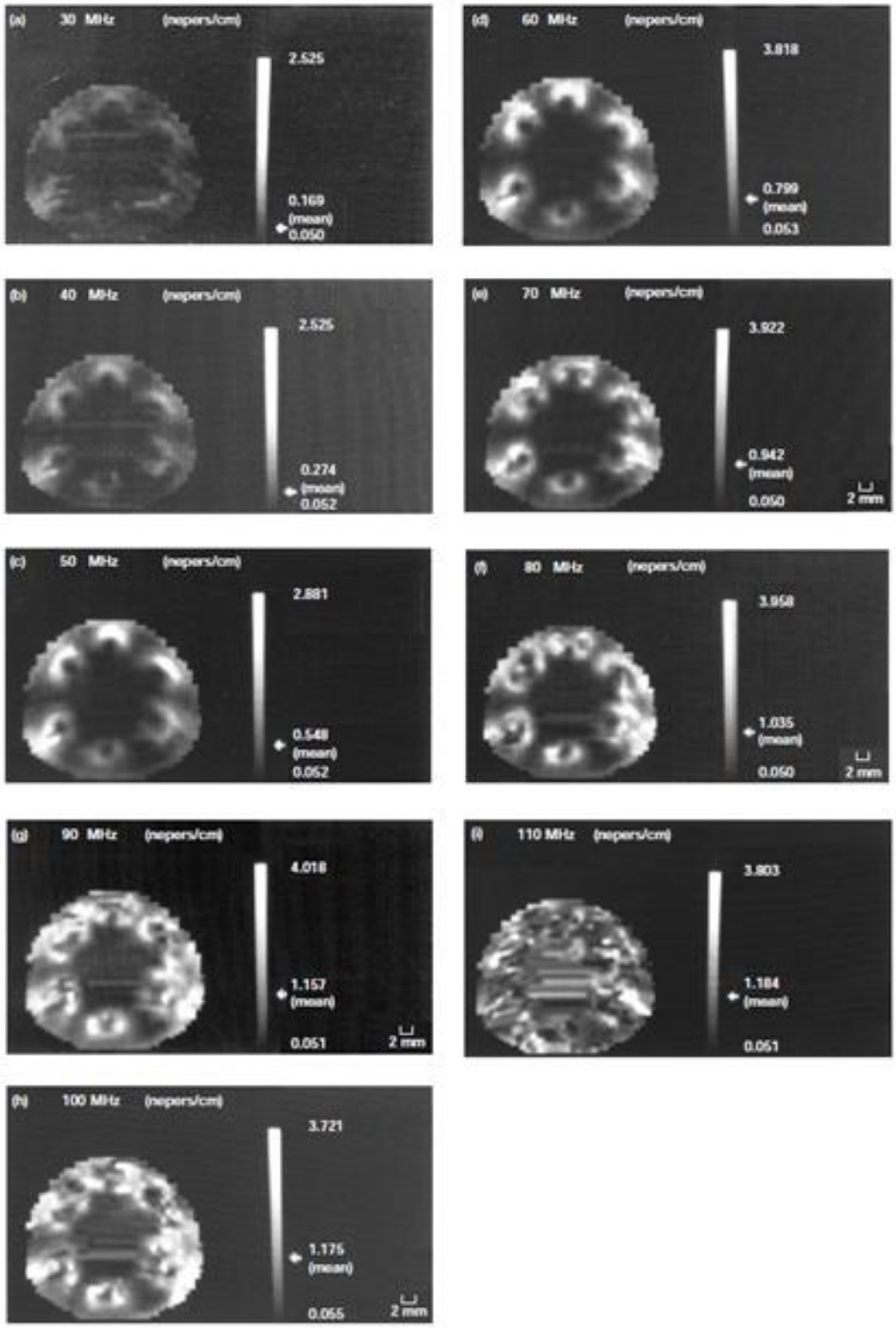

Figure 32. Frequency-based attenuation coefficient images and mean values from 30-110MHz in 10MHz increments of a Si_3N_4 sample containing six regions of high pore-fraction. Each region is separated by approximately 60° [182].

The research to date regarding acoustic spectroscopy in ceramic materials is strongly based on what has been done with metallic systems. The ability to qualitatively

detect known microstructural differences has been demonstrated and the foundation for using acoustic spectroscopy as a quantitative characterization tool has been set.

There exists a lacking in the understanding of how multiple acoustic attenuation mechanisms interact across broad frequency ranges and how such an understanding may be used to obtain the large amount of microstructural data which acoustic physics predicts. Current ultrasonic nondestructive techniques are capable of collecting and analyzing similar types of data seen in Figure 32. The use of automated equipment, stronger computing power, and higher resolution devices allows for the expedition of data collection and analysis. The work in this thesis seeks to build upon these techniques and further the understanding of ultrasonic interaction in dense polycrystalline alumina ceramics.

2.3.4. Curve Fitting and Modeling of Attenuation Coefficient Curves

After collecting measured attenuation coefficient spectra a useful method of extracting useful information is to fit each spectra to a specific function where each parameter of a function would be related to a parameter of the microstructure. The spectral behavior of attenuation is similar for most types of metals and ceramics; some type of absorption mechanism occurs at low frequencies and scattering takers over at high frequencies. The frequency separation of absorption and scattering behavior for metals is quite large when compared to what would be seen in dense, polycrystalline, high hardness ceramics. For the case of aluminum oxide with microstructural features approximately 10μm and less, the peak-like behavior of absorption occurs up to 50MHz. At frequencies between 30 and 50MHz one would usually see a convolution of absorption and scattering behavior in aluminum oxide [183]. As a result this makes

fitting large bandwidth attenuation spectra to a single function quite difficult. It is typically convenient to split attenuation coefficient spectra (taken from dense, polycrystalline, high hardness ceramics) into two separate frequency regimes where each loss mechanism can be studied separately. A schematic of a generalized spectrum showing this can be seen in Figure 33.

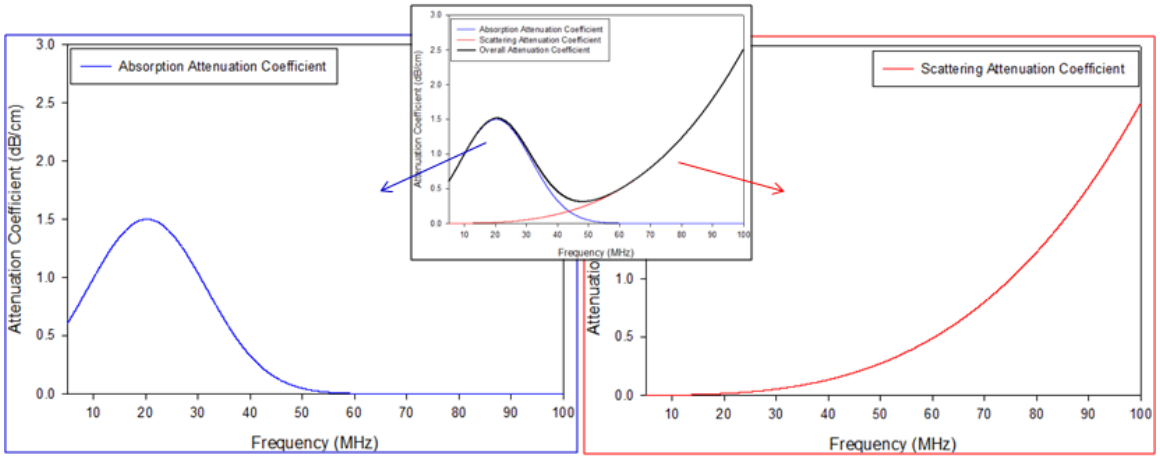

Figure 33. Generalized acoustic attenuation coefficient spectrum split into the lower frequency absorption and higher frequency scattering regimes [183].

The peak-like behavior of thermoelastic absorption operable in dense polycrystalline ceramics and metals has been modeled through the use of a three-parameter Lorentzian distribution [132, 161]. Lifshitz assumed a Lorentzian distribution as it models the damped, driven, harmonic behavior of single particles in flexure undergoing thermoelastic absorption. The three parameters of the Lorentzian distribution relate to specific parameters of the absorbing features within the microstructure according to the equation [21, 161]:

$$E = I\frac{\gamma^2}{(f-f_o)^2+\gamma^2} \qquad \text{Eq.36}$$

where E is the energy absorbed by a single particle according to intraparticle thermoelastic absorption, 'I' is an intensity constant, γ is a damping constant, and f_o is the frequency of maximum attenuation for a single particle as given in equation 30. These three parameters, I, γ, and f_o, are believed to be related to the concentration, boundary conditions, and size of the absorbing particles, respectively [20]. Work done by Portune used a least squares regression analysis for a three-parameter Lorentzian to minimize each parameter for single spectra taken from dense polycrystalline silicon carbide [20]. The results gave a normalized size distribution for carbon and B_4C solid inclusions present in the SiC matrix causing intraparticle thermoelastic absorption. Limitations of computation power make the time considerations when performing this type of analysis such that it is not feasible to perform over all points in a sample; e.g. an analysis of 40,000 data points over a 100x100mm tile would take approximately 30 days [20].

Attenuation caused by scattering is dominated by the grains of the primary phase of metals and ceramics alike [143]. Since the time of Rayleigh, scattering attenuation has been shown to follow power-law behavior. An analysis of attenuation coefficient spectra dominated by scattering is relatively easier to perform than that dominated by an absorption mechanism. All of those previously reporting on acoustic spectroscopy in dense polycrystalline solids have shown the same trend: as mean grain size increases the attenuation coefficient curves show an increase in slope. According to the power-law dependency of scattering curves, as grain size increases the exponent on frequency should decrease from 4 (Rayleigh behavior) to 2 (stochastic behavior) [168]. The exponent of frequency rarely equals exactly 4 or 2 for ceramic materials as there is a

distribution of grain sizes and a bandwidth of frequencies [143]. This made the use of curve fitting to a power law extremely attractive when employing acoustic spectroscopy for the purpose of ranking and measuring grain size dependent properties [176].

As mentioned above an analytical solution and an inverse to that solution which accounts for every scatterer size to wavelength ratio [19]. A generalized power law fit seen in equation 37 has been tested to rank grain size in metals [176].

$$\alpha_{Fit} = cf^{m} \qquad \text{Eq.37}$$

where ‘c’ and ‘m’ change accordingly with microstructural changes which affect the attenuation coefficient. The parameter ‘c’ has been said to relate to the morphology and elastic anisotropy of single grains while the ‘m’ parameter relates to the size of such grains [19]. Theoretically, an ‘m’ value weighted towards 4 or 2 will reflect dominance by Rayleigh or stochastic scattering, respectively. However, it has been shown that curve fitting to a general power law does not necessarily give accurate information for the case of dense, polycrystalline alumina [142]. This is believed to be caused by the relative dominance of the amount of energy scattered by stochastic or diffuse affects compared to that of Rayleigh behavior [141].

Stochastic and diffuse scattering attenuate as much as 1,000 to 10,0000 times more energy than that by caused by Rayleigh scattering [141, 142]. This is due to the nature of the way these different modes of scattering occur: Rayleigh exhibits forward scattering, while stochastic and diffuse display scattering with a wider range of loss [141]. The distribution of grain sizes found in commercial polycrystalline alumina makes it such that all three scattering mechanisms are operable and superimpose to form a single scattering attenuation coefficient spectrum. A deconvolution of a single power law curve

into three power law curves is not mathematically possible without added information on the microstructure. As a result, curve fitting to a general power law, as seen in equation 37, does not work well with ceramic materials.

The approach taken by Nicoletti makes use of forcing acoustic attenuation coefficient spectra to follow Rayleigh, stochastic, or diffuse behavior. The functional models for each type of scattering can be seen below in equations 38-40.

$$\alpha_R = a^3 C_R f^4 \quad \text{Eq.38}$$

$$\alpha_S = a C_S f^2 \quad \text{Eq.39}$$

$$\alpha_D = \frac{C_D f^0}{a} \quad \text{Eq.40}$$

where ‘a’ is mean diameter and ‘C’ are constants related to parameters of the microstructure such as morphology and elastic anisotropy. The subscripts on α and C refer to Rayleigh, stochastic, or diffuse scattering [178]. Curve fitting to the above equations would result in providing the product of the diameter and C constant terms. A prior knowledge through the use of standard samples would be necessary to obtain values for the scattering C constants.

Many of the previous attempts at curve fitting portions of attenuation coefficient spectra gave localized results only applicable to the specific samples tested or revealed qualitative differences with no causal effect explained [168]. Generalized methods for extracting microstructural information from attenuation coefficient spectra are not available. The current governing physics which links attenuation mechanism with microstructure only exist for the materials which have been chosen to be tested by the researchers at the time. Methods to easily deconstruct attenuation spectra to obtain useful

information do not exist for dense, polycrystalline ceramics such as aluminum oxide. One objective this thesis explores is the development of such methodologies.

2.4. Established Ultrasound Nondestructive Testing Methods

There are many possible designs for the generation of ultrasound, receiving ultrasound which has interacted with the material under study, and analyzing the received wave [22]. This section describes the possible ultrasonic testing configurations already established, such as through transmission, pitch-catch, and pulse-echo, and how they can be used in three testing modes: A, B, or C scan modes. Ultrasonic nondestructive evaluation requires certain sample uniformities such that coherent data can be collected. The tolerance limits for solid sample requirements using ultrasonic testing in a pulse-echo configuration is discussed. An explanation of the two fundamental types of measurements; time-of-flight (TOF) and amplitude follows. Ending this section is a discussion of how attenuation coefficient spectra are collected.

2.4.1. Ultrasound Testing Configurations

The emission and detection of ultrasound is carried out by making use of the reversibility of the phenomena of piezoelectricity, electrostriction, and magnetostriction [126]. Ultrasonic measurements are based on examining the properties of an acoustic wave after it has propagated through a material [110]. There are three types of ultrasound testing configurations which may be used for the introduction and measurement of the acoustic wave. While the generation and detection of the ultrasound is the same for each testing configuration through the use of ultrasonic transducers, each configuration differs in how the transducers are used. The following sections describe each ultrasound configuration, placing special emphasis on the pulse-echo configuration.

2.4.1.1. Through-Transmission

In the through-transmission configuration, an ultrasonic transducer used for emission is on one side of the material while a second transducer used for detection is placed on the opposite side. Scanning of the material using this method can spatially locate large features and inclusions in the X-Y plane. Compared to the pitch-catch or pulse-echo configurations, through-transmission ultrasound testing samples the least amount of volume making the received signal stronger [184]. Due to this, the through-transmission configuration is used for the nondestructive inspection of multilayered, multicomponent, composite, or highly attenuative materials [184]. The acoustic signal will pass through the material directly and only once. The multitude of exponentially decaying sample surface reflections is disregarded. Only the amplitude of the transmitted signal is of concern and is reduced by the variety of attenuation mechanisms discussed. This method is useful where a reflected signal could be noisy due to large solid inclusions within the material [88].

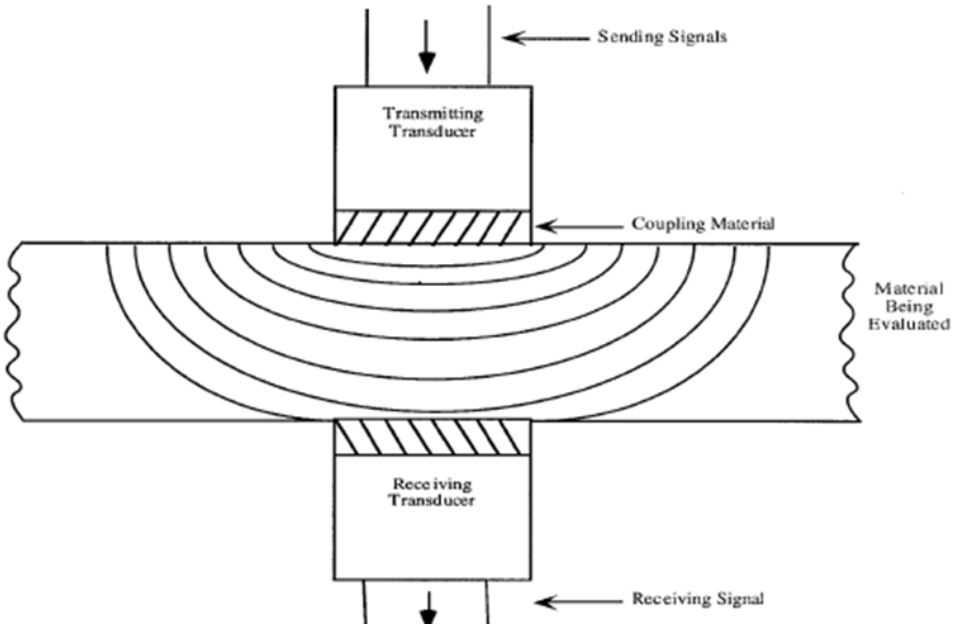

Figure 34. Schematic diagram of through-transmission ultrasonic configuration [184].

Through-transmission ultrasonic NDE can be performed in contact using a high viscosity coupling material or in non-contact with either the use of water or air as the propagating medium for the ultrasound. Through-transmission ultrasonics performed in air-coupled, non-contact mode was pioneered by the Ultran group to perform acoustic testing on highly attenuating materials such as concrete [185].

2.4.1.2. Pitch-Catch

Similar to the through-transmission configuration, pitch-catch ultrasonic testing uses two transducers. This method is primarily used for testing cylindrical tubes and other nonlinear parallel sided surfaces [184]. It is also useful for performing ultrasonic NDE measurements on materials where only one side is accessible; such as testing welds or the structural integrity of aircraft [110]. This type of configuration is typically performed in contact using a high viscosity coupling medium and is used to determine flaw depth and spatial location [184]. Pitch-catch uses angled ultrasound beams to interrogate a sample making it the configuration which samples the largest amount of material volume. Materials which are highly attenuating would not be suitable to test with this configuration.

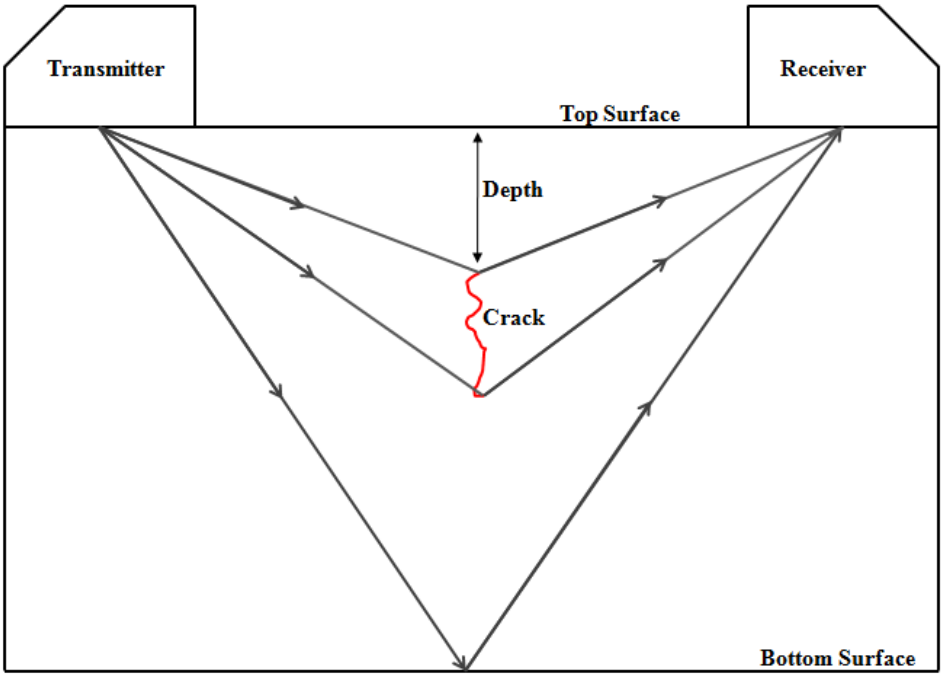

Figure 35. Schematic diagram of pitch-catch ultrasonic configuration [97].

2.4.1.3. Pulse-Echo

The most widely used ultrasonic test configuration is pulse-echo [91]. This type of configuration has its advantages when compared to through-transmission or pitch-catch types. While the other two use two transducers to perform either the transmission or receiving of the ultrasonic pulses, pulse-echo testing uses only one transducer to perform both operations. The ultrasonic transducer is positioned orthogonal to the sample surface to ensure the greatest amount of acoustic energy is introduced into the sample. The reflected acoustic pulses are returned to the transducer and analyzed using an oscilloscope. Pulse-echo testing can be performed in contact or non-contact mode using a high viscosity medium, water, or air as the propagating medium [91, 184, 185].

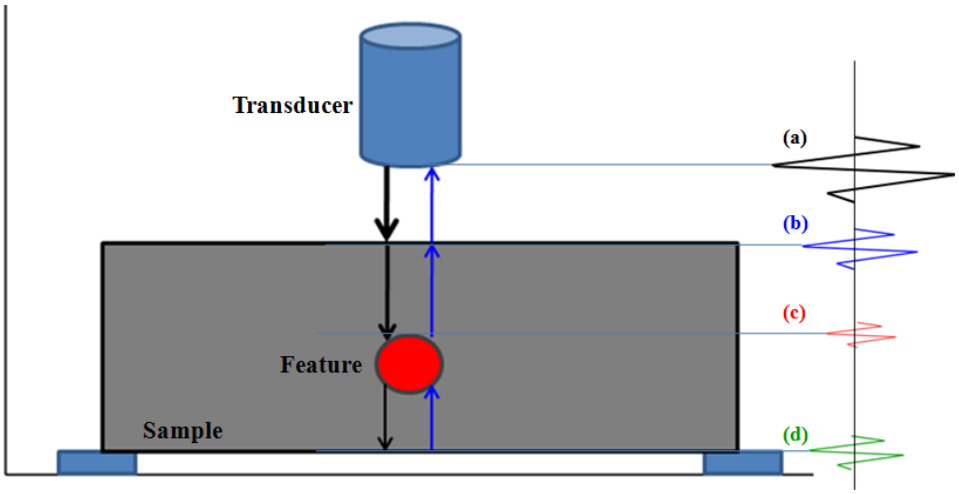

Figure 36. Schematic diagram of pulse-echo ultrasonic configuration. (a) Initial pulse; (b) Top surface pulse; (c) Feature signal; (d) Bottom surface pulse [14].

An advantage of using a pulse-echo setup is the general decrease in cost: one transducer costs less than two. Another advantage for using pulse-echo is there need not be any correction factor to account for slight differences between two transducers as there is with the through-transmission or pitch-catch configurations [89]. This makes pulse-echo the superior ultrasound NDE setup when performing frequency-based measurements as no two transducers have identical frequency profiles [89]. A disadvantage of this configuration is that the ultrasonic wave travels through twice the thickness of the material leading to an increase in attenuation for the received wave. For the case of highly attenuating materials pulse-echo testing is inapplicable and through-transmission or another type of NDE test must be used [16]. The testing performed in this thesis makes use of the pulse-echo configuration and all references of ultrasound NDE hereafter assumes a pulse-echo configuration.

2.4.2. Ultrasound Testing Modes

In ultrasonic NDE there are several types of data display modes used to collect and present information. These modes utilize different methods for acquisition and

display of the collected data each of which having different purposes. The three types of ultrasonic testing modes discussed are A-Scans, B-Scans, and C-Scans [143]. Simply put, A-Scans are point measurements, B-Scans are measurements across a line about the sample, and C-Scans are full sample area property maps [88]. The purpose and data display types for each type of ultrasound testing mode are discussed below.

2.4.2.1. A-Scans

The A-Scan is the most commonly used ultrasound scanning mode [143]. The display of an A-Scan would be shown through the use of an oscilloscope: time versus amplitude. An example of an A-Scan can be seen in Figure 37 where the top and bottom surface reflections (longitudinal) are labeled along with shear component peaks. This A-Scan is recorded from a high density, polycrystalline alumina tile. A-Scan measurements are made by recording the amplitude and time of the received waveforms indicative of specific sample surfaces. A-Scans are only done at a single point of the sample and require the least amount of time to perform [9]. The manipulation of the time and amplitude of specific peaks allows for the calculation of useful properties such as sonic velocity and Young's modulus [95].

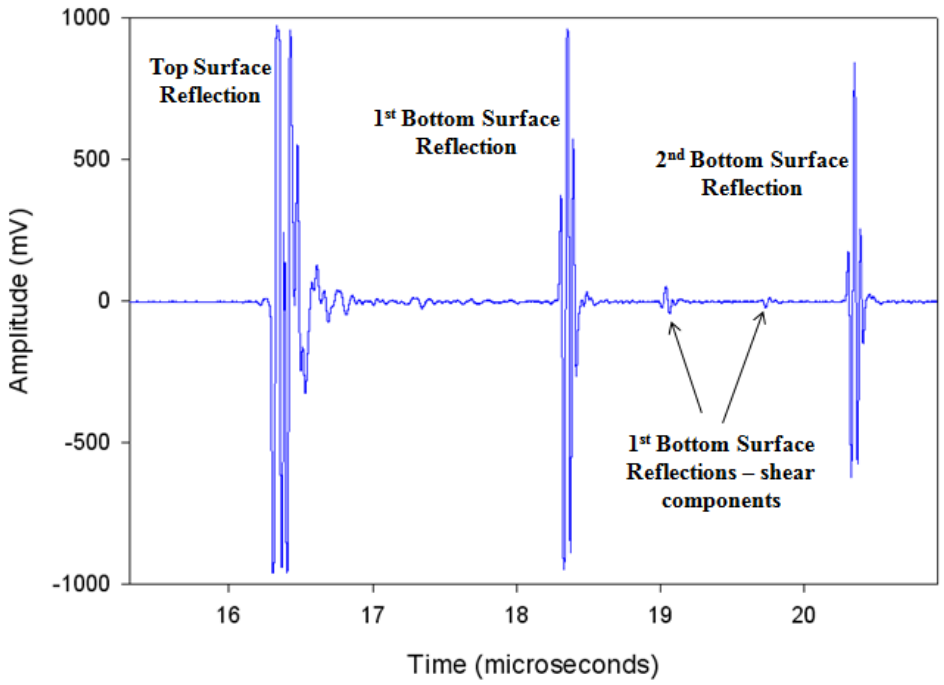

Figure 37. A-scan of dense polycrystalline alumina. Major peaks are longitudinal reflections [114].

2.4.2.2. B-Scans

A linear compilation of A-Scans is known as a B-Scan. A B-Scan is performed by collecting multiple A-Scans in a single direction. This can be thought of as a sameple cross section of data. Typically these scans are taken along the x or y axis relative to the sample placement. An automated motion control unit is typically utilized to collect A-Scans with a predefined step size between points. The resulting data are presented as a three dimensional array where the x-axis represents the axis of travel about the sample, the y-axis shows time, and the z-axis is the amplitude of the collected waveforms [143]. High intensity data in the z-axis usually represent the top and bottom surfaces of the sample being inspected where the presence of a defect will present as a series of exponentially decaying features. An example of a B-Scan can be seen in Figure 38. As with an A-Scan, B-Scans allow for depth profiling of large defects within a material [9,

143]. These defects present as reflections between the top and bottom surface major reflections.

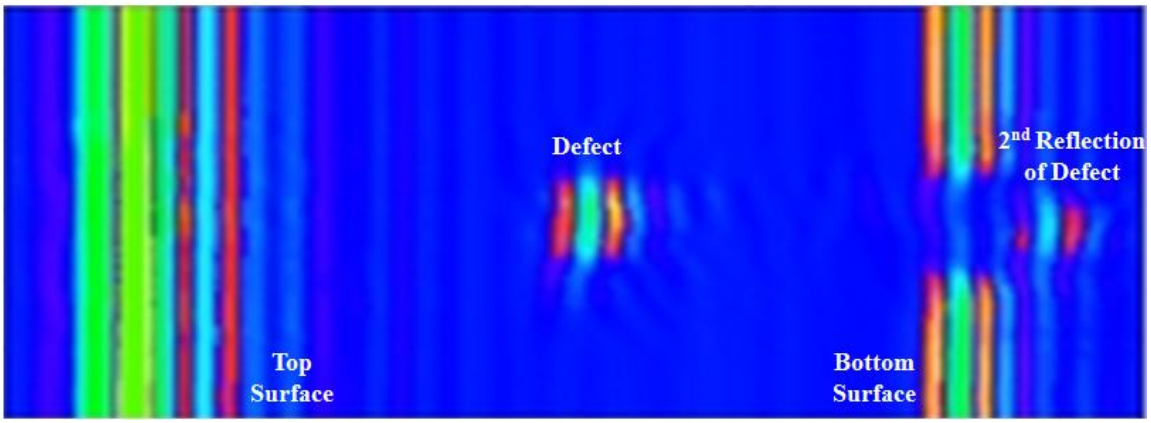

Figure 38. B-Scan of laminar flaw in metal pressure tube [186].

2.4.2.3. C-Scans

An ultrasonic C-Scan is obtained from a two dimensional raster procedure of the transducer about a sample [9]. This measurement mode is useful for the evaluation of large sample areas. Similar to a B-Scan, C-Scans record data in a predefined raster of steps about the sample. A motion control unit is synced with a device to record positional information while data are being collected. This provides sample data over all points along with where in the sample it came from. A schematic of this can be seen in Figure 39. It is important to note that, unlike A and B-Scans, C-Scans give no semblance of where in the depth of a sample a possible defect occurs. This is due to the volumetric nature of the test. All features and data contained within the volume of the ultrasound beam are presented as a two dimensional graph with a third dimension giving a quantized material property value, not depth [9]. Typical ultrasonic C-Scan measurements are capable of spatially locating large flaws and providing possible property variations over

entire sample areas. The measureable properties of a material are based on the time at which its peaks occur, their amplitude, or their frequency.

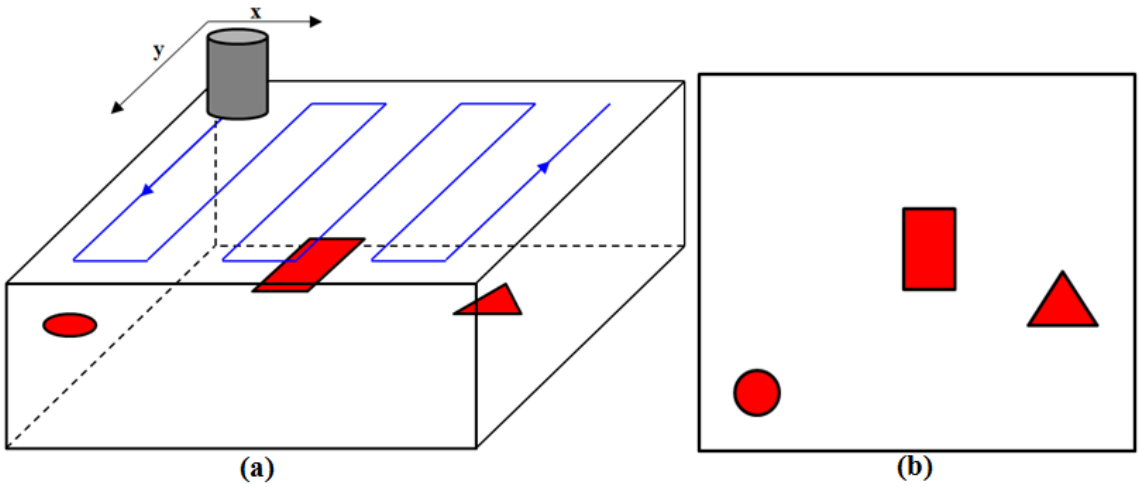

Figure 39. (a) Raster motion of ultrasonic transducer during a C-Scan; defects present at different locations and depths. (b) Schematic C-Scan showing spatial location of defects but not depth location [9].

2.4.3. Peak Measurement

As an acoustic wave propagates through a ceramic material it may encounter multiple interfaces at which there is an acoustic impedance mismatch. At these interfaces there is the transmission and reflection of the acoustic wave. The reflected waves which make it back to the ultrasonic transducer present as peaks viewed on an oscilloscope indicative of whichever surface they were reflected from. The temporal positions of the reflected waveforms correspond to the depth within the sample at which they were originally generated. By measuring the times at which each peak occurs one may obtain the longitudinal and shear velocities of the material interrogated. These values are manipulated such that the Poisson ratio and elastic moduli can be calculated. Amplitude based measurements rely on measuring the intensity and ratios of specific peaks. The frequency dependence of the signal strength is determined through the use of Fourier

transforms. This section explains how time-of-flight and amplitude based measurements are performed, recorded, calculated, and interpreted.

2.4.3.1. Time of Flight Based Measurements

One of the two possible measurements when performing ultrasound NDE is that of time-of-flight (TOF). This is done through the use of electronic gates which measure the temporal position of oscilloscope peaks specific to a sample surface and acoustic wave type; longitudinal or shear [187]. The relatively high sonic velocities of dense, polycrystalline alumina make it such that TOF's are measured in microseconds. TOF measurements of singular peaks can be incorporated together to give calculations of a materials sonic velocities, elastic properties, and thickness [95, 188]. This section describes the procedures in which TOF is measured and how the associated material properties are calculated.

2.4.3.1.1. Time of Flight Measurement Modes

Ultrasonic time of flight describes the variety of methods which measure the time it takes for an acoustic wave to travel through a medium. TOF is simply the time between reflected waves of the same type (longitudinal or shear). There are several methods of measuring the temporal position of reflected sample peaks. All measurement methods rely upon using a static electronic gate which encompasses the peak of interest to be measured. The acquisition software determines which part of the peak is measured to give a time value at where each peak is located. This can be done by measuring the inflection of when the peak first occurs, the threshold of when the peak hits the electronic gate, or the time at which the peak reaches its maximum amplitude. The resolution of TOF measurements through the use of any of the three techniques discussed relies on

how often a datum point occurs on the time versus amplitude oscilloscope plot. This is dictated by the sampling rate of the analog to digital converter (A/D) card component of the oscilloscope.

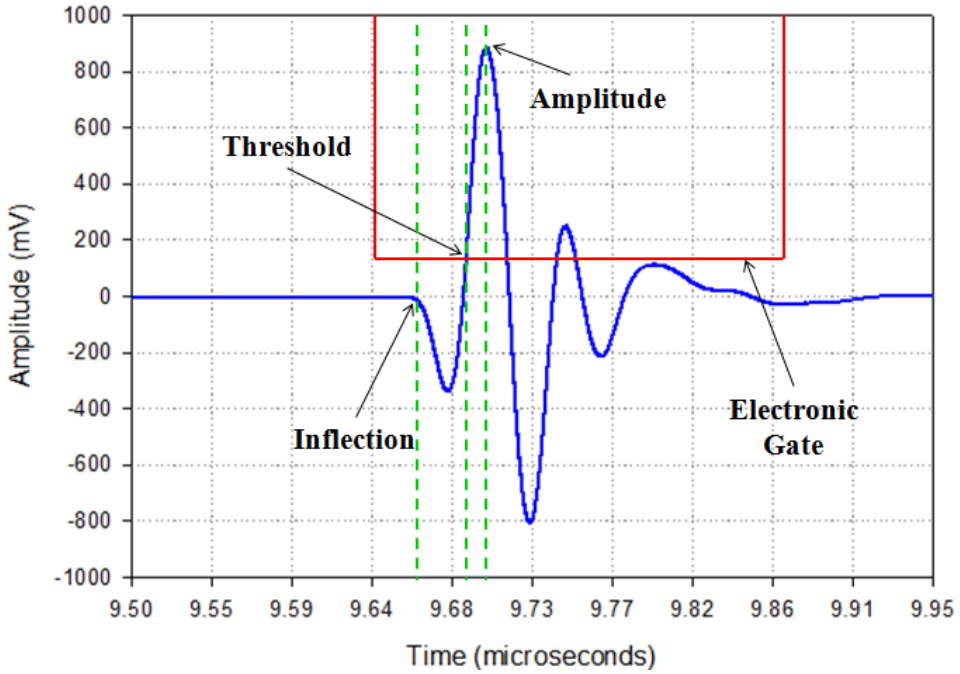

Figure 40. Oscilloscope view of a sample peak. Three measurement modes for TOF: Inflection, 9.658µs; Threshold, 9.688µs; and Amplitude, 9.699µs.

Each measurement type gives slightly different TOF values as they record different times when the peak occurs. This can be seen in Figure 40 where there will be a difference in measured TOF by as much as 0.041µs between TOF measurement modes. The difference in measurement modes seen in the example above (Figure 40) can amount to approximately a 3% difference in sonic velocities and elastic properties. Depending on which mode one chooses to use this difference can amount to the rejection of parts assumed to be lower quality. Most TOF measurements are performed by taking either the threshold or amplitude times [110]. These measurements are not as accurate as taking the inflection time when the peak first occurs and always underestimates the actual value

of the sonic velocities and elastic properties. This is due to inherent sources of error: signal noise, amplitude reduction, and peak broadening [97].

Signal noise caused by electronic reflections in the hardware used adds error to all three types of TOF measurements. This noise presents as high frequency static which is superimposed at every point in an oscilloscope graph. Signal noise presents as the constructive or destructive interference from all electronic components connected to the oscilloscope. A major proponent of noise is caused by reflections in attached cables where longer cables introduce more noise. The superposition of the noise signal on top of reflected sample peaks may lead to inaccuracies as to when the inflection, threshold, or amplitude of the peak actually occurs. Signal noise is comprised of certain frequency components which can also alter the actual frequency bandwidth of a reflected sample peak. High pass or low pass noise filters are standard features which can be found on many modern ultrasonic NDE setups to help alleviate the error introduced when measuring TOF.

When measuring TOF's based on when the threshold of the peak occurs one must ensure that the electronic gate crosses through the same portion of reflected sample peak over all points in sample. If there is a region of a sample which has a large defect or a decrease in density the reflected sample peaks will diminish in amplitude. This causes the electronic gates to capture different time positions of the reflected peaks over these regions and present with a localized stark difference in a C-Scan map. This effect can be seen in Figure 41 below. As the amplitude of the measured peak decreases the electronic gates captures a larger TOF of the same peak. The example in Figure 41 shows the electronic gate measuring a time position of approximately 10.048μs for a large portion

of an alumina sample. As the amplitude of the reflected wave decreases for a portion of the sample a higher TOF is measured. Correction for this effect is not trivial and may require sensitive placement of the static electronic gates or multiple scans over different portions of a sample.

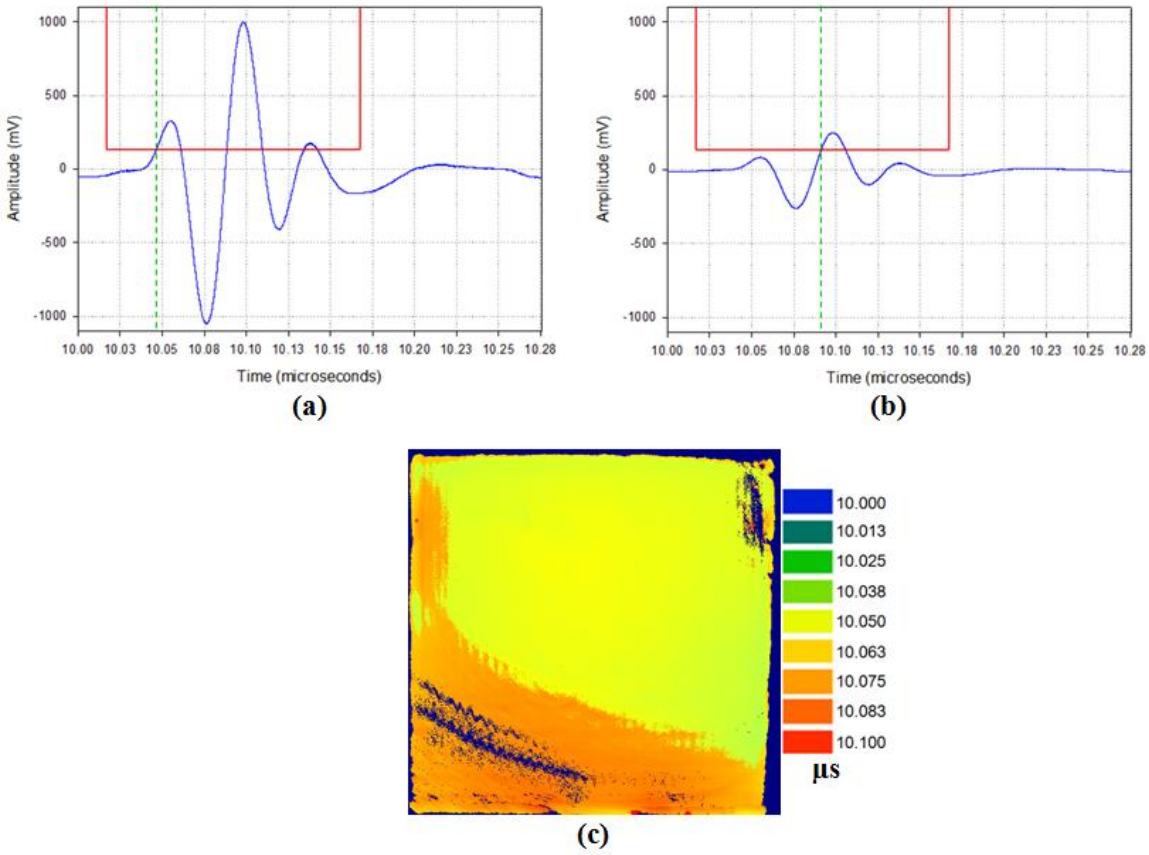

Figure 41. (a) Threshold based measurement of TOF, 10.048µs; (b) Effect of amplitude decrease on TOF measurement using threshold method, 10.092µs; (c) TOF C-Scan map of alumina tile showing spatial effect of amplitude reduction on TOF measurements.

Peak broadening is a phenomenon which causes the multiple reflections of sample surfaces to get wider. This occurs due to the typical attenuation of higher frequencies as the ultrasonic wave propagates through a dense solid material [88]. The width of the peaks is dominated by the strongest frequency present. As higher frequencies are attenuated, lower frequencies become more dominant and broaden the peaks. As a result

the maximum amplitude of subsequent reflections after the top surface shift to occur at longer times [88]. This ultimately gives larger measured TOF's and results in lower reported sonic velocities and elastic properties [110]. An example of this behavior can be seen in Figure 42 where the second bottom surface reflection shows a slightly larger difference in time between the beginning and end of the peak. Testing done for this thesis based on TOF measurements measures the time at which the inflection of each reflected peak occurs. This eliminates sources of error from peak broadening and amplitude reduction.

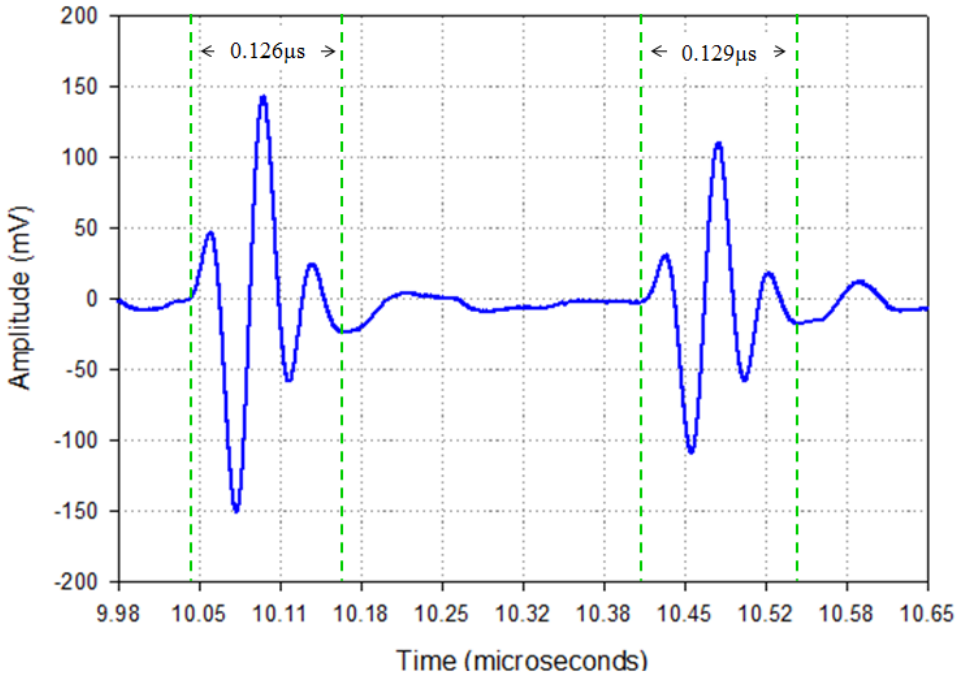

Figure 42. A-Scan showing phenomenon of peak broadening. As time increases the second bottom surface reflection broadens by approximately 3ns.

2.4.3.1.2. Measuring Acoustic Velocity

Acoustic velocity is the distance travelled by a propagating sound wave during a unit of time through an elastic medium [91]. In solid materials there exist different acoustic velocities for different propagation modes of sound such as longitudinal, shear,

surface and other types of waves. This thesis is concerned with the measurement of only longitudinal and shear waves. The speed of sound in a material can be determined by measuring its thickness and how much time it takes for an acoustic wave to traverse such a thickness [189]. An A-Scan gives a display of the temporal positions of sample surfaces in the form of reflected peaks related to either longitudinal or shear waves which can be used to measure TOF. Using the common relationship of velocity being equal to distance divided by time, where distance is the sample thickness and time is the TOF, the longitudinal (C_L) and shear (C_S) wave velocities can be determined through the follow equations [90]:

$$C_L = \frac{2d}{TOF_L} \quad \text{Eq.41}$$

$$C_S = \frac{2d}{TOF_S} \quad \text{Eq.42}$$

where d is the distance travelled by the acoustic wave and the subscripts, L and S, refer to either longitudinal or shear waves. The factor of 2 in each equation accounts for the ultrasonic wave travelling through the material twice due to using a pulse-echo configuration.

When performing immersion-based, non-contact, ultrasound NDE, the measurement of a shear wave may be difficult as the transducers used are meant to introduce only longitudinal waves into the material. Shear waves do not exist in low viscosity fluid medium such as water [190]. The generation of any shear wave measured while performing this type of testing is through a phenomenon called mode conversion. Mode conversion is the conversion of a portion of acoustic wave energy of a specific

wave mode into another wave mode [14]. Shear waves oscillate particles perpendicular to the motion of the ultrasonic wave. The angle in which the ultrasonic wave enters the material dictates whether a longitudinal, shear, or both types of waves will exist in a solid material [191]. A broadband longitudinal wave transducer emits acoustic waves comprised of multiple frequencies simultaneously. Different degrees of diffraction and refraction occur according to each frequency which allows for the angled introduction of longitudinal waves into a solid material. This slight angularity of longitudinal waves produces shear waves.

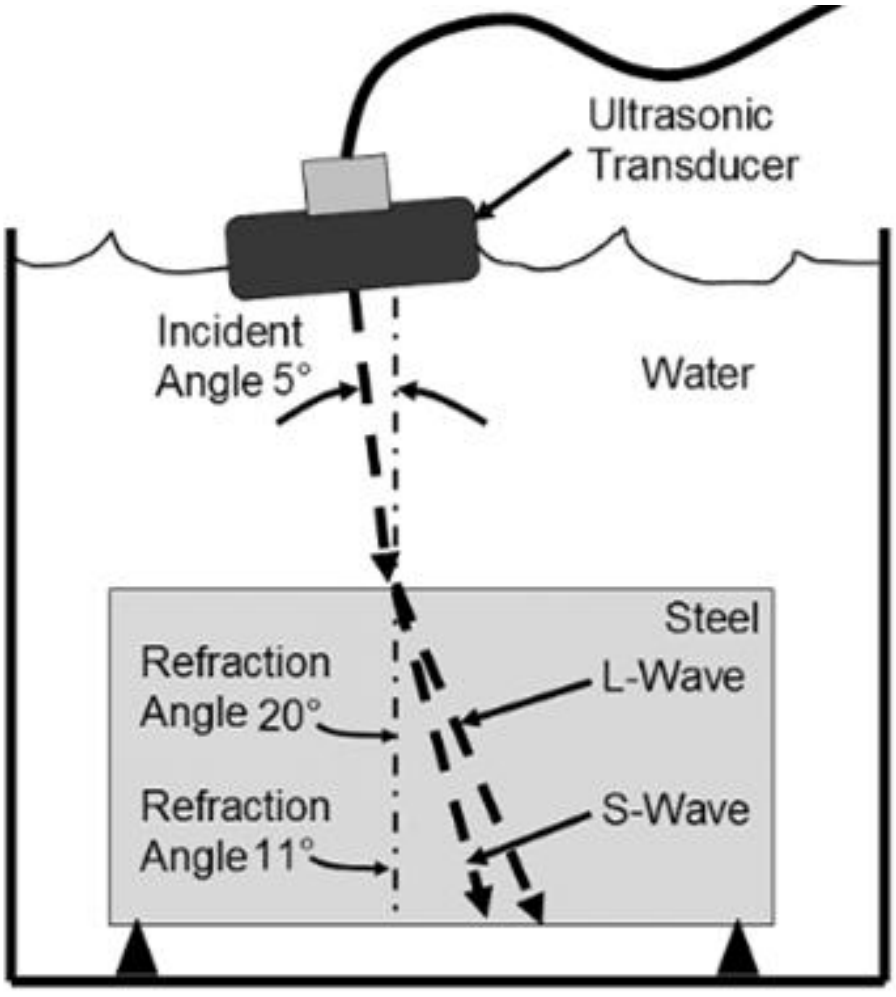

Figure 43. Schematic illustration of the generation of shear waves through mode conversion [191].

Each interface between an elastic solid and another propagating medium causes mode conversion; not just longitudinal to shear, but also shear to longitudinal. As the incident longitudinal wave enters an elastic solid from water a portion of the longitudinal wave energy is converted to create a shear wave. Both longitudinal and shear waves travel through the material, where longitudinal waves travel faster than shear, and encounter the bottom surface-water interface. On this reflection four waves are produced: longitudinal to longitudinal, longitudinal to shear mode converted, shear to longitudinal mode converted, and shear to shear. These four waves travel back through the sample at different rates and return to the transducer as longitudinal waves through the water medium.

Pure longitudinal waves travel the fastest and are expected to appear first. Pure shear waves travel the slowest and appear last in an A-Scan. The longitudinal-shear and shear-longitudinal mode converted waves having both wave components will travel at the same speed, convolute with each other, and are expected to appear at a time exactly between when the pure longitudinal and pure shear peaks are. This peak is referred to as the hybrid peak as it is a hybridization of longitudinal and shear components. The use of the hybrid peak to measure shear velocity is easier than measuring the pure shear peak itself as the hybrid peak always has higher intensity (equation 43). The relative difference in speed of sound gives order to the time positions where each wave peak can be expected. This can be seen through the use of an A-Scan in Figure 44.

$$C_S = \frac{2d}{2TOF_H - TOF_L}$$

Eq.43

where the ‘H’ subscript refers to the hybrid peak.

As the ultrasonic transducers used for this type of testing are manufactured to produce only longitudinal waves and the angularity of the longitudinal waves at an interface are very small, just a small portion of the received acoustic energy will have shear components. This makes measuring the shear speed of sound while using a longitudinal ultrasonic transducer more difficult than measuring longitudinal speed of sound. The error caused by amplitude reduction explained above is the source of this difficulty. Increasing signal gain and using complex algorithms to always measure the inflection of where the shear reflection occurs are methods of abating the inherent difficulty in measuring the shear TOF [20].

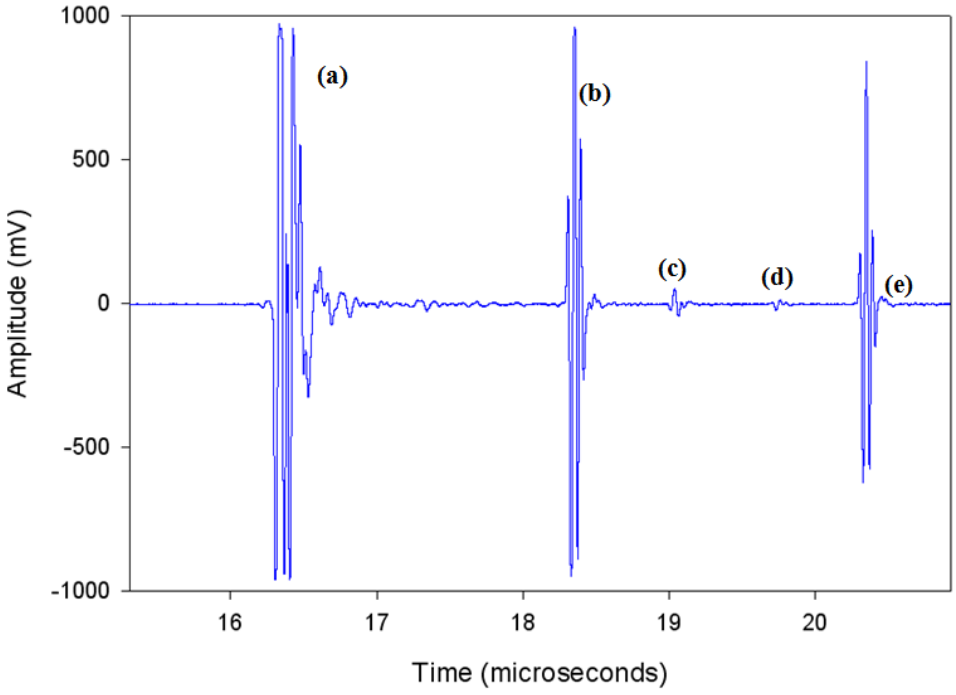

Figure 44. A-Scan showing relative time occurrence of each type of wave according to sample surface reflections. (a) Longitudinal top surface, (b) longitudinal-longitudinal bottom surface, (c) longitudinal-shear convoluted with shear-longitudinal (hybrid) bottom surface, (d) shear-shear bottom surface, and (e) second longitudinal-longitudinal bottom surface.

2.4.3.1.3. Measuring Elastic Properties

The calculation of elastic properties is fundamentally based on the longitudinal and shear velocities of an elastic solid [95]. All elastic property calculations using the equations below were derived based on anisotropic solids. The calculation of the elastic properties of a solid account for any anisotropic behavior through the use of the Poisson ratio. The Poisson ratio, ν, is a unitless parameter which is the negative of the ratio of lateral and axial strains provided by an axial stress. This factor is of great importance when calculating ultrasonic velocities or elastic moduli as many materials exhibit anisotropic behavior [37]. The Poisson ratio of a material can be calculated through the use of equation 44 after measuring both the longitudinal and shear velocities [95].

$$\nu = \frac{1-2(\frac{C_S}{C_L})^2}{2-2(\frac{C_S}{C_L})^2} \qquad \text{Eq. 44}$$

Once the Poisson ratio is calculated the Young's, shear, and bulk moduli can be calculated from combinations of the Poisson ratio, sonic velocities, and density [95]. Young's modulus, E, is the ratio of applied stress to the resulting strain of a material and can be calculated through the equation [36, 95]:

$$E = \frac{C_L^2 \cdot \rho \cdot (1-2\nu) \cdot (1+\nu)}{(1-\nu)} \qquad \text{Eq. 45}$$

The shear modulus, G, is the ratio of applied shear stress to the resulting shear strain and is calculated by using the equation [36, 95]:

$$G = \frac{E}{2 \cdot (1+\nu)} \qquad \text{Eq. 46}$$

A materials resistance to compression can be quantified by its bulk modulus, K, and is calculated using the equation [36, 95]:

$$K = \frac{E}{3 \cdot (1-2\nu)} \quad \text{Eq. 47}$$

Each elastic modulus has units of Pascals (Pa), but is more conveniently given in GPa through a division by $1*10^9$ as many high density, high hardness, elastic solid materials exhibit high elastic properties [1].

2.4.3.1.4. Thickness Measurement

All of the information that is capable of being produced by acoustic testing requires a thickness input of the sample being measured. A common way of obtaining thickness values is using an average of several manually recorded thickness measurements. Another method is to assume the material velocity of a sample is constant about all points in the sample and solve for thickness once a TOF C-Scan is completed. Samples with large defects or density variations will result in a variation in the speed of sound about the sample. Error in ultrasonic property measurements can be introduced due to variation in sample thickness over its entire area. For example, a difference in thickness of only 100μm for an alumina sample amounts to a miscalculation of approximately 7GPa for Young's modulus [111]. Methods for the improvement in the reduction of measurement error due to thickness variation are further explained.

Correction for thickness variation essentially measures time of flights around the sample. This method assumes that the speed of sound in water is constant at room temperature and that pure (distilled and deionized) water is used as the propagation medium. A reflector waveplate that provides a high acoustic impedance mismatch with water is used to ensure that an intense reflection from the immersion tank can be seen

[192]. The measured TOF's are those of which are between the face of the transducer and the top surface of the sample (t2), the bottom surface of the sample and the tank containing the sample (t3), and the face of the transducer and the tank (t1). The TOF of the sample (t4), if it were made of water, results from subtracting the total of t2 and t3 from t1. Using the relation of thickness equals velocity multiplied by time and the speed of sound in water; one can obtain an accurate thickness value which avoids the complications of microstructural inhomogeneity [188]. Figure 45 shows a schematic illustration of the TOF's that are explained.

An entire sample area can be mapped for thickness by using this method and rastering about the sample. Comparison of ultrasonic thickness mapping with a thickness map created by manually measuring 100 points with electronic calipers can be seen in Figure 46 [111]. Ultrasonic thickness mapping provides a much finer lateral resolution than manual caliper measurements can ever reach. The agreement between the two methods shows the veracity of using ultrasound and TOF based measurements as a useful technique for obtaining thickness over all points of a sample.

Figure 47 shows a Young's modulus C-scan of alumina revealing the error introduced by not correcting for thickness error over all points in a sample. The contours of TOF-based C-Scan property maps are affected by thickness inaccuracies more so than that of the actual difference in values. The percent difference map for Young's modulus of an alumina sample show large contour variations compared to the variation of the value itself [111]. The ultrasonic measurements made for the alumina samples studied in this thesis have been corrected for thickness variation error.

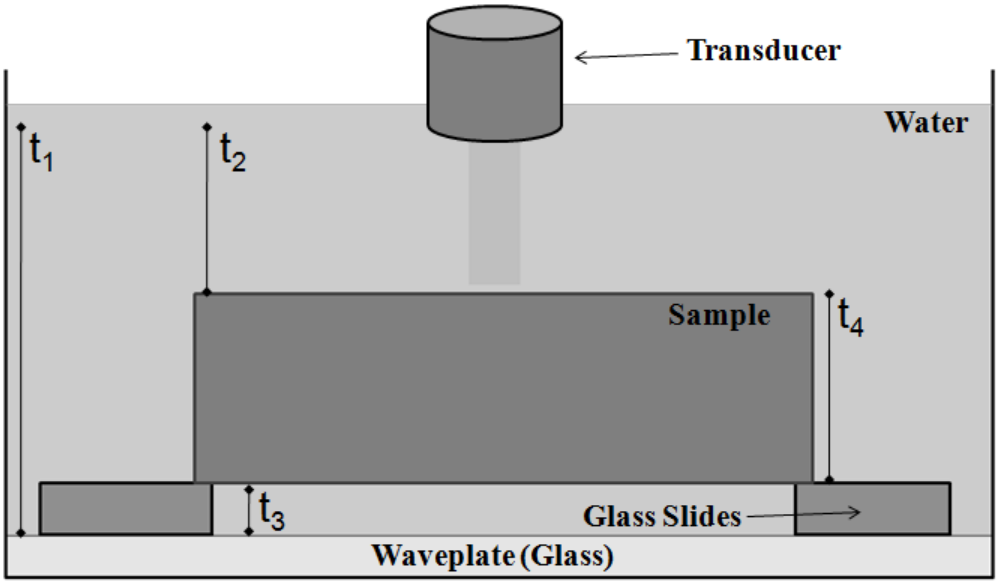

Figure 45. Schematic representation of TOF's used in creating C-Scan thickness maps [111].

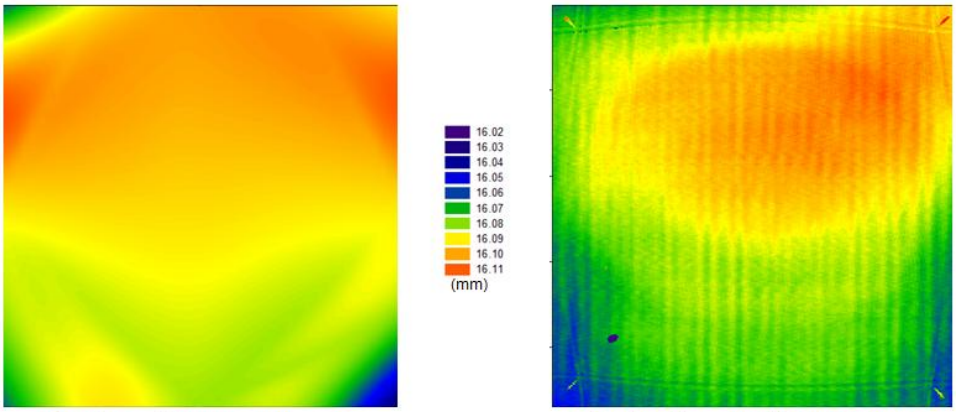

Figure 46. Alumina thickness comparison of caliper versus ultrasound measurements [111].

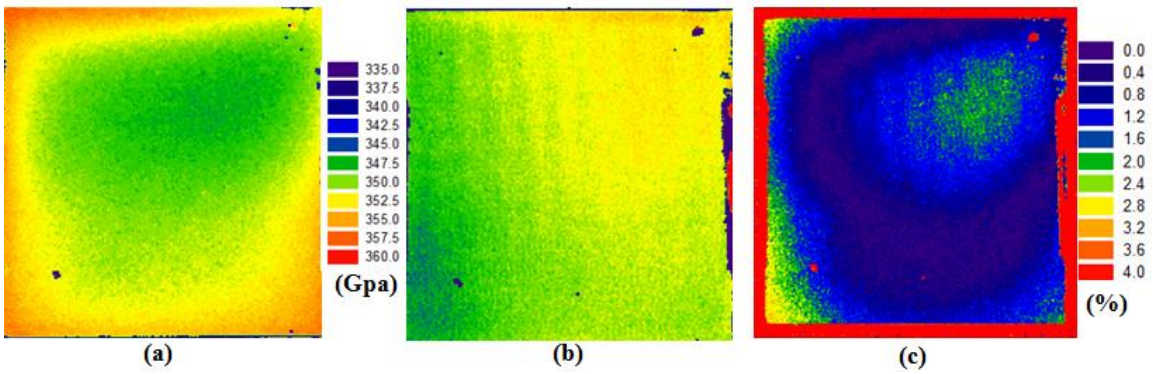

Figure 47. Young's modulus C-Scan maps of alumina: (a) Not corrected for thickness error, (b) Corrected for thickness error, (c) Percent difference between (a) and (b) [111].

2.4.3.2. Amplitude Based Measurements

The second of the two possible measurements when performing ultrasound NDE is that of peak amplitude measurement. This is done through the use of electronic gates which measure the amplitude of oscilloscope peaks specific to a sample surface and acoustic wave type; longitudinal or shear. The higher energy of longitudinal waves compared to shear waves when performing pulse-echo, immersion-based, ultrasonic testing makes it such that longitudinal wave sample reflections are typically measured for their amplitudes. Bottom surface amplitude C-Scan maps are common measurements performed to determine the spatial homogeneity of a sample. If the acoustic wave encounters a discontinuity, such as porosity, solid inclusions, or large grains, its energy is reduced through scattering and absorption. C-Scan amplitude maps reflect this by shows a decrease in peak amplitude about these regions. This section describes the procedures in which amplitude is measured and the process behind converting it to ultrasonic attenuation coefficient.

2.4.3.2.1. Amplitude Measurement Modes

As with measuring TOF there are several measurement modes which can be performed for obtaining the amplitude values of peaks. A simplification of the definition of peak amplitude is the peaks height. However, different testing facilities may report different amplitudes due to differences in measurement techniques. Figure 48 shows a general sample surface peak which is taken from an oscilloscope A-Scan. Four modes for measuring peak amplitude can be delineated through different types of wave rectifications. The first is where the wave is not rectified and its full peak height is recorded. The second measurement mode of amplitude is done by using bipolar

rectification, where the absolute value of the signal is measured. And the third and fourth measurement modes are known as unipolar positive and unipolar negative rectifications. These last types of wave rectifications make it such that only the positive or negative portions of the reflected peaks are measured [193]. The four types of wave rectifications can be seen in Figure 49.

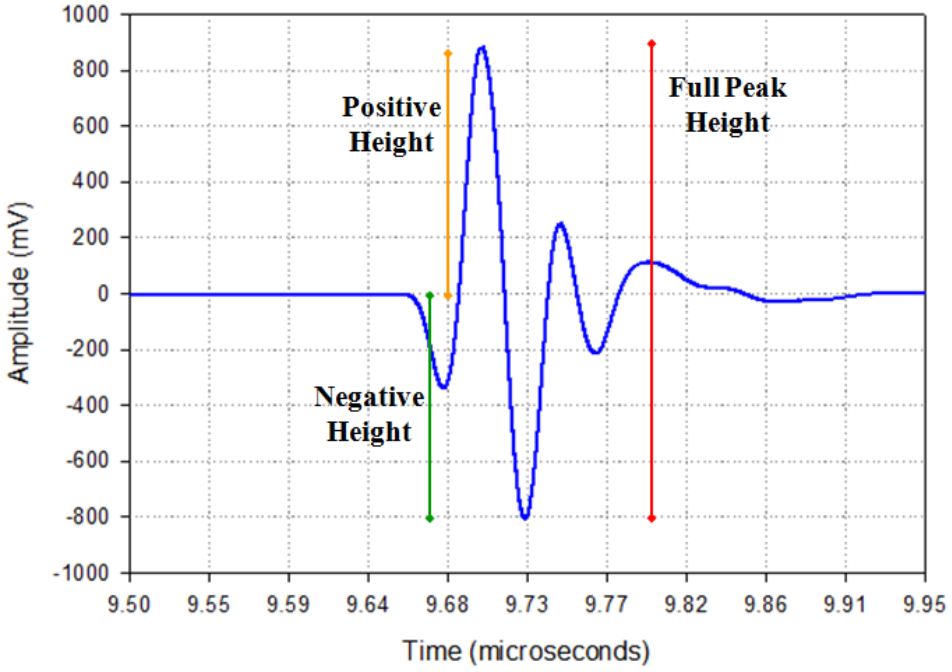

Figure 48. Oscilloscope view of a sample peak. Shows three portions of a non rectified reflected peak.

Amplitude analysis of the full peak height provides more information of what was contained in the microstructure making it the test of choice for using ultrasonic testing as a characterization technique. The other types of wave rectification modes; bipolar, unipolar positive, and unipolar negative, have primarily been used for the rapid identification of large, anomalous, defects or variations over an entire sample area [193]. A large feature present in the microstructure will cause a massive change in peak intensity and would be seen in a C-Scan map of amplitude. The amplitude-based

measurements performed in this thesis make use of measuring the full peak height of a non rectified wave. All future discussion regarding amplitude-based measurements assumes that full peak heights of non rectified waves are measured.

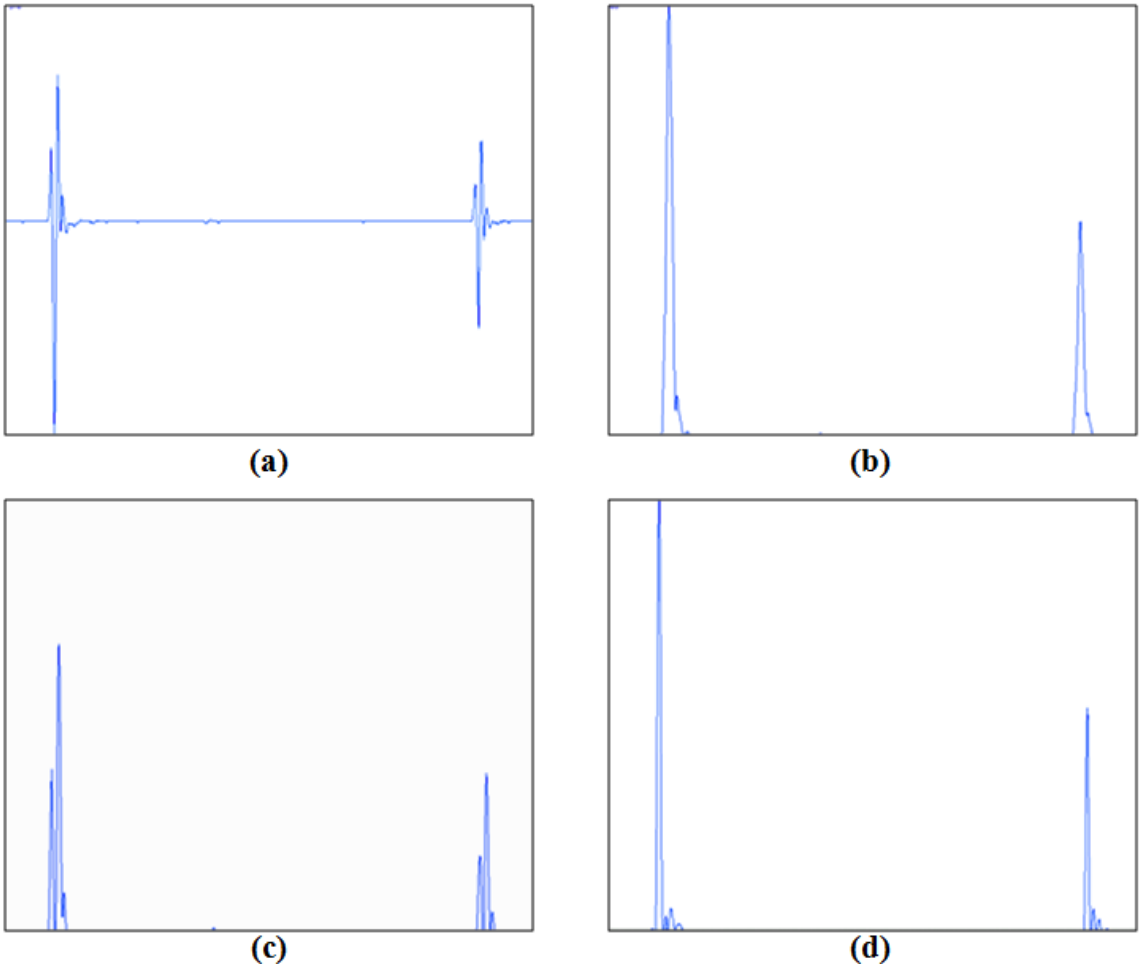

Figure 49. Oscilloscope view of a sample peaks. (a) Non rectified waveform; (b) Bipolar rectification; (c) Unipolar positive rectification; (d) Unipolar negative rectification.

Sources of error when performing amplitude based measurements arise from signal noise and electronic reflections as described above. The underlying signal noise created by all components in an ultrasound NDE system interacts with the sample reflections constructively and destructively. This has the effect of increasing or decreasing the amplitude of the sample peaks from their true amplitude. Again, methods

to alleviate signal noise are to use bandwidth filters commonly found in modern pulser-receivers. The analog to digital converter card which controls all aspects of the oscilloscope resolution also adds to amplitude measurement error. The amplitude scale, usually measured in volts, consists of discrete values separated by the resolution limit dictated by the AD card. The maximum error in amplitude imparted by the AD card is twice its amplitude resolution if the AD card noise combines constructively [194]. AD cards with increased amplitude resolution help with this source of amplitude error as the discrete spacing in amplitude values which the signal can take decreases.

2.4.3.2.2. Measuring Attenuation Coefficient

Although the amplitude of each reflection is proportional to the energy contained within each peak, directly obtaining the energy reflected at each surface is not possible due to signal amplification and gain corrections present in almost all components of an ultrasound NDE system [20, 195]. As a result it is convenient to measure the ratio of the amplitudes of successive same sample surface reflections. This alleviates the effect of surface roughness and sample bevel to an extent and provides the basis of obtaining a quantitative material parameter: the acoustic attenuation coefficient.

The attenuation coefficient is a quantification of the amount of sound energy lost between two points [19]. Ignoring the specific contributions from each attenuation mechanism, the total amount of energy loss per distance can be defined in general through the Beer-Lambert Law [135]:

$$I = I_o e^{-\alpha x} \qquad \text{Eq. 48}$$

where I is the intensity of the wave after passing through a medium, I_o is the initial intensity, α is the attenuation coefficient, and x is the distance travelled. Equation 48 can

be inverted to solve for the attenuation coefficient having units of Nepers per meter, Np/m. A Neper is a unit of loss based on natural logarithm. The decibel, dB, is a more commonly used logarithmic-based loss unit and is equal to 0.115Np. Converting to decibels and using the fact that intensity is proportional to the square of amplitude (equation 9) the Beer-Lambert Law can be rewritten as:

$$\alpha = -\frac{8.686}{2x} ln(\frac{A^2}{A_o^2}) \quad \text{Eq. 49}$$

where A is the amplitude of the acoustic wave after propagating through a medium, A_o, is the initial wave amplitude, and the factor of 8.686 converts from Nepers to decibels. The conversion from intensity to amplitude, shown in equation 9, holds practical value as amplitude-based measurements are commonly made with ultrasonic testing [110].

The value for attenuation calculated through equation 49 gives what is known as the overall signal attenuation coefficient [20]. 'Overall signal' refers to the meaning that the attenuation coefficient is not specific for any singular frequency; it represents the weighted average according to the intensity of each frequency put out by the transducer [196]. Without deconvoluting the sample reflections through the use of a Fourier transform the attenuation coefficient describes the overall loss of acoustic energy of all frequencies present. An example of an overall attenuation coefficient C-Scan can be seen in Figure 50. Overall attenuation coefficient C-Scan maps give a more reliable method of determining any variation or degree of inhomogeneity over large sample areas compared to amplitude C-Scan maps as they are not strongly affected by sample nonuniformities.

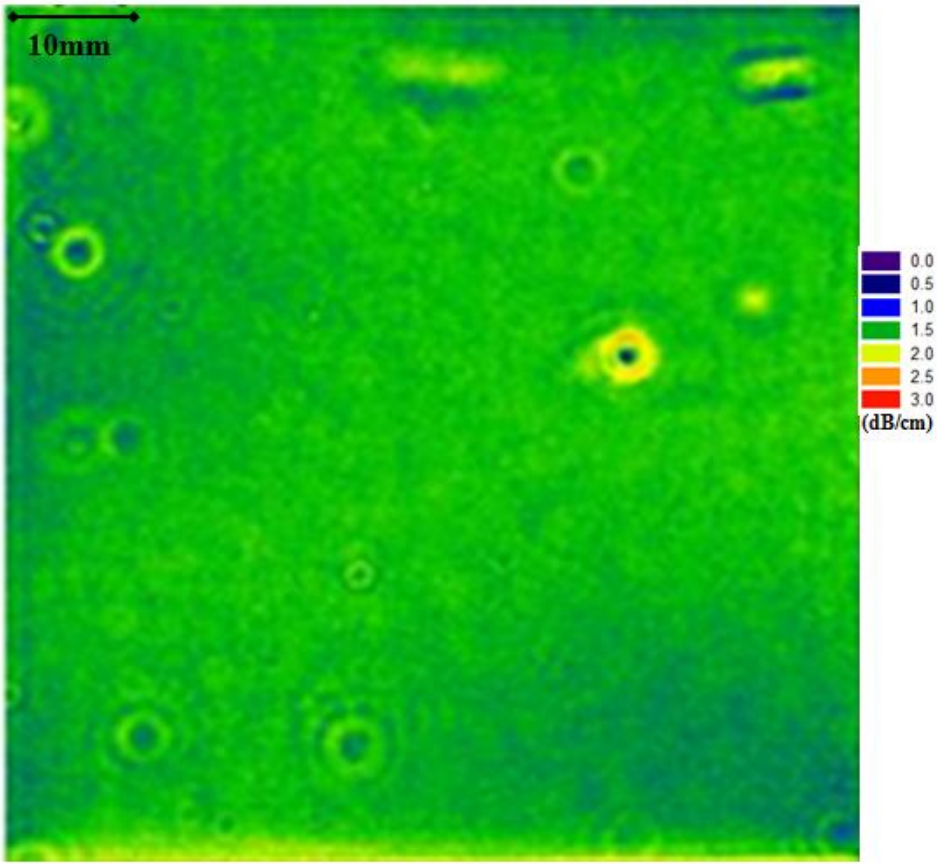

Figure 50. Overall attenuation coefficient C-Scan map of an alumina tile. Reveals spatial location of large defects [114].

2.4.3.2.3. Measuring Attenuation Coefficient Spectrum-Fourier Transforms

The jump from qualitative attenuation coefficient measurements, described above, to obtaining quantitative ultrasonic attenuation coefficient data is done through the use of deconvoluting sample reflections to measure peak intensity as a function of frequency. This gives a frequency-based attenuation coefficient measurement which allows for the microstructural characterization of dense, polycrystalline ceramics using ultrasound [19, 20]. Deconvoluting sample reflections is done by performing a Fourier-based transform about the temporal width of each sample peak [197]. The several types of Fourier transforms which can be used to achieve this function are the Fourier transform, discrete time Fourier transform (DTFT), or the short time Fourier transform (STFT). The DTFT

and STFT are normally computed using the fast Fourier transform (FFT) to expedite the computation time [198].

Fourier transforms map information from time space to frequency space by using the basic Fourier transform function [198]:

$$F(s) = \int_{-\infty}^{\infty} f(x) e^{-2\pi i k x} \qquad \text{Eq. 50}$$

where F(s) represents the computed frequency domain of the signal, f(x) represents the signals time domain, 's' corresponds to inverse time (frequency), 'x' corresponds to time, and 'k' is angular frequency. The DTFT and STFT, described below, are variations of the Fourier transform used for specific applications.

The FFT, discovered by Gauss in 1805 and revolutionized for modern use by Cooley and Tukey in 1965, allows for faster computation times for Fourier series of any type of Fourier-based transform (DTFT, STFT, etc.) [199]. The general form for the fast Fourier transform is given as [198]:

$$F_k = \sum_{n=0}^{N-1} f_n e^{-\frac{2\pi i n k}{N}} \qquad \text{k = 0, …, N-1} \qquad \text{Eq. 51}$$

where F_k represents the computed frequency domain of the signal, f_n represents the time domain, N is the number of uniformly sampled data points, and 'k' is the angular frequency. The fast Fourier transform takes O(Nlog(N)) time to compute for N data points, where the function O is dependent on the computation processes dictated by the computer used. Compared to the DTFT, the FFT is much faster; a DTFT takes $O(N^2)$ time to compute [198]. However, the increase in speed which an FFT comes with causes its frequency resolution to decrease [198, 200]. The frequency resolution of an FFT is proportional to the temporal width of the window in which the FFT is being performed.

An FFT performed on a 1μs time window gives a 1MHz resolution in frequency, where decreasing the size of the time window by a factor of two will cause a decrease in frequency resolution making it 2MHz.

A discrete time Fourier transform requires an input function of discrete data, which is exactly the type of data obtained through acoustic testing; the sampling of continuous ultrasonic waves [200]. DTFT methods show how the intensity of a frequency dependent signal changes over time [200]. It provides frequency-based information over long signal times by operating on a smaller time window about the entire time domain. This window moves across the time domain in predefined, finite time steps. A resulting graph of the received information plots time versus frequency versus signal intensity [201].

A short time Fourier transform is the type of Fourier transform used for the signal processing performed in this thesis. The STFT is similar to the DTFT but is performed on smaller time windows where the signal is divided into uniformly sized segments equal to or less than the size of the sampling window [202]. Mathematically, the STFT is written as [200]:

$$STFT\{x(t)\} \equiv X(\tau,\omega) = \int_{-\infty}^{\infty} x(t)w(t-\tau)e^{-j\omega t}\,dt \qquad \text{Eq. 52}$$

where x(t) represents the signal in the time domain, w(t) is a window function, τ represents the phase of the signal over time and frequency, and $X(\tau,\omega)$ is a DTFT of a windowed data centered about τ [200]. There are multiple types of window functions, w(t), which can be used for this type of analysis but the window function used for the STFT performed in this thesis is a Blackman-Harris window. The equation for computing the coefficients of a four-term Blackman-Harris window is given as [203]:

$$w(t) = a_0 - a_1 \cos\left(\frac{2\pi}{N} n\right) + a_2 \cos\left(\frac{2\pi}{N} 2n\right) - a_3 \cos\left(\frac{2\pi}{N} 3n\right) \quad \text{Eq. 53}$$

where N is equal to the window length, L-1, 'a' are constants for specific window sizes, and $0 \leq n \leq N$. The STFT does not inflict limitations on frequency resolution based upon the size of the time window. The STFT also allows for one to transform singular peaks of interest from an A-Scan which makes it more efficient than transforming the entire time domain [200]. Figure 51 shows an example of the results of an STFT performed on a signal in the time domain.

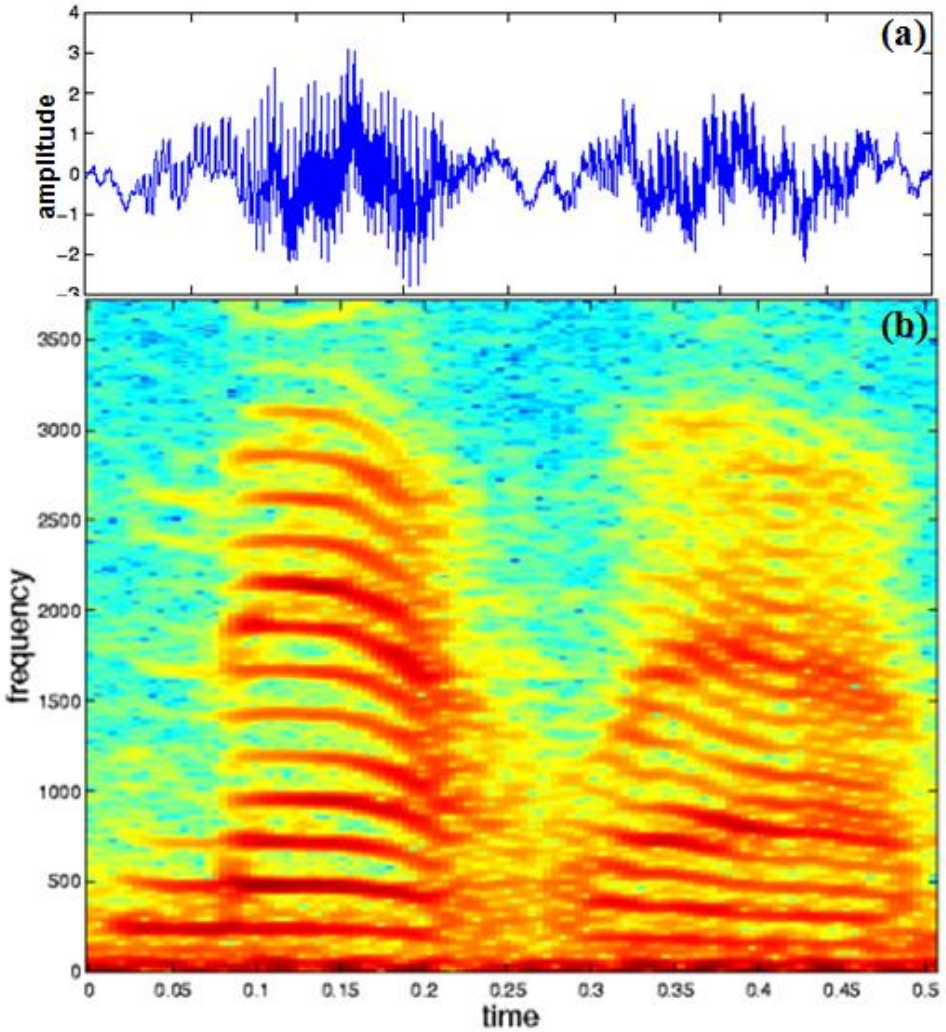

Figure 51. (a) Signal in time domain; (b) STFT of signal to give time vs. frequency vs. signal intensity [204].

2.4.3.2.4. Measuring Attenuation Coefficient Spectrum-Power Spectral Density

The STFT returns a three-dimensional array of data: time, frequency, and intensity. The measurement of frequency-based attenuation coefficient is only concerned with the frequency and signal intensity of this data array. The power spectral density (PSD) is a plot of frequency versus the signal intensity contained within the peak reflection. More simply put the PSD is often called the spectrum of the signal [205]. Aside from obtaining the intensity of the signal at each frequency after the wave has passed through a material, the PSD is also used to determine the frequency output of an ultrasonic transducer. This is done by measuring the PSD of the reflection off of the top surface of a highly polished material (usually silicon carbide or steel) or by measuring the PSD of a transducer delay [193]. Transducer delay lines are discussed in a future section. An example of a transformed sample reflection to obtain its PSD can be seen in Figure 52.

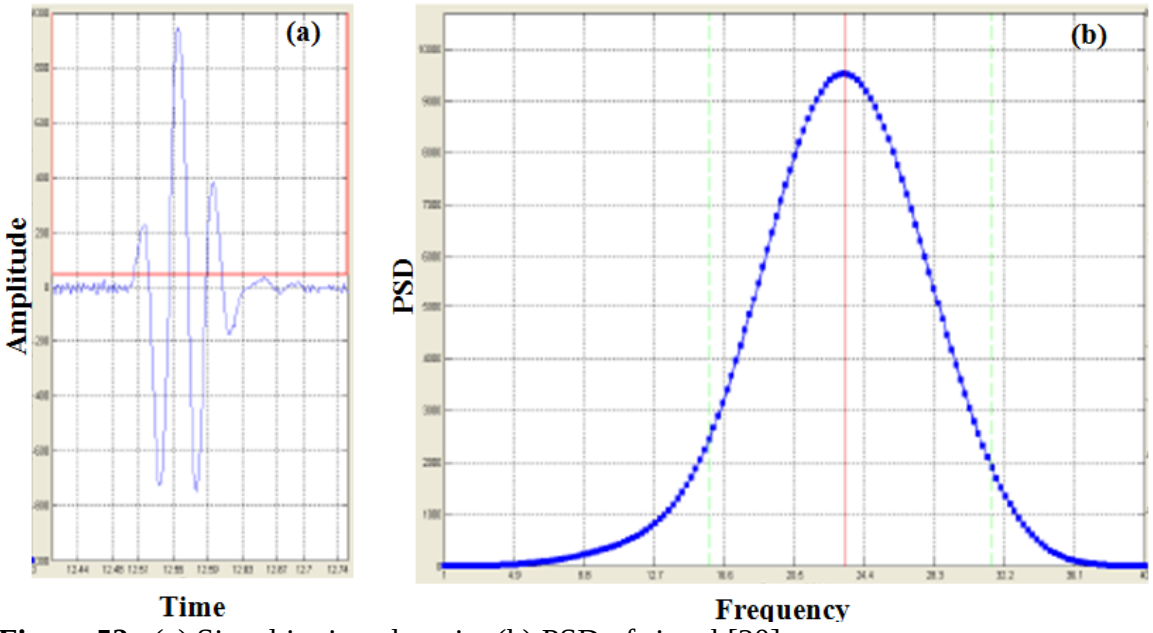

Figure 52. (a) Signal in time domain; (b) PSD of signal [20].

The power spectral density can have units of power per Hz which equates to Joules, or the energy output of the transducer at each frequency. It is customary practice to use units of $V^2 \cdot Hz^{-1}$ for voltage signals; however, this thesis makes use of the PSD being capable of having units of Joules. To obtain the actual energy output of a transducer, in Joules, one must normalize the area of the PSD to the total energy supplied to the transducer from a pulser-receiver [193, 206]. This is due to amplification and gain factors present in the individual components of an ultrasonic NDE system. The energy output at the strongest frequency is expected to be on the order of μJ or less [193, 206].

2.4.3.2.5. Measuring Attenuation Coefficient Spectrum-Corrective Techniques

The attenuation coefficient is not only affected by microstructural features, but also by inherent geometric loss factors. These geometric loss factors are caused by reflection and diffraction [19, 207]. Corrections for these losses ensure that a measured attenuation coefficient is a parameter influenced by solely the material microstructure. Reflective losses are constant with frequency as reflection is dependent on sonic velocity which does not exhibit dispersion in dense, polycrystalline, ceramics. Diffractive losses show a strong dependency on frequency as well as the size of the transducer aperture [208].

As explained above, reflection and transmission occur at any surface where there exists a mismatch in acoustic impedance. When measuring the attenuation coefficient the first two successive bottom surface reflections are used (see Figure 44). These reflections can be labeled as A_o and A to represent the first and second reflections, respectively. The reflection which is representative of the top surface of the sample indicates how much energy never penetrated the sample. Upon each interaction with an interface there are

different percentages of energy which are reflected and transmitted. Therefore, considerations must be made to account for the percentage of energy (of the original output) of which the measured peaks actually represent. An iterative algebraic process, outlined in Figure 53, detailing the acoustic energy according to the reflection and transmission coefficients at each interface, yields a more accurate form for the measured attenuation coefficient [110].

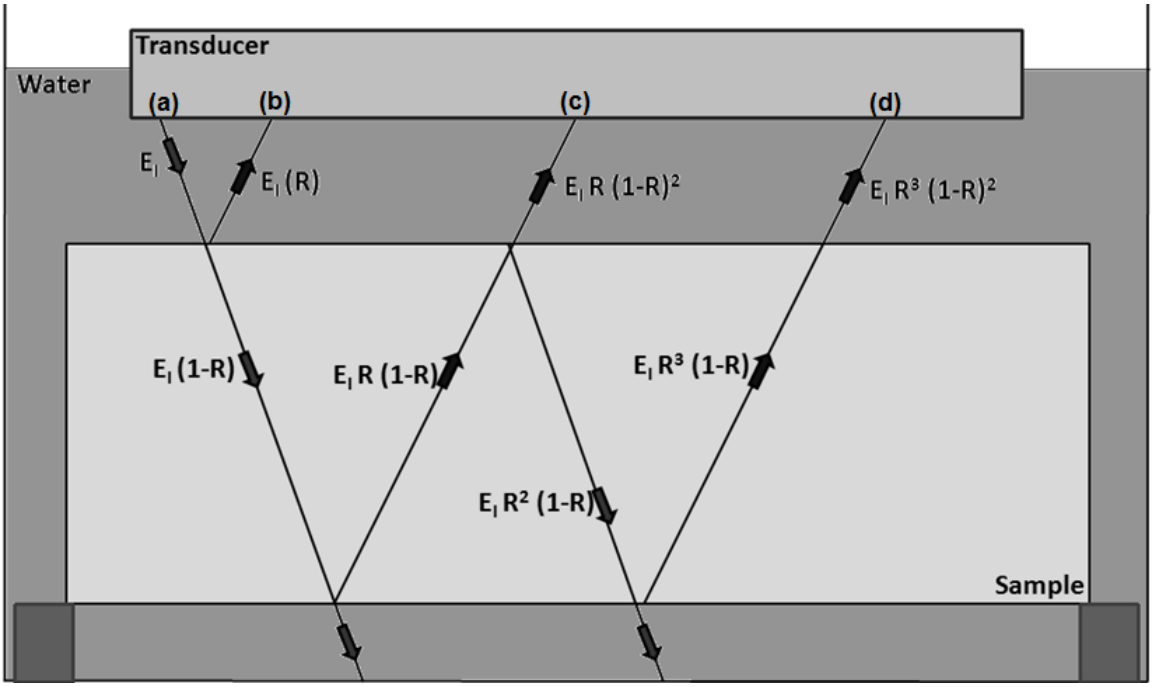

Figure 53. Schematic diagram of acoustic reflection and transmission. E_I is initial energy output from transducer (a). Oscilloscope temporal positions corresponding to (b) top surface reflection, (c) first bottom surface reflection, (d) second bottom surface reflection [111].

Figure 53 demonstrates the processes of ultrasonic reflection and transmission through a dense elastic solid. If one were to consider an ideal material which is acoustically transparent and no diffractive losses occurred, attenuation would still occur due to the reflection phenomena. This attenuation can be described as a quadratic combination of the reflection and transmission coefficients multiplied by the initial

amount of energy emitted by the transducer. After the first reflection about the top surface of the sample, the subsequent bottom surface reflections decrease by a factor of R^2 upon each pass. Correction of the attenuation caused by reflection amounts to a linear decrease in attenuation coefficient for both C-Scan and frequency-dependent attenuation coefficient spectra by a factor of [111]:

$$\alpha_{reflection} = -\frac{8.686}{2x}(ln(R)^2) \quad \text{Eq. 54}$$

Combining the attenuation due to reflection with the inverted Beer-Lambert law produces a more exact form for the measured material attenuation coefficient.

$$\alpha_{measured} = -\frac{8.686}{2x}(ln\left(\frac{A}{A_o}\right)^2 - ln(R)^2) \quad \text{Eq. 55}$$

Diffraction is the phenomenon in which sound waves spread out or bend at an interface of discontinuity [208]. The causes of diffraction inherent with a non-contact, pulse-echo ultrasonic NDE system are due to transducer aperture size, the path length of beam travel, and frequencies used [195]. The error due to diffraction is related to the ratio of the frequencies used and transducer aperture. Error is increased with smaller apertures and lower frequencies [208]. After the acoustic beam exits the transducer there is a natural Gaussian focusing effect as the beam transitions from the near field to the far field (explanation in future section) [209]. This becomes amplified by any refraction that occurs at a water-sample interface. By the time the ultrasonic pulse is returned back to the transducer, a considerable amount of energy has been directed away from the transducer aperture. This loss in energy is not due to the material and should not be convoluted with an attenuation coefficient measurement.

The mathematics used in the correction for diffractive losses invoke the use of spherical Bessel functions and other non-linear transforms. Specifics on the actual algorithms used for diffraction correction are highlighted in the referenced literature [195, 208]. Custom made software from Rutgers University Center for Ceramic Research (CCR) performs the rigorous operations necessary to calculate diffraction losses based on sample thickness, water path, frequency, and transducer aperture radius [20]. When performed as a function of frequency, the overall effect is a subtraction of diffraction losses from the measured attenuation coefficient; an example can be seen in Figure 54. Figure 54 demonstrates the frequency dependence of diffraction: as frequency increases diffractive losses begin to become negligible.

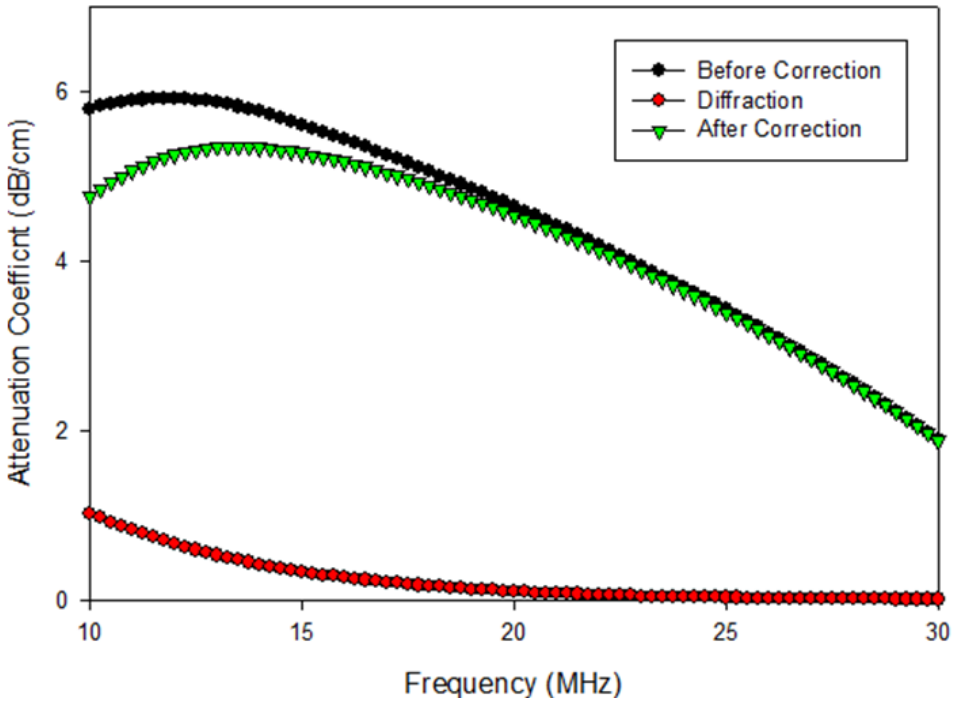

Figure 54. Example of frequency based diffraction correction on measured attenuation coefficient spectrum. 20MHz central frequency transducer, 3.55mm radius aperture, sample thickness of 10mm.

To account for the attenuation due to beam spreading one must use a spherical coordinate system and a solution of Bessel's differential equation, the spherical Bessel function of the first kind [207]. It can be represented as an integral of trigonometric functions, but more concise notation will be used here. The m^{th} order Bessel function of the first kind will be shown as $J_m(x)$ in its generalized form. Transforms must be used for each sample surface reflection that is of interest. The surface peaks that are typically used are the first and bottom surface reflections, noted as D_1 and D_2, respectively. Equation 56 is the form used to calculate the intensity of the diffracted portion of the ultrasonic beam, or percentage of energy lost due to diffraction at each surface [207].

$$D_n = 1 - e^{-(\frac{2\pi i}{s})}[J_0\left(\frac{2\pi}{s}\right) + J_1(\frac{2\pi}{s})] \qquad \text{Eq. 56}$$

Where J_0 and J_1 are representative of the first kind of Bessel's functions that account for the zeroth and first order perturbations. The subscript 'n' on D is indicative of which surface reflection the transform is manipulating and s is defined as equation 57.

$$s = \frac{2 \cdot t_w \cdot c_w + 2 \cdot n \cdot t_m \cdot c_m}{f \cdot a^2} \qquad \text{Eq. 57}$$

The path lengths of the sample and the water between the transducer aperture and sample top surface are labeled as t_m and t_w, respectively. The sonic velocities in the sample and water are shown as c_w and c_m, respectively. Frequency is denoted as f, transducer aperture is a, and n is either 1 or 2 correlating to the 1^{st} or 2^{nd} bottom surface reflections. Equation 58 shows the diffraction corrected, modified version of equation 55. This final equation accounts for geometric losses caused by both reflection and diffraction.

$$\alpha_{measured} = -\frac{8.686}{2x}\left(ln\left(\frac{A}{A_o}\right)^2 - ln(R)^2 - ln(\frac{D_2}{D_1})\right) \quad \text{Eq. 58}$$

An overall attenuation coefficient C-Scan map, which is incapable of showing frequency dependence, can be corrected for the effect of diffraction over all frequencies. As an attenuation coefficient C-Scan map represents acoustic energy loss as the weighted average over all frequencies output by a transducer, a weighted average accounting for the effects of diffraction can be calculated. This is done by using the frequency profile of the transducer output and weighting the frequency dependence of diffraction to the corresponding strength at each frequency. The overall diffraction correction is then a summation of the weighted frequency diffraction corrections over all frequencies [111].

Overall diffraction losses are also dependent on sample thickness. Any thickness dependency on the correction for overall diffraction when used when creating an overall attenuation coefficient C-Scan image is corrected for automatically through the use of custom made software at Rutgers CCR. Figure 55 shows an example of thickness dependency on overall diffraction corrections in aluminum oxide. The regression lines shows what is to be expected: attenuation coefficient is a material property and should not vary with sample thickness. Figure 56 shows comparative overall attenuation coefficient C-Scan maps of an alumina sample before and after correcting for overall diffraction losses. The effect is essentially a linear decrease in attenuation by approximately 1.70dB/cm across the entire sample. Any attenuation coefficient data shown in this thesis have been corrected for of the effects of reflection and diffraction.

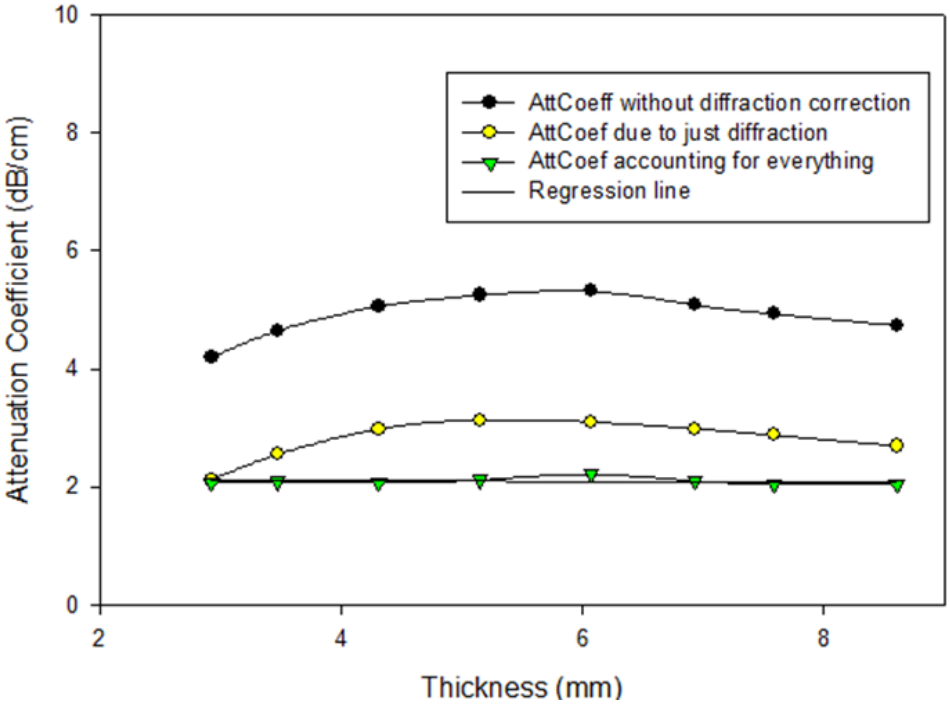

Figure 55. Thickness dependency on overall diffraction correction [111].

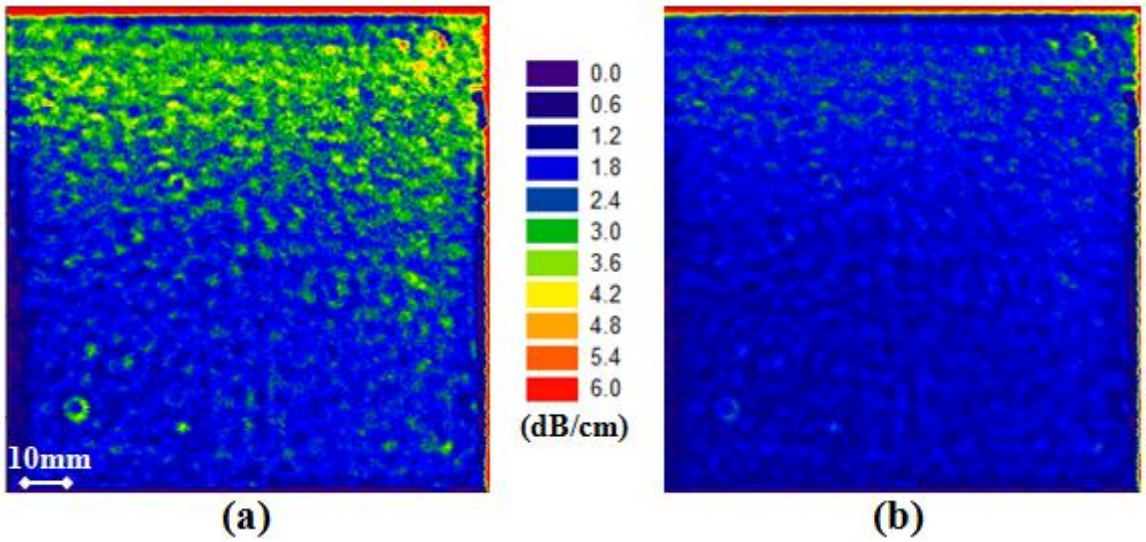

Figure 56. (a) Overall attenuation coefficient C-Scan image of an Al_2O_3 sample without diffraction correction; (b) overall attenuation coefficient C-Scan image of Al_2O_3 sample in (a) after diffraction correction. Alumina sample is 5mm thick [111].

2.4.3.2.6. Measuring Attenuation Coefficient Spectrum-Standard Method

The final measurement of an attenuation coefficient spectrum can be made after careful corrections from all non-material loss mechanisms are done. Figure 57 shows a flow diagram of the standard method used for collecting ultrasonic attenuation coefficient spectra [168]. Using a piezoelectric ultrasonic transducer (a), one obtains an A-Scan of sample surface reflections (b). The power spectral density of the two successive bottom surface reflections is determined through the use of a short time Fourier transform (c). As the power spectral densities represent the square of amplitude, the powers of 2 on amplitudes, seen in equation 58, are not necessary [210]. The final equation used for obtaining attenuation coefficient spectra is shown as equation 59. This equation is a modification of equation 58 to account for the use of the PSD's of each bottom surface reflection.

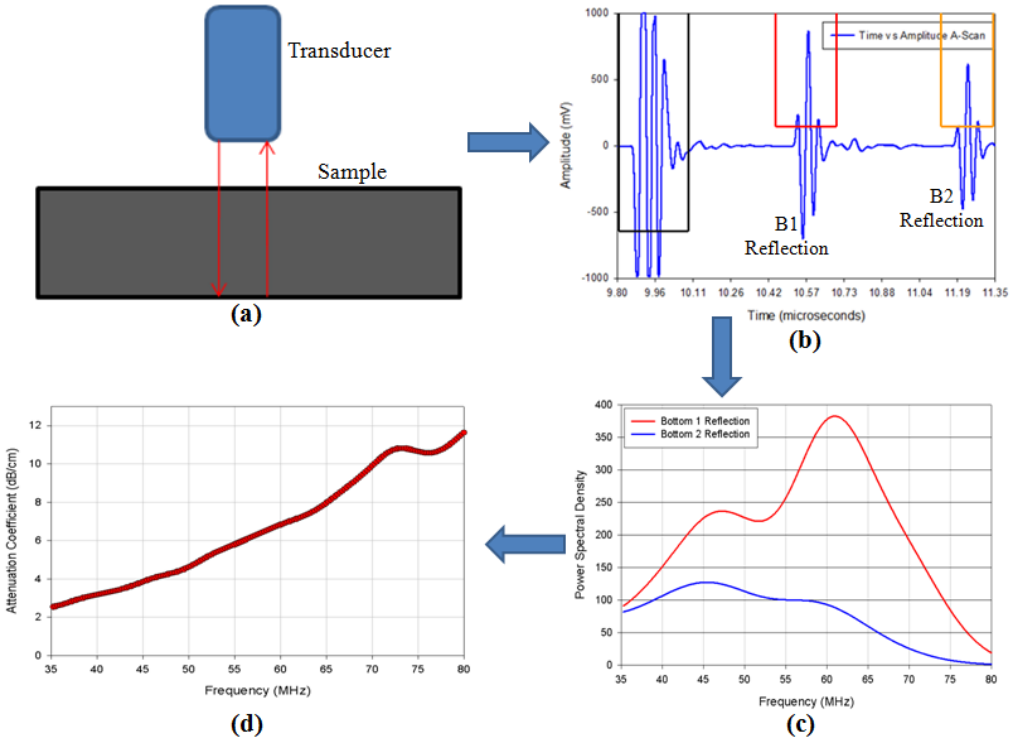

Figure 57. Schematic diagram of procedure used to obtain ultrasonic attenuation coefficient spectrum [183].

$$\alpha(f) = -\frac{8.686}{2x}\left(ln\left(\frac{PSD_2(f)}{PSD_1(f)} - ln(R)^2 - ln\left(\frac{D_2(f)}{D_1(f)}\right)\right)\right) \quad \text{Eq. 59}$$

Interpreting an attenuation coefficient spectrum depend upon knowing the output frequency profile of the transducer used to make the measurement. Figure 52 shows a frequency output profile of a 20MHz central frequency transducer. As the signal deviates from the central frequency, the statistical reliability regarding the accuracy of the signal at those frequencies decreases. The tail ends of the PSD shown in figure 52 have lower signal intensity at these frequencies where signal noise could potentially account for a greater percentage of the measured data [20]. Setting a bandwidth from where the signal can be considered to be reliable is common practice when dealing with acoustics [90]. Typically, a -6dB bandwidth is set such that only the center 50% of the frequency output profile is used. A -6dB line represents the portions of a PSD which is equal to 25% of the maximum PSD intensity. The -6dB points are shown in Figure 52 as green lines. Attenuation coefficient data outside of these bounds are considered to be unreliable and disregarded [90]. An interpretation of the attenuation coefficient within the -6dB points require an understanding of the different acoustic loss mechanisms as well as some knowledge regarding the microstructure of the interrogated material [19].

2.4.4. Sample Requirements

Specifics regarding sample requirements for ultrasonic testing are highlighted in this section. When performing automated C-Scan measurements electronic gates are set prior to the start of the transducer raster motion and data acquisition. These electronic gates are set about specific sample surface reflections and are unable to move during a scan. If there exist certain sample nonuniformities the sample surface reflections will move outside of the measurement gates and incoherent data will be recorded. The

sample nonuniformities which must be checked for prior to performing ultrasonic C-Scan analysis are sample thickness, beveled sample surfaces, uneven sample surfaces, surface roughness, or too much porosity [142]. Different ultrasonic NDE test setups have different tolerance limits for each of these sample nonuniformities where setups with greater resolution will be affected to a greater degree [142].

Ultrasonic C-Scan maps of sample surface amplitude are common measurements which go into attenuation coefficient and used to determine full sample area homogeneity [14]. If the acoustic wave encounters a sample surface at any angle which is not perpendicular to its direction of travel a portion of the wave is reflected away from the transducer. This causes a decrease in peak amplitude which is not caused by any feature present in the bulk material microstructure. A resulting C-Scan map can be mislead one into believing that these regions of low amplitude were caused by microstructural effects when in fact they were caused by sample nonuniformity. Figure 58 shows two examples of how surface roughness and beveled or uneven surfaces affects C-Scan amplitude maps [20, 142].

If a sample is too thick or contains too much porosity the ultra high frequency wave is far too attenuated by the time it makes it back to the receiving transducer. For these cases, the sample surface reflections of interest are too small to measure. The limits for sample thickness and porosity are different depending on the output strength of the transducer. If the output strength is on the order of a microJoule, as is with the ultrasonic testing system at Rutgers CCR, the approximate thickness of a high hardness ceramic sample should be less than 50mm and its pore volume should not exceed more than 10% [142].

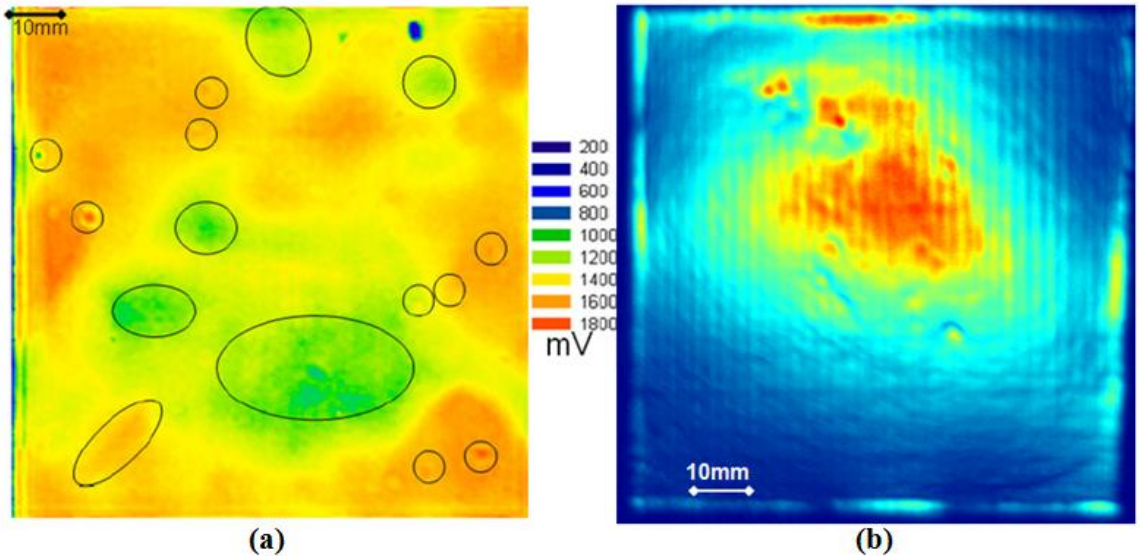

Figure 58. C-Scan amplitude maps of (a) sintered SiC showing error caused by surface roughness (circled) and (b) sintered Al_2O_3 showing error caused by sample bevel and uneven surfaces [20, 142].

2.5. Ultrasound Test Equipment

There are many brands of necessary ultrasound hardware which can be integrated to create a fully functional, automated scanning, ultrasonic NDE system. Many companies, such as Olympus, Imperium, and General Electric manufacture and sell ultrasonic NDE systems already integrated. Advantages of purchasing a turnkey NDE system lie in ease of use and full technical support. Usually on-site training accompanies a purchase agreement for a fully built system and the end user does not have to worry about understanding the minutia of every component. A disadvantage of using such preassembled equipment is the higher cost. Users who purchase prebuilt NDE setups are at the mercy of the manufacturer in the sense of only being able to use predefined functionality. Any increase in different types of resolution or changes to data acquisition and processing modes a user may require are not concerns of large manufacturers. The NDE system used for the work done in this thesis was assembled using integral parts

from individual suppliers. Software which controls automated motion, data acquisition, and data manipulation was created at the Rutgers CCR by Portune and others [20]. The construction of both the NDE system and software allows for the freedom of controlling all aspects of data collection. This section is concerned only with the specific types of individual components used as part of the whole NDE system used for this thesis. Figure 59 shows a black box schematic of each component which are described in full detail.

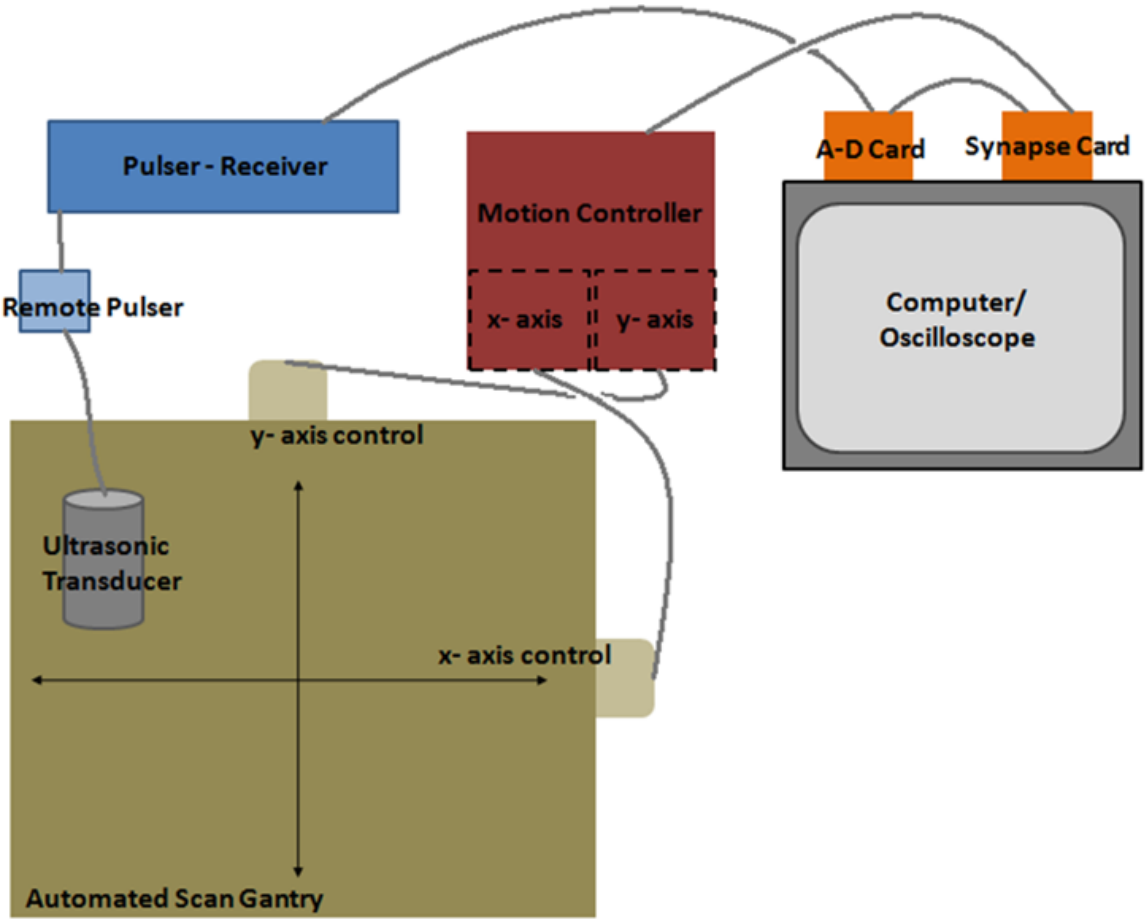

Figure 59. Black box schematic diagram showing individual components of ultrasound NDE system.

2.5.1. Ultrasonic Transducers

The ultrasonic transducer is the crux of ultrasonic nondestructive testing. These are the devices which emit and receive the ultrasonic pulses. The transducer controls all

aspects of the emitted ultrasonic wave which ultimately dictate the end measurements; sonic velocities, elastic moduli, or attenuation coefficient. The shape and geometry of the active element within a transducer controls its frequency output along with the degree of bandwidth [88]. Transducer operation, wave parameters, determination of frequency output, and types of resolution is discussed. Specific types of transducers including planar, focus, or phased array are explained.

2.5.1.1. Ultrasonic Transducer Components and Operation

Ultrasonic transducers operate on the principles of electrostriction piezoelectricity. This is the phenomenon certain types of materials exhibit which convert electrical pulses to mechanical vibrations and vice versa [211]. The application of alternating current to a piezoelectric material causes it to strain while an applied stress generates a voltage [88]. The active element is a polarized material with electrodes attached to two of its opposite faces. An electric field causes the polarized molecules to align causing the material to change dimensions [211]. Permanently polarized materials will produce an electric field when a material is strained as a result of an imposed mechanical force.

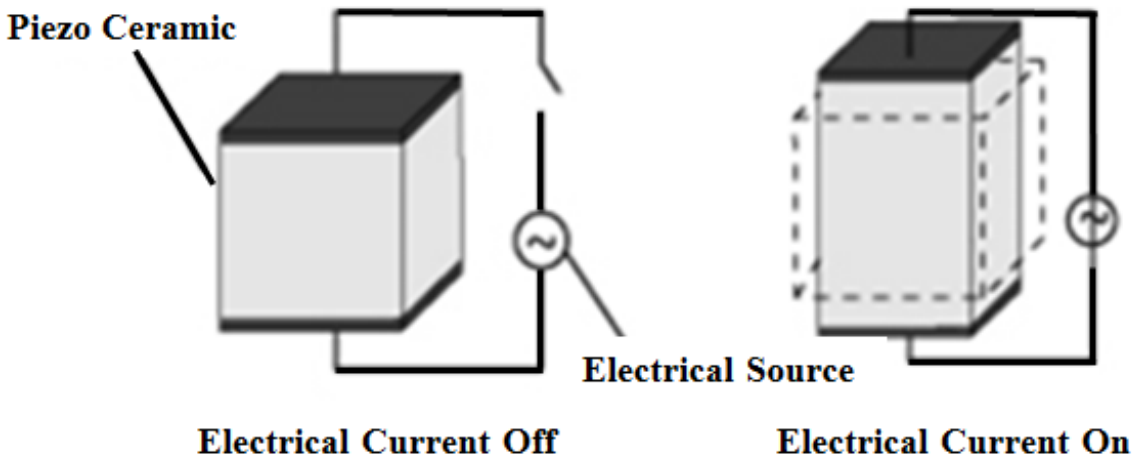

Figure 60. Illustration of piezoelectric effect [211].

The active piezoelectric element of most acoustic transducers used today is a piezoelectric ceramic such as quartz, barium titanate, or ceramic composites. Common ceramic composite piezoelectric materials include PMNT (lead, magnesium, niobium, titanium) and PZT (lead, zirconia, titanium) [212, 213]. The thickness of the active element dictates the desired frequency it will vibrate at upon an applied voltage. A thin element vibrates with a wavelength which is twice its thickness; therefore, thinner piezoelectric elements provide higher frequencies and the need for higher frequency transducers is primarily limited by machining capabilities and how thin the element can be made [211].

Reasoning as to why an acoustic transducer emits more than one frequency, or has an associated bandwidth, is due to how the piezoelectric element is packaged within the transducer assembly. Figure 61 shows a cross section of an ultrasonic transducer. The external housing and inner sleeve of the transducer protects the active element and backing material while providing a means of gripping and manipulating the device. The electrical leads are connected through the backing material to both faces of the piezoelectric element [214]. The backing material provides a damping force which creates the broadband nature of an emitted wave [88]. A backing material with similar acoustic impedance to that of the active element will produce high damping and give a wider bandwidth [215].

The physics behind how the transducer operates can be described through the second order differential equation for a damped, driven, harmonic oscillator [90]. Equation 14 describes the amplitude of oscillation over a range of frequencies. The amplitude of oscillation is analogous to the intensity output at each frequency; the driving

force is related to the electrical voltage; and the damping force is provided by the backing material. The output profile of a transducer is identical to its sensitivity spectrum [216]]. This means that any acoustic wave which does not match a portion of the frequency bandwidth associated with the transducer will go unmeasured [88].

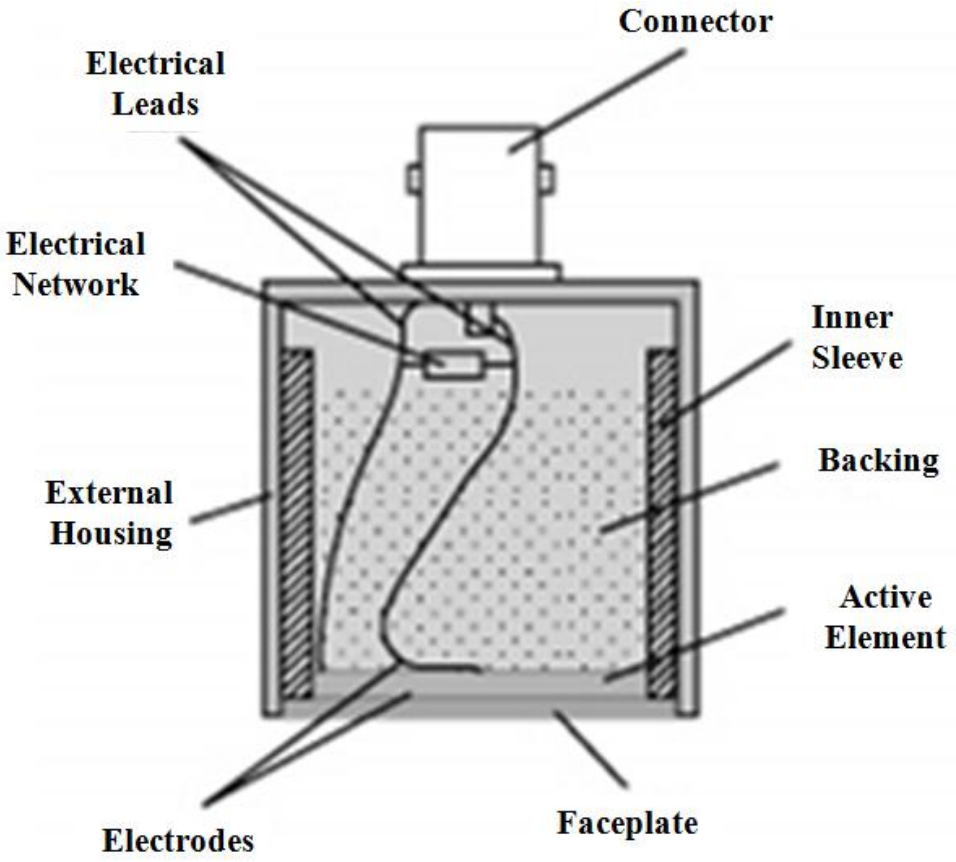

Figure 61. Cross section of acoustic transducer [214].

To get as much energy out of the transducer as possible an impedance matching layer is placed between the active element and the faceplate of the transducer (Figure 62). This is necessary due to the inherent acoustic reflections which occur at every interface where there is an acoustic impedance mismatch. To optimize acoustic impedance matching the size of the matching layer is machine to be the thickness of ¼ the desired emitted wavelength. This allows for the reflected waves within the matching layer to stay in phase when they eventually exit the layer [215]. Immersion transducers use an

impedance matching layer with an acoustic impedance value which is between that of water and the piezoelectric element [215]. The dB loss of energy on transmitting a signal from one layer to another is given as [217]:

$$dB\ loss = 10log_{10}[1 - (\frac{Z_1 - Z_2}{Z_1 + Z_2})^2] \qquad \text{Eq. 60}$$

Where it can be seen that by having a matching layer (or multiple matching layers) which have acoustic impedances close to that of the active element and water will result in lower amounts of energy lost.

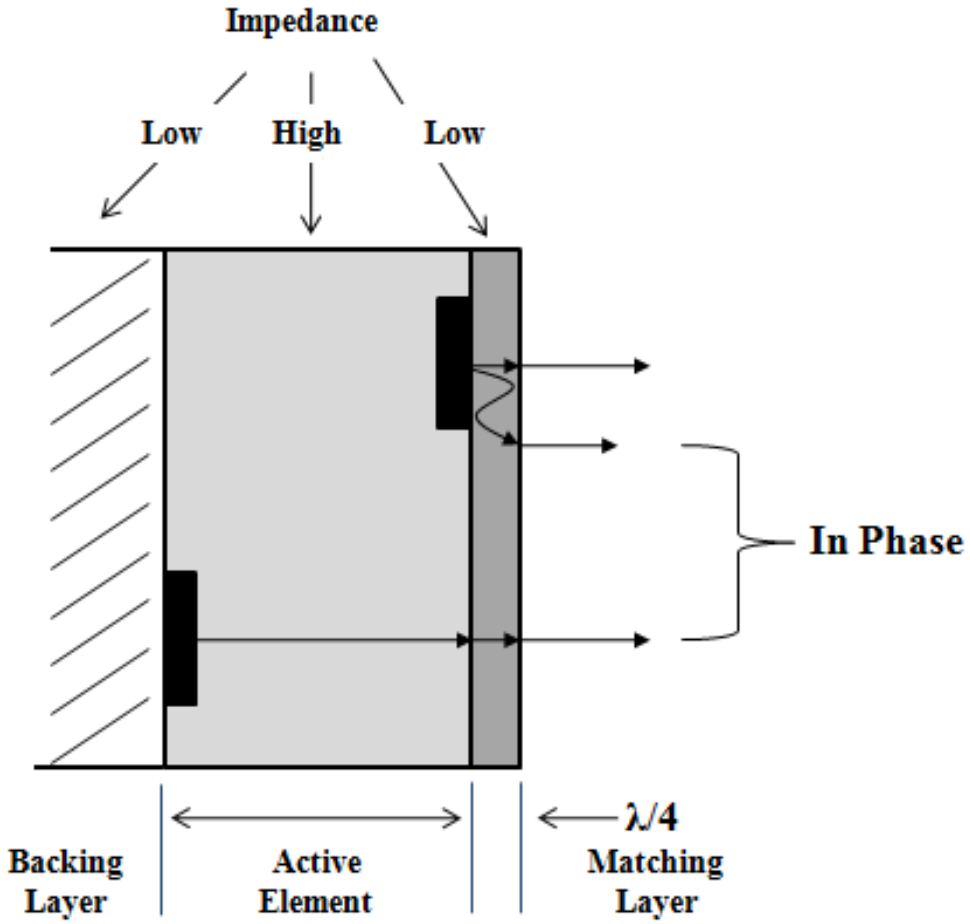

Figure 62. Illustration showing optimal thickness of matching layer according to wavelength [217].

2.5.1.2. Ultrasonic Transducer Wave Aspects

The sound field emitted by a transducer is divided into two zones; the near field and the far field. The near field, or Fraunhofer Zone, is directly in front of the transducer and the echo amplitude goes through a series of maxima and minima (Figure 63a and 63b) [217]. At some distance, N, from the transducer the near field terminates and the far field begins. Beyond N the far field begins and the sound pressure level gradually drops to zero. Due to the variations within the near field it can be difficult to characterize flaws using amplitude-based measurements [217]. The acoustic beam in the far field spreads out in a predictable manner due to Gaussian beam spreading [88].

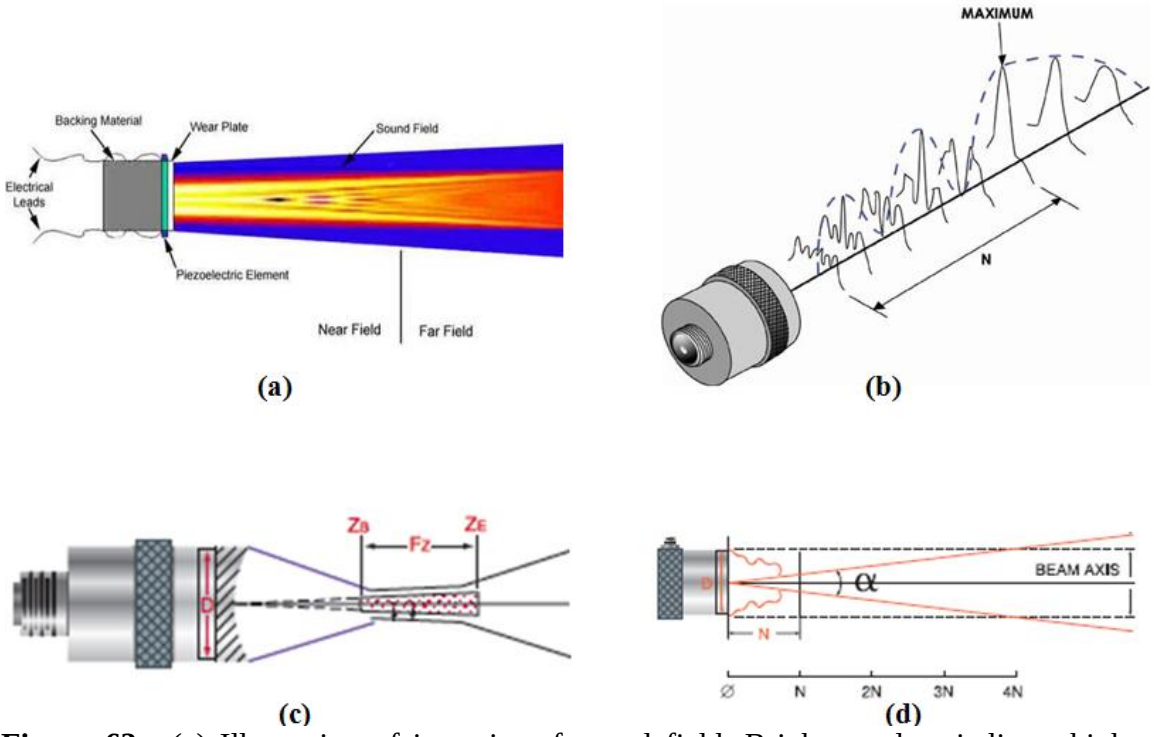

Figure 63. (a) Illustration of intensity of sound field. Brighter colors indicate higher intensity; (b) Illustration of amplitude variations between near and far fields; (c) Illustration of focal zone, F_Z; (d) Illustration of far field beam spreading [217, 218].

The length of the near field (N) can be described as a function of the transducer frequency, transducer aperture diameter (D), and speed of sound in the test material (c) [217].

$$N = \frac{D^2 f}{4c} \quad \text{Eq. 61}$$

Other than knowing near field distance, there are a number of other sound field parameters that are useful in describing transducer characteristics. The transition region between the near and far fields is called the transducer's focal zone, F_Z (Figure 63c). The focal length, F, in a planar transducer is approximately equal to the near field distance. The focal zone for a planar wave transducer is given as [217]:

$$F_Z = NS_F^2 \left[\frac{2}{\left(1+\frac{S_F}{2}\right)}\right] = \frac{4N}{3} \quad \text{Eq. 62}$$

Where S_F is the normalized focal depth given as F/N. Optimal detection of flaws is obtained when the focal zone envelopes such features.

All ultrasonic beams diverge or undergo beam spreading. This effect is more noticeable in the far field region. The degree of beam spreading is controlled by transducer aperture and frequency [217]. A quantification of the amount the beam has diverged is given by the half angle spread (α/2) at the point where the beam energy is 25% of its maximum (Figure 63d).

$$sin\left(\frac{\alpha}{2}\right) = 0.514\frac{c}{fD} \quad \text{Eq. 63}$$

The degree of beam spreading for ultra high frequency transducers (MHz) regime is somewhat negligible, and the ultrasonic beam can be approximated as a cylindrical

column of acoustic energy [20]. For example, a transducer with an aperture of 7mm and nominal frequency of 20MHz, the ultrasonic beam will only diverge by approximately 1° in an alumina tile. The maximum sound pressure is always found along the acoustic axis, or centerline, of the transducer; therefore, the strongest reflections occur from the area directly in front of the transducer [219].

2.5.1.3. Ultrasonic Transducer Resolution

There are two primary types of resolution associated with ultrasonic transducers: lateral and axial. Lateral resolution refers to the ability of resolving two adjacent boundaries which are orthogonal to the acoustic beam axis. Axial resolution is described as the ability of resolving two planes which are normal to the beam axis as being either top or bottom surfaces [220]. Both types of resolution are greatly affected by frequency. The frequency dependence of resolution leads to another factor which must be taken into account when performing ultrasonic NDE: depth of penetration. Essentially there is a tradeoff between having greater resolution versus higher depth of penetration. Depth of penetration increases with decreasing frequency, where a decrease in frequency will also cause a decrease in both types of resolution [221]. Higher frequency sound waves are attenuated to a greater extent than that of lower frequencies by almost all materials [19, 151, 221]. Successful ultrasonic inspection requires some knowledge of the ultrasonic transducers used, the tolerance limits for resolution, and the interrogated material.

2.5.1.3.1. Ultrasonic Transducer Resolution: Lateral Resolution

The lateral resolution of a transducer is inversely proportional to frequency. The main factor dictating lateral resolution is the beam diameter of a transducer. As stated above, the ultrasonic beam emitted from a transducer can be approximated as a

cylindrical column of energy. The diameter of this column of acoustic energy, B_D, can be calculated using the equation [217]:

$$B_D = 1.02\frac{F \cdot c}{f \cdot D} = 0.26D \cdot S_F \quad \text{Eq. 64}$$

Equation 64 gives the diameter of the beam where the signal amplitude drops to -6dB of its maximum amplitude; the focal zone of the ultrasonic beam [217]. The sensitivity of obtaining a reflection from a defect or feature within the microstructure is affected by beam diameter as well. This is caused by a smaller beam diameter resulting in a greater amount of acoustic energy reflected by a defect [217]. Decreasing the aperture size of the transducer allows for one to increase lateral resolution to a degree. An increase in frequency will also increase lateral resolution, but it decreases the focal zone, and thereby reduces the range of intensity where the beam diameter can encompass flaws [88].

2.5.1.3.2. Ultrasonic Transducer Resolution: Axial Resolution

Axial resolution is the ability of an ultrasonic system to produce distinct reflections from features located at nearly the same position with respect to the axis of the propagating ultrasound beam [88]. Axial resolution of an ultrasonic system is only applicable when there exists the possibility of resolving two features. For two features to be separately resolvable they each have to cause an intense enough reflection of acoustic energy from each surface such that different peaks in an oscilloscope are formed [89].

A direct reflection from a feature in the volume of a material will only be seen in an oscilloscope as a peak if it is large and provides a large acoustic impedance mismatch between itself and another feature. The greater the acoustic impedance mismatch between inclusions gives a larger amount of reflected acoustic energy. A reflection is a type of scattering where the size of the scattering feature dictates which direction the

energy is redirected. For features approximately 5 to 10 times less than that of the size of the acoustic wavelength, Rayleigh scattering occurs [136, 139]. Rayleigh scattering can be characterized as forward scattering behavior with a narrow cone of redirection. Therefore smaller features will cause scattering of the ultrasonic energy in directions not directly back to the transducer in a pulse-echo configuration [128]. For this reason the size of an inclusion will have to be commensurate with the wavelength to cause a backwards scattering reflection.

When viewing an A-Scan in an oscilloscope, the resolvable limit of peak reflections is dictated by the wavelength and size of feature. The minimum distance between two features such that each shows distinct reflections is 3λ [94]. Higher frequency transducers exhibit grater axial resolution as they emit smaller acoustic wavelengths. Transducers can be engineered to emit acoustic pulses of only fractions of a wavelength [94]. Therefore a 20MHz central frequency transducer emitting pulses of only 0.1λ will have an axial resolution limit of approximately 158μm in alumina. This can be calculated by determining the size of the wavelength in alumina, dividing by the pulse length, and then multiplying by 3 [94, 217].

2.5.1.4. Ultrasonic Transducer Types

Many types of ultrasonic transducers exist for different applications. The types of transducers discussed in this section include planar, focused, and array. Planar and focused transducers rely on using a single active piezoelectric element while array transducers use multiple elements in different arrangements [222]. The multiple active elements in an array transducer are separately controlled as to when they are pulsed to

control the size and shape of the wavefront. A discussion of delay lines, a feature found in ultra high frequency transducers, finishes this section on ultrasonic transducers [222].

Planar transducers have a flat face aperture with no focusing lens inside the column assembly [217]. These types of transducers emit acoustic beams that only exhibit focusing due to natural refraction and diffraction. A planar transducer exhibits the longest focal zone making it useful for inspecting bulk volumes of material. Intense reflections from the large focal zone of a planar transducer make it suitable for use with thick specimens [217]. Planar transducers have decreased axial resolution when compared to other types of focused transducers [222]. Being easier to manufactur, the planar type of transducers is typically of a lower cost and can be purchased off the shelf without any special order needed.

Single element focused transducers are available in two configurations: spherical (spot) and cylindrical (line) focused (see Figure 64) [217]. Focusing of the acoustic beam can be achieved by machining the active element to be curved or, more commonly, add a focusing lens into the column of the transducer [217]. The radius of curvature of either the element or lens is dictated by what the specific focal length and focal target needs to be. Focused immersion transducers use an acoustic lens to shorten the focal zone. This can give a dramatic increase in axial resolution and sensitivity to whatever defect would be present in the focal zone [222]. However, when using a focused transducer one will encounter the effect of focusing gain [217]. Focusing gain is essentially an increase in the signal amplitude at the focal zone. An A-Scan would reflect this by not showing the typical, intuitive, exponential decrease in amplitude of successive bottom surface reflections. In this case, the first bottom surface reflection decreases in amplitude from

the top reflection, but after which the second bottom surface reflection increases signifying a gain in energy. It is for this reason that focused transducers are not used in this thesis. Accounting for the relative increase in energy due to focusing gain is not trivial when using ultrasound NDE as a microstructural characterization tool.

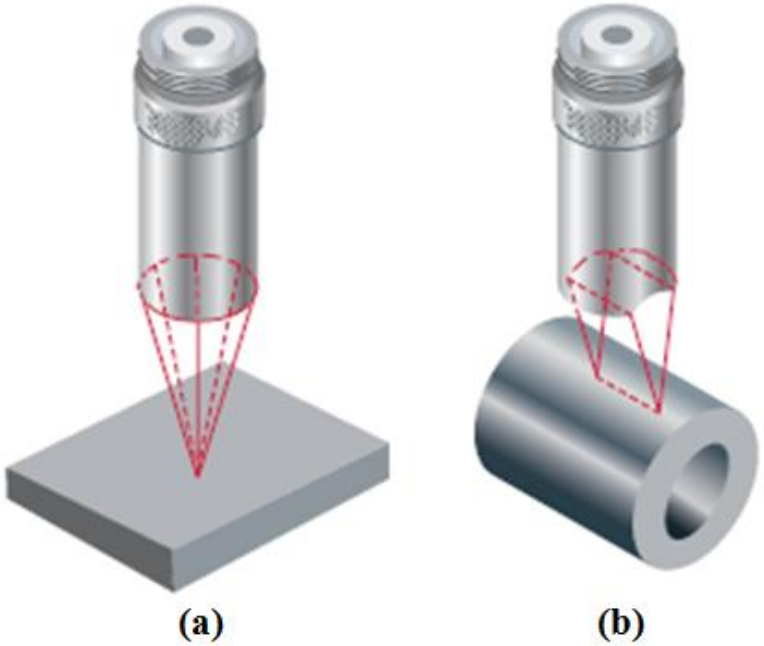

Figure 64. (a) Spherically focused transducer; (b) cylindrically focused transducer [217].

Ultrahigh frequency single element planar and focused transducers typically have a delay line inside the transducer column. A delay line is a physical structure which allows the active element to stop vibrating before a returned signal can be received [217]. Some transducers have the option to change the delay line to obtain different effects. For the type of testing performed in this thesis delay line transducers can be troublesome as the delay line itself gives multiple echoes on an A-Scan. An image of an A-Scan using a 150MHz central frequency transducer can be seen in Figure 65. Every peak seen in this A-Scan is caused by a reflection off of the delay line. This makes it difficult when trying to discern sample peaks with low amplitudes.

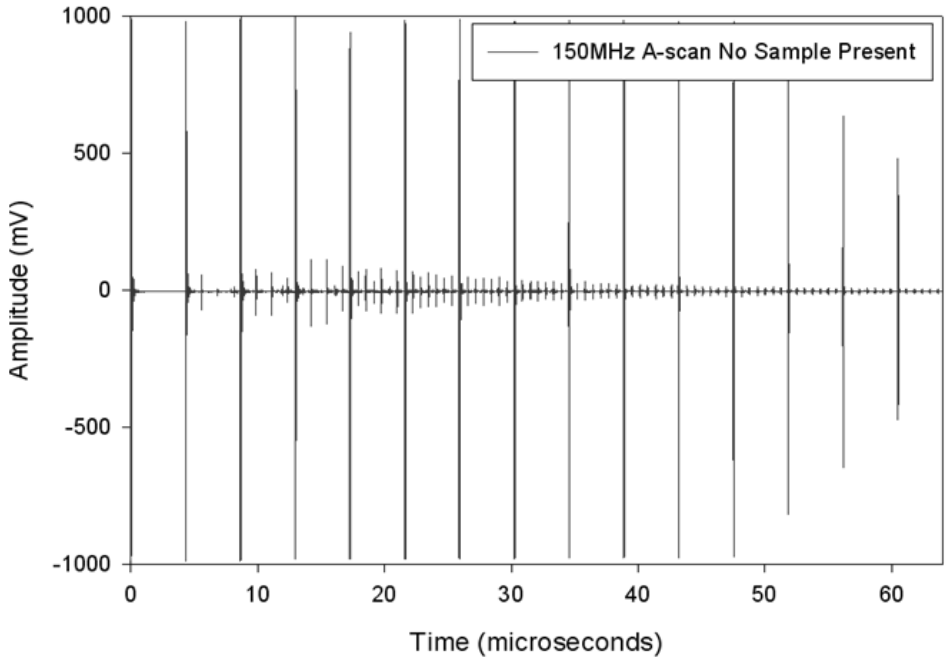

Figure 65. A-Scan showing multitude of delay line echoes [142].

An array transducer (or phased array) is an organized arrangement of large quantities of active piezoelectric elements [217]. The simplest form of an ultrasonic array for NDE is a series of several active elements arranged linearly to increase inspection coverage and the speed of inspection. A phased array is commonly used for tube, weld, and bridge inspections [217]. Phased array systems require high speed multi-channel processing with proper pulsers, receivers, and computation power to process the data from each individual element. Due to limitations of processing power and machining capabilities, phased array transducers can only be made to emit frequencies up to approximately 40MHz [223].

Phased array transducers come in a wide range of sizes, shapes, frequencies, and number of active elements [223]. Phased array transducer elements are typically made of piezocomposite materials which are thin rods of piezoelectric ceramics embedded in a polymer matrix. Segmented metal plating is used to divide the piezoelectric composite

into a specific number of elements which can be pulsed individually [223]. The segmented plating includes a protective matching layer, backing layer, and cable connections to each element segment (Figure 66). Each element can be pulsed simultaneously or individually at different times to control beam parameters such as focus depth, propagation direction of the wavefront, or intensity of the focal point [223]. By digitally controlling each elements pulse delay and excitation voltage several possible beam profiles can be created by a linear phased array transducer (Figure 67).

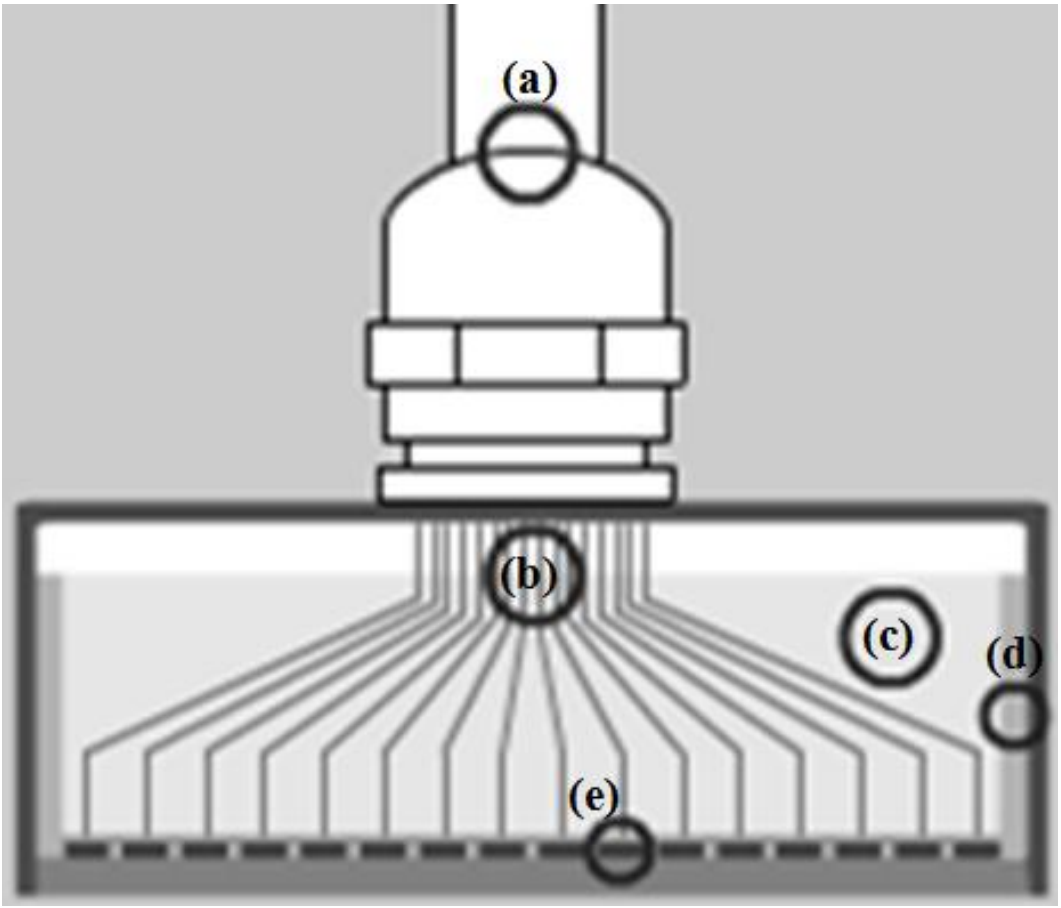

Figure 66. (a) Coaxial connector cable; (b) element wiring; (c) backing materials; (d) inner sleeve; (e) piezocomposite element [223].

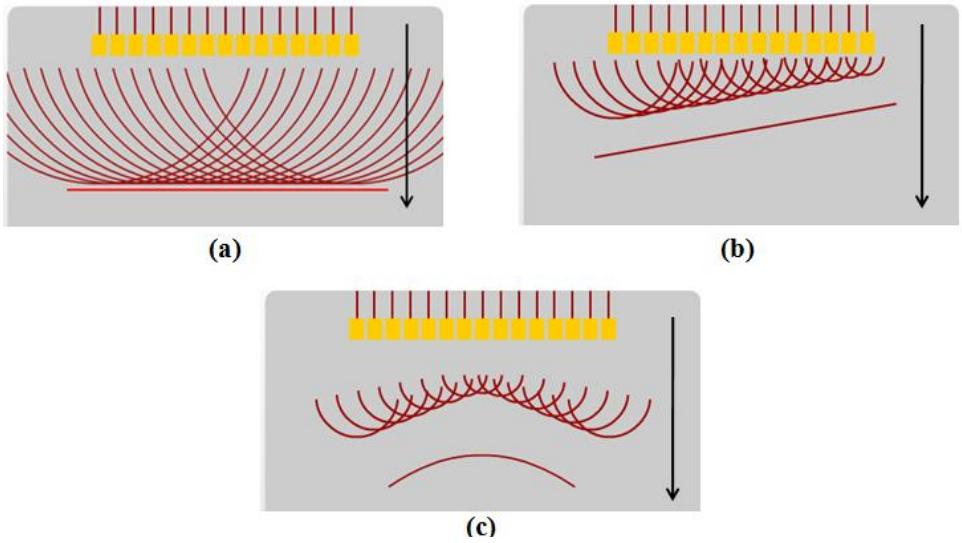

Figure 67. (a) Linear wavefront, all elements pulsed simultaneously; (b) angled wavefront, elements pulsed at increasing times from left to right; (c) focused wavefront, outer to inner elements pulsed at increasing times. Direction of pulses indicated by black arrows [223].

2.5.2. Pulser-Receiver

The pulser-receiver is the device which controls when the transducer emits a pulse. The pulser portion of the apparatus generates short, large amplitude electric pulses of energy, which are converted to short pulses applied to an ultrasonic transducer. The receiver end of the device collects the returned voltage response generated by the piezoelectric, filters the signal, and amplifies it such that it can be displayed on a digital oscilloscope as an A-Scan [206]. Typical functionality of pulser-receivers includes the ability to control the amount of time the pulse is applied to the transducer as well as the voltage supplied to the transducer. These two functions operate on the pulser circuit while the receiver circuit includes the abilities of signal rectification, filtering, and amplification [224].

Pulser-receivers are capable of operating in two modes; internal and external triggering. Internal triggering allows the pulser-receiver to supply its own continual

pulse to the transducer while external trigger mode uses pulses supplied by other attached hardware. The use of an external trigger for C-Scans is accomplished by synchronizing the pulser-receiver with a motion control device and forced to pulse when the device causes motion of the transducer [14].

The functionality and settings of the receiver circuit can greatly affect the outcome of ultrasound testing. Control over frequency filters, or band pass filters, allows for the reduction of either low or high frequency noise [206]. Band pass filter settings must be made to optimize the intensity of the received signal and increase the signal to noise ratio such that the received signal is not also filtered. The bandwidth of the receiver dictates what frequencies are capable of being resolved by the pulser-receiver [224]. If performing ultra high frequency testing one will need a high frequency, broadband pulser-receiver. Receiver bandwidth varies depending on the type of system and testing performed, but common high frequency ultrasonic testing typically use pulser-receivers with receiver bandwidth between 1 and 500MHz [206].

Modern pulser-receivers utilize remote pulsers. This effectively shortens the distance between the pulser circuit and transducer to minimize noise or electronic reflections in cables [206]. Remote pulsers amplify the signal before reaching the transducer. Remote pulsers are made to be interchangeable such that different ones can be chosen to match the frequency of the transducer to be used. Only a few types of remote pulsers are necessary as they cover a wide frequency bandwidth: low frequency, high frequency, and ultra high frequency. These frequency terms for remote pulsers are general where the manufacturer can supply information on what type of remote pulser should be used with different frequency transducers [206].

2.5.3. Analog-to-Digital Converter Card

The analog-to-digital (A/D) card is the device which converts the pulses sent from the pulser-receiver to a digital signal which can be read on an oscilloscope or through software which supports oscilloscope functionality [225]. A/D cards dictate all aspects of digital oscilloscopes such as time resolution, time range, amplitude resolution, and voltage range [225]. Choosing the right A/D card is mainly dependent on the frequency of the transducer needed to be used. Depending on its functionality, A/D cards can be somewhat expensive reaching into tens of thousands of dollars.

When performing ultra high frequency ultrasound testing it is critically important to use an A/D card with a sampling rate which is capable of matching the transducer frequency. Sampling, or digitization, rate dictates the time resolution of the oscilloscope. Essentially it will define how often a new data point is plotted. Each peak seen in an oscilloscope is the convolution of multiple sine waves of different frequencies put out by the transducer. For an oscilloscope to plot sine waves of accurate frequencies it must be capable of discerning at least five data points [20]. For large wavelengths (low frequencies) the time resolution need not be that high, but as wavelength decreases (frequency increasing) the time resolution of an A/D card must be greater. A/D cards measure sampling rate in Hertz, or samples per second, where most A/D cards can be found in the range of 100-2000MHz [225]. As at least five data points are necessary to distinguish one sine wave from another, this effectively means that transducers of frequencies at least five times less than that of the sampling rate are capable of being used with such an A/D card.

The time range of an oscilloscope is dictated by the amount of on-board acquisition memory the card comes with [225]. Cards with more on-board memory are capable of extending to higher time. This is useful if one is inspecting a material with low sonic velocity and a surface reflection won't appear until a certain time. An A/D card with 256MB of on-board memory is capable of reaching out to 64μs. Cards can be purchased to have as much as 4 GB of on-board memory which would extend the time range to 1000μs [225].

Amplitude resolution of oscilloscopes is measured in bits supplied by the A/D card. The number of bits in an A/D card along with what the cards voltage range is determines the minimum separation in volts between two adjacent amplitude values [20]. The amplitude resolution supplied by an A/D card can be determined by dividing the voltage range by two raised to the power of number of bits. For example, an 8 bit A/D card with a voltage range of 2V (±1V) will have an amplitude resolution of 2/256 or 7.8125mV. Error in amplitude based measurements such as attenuation coefficient can be decreased by using a higher bit A/D card [226].

2.5.4. Motion Controller and Scanning Gantry

Automated motion of a transducer about a sample is accomplished through the use of a motion controller and scanning gantry. Both B-Scans and C-Scans require the use of a precision motion control unit. A transducer, or other measurement device, is affixed to an assembly which can be controlled to move in however many axes the motion control unit is capable of driving. For simplicity only two axis motion controller which facilitates movement in the x and y axes are considered. Each axis is controlled by microstepping drivers which are housed in the motion controller itself. The drivers give

pulse and direction signals to stepper motors (or servo motors) attached to the scanning gantry. The use of DB-9 or amphenol connector cables is typically found on many modern motion control units [227]. Each pin of the DB-9 or amphenol cable relays a different function from the microstepper driver to the stepper motor. Newer microstepper drivers use dipswitches which can be used in conjunction with a truth table to change functions such as steps per revolution or signal current.

Many newer models of motion controllers have the capability of easily bridging off of the pulse amplitude circuit of the microstepper driver to reroute and collect positional information with different types of software [227]. Motion control units used in conjunction with stepper motors are required to physically tap into the circuitry of the driver to record positional data while motion control units used with servo motors are not. Servo motors have the ability to export encoder data which are meant to provide some relative positional information [227]. Positional information is crucial when collecting ultrasonic information during a C-Scan. Without it one would just collect the ultrasound data and have no perception of where in the sample it came from [14].

2.5.5. Counter-Timer Card

A counter-timer card is used to interface between the pulser-receiver and the microstepper drivers of the motion control unit. Simply put a counter-timer card acts as a timer; every preset number of steps the servo motors takes, a high voltage pulse is sent to the transducer from the pulser-receiver [228]. A program can be written to control how long the counter-timer card has to wait before triggering the pulser-receiver to pulse the transducer. As stated above, newer motion control and scan gantry units which utilize servo motors do not need such a device. Older motion controllers and stepper motors

need to be used in conjunction with a counter-timer card such that the motion controller and pulser-receiver can be synced to record where in the sample acoustic data is collected from [14].

2.5.6. Cables

The cables used to connect all of the components previously mentioned become important when performing ultra high frequency ultrasonic testing. Every component of an ultrasound system introduces some noise at different frequencies. The cables themselves also increase noise which can overwhelm high frequency signals. Higher frequency pulses have low signal intensities and the longer a cable gets the more it will deplete the signal strength [90]. For this reason shielded cables of short lengths should be used for ultra high frequency testing. The effect of cable length have been studied by Portune et al, where it was shown that longer cables decrease signal intensity for ultra high frequency testing where shorter cables will decrease intensity for lower frequency transducers [20]. Typically it is beneficial to use an array of different cables specified for each transducer type to decrease electronic reflections and noise while also optimizing signal intensity [20].

2.5.7. Personal Computer and Software

All individual components of an ultrasound nondestructive testing system are linked to a personal computer capable of running software which controls each aspect of data collection and analysis. The use of modern computing power with multi-threading with multiple cores is beneficial as a large amount of data can be collected in a single ultrasound scan. The amount of physical memory, RAM, and clock speed of a computer

should be maximized when performing acoustic testing, especially if it relies on heavy signal processing as is the case when performing acoustic spectroscopy [20].

Linking the A/D card, motion controller, counter-timer card, and pulser-receiver is done through the use of software created for such a purpose. Software used for data collection should be capable of doing this to effectively collect information. This type of software should also allow users to directly interact with sample surface reflections in real time through the use of a digital oscilloscope [20]. Oscilloscope-based peak interactions typically include being capable of setting electronic gates for measurement, setting properties to be measured, and setting some acquisition area for automated scanning. Data processing software can be separate from data acquisition software but should allow a user enough freedom to manipulate collected data. Data manipulation includes cropping, rescaling axes, obtain statistical information, and exporting data in common file formats [20].

2.5.8. Commercially Available Ultrasound Systems

There are many companies and manufacturers of ultrasound test equipment and the hardware which can be integrated for use as part of an entire setup. For the sake of this section only three of the more popular commercial manufacturers of ultrasound setups and components will be highlighted: The Ultran Group, The Mistras Group, and Olympus NDT. The majority of the products manufactured and sold by these companies are used for large scale industrial nondestructive testing. Each company does, however, perform research and development to come up with innovative products, methods, and software.

The Ultran Group has been creating unique ultrasonic inspection devices for the last 25 years. Their goal is to target cost-effective production of acoustic testing equipment targeted for applications which their clients can test and characterize materials in the earlier stages of formation [229]. Ultran is the inventor of the modern non-contact, air-coupled, ultrasonic testing system. Non-contact acoustic testing allows for the testing of porous, hygroscopic, or touch sensitive materials. Ultran has improved the field of ultrasonics by creating devices capable of testing a wide range of materials, from composites, plastics, and foams, to wood, ceramics, and metals [229]. Although the Ultran Group is better known today as the leading manufacturer of air-coupled transducers, they are still proponents of integrating ultrasonic testing systems capable of many testing configurations such as pulse-echo, through-transmission, pitch-catch, and water immersion [229].

The Mistras Group is a global nondestructive testing corporation which researches and manufactures many types of NDE equipment, such as eddy current, digital radiography, acoustic emission, and automated ultrasonic inspection [230]. Their automated ultrasonic testing services offer benefits to clients including high speed corrosion scanning systems, on-line weld inspection, phased array ultrasonics, and time of flight diffraction testing. Aside from manufacturing fully integrating ultrasonic testing equipment, Mistras also provides individual components of setups as part of their services. Such components include motion control units, transducers, and A/D cards. However, while Mistras' readily available fully integrated systems or components will meet most needs for industrial testing, they make custom equipment for research facilities looking to improve in areas such as digitization rate or transducer frequency [230].

A final commercially available ultrasound testing system can be acquired through Olympus and their NDT branch [231]. They provide equipment for inspection applications including weld inspections, cracks, voids, porosity, and other types of heterogeneities within metals, composites, plastics, and ceramics [231]. Olympus specializes in making versatile, rugged, portable units capable of running different NDE types through the use of plug and play modules. The types of NDE modules supported by Olympus' Omniscan system include eddy current to phased array ultrasound to thermography [231]. The Omniscan unit coupled with a phased array ultrasound module is capable of running A, B, and C-Scans for the detection and sizing of anomalous within bulk material. This system is only able to use lower frequency transducers due to processing power limitations and machining limitations of the transducers piezoelectric element [231]. Olympus also offers software used to acquire and process data collected using the Omniscan unit linked with a personal computer.

3. Method of Attack

The goal of this work was to develop a nondestructive ultrasonic measurement technique which gives mean grain size of aluminum oxide over large sample areas as well as the concentration and size distribution of secondary phases within dense aluminum oxide. The primary method of meeting this goal is to measure frequency dependent attenuation coefficient spectra of aluminum oxide to obtain data from both the absorption and scattering frequency regimes. From this, four necessary objectives are delineated to meet this goal. The first objective was to determine and implement equipment upgrades such that a wider range of acoustic frequencies could be used and measured. The second objective involved the creation of analytical equations and standard values which are used to describe energy loss and attenuation caused by absorption and scattering in dense aluminum oxide. A third objective was defined to list appropriate alumina sample sets which include standard materials, materials with known varying microstructures, and materials with unknown microstructures to test created concepts. The fourth objective was to corroborate ultrasound results given by the first three objectives by characterizing these samples with conventional microstructural measurement techniques.

Distinctive tasks were assigned to reconcile each objective. Determination of appropriate frequency ranges to measure attenuation coefficient for each sample set dictated the specifics of equipment upgrades. Regarding the creation of analytical equations which describe thermoelastic energy loss to expedite the measurement of secondary phase size distributions in alumina, specific assumptions were made and explanations for the validity of their use was determined. The effect of grain size

distributions and concentrations of alumina and secondary phases contained within alumina on attenuation coefficient spectra was necessary to properly characterize real samples. A determination of the accuracy of the methodology created was accomplished through a series of common bulk characterization techniques. These objectives and tasks were developed as a systematic method of attack used for meeting principal goal of this thesis.

The method of attack used to meet specific objectives and subtasks assigned to each objective is outlined in this section. Reasoning as to why innovative equipment upgrades were necessary is discussed first. This is followed by an explanation of the necessity of creating analytic equations which describe the amount of acoustic energy lost due to thermoelastic absorption and the number of grains actively causing this type of absorption. The desired aspects of samples to be used for testing will be explained, along with the chosen characterization methods used to determine bulk grain size information. A justification of the techniques used to validate acoustic testing results with microscopy will be explained.

3.1. Enhancements and Upgrades to Ultrasound System

When measuring acoustic attenuation coefficient one will obtain results specific to the microstructure of the material as well as the frequency of the ultrasound. Having a robust ultrasound testing system capable of measuring attenuation coefficient over a wide frequency range allows for the collection of attenuation data caused by different loss mechanisms. The ability to measure attenuation coefficient spectra in frequency regimes where absorption and/or scattering are dominant is the crux of achieving the goal of this thesis. It has been shown that intraparticle thermoelastic absorption dominates loss

spectra up to approximately 50MHz in commercially available dense aluminum oxide used for structural applications with average grain size less than 10μm. To obtain statistically relevant loss spectra caused primarily by scattering mechanisms with minimal convolution of absorption losses one must either increase the frequency range used or create materials which have significantly larger grains. The latter choice violates the integrity or purpose of creating alumina with grains of this size, thereby making the only option for obtaining scattering information in real, commercial, alumina samples is to increase the range of frequencies used for measuring attenuation coefficient spectra.

As absorption in alumina can be seen up to approximately 50MHz, equipment upgrades to obtain reliable attenuation coefficient spectra caused primarily by scattering were made to extend the measureable frequency range to 150MHz. The necessity for such a large frequency range where scattering would be the primary loss mechanism is due to the fact that there are different types of scattering mechanisms which are dependent on the wavelength of ultrasound and size of the scatterer. By changing frequency, changes in wavelength occur and the different types of scattering can be measured according to grain size. A general rule of thumb for obtaining accurate scattering data is to use wavelengths which range between the average size of the grains and 10 times larger than the grains. This range will ensure that both Rayleigh and stochastic scattering mechanisms will be seen and measured. The average grain size of alumina used for structural applications and tested in this thesis is on the order of microns; with a distribution that allows for grains above 10μm. This translates to using frequencies up to approximately 150MHz.

There were two tasks involved in meeting the goal of extending the measureable frequency range: integrate an analog-to-digital converter card which has a sampling rate capable of distinguishing these frequencies and acquiring a broadband, planar, longitudinal transducer which is also capable of emitting frequencies in this range. As stated earlier, the sampling rate of an A/D card must be approximately 10 times greater than the transducer used meaning an A/D card capable of resolving frequencies up to 150MHz must have a sampling rate of 1.5GHz or greater. The integration of new hardware requires upgrades to the software as well as testing to ensure accurate frequencies are being emitted and received.

3.2. Creation of Analytical Equation for Thermoelastic Energy Loss

An analytical equation which describes the amount of acoustic energy lost due to intraparticle thermoelastic absorption does not exist. A derivation of an equation which returns the number of secondary phase grains in an aluminum oxide microstructure was the first task of this objective. It is known that there is a relationship between frequency, the thermal properties of the absorbing material, its density, and the size of the grain actively causing absorption. However, an equation was lacking which quantifies the amount of acoustic energy lost as a function of frequency-based attenuation coefficient, size, and concentration of grains. A solution such as this was necessary to be derived such that an acoustic attenuation coefficient measurement can be used to determine a particle size distribution of the actively absorbing grains within a microstructure. This solution led to the derivation of an analytical equation which allowed for the transformation of frequency dependent attenuation coefficient, in an absorption regime, to give grain size distributions of secondary phases in two types of alumina containing

different microstructural features. The task of developing this equation was necessary in completing the overarching goal as it directly links measured attenuation coefficient to alumina microstructure.

3.3. Sample Sets

Two sets of alumina-based samples were chosen to systematically study the effects of and differences between absorption and scattering loss mechanisms. The samples studied in this thesis needed to meet certain criteria such that they would prominently exhibit specific types of acoustic loss behavior at specific frequencies. All samples were required to have greater than 98% of theoretical density such that any attenuation would not be caused by porosity and a strong bottom surface reflection could be seen. The lateral dimensions of the samples must have been greater than 20mm in diameter with the only restraint on their upper size limit being the size of the immersion tank. All samples were, however, confined to being between 3 and 25mm thick. If the samples were too thin then all of the surface reflections shift towards each other and convolute; if they were too thick then high frequency acoustic waves would have been too highly attenuated.

3.3.1. Custom Engineered Alumina Sample Series for Absorption

The samples used to study acoustic absorption were two sets of aluminas containing incremental amounts of different secondary phases. One sample set was created at the Rutgers CCR while the second set was acquired from a commercial manufacturer. The average grain sizes of the secondary phases were targeted to fall in a certain range such that these samples would exhibit strong thermoelastic absorption in the frequency range of approximately 10-30MHz. Along with these two sample sets, a 100%

alumina disc was created to be used a baseline. By having samples with known secondary phase concentrations and a baseline pure alumina to compare against, the derived equation from a previous objective was verified to be accurate.

3.3.2. Custom Engineered Alumina Sample Series for Scattering

Work done by previous authors laid the foundation of developing acoustic scattering loss theory which relates the attenuation coefficient to the average size of grains within a microstructure. This has only been done in metals with minor success. The lack of modern computing power or standard sample sets limited the study of using scattering attenuation coefficient spectra as a means of obtaining mean grain size. This task relies on defining a method for obtaining standard values for the Rayleigh and stochastic scattering prefactors, C_R and C_S, respectively. In doing this a standard alumina sample set was used which systematically varies the average grain size. This sample set was acquired from a commercial manufacturer using their standard production powder which is primarily Al_2O_3 containing a small percentage of sintering additives.

Nine lots of alumina samples were created where each lot was varied in firing temperature, dwell time, or both with the goal of coarsening the grains. Each sample in this set should not contain any large solid inclusions. These samples were examined using acoustic spectroscopy to obtain attenuation coefficient spectra and FESEM imaging to determine actual grain size distributions. The results of this task provided a carefully controlled sample set used to obtain standard values to be used with the Nicolleti Rayleigh and stochastic prefactors. An alumina sample series with unknown grain size, provided by the same manufacturer having the same composition as the above sample series, was used for testing the accuracy of the created scattering factors.

3.4. Ultrasonic Testing

Ultrasonic testing included both evaluation and characterization based methods. With the exception of one sample set, each sample had ultrasonic C-Scan measurements performed for longitudinal velocity, Young's modulus, and overall signal attenuation coefficient. This was done to determine any variation or large features within the bulk microstructure. The sample set which could not have C-Scan measurements made had samples which were too small in their lateral dimensions. This sample set had A-Scan point measurements of sonic velocities and elastic moduli performed. Acoustic spectroscopy measurements were performed on all samples. The frequency range of the spectra taken was dependent on the loss mechanism studied for each specific sample set. Samples to be studied for absorptive-based loss mechanisms had attenuation spectra taken from approximately the 10-30MHz range. Samples to be studied for a scattering-based mechanism had attenuation spectra taken from higher frequencies, approximately 40-110MHz. Possible anomalous agglomerations of sintering additives were located through C-Scan imaging and these points were omitted during acoustic spectroscopy testing.

3.5. Conventional Microstructural Testing

This task sought to reveal and examine the microstructures of the several alumina-based samples studied in this thesis. A full microstructural characterization of each sample tested ultrasonically was necessary to begin creating quantitative correlations and causal relationships between acoustic spectra, specific loss mechanisms, and the microstructure of aluminum oxide. Testing included X-ray diffraction (XRD), field

emission scanning electron microscopy (FESEM), energy dispersive spectroscopy (EDS), and grain size analysis. The purpose of each test for this task is further explained.

3.5.1. X-ray Diffraction

XRD was conducted to determine the type of secondary phases present in each of the two sample sets used to study acoustic absorption. As each sample set used for this purpose was created to contain incremental amounts of separate secondary phases, XRD was needed to quantify the volume percent of each phase present in each sample. X-ray diffraction is an integral step in using the derived analytical equation to determine secondary phase grain size distributions using acoustic spectroscopy. Sections from each sample to be tested using XRD were taken after all nondestructive testing was performed.

3.5.2. FESEM and EDS

FESEM imaging was performed to collect micrograph images such that correlations could be made between acoustic spectroscopy results and alumina microstructure. Each sample was sectioned about a region which did not present with any large or anomalous feature from C-Scan testing. These sections were polished to a submicron finish and etched to reveal the granular microstructure. The different sample sets of alumina containing various secondary phases required different etching procedures. Multiple micrograph images were taken from each sample at different magnifications depending on the size scale of the grains to be measured. Many images were necessary to be collected from each sample such that a statistically relevant population of grain sizes could be measured. EDS was performed to determine which features were the grains to be measured.

3.5.3. Grain Size Analysis

After each set of micrograph images were collected from each individual sample, analyses of grain size began. This task involved using image processing software which allows for the measurement of grains from micrograph images. Requirements for using this software included knowing calibration factors of pixel length to actual length, which was given as part of the micrograph image header file. Obtaining measured grain size distributions for each sample is critically important in the creation of the equation described in the second objective, obtaining standard scattering prefactors, and validating the methodologies put forth in this thesis.

3.6. Data Correlation

Once all data were collected from both nondestructive ultrasound testing and destructive microstructural characterization, it became admissible to begin correlating the two sets of results. Correlations of predicted grain size measurements using ultrasonic-based techniques with actual grain size measurements provided theoretical validation regarding the causal relationship between acoustic loss mechanisms, frequency, and alumina microstructure. The connection of ultrasonic measurements with microstructure built on the foundation for using acoustic spectroscopy as a characterization technique to nondestructively characterize dense aluminum oxide used for structural applications.

4. Experimental Procedure

This section describes the specific the equipment and procedures used for meeting the objectives outlined in Method of Attack are described in this section. A detailed discussion explaining each component of the ultrasound testing system used in this work is first given. Special attention is committed to the acquisition, integration, and testing of the ultra high frequency transducers and A/D card utilized to achieve the goal of this thesis. The attributes of the custom made and commercially acquired alumina samples studied in this thesis is discussed. Details of ultrasonic testing parameters with respect to A-Scans, C-Scans, and acoustic spectroscopy are highlighted along with the procedures used for transforming acoustic spectra into reliable grain size information. An explanation of the methodologies used with the conventional microstructural characterization techniques for the alumina samples studied in this thesis conclude this section.

4.1. Ultrasound System

While transducers, individual components of ultrasonic NDE systems, and commercially available preassembled systems were discussed in general in the background section, this section seeks to explain the full details of the individual constituents of the equipment used to complete the work done in this thesis. Discussions regarding the parameters of the transducers used are first, followed by explanations of the motion control unit, scanning gantry, pulser-receiver, counter-timer card, and the personal computer which controls each component. An account on the importance of the A/D card acquired specifically for this work and its integration with other components

and software reconciliation is given. The final discussion concerning the ultrasound system used for this thesis work gives attention to the acoustic testing software.

4.1.1. Ultrasonic Transducers

Acoustic testing performed on the samples in thesis made use of three separate transducers. Attenuation coefficient spectra which contain information relating to thermoelastic absorption for specific sample sets was obtained using the transducer which emits the lowest frequencies out of the three used. This transducer emits a central frequency of 20MHz and is sold commercially by Olympus. As a labeling scheme, this specific transducer will be referred to as the '20MHz transducer' hereafter. The 20MHz transducer is an immersion, planar wave, transducer with an aperture diameter of 3.1mm.

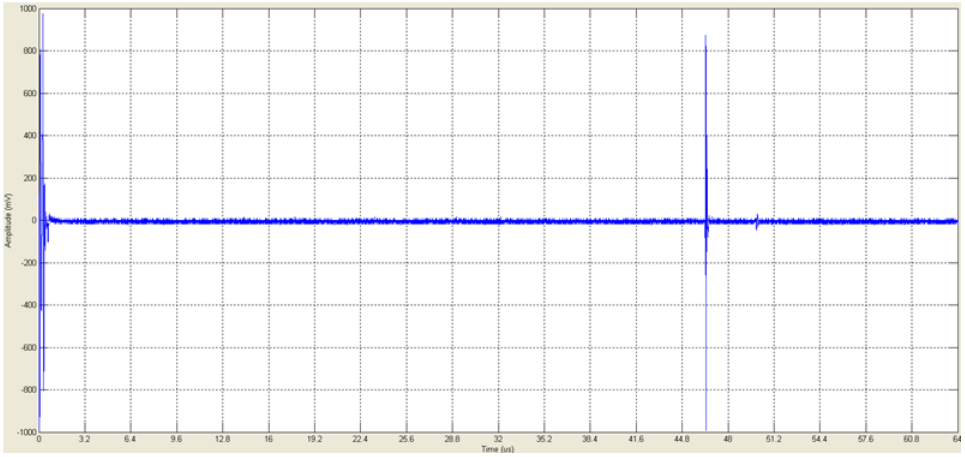

Figure 68. Oscilloscope A-Scan using 20MHz transducer. No Sample present. No delay line reflections. Reflections above 45μs are from immersion tank.

An oscilloscope view of a clean signal shows that this transducer does not contain a delay line (Figure 68). The noise variations with a signal gain of 18dB set by the pulser-receiver range from ±23.4375mV. A signal gain of 18dB is the typical gain set for this transducer when measuring attenuation coefficient. It should be noted that this noise will increase as signal gain increases. The -6dB bandwidth, or the frequency range where

a signal is considered to be useable, varies depending on the degree of attenuation caused by different materials. The -6dB bandwidth for the 20MHz transducer and the alumina samples studied in this thesis was consistently 12-30MHz. Figure 69 shows the power spectral density of the 20MHz transducer taken from the top surface of a highly polished silicon carbide mirror.

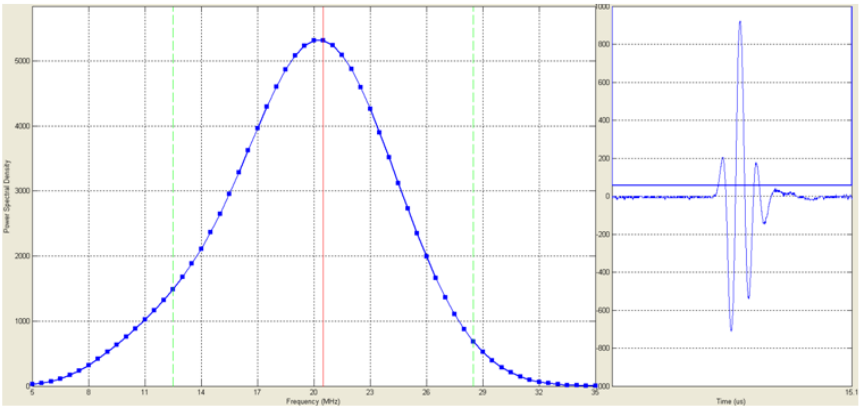

Figure 69. Power spectral density of 20MHz transducer output and oscilloscope view of top surface reflection from silicon carbide mirror.

Testing performed on alumina samples to acquire attenuation coefficient spectra dominated by scattering losses made use of two ultra high frequency, immersion-based, planar transducers. These transducers emit central frequencies of approximately 60MHz and 150MHz, respectively, and will hereafter be referred to as the '60MHz transducer' and the '150MHz transducer'. The 60MHz transducer was acquired through the Ultran Group, having an aperture of 8.9mm, and the 150MHz transducer was provided by Imaginant, having an aperture of 14.65mm. Both of these transducers contain delay lines as they emit exceptionally high frequencies. Oscilloscope views of each, not centered about any sample, are shown in Figures 70 and 71. Every reflection that is seen in these two oscilloscope images is caused by the delay lines within the transducers. As a result, reflections which are generated by the sample are placed within the two temporal regions

highlighted in red. The signal gain used for the 60MHz transducer is 10dB which results in noise variations of ±11.5mV. The 150MHz transducer is used with a signal gain of 24dB, giving a noise variation of ±23.5mV.

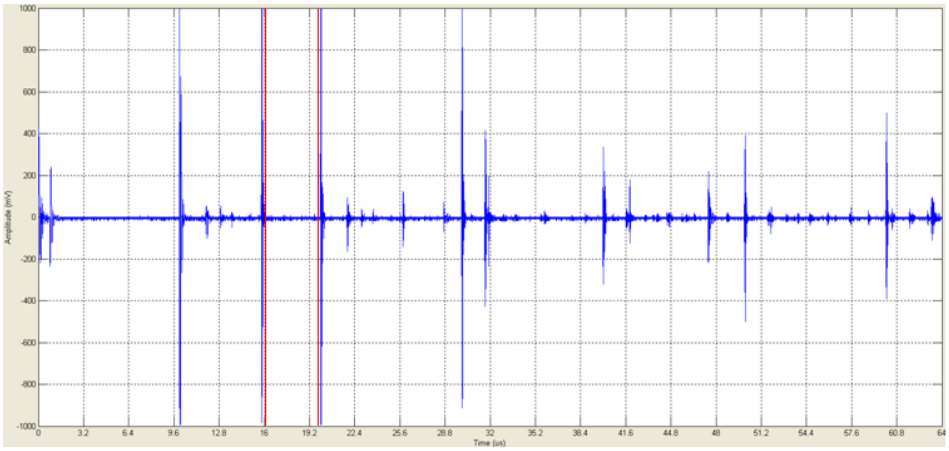

Figure 70. Oscilloscope A-Scan using 60MHz transducer. No sample present. All peaks caused by delay line reflections. Red window is where sample reflections are placed for measurement.

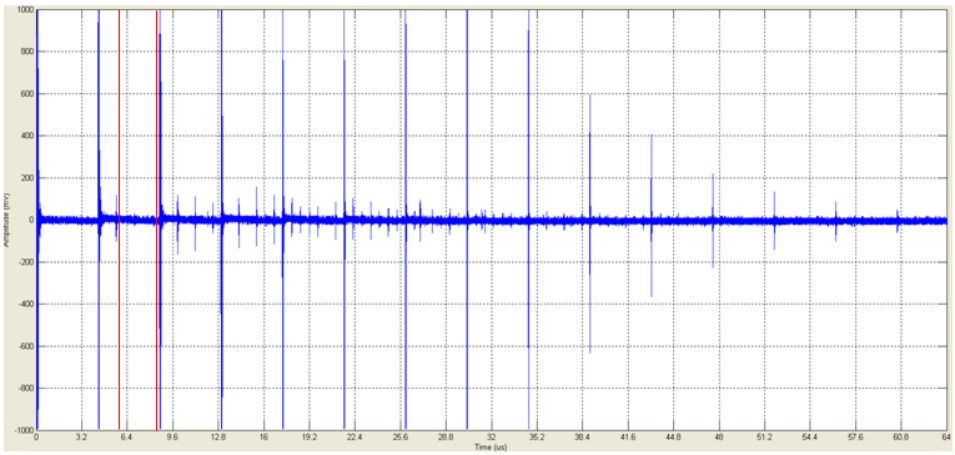

Figure 71. Oscilloscope A-Scan using 150MHz transducer. No sample present. All peaks caused by delay line reflections. Red window is where sample reflections are placed for measurement.

The bandwidths used from the 60MHz and 150MHz transducers for the samples studied in this thesis are 40-70MHz and 80-110MHz, respectively. It should be noted that there is a 10MHz gap between these two separate transducers where no data are available to be recorded due to the output profiles of each transducer. Secondly, the

bandwidth profile of the 150MHz transducer drops due to massive high frequency scattering attenuation caused by the alumina samples. Power spectral densities of each of these two ultra high frequency transducers can be seen in Figures 72 and 73. These intensity profiles were taken by performing an FFT of the delay lines within the transducer, a common method of measuring transducer output profiles as the wave has yet to be attenuated by any material. Ultra high frequency planar transducers with large bandwidths and high energy output over all frequencies are uncommon, requiring the need for multiple transducers to be used. Ideally, the use of a single transducer which emits frequencies of the same intensity over a broad range should be used for acoustic spectroscopy measurements; however, these types of transducers do not currently exist.

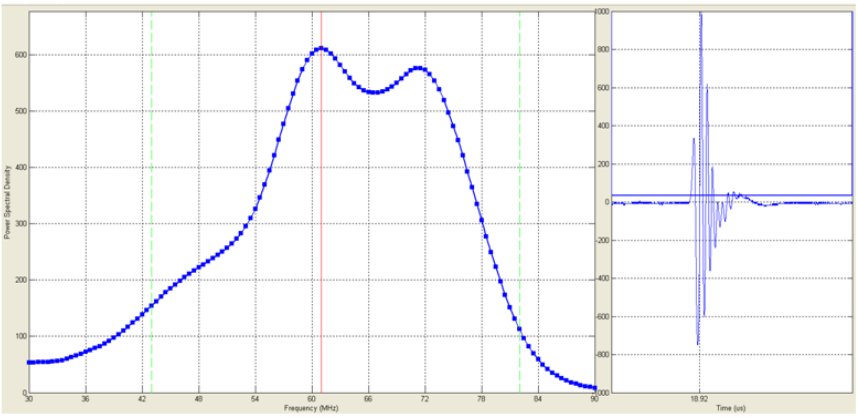

Figure 72. Power spectral density of 60MHz transducer output and oscilloscope view of first delay line reflection.

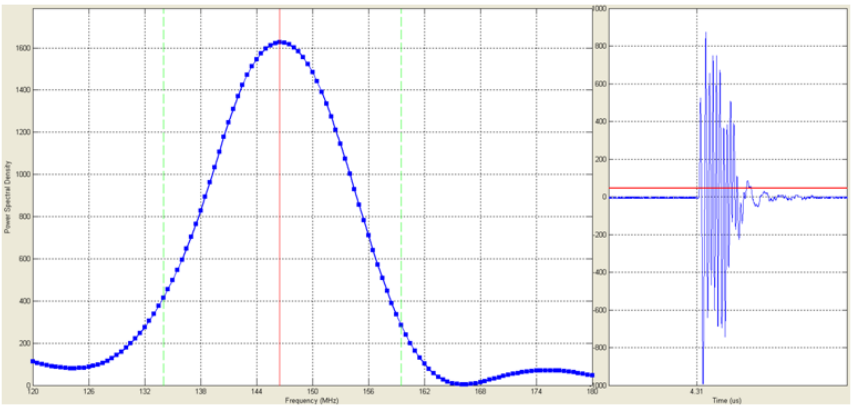

Figure 73. Power spectral density of 150MHz transducer output and oscilloscope view of first delay line reflection.

4.1.2. Ultrasound Test Equipment

The hub of all ultrasound components necessary for the acoustic tests performed in this thesis is the personal computer (PC). It connects with each component to allow for direct control of all the ultrasonic equipment. Data acquisition, formatting, and processing are also accomplished through the use of the PC. The calculations performed about tens of thousands of points in a sample used to obtain property maps require exceptionally high computing power to make acoustic testing a time feasible process. The computer used for ultrasonic testing was tailor-made to accommodate the high speed processing of the large data sets collected from each sample. The specifications of the computer are as listed: 2.83GHz Intel Core2 Quad core processor, 8GB PC6400 800MHz DDR2 RAM, 750GB hard drive, an EVGA GeForce 9400 GT 512MB PCIe video card, and a 700W 80+ power supply. Real-time data of acoustic spectra are capable of being viewed due to the use of multithreaded processing by the quad core processor.

The software used to perform data acquisition, formatting of datasets, processing, and manipulation was created in-house at the Rutgers CCR using MATLAB as the programming platform [20]. The software which was used to acquire and format the data is called Legacy© and the data processing and manipulation software is called Hermes©. Legacy© has the capability of viewing oscilloscope, power spectral density, and attenuation coefficient spectra modes all in real time. Six electronic gates allow for the measurement of predefined properties such as sonic velocities, elastic moduli, and attenuation coefficient along with options for user-defined measurements. Full wave data

are also capable of being stored during a C-Scan such that one is able to save all information and run virtual scans after the initial C-Scan is performed. Hermes© is capable of reading in files created by Legacy© to show A-Scans, power spectral densities, attenuation coefficient spectra, C-Scans, and four dimensional attenuation coefficient spectra taken about all points in a sample. Axes manipulation and palette realignment are also accomplished through this program. Hermes© gives real time statistics of whatever file is loaded on screen such as mean value, standard deviation, minimum and maximum, and the range of values.

The pulser-receiver which was used was provided by JSR (a division of Imaginant) and is known as a JSR DPR500. The receiver bandwidth is 295MHz due to its high and low pass filters. The JSR DPR500 has a high-pass filter of 5 or 30MHz and a low-pass filter of 150 or 300MHz, giving a maximum bandwidth of 295MHz. Depending on the frequency bandwidth of the transducer used, these filters are changed to provide optimal matching. For example, a 150MHz transducer will be used with a high-pass filter setting of 30MHz and a low-pass filter setting of 300MHz. The need for remote pulsers was described in general in the background section. The DPR500 can make use of several remote pulsers depending on the frequency of the transducer.

The ultrasonic testing done in this thesis required the use of three remote pulsers, all manufactured by JSR and designed to function seamlessly with the DPR500 pulser-receiver. Each remote pulser has a specific associated bandwidth meant to be matched with low, high, and ultrahigh frequency transducers. The three remote pulsers used in this thesis are called RP-L2, RP-H2, and RP-U2, where L, H, and U relate to being either low, high, and ultrahigh, respectively. The RP-L2, RP-H2, and RP-U2 have bandwidths

of 1-65MHz, 40-165MHz, and <100MHz, respectively. Depending on the remote pulser used, different settings for damping become available in the software used to control pulser-receiver parameters. The damping is always kept at a maximum for each remote pulser to ensure safety from the electronic noise. The RP-L2 uses a damping setting of 330Ω, while the RP-H2 and RP-U2 both use a setting of 100Ω. To further protect against erroneous noise reflections, shorter cables with microdot receptacles were used to connect the remote pulsers to the transducers.

The motion control unit, scan gantry table, and stepper motors were manufactured by Techno-Isel Inc. The motion control unit was a C-10 series controller which allows for up to three axes to be controlled by using microstepper drivers for each axis. The acoustic testing done for this thesis makes use of only two axes (x and y) to accomplish automated raster scanning. Each of these drivers is connected to stepper motors by RS232 DB9 to amphenol cables. The two stepper motors are mounted to the x-y scanning frame; a Gantry II Cartestian Robot with a vertical clearance of 200mm and table size of 850mm by 750mm. The useable x-y travel distance of this scan gantry is 500mm by 540mm. The stepper motors provide a discrete step size of 0.0125mm for either the x or y axes. The z-axis, pitch, and yaw were controlled manually by a stacked rotational goniometer designed at the Rutgers CCR. The goniometer has a dummy UHF attachment which allows for the connection of the ultrasonic transducers.

The stepper motors used did not have the means to provide absolute or relative positional information to the computer on their own. As a result the microstepper x-axis driver was bridged to create a connection which takes the signal containing positional information to the computer via a counter-timer card. The counter-time card creates the

positional information of the measured ultrasound data while a C-Scan is being performed. The counter-timer card used was a PCI-CTR05 five channel counter-timer board manufactured by Measurement Computing. The counter-timer card was connected to the mother board by a PCI slot. It collects the +5 voltage pulse given by the motion controller each time a step is taken in the x-axis. Each time the counter-timer card counts a predefined number of pulses it triggers the pulser-receiver to fire the transducer. As the step size of the scan gantry was 0.0125mm, each time the counter-timer card counts either 16 or 40 pulses it will cause the transducer to fire at either 0.2mm or 0.5mm intervals, respectively. This provides a method of changing the C-Scan image resolution by either increasing or decreasing the number of data points collected.

As part of the first objective for this thesis, the analog-to-digital converter card had to be upgraded such that it provided a higher digitization rate to be used with an ultrahigh frequency transducer. The original A/D card which was used had a digitization rate of 500MHz which effectively allowed for transducers up to 100MHz to be used with reliably. Acquired through Gage, a CobraMax high speed A/D card allowed for reliable transducer use up to 300MHz. The A/D card is inserted into a PCI slot on the PC's motherboard. This A/D card had a dual channel, 8 bit vertical resolution, 356MB on-board memory, 1.5GHz bandwidth, with a 3GHz sampling rate. The CobraMax A/D card provides a 64μs time range, a ±1000mV amplitude range, with a temporal resolution of 0.3ns, and an amplitude resolution of 7.1825mV.

Hardware modifications on the card were necessary to change the cards channel receptacle from SMB to BNC such that it can be linked to the pulser-receiver and counter-timer card. Aside from hardware modifications, recoding of the Legacy©

software was also necessary. This involved changing resistance parameters from 50Ω to 1MΩ in the A/D card initialization portion of the software along with changing code to reflect the new 3GHz digitization rate.

4.2. Sample Sets

Alumina sample sets capable of demonstrating high absorptive or high scattering losses were necessary to acquire to complete the goal of this thesis. As a result, several sets of alumina tiles or discs, each containing multiple samples, were either fabricated at the Rutgers CCR or acquired through commercial manufacturers. This section delineates each sample set based on its use for testing with acoustic absorption or scattering. The parameters for manufacturing each sample set are described along with basic sample measurements.

4.2.1. Alumina for Absorption Testing

To test the absorptive nature of ultrasound as is passes through a material two alumina-based sample sets were chosen to have increasing concentrations of separate secondary phases. As described by equation 30, the frequency of attenuation is affected by a variety of factors, but most strongly dependent on the size of the absorbing feature within the microstructure. The grain sizes of the secondary phases present in each sample set were controlled such that they would cause strong absorption in the frequency range of approximately 12-30MHz. As the secondary phase concentration increases it is expected to cause an increase in thermoelastic absorption which was seen as an increase in the attenuation coefficient spectra at these frequencies.

To provide a baseline for this testing, a 100% aluminum oxide sample was created using the spark plasma sintering method. It was believed that the only thermoelastic

absorption that occurred in this 100% alumina sample would solely be caused by the alumina grains and any attenuation above this base spectrum is caused by the presence of secondary phases. The 100% alumina standard sample was made from A16 alumina powder which was ball milled to give a d90 particle size of 5.4μm. Six grams of this powder was rapidly sintered using a heating rate of 200°C/min and holding at 1600°C for 10 minutes. A pressure of 30MPa was applied to the sample during the maximum hold temperature. The final product had a density of 3.97g/cm^3 (Archimedes method) and thickness of 6mm. The surfaces of the dense 100% alumina standard were sand blasted to remove residual graphoil (used for conductance during SPS) and ground flat for acoustic testing.

4.2.1.1. Mullite Series

The first of two alumina-based sample series used for acoustic absorption testing was created at the Rutgers CCR using the spark plasma sintering method. The milled A16 powder which was used to create the 100% alumina standard sample was used as the primary powder as the basis of the samples in this set. Degussa Aerosil 200 SiO_2 powder, with an average particle size of 12nm, was added to the A16 alumina powder to make five batches of powders containing between 1-5wt% SiO_2. According to the Al_2O_3-SiO_2 phase diagram (Figure 7) it was expected that five, alumina-rich, mullite samples containing between 2.7wt%-13.5wt% mullite would result after sintering. Alumina-rich mullite was chosen as a sample set to study as it is somewhat common structural ceramic being widely used in the field of refractories. Using Equation 30, the thermal conductivity of mullite (3.5W/m·K), specific heat of mullite (962J/kg·K), and the density of mullite (3050kg/m^3), suggest that mullite grains of approximately 300nm would

strongly cause thermoelastic absorption in the range of 12-30MHz [232]. Therefore the starting powder size of the SiO_2 was chosen to be exceptionally small such that fine grain mullite would be produced.

Each powder batch, containing different concentrations by weight of SiO_2, was ball milled in isopropanol for three hours to ensure relatively uniform mixing using millimeter-sized alumina media. After mixing, the resultant slurries were sieved to remove the milling media and heated on a hot plate to evaporate the isopropanol. The dried, mixed, powders were placed in a drying oven for 24 hours at 100°C to further dry the powders. Each fully dried powder batch had any large agglomerates broken apart using a mortar and pestle. Approximately 50 grams of each alumina-silica powder batch was created. Six grams of each powder mixture was rapidly sintered using an SPS using a heating rate of 200°C/min and holding at 1600°C for 15 minutes. 30MPa of pressure was applied to the sample during the maximum hold temperature.

The resulting alumina-rich mullite samples were disc-shaped. They were sand blasted to remove excess graphoil and surface ground such that they could be tested ultrasonically. Table VI shows the measured densities (via Archimedes method) and dimensions of each alumina product containing increasing amounts of secondary phase mullite. The theoretical densities of each sample were unable to be calculated before X-ray diffraction was performed. This alumina-based sample set is referred to as the mullite series. For the sake of Table VI each sample is labeled according to the weight percent of SiO_2 in each starting powder. XRD results, shown in the Results and Discussion chapter, give the volume percentage of mullite which was formed. These

samples will later be relabeled according to the volume concentration of mullite present in each.

Table VI. Diameter, thickness, and density of samples from the mullite series.

	Diameter (mm)	**Thickness (mm)**	**Density (g/cm^3)**
SiO_2 - 1wt%	20	5	3.84
SiO_2 - 2wt%	20	5	3.84
SiO_2 - 3wt%	20	5	3.83
SiO_2 - 4wt%	20	5	3.77
SiO_2 - 5wt%	20	5	3.76

4.2.1.2. Titanium Carbide Series

An aluminum oxide sample set containing incremental concentrations of titanium carbide (TiC) between samples was acquired through the commercial manufacturer, the Greenleaf Corporation. In total, five alumina-based samples were manufactured to contain approximately 5, 10, 15, 25, and 35 percent by volume of titanium carbide. Alumina-TiC composites can commonly be found in use as high speed, high hardness, cutting tools and abrasives. As with the mullite sample series, the TiC series was used to validate the theory put forth in this thesis regarding the effects of thermoelastic absorption in dense, polycrystalline, ceramics.

These samples were hot pressed at slightly varying conditions, shown in table VII, to accommodate the change in powder composition between samples. The exact powder composition and preparation procedure was proprietary to Greenleaf. The resulting, dense, discs were 60mm in diameter and 8.25mm thick. Each sample was surface ground to a hundredth of a millimeter to remove any surface roughness which would affect the acoustic tests. The density of each sample was measured using the Archimedes method where the theoretical densities were calculated after X-ray diffraction was performed to

verify the volume percent of TiC within each sample. The TiC series samples were labeled according to the concentration of the titanium carbide present in each sample (e.g. TiC-5vol% refers to the TiC series alumina-based sample which was created to contain 5 volume percent of TiC). The average size of the titanium carbide grains was expected by the manufacturer to be approximately 1μm. Titanium carbide has a thermal conductivity of 16.7W/m·K, specific heat of 710J/kg·K, and density of 4930kg/m^3 [26]. In a frequency range of 12-30MHz, for titanium carbide to cause thermoelastic absorption, it would have to be approximately 0.5-0.8μm, which was the approximate size range of the TiC grains in the acquired samples.

Table VII. Hot pressing conditions, diameter, thickness, and densities for TiC series.

Sample	Temp. (°C) (held for 30min)	Pressure (MPa) (held for 30min)	Diameter (mm)	Thickness (mm)	Density (g/cm^3)
TiC-5vol%	1750	13.8	60	8.25	4.044
TiC-10vol%	1800	13.8	60	8.25	4.076
TiC-15vol%	1850	13.8	60	8.25	4.120
TiC-25vol%	1850	13.8	60	8.25	4.027
TiC-35vol%	1850	13.8	60	8.25	4.308

4.2.2. Alumina for Scattering Testing

It has been shown that the grains of the primary phase of a material dominate acoustic scattering losses at high frequencies. In high hardness, dense, polycrystalline ceramics, this refers to frequencies above approximately 50MHz where absorption losses are negligible. The phenomenon of scattering attenuation has been well studied in metals where several analytical equations exist for different materials systems. Each theory

shows that attenuation due to scattering is dependent on frequency being raised to a power. It was shown by Portune that most of the various scattering equations already in place are not applicable to dense, polycrystalline, ceramics [20]. These equations only worked for the material system being tested at the time (metals in every case) with empirically determined constants specific for each system [20].

An objective of this thesis was to determine a method of calculating the average grain size of alumina over large sample areas using acoustic spectroscopy. The universally accepted Nicoletti equations which relate scattering attenuation to average grain size, frequency, and constants specific to each material are the most general solutions to this problem. After measuring the acoustic spectra of a material, one is left with the Nicoletti equations being ill-defined; the constants and average grain sizes are not known. The alumina sample sets used in the creation of the method to calculate average grain size of alumina over large sample areas are described in this section. All alumina samples used for this purpose were provided by the commercial manufacturer, Industrie Bitossi. Exact specifications regarding the powder compositions and sintering conditions were proprietary to Bitossi.

4.2.2.1. Microstructural Evolution Alumina Series

Nine lots of alumina samples, containing several samples per lot, were custom made to have varying grain sizes. It was told by the manufacturer that the powders for these samples contained 98% alumina by weight and a 2% mixture by weight of CaO, SiO_2, and MgO. The samples were fired in a stacked position using an electric furnace with a corundum powder bed between samples to prevent them from sticking to one another. Information regarding the exact firing temperatures or holding times was not

accessible, so a labeling scheme for each sample relative to Industrie Bitossi's standard hold temperature and dwell time was created. Table VIII shows how each sample was labeled. The standard maximum firing temperature which Bitossi uses is referred to as T0 and the standard dwell time at T0 is given as D0. The sample lots in this series had their firing temperatures and dwell times systematically, and independently, varied with the goal to promote a controlled degree of alumina grain growth between lots. Any increase in temperature was given in Celsius while increases in dwell time were given in hours. A single sample from each lot was chosen for complete study including acoustic testing and conventional microstructural testing. The sample dimensions and densities (via Archimedes method) for each sample chosen are shown in Table IX.

Table VIII. Labeling scheme for Microstructural Evolution Alumina series. T0 is standard maximum firing temperature, D0 standard dwell time.

	D0	**D0+5**	**D0+15**
T0	(T0,D0)	(T0,D0+5)	(T0,D0+15)
T0+50	(T0+50,D0)	(T0+50,D0+5)	(T0+50,D0+15)
T0+100	(T0+100,D0)	(T0+100,D0+5)	(T0+100,D0+15)

Table IX. Dimensions and densities of selected samples from each lot of the Microstructural Evolution Alumina series.

	(T0,D0)	**(T0,D0+5)**	**(T0,D0+15)**
Dimensions **Lateral (mm x mm)** **Height (mm)**	50.16 x 50.26 10.41	50.08 x 50.05 10.38	50.03 x 50.01 10.46
Density (g/cm^3)	3.89	3.89	3.90
	(T0+50,D0)	**(T0+50,D0+5)**	**(T0+50,D0+15)**
Dimensions **Lateral (mm x mm)** **Height (mm)**	50.08 x 50.03 10.38	50.05 x 50.10 10.42	50.10 x 50.09 10.41
Density (g/cm^3)	3.89	3.89	3.84
	(T0+100,D0)	**(T0+100,D0+5)**	**(T0+100,D0+15)**
Dimensions **Lateral (mm x mm)** **Height (mm)**	50.11 x 50.11 10.46	50.11 x 50.11 10.41	50.11 x 50.11 10.41
Density (g/cm^3)	3.88	3.88	3.85

4.2.2.2. Unknown Grain Size Alumina Series

The purpose of the Microstructural Evolution Alumina series is to empirically obtain the scattering constant prefactors for use with the Nicoletti scattering equations. Once this was done, the constants had to be tested for their validity. These scattering constants were specific to the Microstructural Evolution Alumina series and their composition. Therefore, to test these constants, three arbitrarily chosen alumina samples, manufactured by Bitossi and known to be of the same composition as the previous test samples, were used to ultrasonically predict their average grain sizes. These three samples each had densities of 3.89g/cm^3 with lateral dimensions of approximately 50mm

x 50mm. They were labeled according to differences in their thickness: small (5mm), medium (6mm), and large (11mm).

4.3. Ultrasound Test Procedures

Before any mechanical sectioning and preparations for microscopy could take place, all of the alumina-based samples previously described were tested ultrasonically. The objectives of specific sample series were to test different facets of ultrasonic attenuation mechanisms. The ultrasonic testing performed on these samples followed the established criteria described in the background of this thesis. C-Scans were performed on samples whose surface area was large enough, while samples with smaller lateral areas had singular point measurements performed. This section categorizes the specifics of acoustic testing performed on each sample set.

4.3.1. Ultrasound Testing of Alumina for Absorption

Acoustic testing done on alumina to gain an understanding of thermoelastic absorption was done at relatively low frequencies; using the 20MHz transducer. The frequency bandwidth in the two alumina sample series tested for acoustic absorption is 12-30MHz. When viewing an acoustic attenuation coefficient spectra from one of these samples (shown in Results and Discussion), the peak-like behavior associated with absorption tends to drop off as frequency increases. Therefore, only the use of the 20MHz transducer is necessary as possible coherent absorption attenuation does not occur past approximately 40MHz. Each sample was submerged in the immersion tank, gently brushed to remove air bubbles, and set resting on two 6.4mm glass slides. As mentioned in the Background section, a water-alumina interface, rather than a tank-alumina interface, is necessary to avoid convolution of the bottom surface of the sample

and the tank peaks. Once the 20MHz transducer was moved about the samples, it was lowered to a depth of approximately 7.4mm above the sample. This ensured that the measured bottom surface reflections were in the far field of the acoustic beam. This depth was calculated such that accurate correction for diffractive attenuation could be made.

4.3.1.1. Ultrasound Testing of Mullite Series

The alumina-based mullite sample series exhibited too small of an area to obtain full area C-Scan maps. This sample set had A-Scan point measurements performed on them to obtain all elastic properties as well as attenuation coefficient spectra. The 20MHz ultrasonic transducer was centered about the disc-shaped samples, lowered to the appropriate depth, and had its pitch and yaw maximized such that the acoustic beam was normal to the sample surface. The measured thicknesses and densities were input into Legacy© and four electronic gates were placed around oscilloscope peaks relating to the top surfaces, the first two successive bottom surface reflections, and the hybrid peak of each sample. Elastic properties were calculated by hand using the inflection method highlighted in section 2.4.3.1.1. and using the equations shown in sections 2.4.3.1.2. and 2.4.3.1.3. Acoustic spectra were measured by setting the electronic gates about the top surface and first two successive bottom surface reflections. A signal gain was used such that the bottom surface reflections were not clipped on either end. The attenuation coefficient spectra function in Legacy© was used to view in real time the loss spectra for each sample. A frequency step size of 0.5MHz was used as the discrete interval for each attenuation coefficient spectra graph. These spectra were saved as comma-delimited text files capable of being open with Hermes© or other graphical analysis software.

4.3.1.2. Ultrasound Testing of Titanium Carbide Series

C-Scan measurements of elastic properties, overall signal attenuation coefficient, and attenuation coefficient spectra maps were collected for each sample in the Titanium Carbide Series. The pitch and yaw were manually aligned to maximize the orthogonality of the transducer relative to the sample surfaces. Four electronic gates were used to measure longitudinal and shear time of flights using the inflection method about several thousand points in each sample. These two TOF measurements were transformed by the software to give all of the elastic properties for each sample. A signal gain of 28dB was used to ensure that the hybrid reflection was intense enough to be measured during the automated scans. A step size of 0.5mm was used between the collections of data points giving approximately 11,300 measurements per sample for each C-Scan performed. The elastic moduli from each scan were saved as a comma-delimited text file.

The overall signal attenuation, longitudinal velocity, and attenuation coefficient spectra maps were measured as part of a separate scan as the signal gain had to be reduced to eliminate the effects of signal clipping of the measured bottom surface reflections. Longitudinal velocity is a critical parameter to measure alongside attenuation coefficient as it is necessary for the correction of diffraction. The overall signal attenuation C-Scan maps were used to determine the presence of any large heterogeneity which would be excluded during further testing. The step size of these scans was 0.5mm with a frequency step of 0.5MHz for the attenuation coefficient spectra maps. The four dimensional data array for the attenuation coefficient spectra maps had approximately 400,000 data points per sample.

4.3.2. Ultrasound Testing of Alumina for Scattering

The ultrasound testing performed on the specific alumina sample sets to be used as part of the methodology of nondestructively determining average grain size was performed at much higher frequencies than what was used for absorption testing. This testing relied on two transducers, the 60MHz and 150MHz transducers. The frequency bandwidth observed in the Microstructural Evolution Alumina Series and Unknown Grain Size Alumina Series deviated strongly from what the actual transducer output is, shown in section 4.1.1. The useable bandwidth for these two transducers was 40-70MHz and 80-110MHz, giving a gap of 10MHz between 70 and 80MHz. Based on the measured spectra, shown in the Results section, the common power-law behavior attributed to scattering mechanisms dominates in the measured frequency range. Each sample was submerged in the immersion tank, brushed to remove air bubbles, and rested on two 6.4mm glass slides. The height of the two transducers over each sample was fixed to be approximately 4.6mm using the 60MHz transducer and 3.3mm using the 150MHz transducer. These heights ensured that the successive bottom surface reflections were such that the acoustic beam was in the far field. At these heights there were temporal windows where sample reflections could be placed which would not interfere with the delay line reflections.

4.3.2.1. Ultrasound Testing of Microstructural Evolution Alumina Series

C-Scan measurements of elastic properties and overall signal attenuation coefficient were collected using the lower frequency 20MHz transducer. These maps were performed to determine the presence of large, anomalous defects, as well as property variability. C-Scan measurements of overall signal attenuation and attenuation

coefficient spectra maps could not be performed using the 60MHz or 150MHz transducers. This was due to the massive scattering attenuation caused at these frequencies which caused a drop in signal intensity. Slight surface beveling across each sample had the effect of dropping the signal intensity even further about the edges of the samples. A-Scan point measurements for attenuation coefficient spectra were performed about the center of each sample. The pitch and yaw were manually aligned to introduce the maximum acoustic energy into the samples. A signal gain of 10dB was used with the 60MHz transducer while a gain of 24dB was used with the 150MHz transducer. A step size of 0.5MHz for the frequency interval of the attenuation coefficient spectra was used. The total spectra from each sample on a range of 40-70MHz and 80-110MHz contained 120 data points each.

4.3.2.2. Ultrasound Testing of Unknown Grain Size Alumina Series

The three alumina samples to be used as a test for the alumina scattering constants determined from the prior sample set were all scanned at 20MHz to for overall signal attenuation coefficient and elastic properties using a 0.5mm step size. This was done to evaluate the three alumina samples for large defects or gradients in properties. Full area attenuation coefficient spectra maps using the 60MHz transducer were not possible due to sample beveling (a common problem seen when testing alumina materials). A smaller area about the center of each sample (approximately 7.5mm x 7.5mm) was scanned for attenuation coefficient spectra maps to alleviate the effects of sample beveling. Only the 60MHz transducer with a signal gain of 10dB was able to be used with these three samples as acoustic waves emitted by the 150MHz transducer exhibited extreme attenuation to the point where the second bottom surface reflection was not

distinguishable from the noise. A step size of 0.5mm was used for these selected area scans with a frequency step of 0.5MHz giving 225 data points per sample.

4.4. Transforming Acoustic Attenuation Coefficient Spectra

After acoustic spectroscopy was performed on the various sample sets at different frequencies, the attenuation coefficient spectra were transformed to give relevant microstructural information. There are two methods outlined to transform attenuation coefficient spectra from both the absorption and scattering regimes. The absorption method relies on an analytical equation derived as part of an objective of this thesis. The actual derivation is shown in the Results and Discussion section. The second method, for use with measured scattering spectra, makes use of the Nicoletti equations for Rayleigh and stochastic scattering along with the determined alumina constants for each. The outcome of these transformations on measured ultrasound data is shown in chapter 5.

4.4.1. Absorption Regime

The equation given below (derivation in section 5.1.2.) was derived to give the number of absorbing grains as a function of frequency and frequency dependent attenuation coefficient. All assumptions made for the derivation of this equation are shown the Results section. The procedure for creating grain size distributions of secondary phases within alumina is outlined through several steps.

$$N_G(f) = \frac{3 \cdot E_i(f) \cdot (1 - e^{-\alpha(f) \cdot d})}{2 F_T(f) \cdot a(f)} \qquad \text{Eq. 65}$$

Where the variables are given as $N_G(f)$ being the number of grains in the path of the ultrasound beam, $E_i(f)$ the energy output of the transducer over its bandwidth (Joules), $\alpha(f)$ is the frequency dependent attenuation coefficient (dB/cm), ‘d’ is sample thickness

(cm), $F_T(f)$ is the force output of the transducer, and a(f) is the diameter of the absorbing grain according to the Zener relationship given by equation 30. This ultrasonic grain size equation gives the grain size distribution of grains on a size range dictated by the inversion of the Zener relationship (seen in equation 66). This size range is dependent on the thermal properties and density of the absorbing grains in the path of the ultrasound beam as well as the frequency bandwidth of the transducer used for testing.

$$a = \sqrt{\frac{\pi\chi}{2\rho C_v f}} \qquad \text{Eq. 66}$$

The first step in using equation 65 to ultrasonically predict grain size distributions was to measure the attenuation coefficient spectra in a frequency range where it was expected thermoelastic absorption occurred (Figure 74 (a)). Determination and quantification of the volume percent of the secondary phase was necessary through the use of XRD (Figure 74 (b)). This volume percent was converted to the actual volume (in terms of m^3) of the secondary phase that was present in the path of the ultrasound beam. This was done by multiplying the volume percent of the secondary phase measured via XRD by the sample volume which the ultrasound beam interacts with (calculated by knowing sample thickness and transducer aperture radius). A 100% alumina sample was used as the baseline for attenuation coefficient spectra. Depending on the volume percent of the different secondary phases for each sample set, the measured attenuation coefficients were corrected for the contribution of absorption due to the alumina grains (Figure 74 (c)). The corrected attenuation coefficient spectra for each sample were then used in equation 65 along with the respective thermal properties and densities, depending on which sample set was being interrogated at the time (Figure 74 (d)). The thermal

properties of alumina, mullite, and titanium carbide were taken from online databases and engineering materials reference books. Once a size distribution for the secondary phases were found relative to the frequency bandwidth used, the remainder of the grain size distributions was constructed by performing Gaussian curve fitting. An expected or estimated smallest grain size was set, after which the upper bounds of the grain size distributions were extended until the area under each curve matched the actual volumes of the secondary phases present in each sample (Figure 74 (e)).

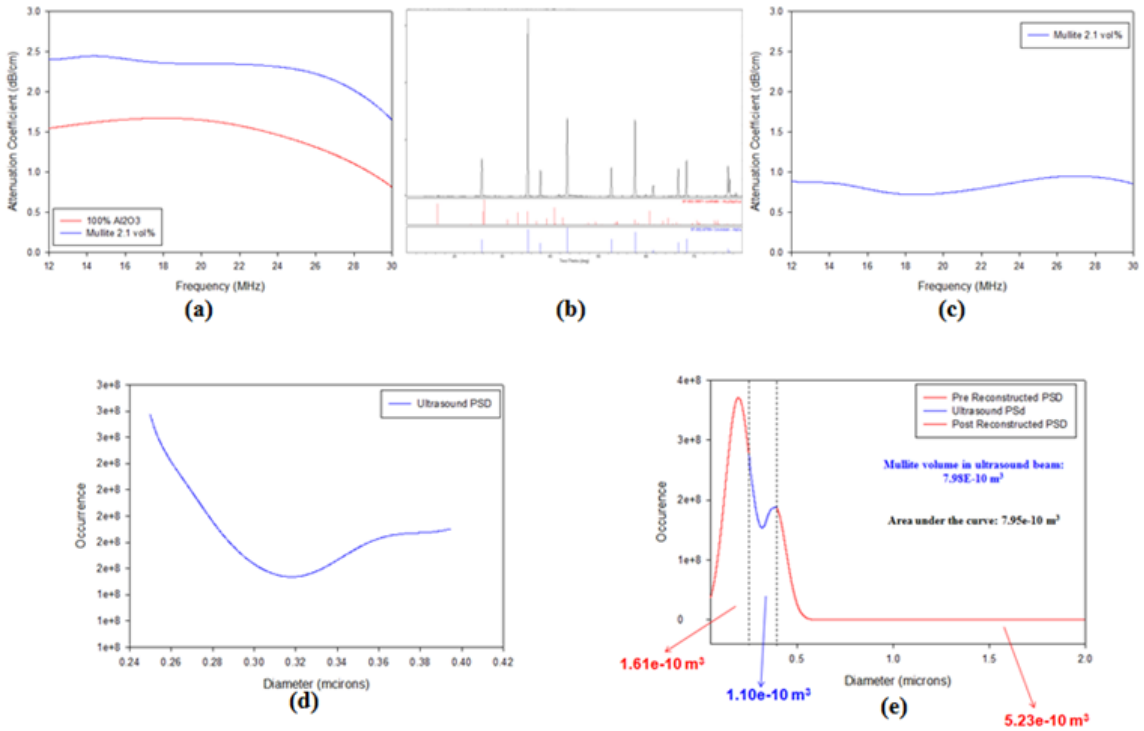

Figure 74. Procedure for obtaining secondary phase size distributions in alumina using acoustic spectroscopy. (a) measure attenuation coefficient spectra of sample of interest and 100% standard alumina; (b) perform XRD to determine secondary phase and volume percent; (c) subtract absorption attenuation contribution caused by alumina; (d) use equation 65 to determine acoustic grain size distribution; (e) curve fit to Gaussian function and force area under the curve to equal actual volume of secondary phase.

4.4.2. Scattering Regime

The theory of ultrasonic scattering in dense polycrystalline materials is better known than that of acoustic absorption. Equations which seek to model acoustic scattering as functions of grain size and frequency exist as the Mie scattering solution, a general power law, power laws specific to the Rayleigh, stochastic, or diffuse scattering regimes, or ad hoc mixtures which attempt to mix the specific power laws to accommodate all three scattering regimes. The Mie scattering solution is the most powerful, but an inverse solution to take attenuation coefficient spectra as an input to obtain grain size as an output does not exist. The mixtures of the power laws specific to the Rayleigh, stochastic, and diffuse scattering regimes were created specifically for cubic metals and do not apply to dense, polycrystalline, alumina.

Transformations of attenuation coefficient spectra which reflect scattering behavior in aluminum oxide were done using the Nicoletti scattering equations. These equations can be seen in section 2.2.5., Table VII. The Nicoletti Rayleigh and stochastic equations were used to transform the scattering attenuation coefficient data from the Microstructural Evolution Alumina series and the Unknown Grain Size Alumina series. Once the scattering prefactors, C_R and C_S, were found, the Rayleigh and stochastic scattering equations were inverted to give a solution for average grain size as a function of frequency based attenuation coefficient spectra. The equations which were used for this are given as:

$$a = \sqrt[3]{\frac{\alpha_R}{C_R f^4}} \qquad \text{Eq. 67}$$

$$a = \frac{\alpha_S}{C_S f^4} \qquad \text{Eq. 68}$$

4.5. Selecting Regions of Interest for Ceramographic Preparation

After all nondestructive testing was performed on the above sample sets, areas from each sample were chosen for the preparation of conventional microstructural testing. The criterion for the selection of sample regions was based on the lateral homogeneity seen in each samples respective C-Scan images. Any peculiar regions of a sample seen in the C-Scan maps were excluded as candidates for sample areas to be sectioned and prepared. These regions were deemed to be peculiar based on the C-Scan images showing noticeable large defects within the sample bulk or having a large elastic property gradient. These features implied that the sample microstructure was not uniform in these regions and were therefore not suitable candidates for what an ideal microstructure would indicate. As the Mullite Series was not large enough to collect C-Scan images, they were sectioned about their centers, where all ultrasound measurements were made. The edges of all other samples were excluded as regions to be studied due to ultrasonic reflections from the sides of each sample which result in incoherent data.

4.6. Sample Preparation for Microstructural Characterization

The conventional microstructural testing techniques used to corroborate ultrasound results with each relied on a methodical and careful step-by-step procedure for sample preparation. The preparation of the four alumina sample series studied in thesis resulted in their destruction which is why all acoustic data had to be measured before revealing the microstructure. This section outlines the exact procedures used for preparing each sample for FESEM, EDS, and XRD analysis.

4.6.1. Mechanical Sectioning Methods

Selected regions of interest from each sample were sectioned using a variable speed LECO Vari/ Cut VC50 cutoff saw. With the exception of the Unknown Grain Size Alumina Series, each sample was sectioned vertically to reveal the volumetric cross sectional area which the acoustic wave has travelled through. It was necessary to reveal the sample surfaces which relate to height dimension of each sample as the acoustic tests were volumetric. The Unknown Grain Size Alumina Series were sectioned such that inside center horizontal surfaces were revealed. This was done to obtain lateral microstructural information about a single surface which the ultrasonic wave passed through. Each sectioned sample region was approximately 0.5-1cm in the length and width dimensions and approximately 0.5cm in the height dimension.

4.6.2. Preparation for FESEM and EDS

Each sectioned region underwent a series of steps necessary for obtaining surfaces suitable for imaging in the FESEM. Each section was mounted in a thermoset polymer resin using a Beuhler automated mounting press. A grinding and polishing process using a Beuhler autopolisher was used for each section mounted in the thermoset polymer. The polishing procedure was performed using diamond abrasive pads where the diamond grit size was reduced between steps. The sizes of the diamond abrasives are as follows: a 45µm, 15µm, 9µm, 6µm, 1µm, 0.25µm. Table X shows the specifics regarding each polishing step used for all samples. Each pad was cleaned with water between uses to avoid cross contamination. Between polishing steps each sample was rinsed in their epoxy mounts and evaluated using an optical microscope to ensure that scratches from the previous steps were completely removed. After the polishing procedure was finished,

each section was removed from their epoxy mounts and ultrasonicated separately in baths of isopropanol, a 10% solution of hydrogen peroxide, and distilled deionized water. This cleaning procedure removed oils and other hydrocarbons from the final polished surfaces. Each sample series then underwent different etching procedures to reveal their fine microstructures. The various etching procedures used depending on the sample series is outlined in section 4.6.2.1. The final prepared samples were mounted on aluminum SEM studs using double-sided carbon tape and placed in a vacuum dessicator for at least 24 hours prior to FESEM imaging.

Table X. Polishing procedure used for the preparation of all alumina samples studied in this thesis.

	Pad Type	**Pressure (lbs/sample)**	**Time (minutes)**	**RPM**	**Direction**	**Fluid**
45µm	Diamond Embedded	5	Until Flat	250	Contra	Water
15µm	Diamond Embedded	5	10	220	Contra	Water
9µm	Nylon - Diamond Suspension	6	10	180	Contra	Oil
6µm	Nylon - Diamond Suspension	6	20	180	Contra	Oil
1µm	Felt - Diamond Suspension	7	5	150	Comp.	Oil
0.25µm	Felt - Diamond Suspension	7	5	150	Comp.	Oil

4.6.3. Etching Procedures

Etching implies some sort of selective corrosion for the visual enhancement of micrograph images. Each sample series studied in this thesis had some form of etching performed on them to reveal their microstructures and the phases of interest. A common etching procedure for alumina is thermal etching. This is where a polished section is put into a furnace and brought to approximately 50°C below its sintering temperature. This has the effect of selectively removing the lower temperature grain boundary phases. Thermal etching of the alumina-based samples used in this thesis was not an option. Thermally etching alumina may run the risk of growing the grains if it is performed at too high a temperature and for too long. Three different etching methods were used for the four sample series in this thesis; two which rely on chemical etching and one which relied on plasma etching.

Following the order of the sample designation listed above, the etching procedures used for each sample series are further described. The Mullite Series was etched using a dilute solution of hydrofluoric acid (HF) and water. A 50% HF solution was further diluted to 10% by carefully adding it to a large amount of distilled, deionized, water. A more dilute HF solution was necessary to better control the time each of the Mullite Series sample sections were etched for. Each sample section was placed in individual, shallow, plastic cups where a plastic pipette was used to place several drops of the HF solution on each polished surface. The HF solution was allowed to chemically attack the grainboundaries between the mullite and alumina grains for 60 seconds. To stop the reaction and neutralize the HF acid, each sample was doused with sodium

bicarbonate powder. Hydrofluoric acid was used for etching the Mullite Series samples as it preferentially attacks glassy phases, which formed the mullite grain boundaries.

The Titanium Carbide Series had to be etched using a plasma etching method. Typical chemical etching procedures for alumina-based materials involve removing glassy grain boundaries. The purpose of preparing the Titanium Carbide Series for FESEM analysis was to gain an understanding of the titanium carbide grain sizes present in the alumina matrix. To do this, an etching procedure for TiC had to be used and it was suggested by the manufacturer to use a plasma etching technique. Sample sections from this series was placed on an alumina dish and put under vacuum in an SPI Plasma Prep II plasma etching unit. Carbon tetrafluoride (CF_4) gas was used as the etching plasma which preferentially attacks carbide-based materials. For TiC etching, the fluorine species in the plasma absorbed onto the sample surfaces, reacted with the titanium carbide, and created volatile titanium fluoride. The volatile TiF, and residual CF_4 was removed through the attached vacuum. This left each sample with etched TiC grains within an unetched alumina host matrix.

The Microstructural Evolution Alumina Series and Unknown Grain Size Alumina Series were both chemically etched using boiling phosphoric acid (H_3PO_4). As with plasma HF etching this chemical etching procedure ensures that no grain growth can occur. An 80% solution of H_3PO_4 was placed in a glass beaker and brought to a rolling boil using a hot plate. Once a boil was achieved, each sample was separately placed in the acid and kept there for varying amounts of time depending on how long the phosphoric acid was allowed to boil and how many samples were being etched. The first sample to be etched was placed in the acid for approximately 2 minutes and checked

using an optical microscope at 500x magnification to determine the degree of etching. As the acid was allowed to boil for several minutes, it became more concentrated (the water evaporated). As this occurred, each subsequent sample was etched in 15 second intervals to ensure that over-etching did not occur. For the nine sections which came from the Microstructural Evolution Alumina Series, by the time the last section was to be etched only an etching time of 15 seconds was necessary to achieve a well defined microstructure. As with HF etching, boiling phosphoric acid preferentially removed the glassy grain boundary between alumina grains.

4.6.4. Preparation for XRD

Sample preparation for X-ray diffraction was somewhat less involved than that for FESEM preparation. After FESEM imaging was performed on all of the alumina-based samples used in this thesis, those sections were used for XRD analysis. Each sample was affixed to a shallow aluminum sample holder using a small amount of adhesive Blu-Tack. Preparation of samples for XRD required that the sample surface which the X-rays impinge be even with the X-ray line of axis to ensure that peak shifting did not occur. Each sample section which was placed into the aluminum holder is pressed into the Blu-Tack such that it was flush with the top face of the holder itself.

4.7. FESEM Characterization and Micrograph Analysis

Electron microscopy was performed using a Zeiss Sigma Field Emission Scanning Electron Microscope. Each alumina-based sample from each series had four micrograph images taken at various magnifications depending on the grain sizes. It was desirable to obtain FESEM images which contained at between 50-100 grains per image. Image magnification ranged from 3000x to over 100,000x magnifications. All samples

were left uncoated to ensure that any small-grained features would not be obscured. The Mullite Series sample images were taken using the in-lens detector while the Titanium Carbide Series sample images with the secondary electron detector. Both the Microstructural Evolution Alumina Series and Unknown Grain Size Alumina series sample images were taken using the secondary electron detector. As these samples were left uncoated, a very low accelerating voltage of 2kV-5kV was used to approach these alumina-based materials zero point of charge.

Determination of the mullite phase and titanium carbide phase in the Mullite and Titanium Carbide Series was done using an Oxford Inca PentaFetx3 energy dispersive spectroscopy system in conjunction with the FESEM described above. EDS was performed using a 10kV accelerating voltage to obtain a 0-10keV spectrum range with 2000 channels. At these voltages, surface charging built quickly which resulted in significant beam drift. Due to this, elemental mapping using the EDS system was not feasible. Single point spectra were taken from regions which appeared to be alumina, mullite, or TiC grains to verify their presence in each of the samples.

Image analyses and measurement of grain size distributions were done using the image analysis software, Lince. Lince is a software package which performs the semiautomatic linear intercept method of measuring grain sizes according to Heyn's model and ASTM E-1382 [233, 234]. Approximately 80 grains per micrograph image for each sample section were measured using the linear intercept method. This provided between 300-400 grain size measurements for each sample studied in this thesis which were used to created grain size distributions and calculate statistical information such as grain size averages, standard deviations, and range.

A stereographic correction was applied to each grain size measurement to account for the inherent error introduced when sectioning through a randomly distributed microstructure. For example, if one assumes a material is comprised of a random distribution of spherical grains, upon section, polishing and measuring such grains, one would find that the measured grain size is underestimated by 1.5 times. This is due to the fact that sectioning and polishing is not likely to reveal the greater diameter of each sphere. An illustration of this can be seen in Figure 75. The alumina, mullite, and titanium carbide grains all vary from being spherical by some degree, so an underestimate of 1.5 times for each measured grains gave an upper bound of what the measured deviation from the true grain size. Each measured grain size was corrected for stereographic effects by a multiplication of 1.5.

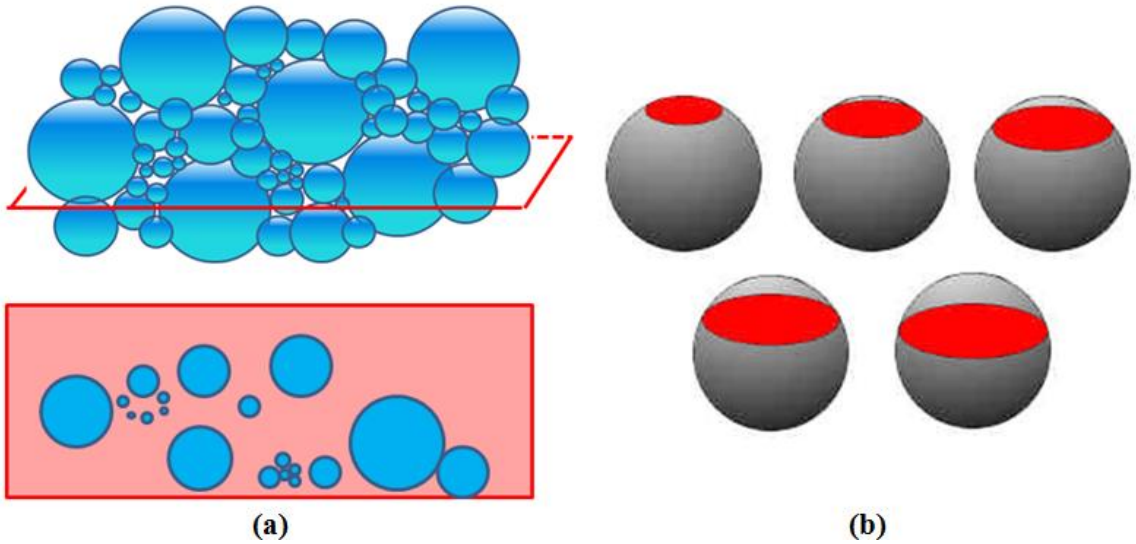

Figure 75. (a) Cross section through random distribution of spherical grains. (b) Illustration of different cross sectional areas obtained for same size sphere [114].

4.8. XRD Characterization

X-ray diffraction was performed on the Mullite Series and Titanium Carbide Series alumina-based samples to verify the presence of each of these secondary phases

and quantify the volume percent present within each sample. XRD characterization made use of a Philips XPert Panalytical XRD unit. The acquisition settings were kept constant for all samples having this characterization performed. The scan range was 10-80 degrees with a step size of 0.03 degrees and a dwell time of 2 seconds per step. These scans took approximately 1 hour and 17 minutes to complete, giving an average intensity of 12,000 counts with a background of approximately 1000. The XRD analysis software used to analyze each spectrum was MDI Jade version 9.2.0. using the inorganic crystal structure database (ICSD) acquired through FIZ Karlsruhe, the Leibniz Institute for Information Infrastructure.

Each collected spectra was saved as a .xrdml file which was then read into the Jade software. A background subtraction was used along with a Golay-Savitz filter to smooth any high frequency noise. Each spectral peak was identified using a search-match function according to expected elemental compositions of each secondary phase of interest. The volume percentage of the secondary phases contained within each sample was determined using the Jade Easy Quant function for the Reference Intensity Ratio method outlined in the cited reference [235].

5. Results and Discussion

The goal of this thesis was to apply acoustic spectroscopy to dense aluminum oxide to predict average grain size of the alumina as well as determine grain size distributions of secondary phases. This section furnishes the results of the testing described in the Experimental Method section. Derivations of equations regarding thermoelastic energy loss and the number of grains causing such a loss are given first. This includes obtaining frequency-based standards used in each equation, discussing the specifics of various assumptions. Following this, results regarding each of the four alumina-based sample series studied in this thesis will be presented. Information of ultrasonic nondestructive testing along with conventional destructive FESEM and XRD testing are shown for each sample series. This includes FESEM image analysis of measured grain size distributions and XRD obtained volume percentages of secondary phases contained within two of the four sample sets. An analysis of the acoustic spectroscopy results attempts to create a causal relationship between measured frequency-based attenuation coefficients with measured microstructural features. This is done for each of the two acoustic loss regimes; absorption and scattering. A discussion of potential sources of error is given.

5.1. Development of Analytical Equations

A currently established method of analyzing acoustic attenuation coefficient spectra from an absorption-dominated frequency regime is to perform a nonlinear least squares regression on multiple three-parameter Lorentzian functions. As stated in section 2.3.4., it was believed that minimizing the three parameters of how ever many Lorentzian functions it took to constructively combine into an attenuation coefficient spectra would

give information relating to specific microstructural features. This amounts to having an infinite number of solutions (as there are an infinite number of ways to combine an unlimited number of Lorentzian functions to create a single curve) where only several of these solutions may hold true information regarding the microstructure. A minimization of three parameters for as many Lorentzian distributions a computer algorithm requires for every point in a tile of aluminum oxide takes a staggering amount of time. The development of equations which do not require a least squares regression can have the effect of significantly decreasing this time. The results presented in this section describe the derivations for that of thermoelastic-energy-loss and attenuation coefficient based grain size distribution.

5.1.1. Derivation of Thermoelastic Energy Loss Equation

According to the theory put forth by Zener and Bhatia on intraparticle thermoelastic absorption (section 2.2.6.4.2.), the ability for a grain or solid inclusion to cause this type of absorption is directly dependent on its size compared to the interrogating wavelength. The discussion on thermoelastic absorption in the Background section regarded grain size being constant and the conditions of adiabatic or isothermal equilibration at small or large wavelengths compared to grain size. Considering the converse of this, when the frequency is fixed and grain size is allowed to vary, the same argument for the conditions of intraparticle thermoelastic energy loss apply. Inferred from this is the statement, *If the grains are of a size which would cause intraparticle thermoelastic energy loss in the measured frequency range, larger grains will cause a greater loss at lower frequencies compared to smaller grains at higher frequencies*. An important factor which also arises is the energy output profile of a transducer; the

available acoustic energy to be absorbed across a frequency bandwidth (and grain size distribution) is not constant. For example, the 20MHz transducer is peak-like about approximately 20MHz, where the energy decreases from this maximum as frequency is decreased or increased. This means that there is considerably less energy available for the smaller and larger grains to absorb compared to grains somewhere in between.

The basis of this derivation attempts to account for these facets:

$$E_{\alpha TE}(f) = V_{TE}(f) \cdot N_G(f) \cdot S(f) \qquad \text{Eq. 69}$$

where $E_{\alpha TE}$ is the energy absorbed due to intraparticle thermoelastic absorption having units of joules, V_{TE} is the spherical volume of a grain according to the diameter term given by Zener (equation 30), N_G is the number of grains capable of absorbing at a given frequency, and 'S' is a frequency-dependent factor to account for the nonuniform output of the transducer. The 'S' factor will be specific to the ultrasonic transducer used for testing and must have units of pascals for dimensionality agreement.

$$V_{TE}(f) = \frac{\pi \cdot a(f)^3}{6} = \frac{\pi}{6}\left(\frac{\pi\chi}{2\rho C_v f}\right)^{\frac{3}{2}} \qquad \text{Eq. 70}$$

The determination of the 'S' parameter for the 20MHz transducer used in this thesis is necessary to continue with the derivation of creating an equation which relates intraparticle thermoelastic absorption to attenuation coefficient.

The following derivation gives a method of obtaining the 'S' parameter as a function of measured attenuation coefficient, spherical volume of an absorbing grain, and energy output of the transducer each of which are dependent on frequency.

$$E_M(f) = E_i(f) - E_{\alpha TE}(f) \qquad \text{Eq. 71}$$

Where E_M is the energy returned to the transducer after the energy lost due to intraparticle thermoelastic absorption is subtracted from the initial energy, E_i, output from the transducer. The energy returned to the transducer can also be given by the Beer-Lambert law, as shown below.

$$E_M(f) = E_i(f) \cdot e^{-\alpha(f) \cdot d} \quad \text{Eq. 72}$$

where α is the measured attenuation coefficient according to the method described in section 2.4.3.2.6. and 'd' is sample thickness. A combination and algebraic rearrangement of equations 71 and 72 give:

$$E_{\alpha TE}(f) = E_i(f) \cdot (1 - e^{-\alpha(f) \cdot d}) \quad \text{Eq. 73}$$

Substitution of equation 69 into equation 73 results in the equation:

$$V_{TE}(f) \cdot N_G(f) \cdot S(f) = E_i(f) \cdot (1 - e^{-\alpha(f) \cdot d}) \quad \text{Eq. 74}$$

Algebraic rearrangement gives a final equation for the 'S' parameter.

$$S(f) = \frac{E_i(f) \cdot (1 - e^{-\alpha(f) \cdot x})}{V_{TE}(f) \cdot N_G(f)} \quad \text{Eq.75}$$

To obtain the 'S' parameter as a standard, functional data set according to the frequency output of the 20MHz transducer used, the E_i and N_P parameters must be known first. Determination of the N_P parameter was taken from a standard 100% alumina sample and is described below. The V_{TE} parameter can be calculated and the attenuation coefficient is measured.

To obtain the E_i parameter, a Fourier transform of the top surface reflection off of a polished silicon carbide mirror (considered to be a perfect reflector) was taken. This

gave the power spectral density over all frequencies emitted by the transducer. The measurement of power spectral density using the Legacy© software gives it in terms of counts relating to the discrete intensity of the oscilloscope peaks. The E_i factor must take the form of a power spectral density in terms of Joules. This was done by normalizing the area under the curve of the measured PSD to the known overall energy output of the transducer supplied by the pulser-receiver. The overall energy output was given as 12.4µJ. The energy output profile of the 20MHz transducer, given in Joules, can be seen in Figure 76.

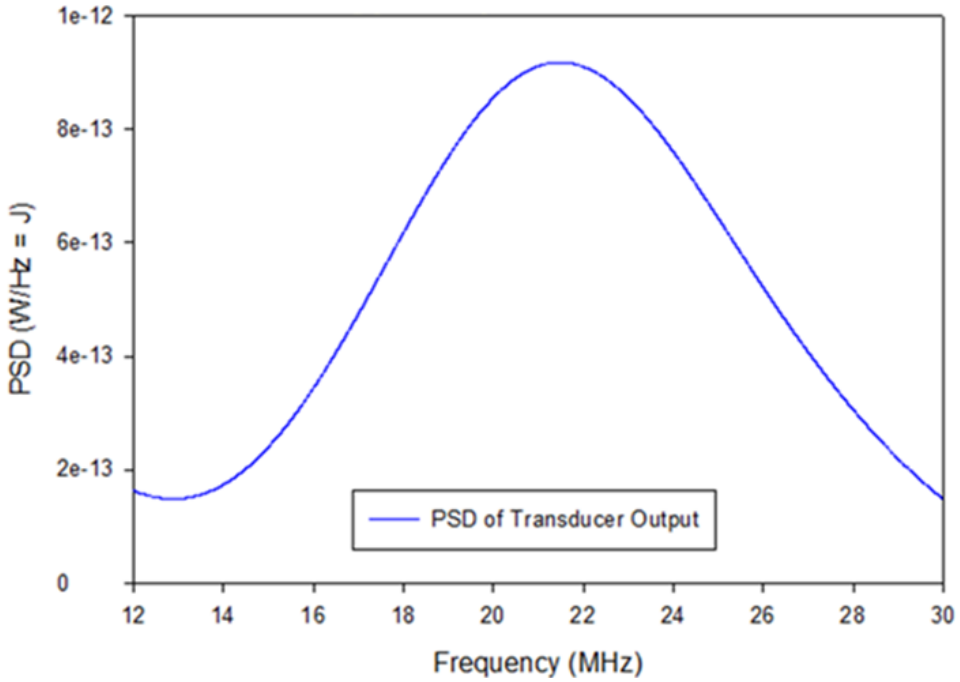

Figure 76. Energy output of 20MHz transducer measured off SiC mirror surface. AUC normalized to known overall energy output.

The standard 100% alumina sample described in Experimental Method was used to ascertain an approximate number of grains which would cause intraparticle absorption at frequencies corresponding to sizes according to the Zener relationship in equation 30. This involved measuring an attenuation coefficient spectrum about the center of the

alumina sample, as seen in Figure 77, and then sectioning about that point to obtain micrograph images (Figure 78) and measure a grain size distribution. The measurement of the grain size distribution only gave the number of grains which were counted from the micrograph images (Figure 79).

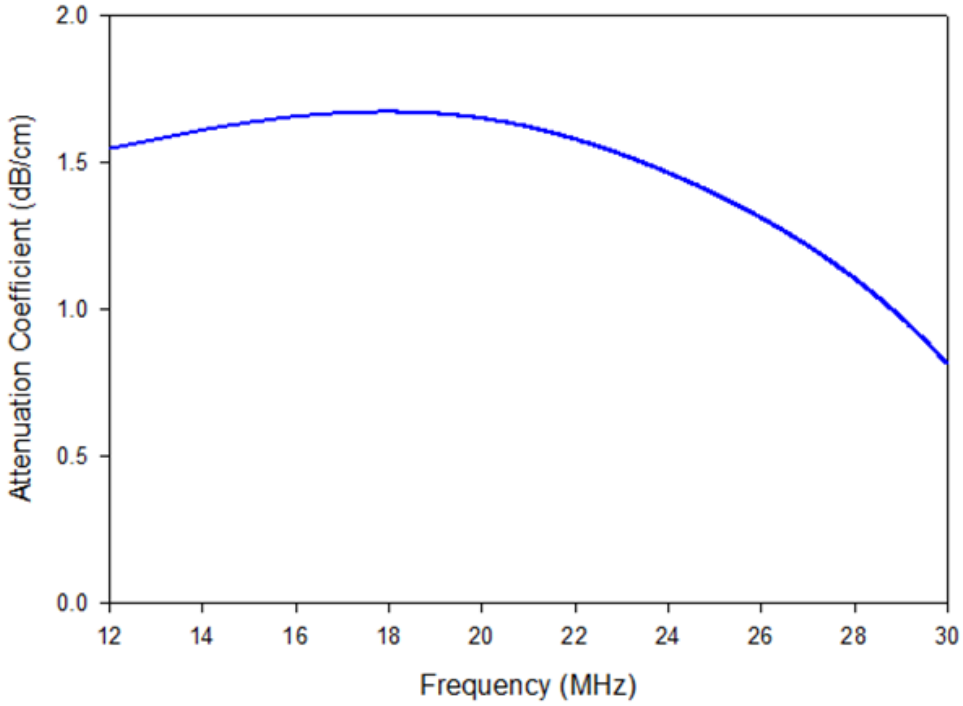

Figure 77. Measured attenuation coefficient spectrum of 100% Al_2O_3 standard sample.

An accurate description of the 'S' parameter relies on N_P being the actual number of grains encountered by the ultrasonic beam as it passed through the sample. To obtain this, the measured grain size distribution about the point where the attenuation coefficient spectrum was measured; was curve fitted to a Weibull distribution, and its area under the curve was normalized to the total volume of the interrogating ultrasonic beam. The volume of acoustic beam was calculated to be approximately 4.53×10^{-8} m^3 having a radius of 1.55mm and a height of 6mm through the sample. Figure 80 shows the normalized curve fit grain size distribution for the 100% alumina standard sample. Only

the portion of the grain size distribution which matches alumina grain size to frequency through the Zener relationship (equation 30) can be used for N_P. The alumina grain sizes which correspond to a frequency range of 12-30MHz are necessary. Values for χ, C_v, and ρ of 40W/m·K, 930J/kg·K, and 3970kg/m^3, respectively, were used as inputs into equation 30 to determine the appropriate size range from the grain size distribution to be used for N_P. In a frequency range of 12-32MHz, alumina grains of approximately 0.75-1.2μm will cause intraparticle thermoelastic absorption.

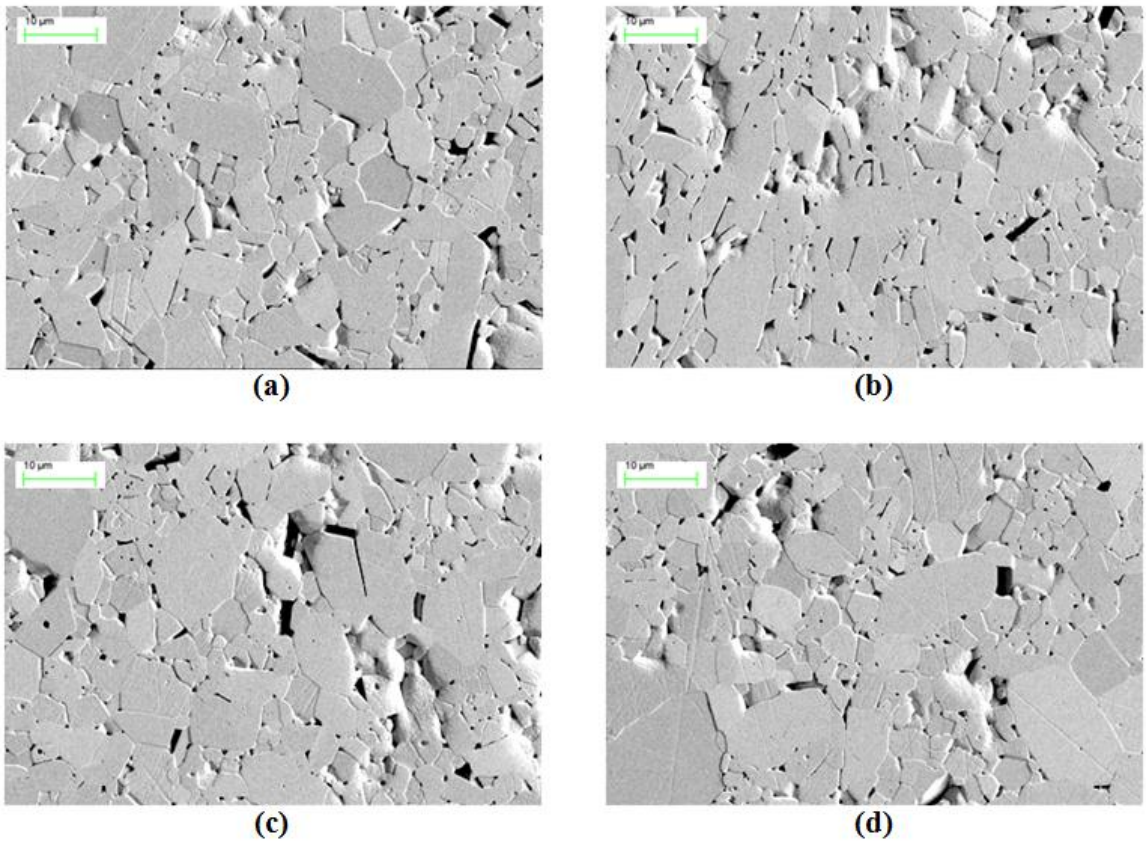

Figure 78. (a)-(d) Micrograph images used to create grain size distribution for 100% Al_2O_3 standard sample.

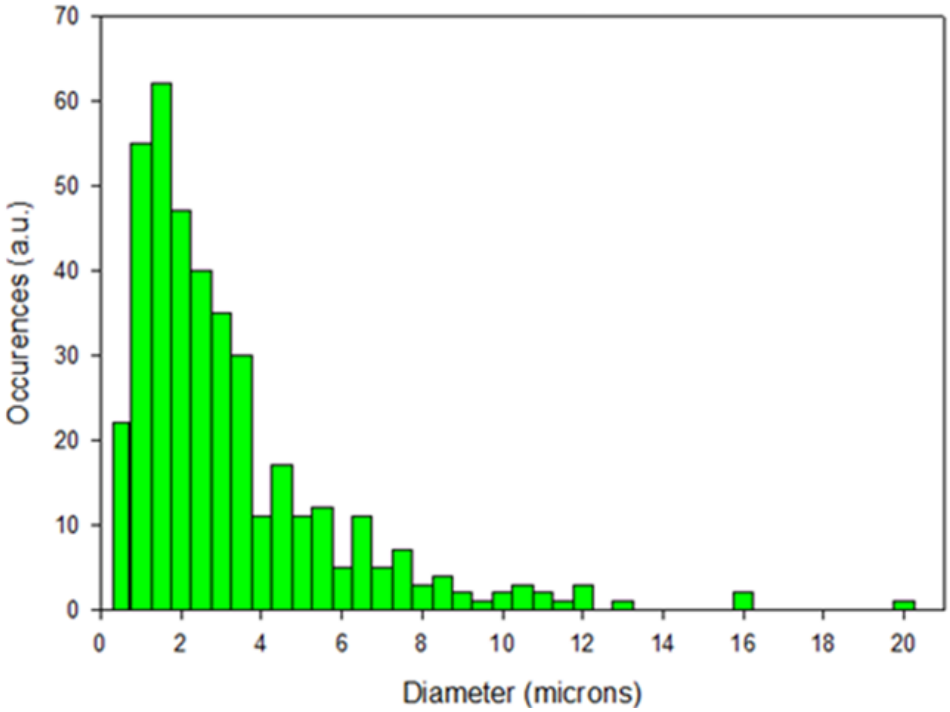

Figure 79. Histogram of measured grain size distribution for 100% Al_2O_3 standard sample.

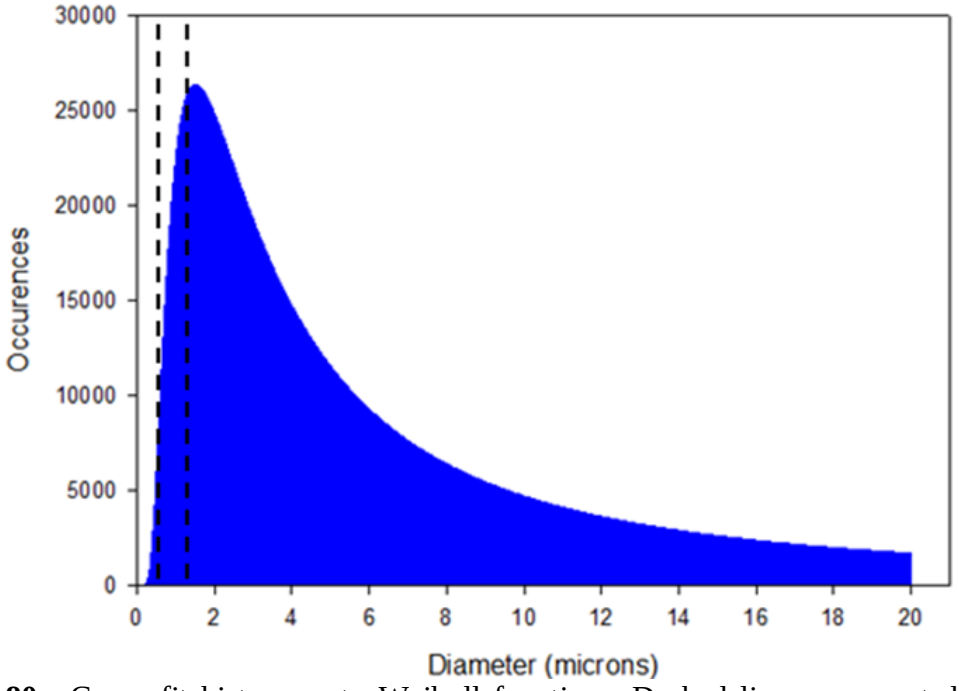

Figure 80. Curve fit histogram to Weibull function. Dashed lines represent diameter range of alumina grains to actively cause absorption in 12-30MHz range.

Inputting the E_i, N_P, α, factors along with calculated values for V_{TE} a standard data set for the 'S' parameter is found. As stated above, the 'S' parameter has units of Pascals and is related to pressure. In the form shown in Figure 81, the 'S' parameter is still dependent on the both the transducer output as well as the grain volumes of the standard alumina material which went into its derivation.

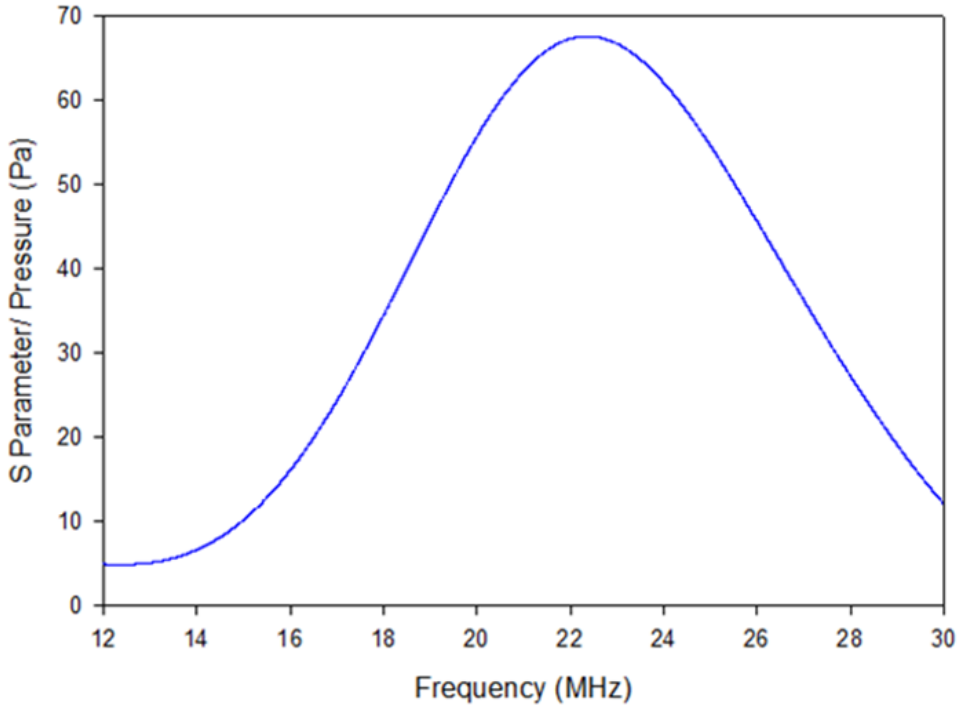

Figure 81. Graphical form of 'S' parameter data set as a function of frequency.

Ideally, any constant factor used as part of the whole equation should not be a function of any single material sample. The 'S' parameter, being a pressure, is deconstructed to give the force exerted by the acoustic wave at a given frequency on a grain of a size corresponding to such a frequency. This can be seen in equation 76.

$$S(f) = \frac{4F_T(f)}{\pi a(f)^2} \qquad \text{Eq. 76}$$

Where F_T is the frequency-based force output of the transducer. A graphical illustration of the F_T data set can be seen in Figure 82.

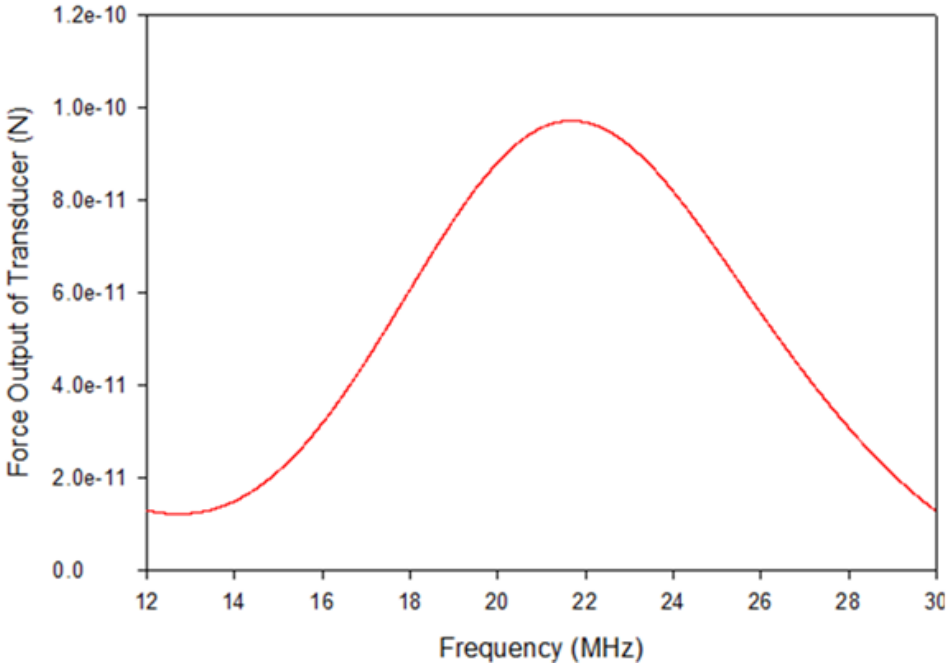

Figure 82. Graphical form of F_T data set as a function of frequency. Units are in Newton's.

Combining equation 76 with equation 69 gives an analytical form for the amount of energy absorbed due to intraparticle thermoelastic absorption. This final equation is a function of the force output of the transducer, the diameter of the grains actively causing absorption as well as the number of grains present.

$$E_{\alpha TE}(f) = \frac{2}{3} \cdot F_T(f) \cdot a(f) \cdot N_G(f) \qquad \text{Eq.77}$$

5.1.2. Derivation of Grain Size Distribution Equation

Now that a term which relates the amount of acoustic energy lost due to intraparticle thermoelastic absorption in terms of size and number of grains has been found, a simple algebraic transformation gives an equation for grain size distribution. This equation is dependent on two constant data sets relating to the transducer used,

calculatable diameter according to equation 30, and a measured attenuation coefficient. Combining equations 73 and 77 produce the analytical equation used to provide an ultrasonic grain size distribution of secondary phases within dense aluminum oxide. The exact procedure for using this equation, shown again below, is outlined in section 4.4.1.

$$N_G(f) = \frac{3 \cdot E_i(f) \cdot (1 - e^{-\alpha(f) \cdot d})}{2 F_T(f) \cdot a(f)} \qquad \text{Eq. 78}$$

5.1.3. Derivation Assumptions

The derivation of equations 77 and 78 required assumptions to simplify the complex nature of the system. The effect of these assumptions as a source of error is discussed in section 5.6.3. The first assumption which is made regards the width of the absorption profile of a single grain. A single grain causes absorption across multiple frequencies according to a Lorentzian distribution. Defining Lorentzian-based absorption profiles for materials with a wide range of grain sizes requires the use of a lengthy least-squares regression analysis where its disadvantages of being ill-defined and time consuming were discussed earlier. The assumption that each grain of a specific size only absorbs at a singular frequency provides a basis for not needing a regression analysis over all frequencies. The full width at half maximum (FWHM) of a Lorentzian distribution is defined as 2γ. This first assumption requires that the FWHM of the Lorentzian absorption profile of a single grain collapses to either a Delta function or to the point where 2γ is less than the frequency resolution of the attenuation coefficient spectrum (Figure 83). The case of the latter is more easily argued as the frequency resolution can be altered to provide this scenario. A physical interpretation of this assumption posits that intraparticle thermoelastic absorption occurs instantaneously in dense aluminum

oxide containing rigidly bound secondary phase grains. This assumption is the leading factor which allows for a deviation of the time consuming least squares regression analysis.

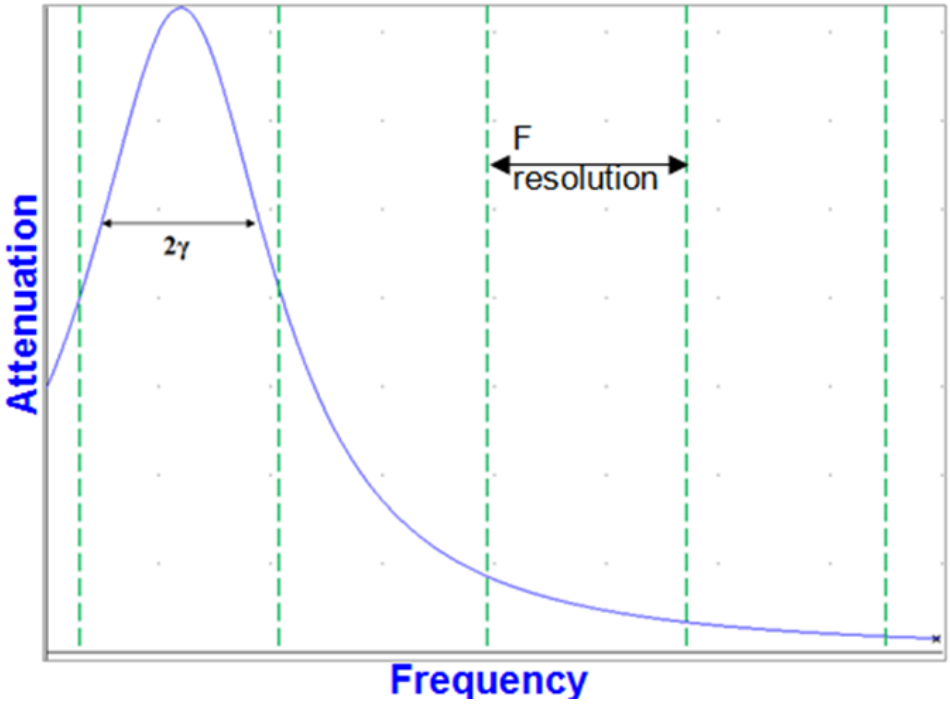

Figure 83. Illustration of Lorentzian absorption profile of single grain having FWHM less than frequency resolution.

The following assumptions were made out of necessity to account for extraneous sources of attenuation, grain morphology, and acoustic beam interaction. It already known that scattering attenuation dominates attenuation coefficient loss spectra at high frequencies, regardless if absorption components exist at such frequencies. The assumption that scattering losses for the Mullite and Titanium Carbide Series is negligible in the frequency range of 12-30MHz was made to avoid the deconvolution of an unknown degree of scattering with what is believed to be an overwhelming amount of absorption. Along with this assumption is that intraparticle thermoelastic absorption is the only absorption mechanism occurring in the frequency range of 12-30MHz and that

its effects are negligible at higher frequencies. Relating to assumptions based on acoustic loss mechanisms, a final assumption is that only grains which fall in the size range according to the frequencies used and equation 30 are actively causing absorption and any increase in absorption is due to an increase in the concentration of grains of this size.

Assumptions relating to the geometry of the system have already been stated throughout the derivation of equations 77 and 78. Namely that the ultrasound beam interacts with a finite volume of material approximated as a cylinder and the morphology of the grains are considered to be spherical. The deviation from a cylinder-like beam volume can be calculated through the use of equation 63. At 12MHz the largest deviation from the central axis of the acoustic beam is approximately 17°. Using trigonometry it can be shown that the acoustic wave will have to travel further than the thickness of the sample to cause a significant difference in what can be considered to be a cylinder of ultrasound energy. As frequency increases, the acoustic wave must travel an even greater distance to refract to the point where the interaction volume cannot be considered a cylinder.

Justification for considering grain shapes to be spherical lies in the method used to create measured grain size distributions and the theory of intraparticle thermoelastic absorption. Using Heyn's lineal intercept method for measuring grain sizes assumes that any line drawn through a grain gives a measurement of the diameter of a circle or sphere. Intraparticle thermoelastic absorption occurs due to a bending of the grains about their largest dimension perpendicular to the acoustic wave. Essentially, the theory of intraparticle thermoelastic absorption also provides information on grains as if they were

spheres. Both the measured grain sizes and acoustic predicted grains sizes are using the same assumption that the grains are spherical.

5.2. Characterization of Mullite Series

The characterization results with respect to ultrasound testing, FESEM imaging, EDS analysis, micrograph analysis, and XRD testing for the Mullite Series sample set are shown in this section. A discussion on the set of results is given to highlight specific trends or irregularities. Analysis of acoustic spectra are given in this section while the linkage of measured acoustic spectra, theory of intraparticle thermoelastic absorption, use of derived equations for predicting grain size, and comparison to measured grain sizes is given in section 5.6.1.1.

5.2.1. Mullite Series Ultrasound Testing Results

As the Mullite Series samples only had diameters of 20mm, full C-Scan testing could not be performed. A-Scan point measurements were taken about their centers to give singular values of longitudinal velocity, shear velocity, Poisson ratio, Young's modulus, shear modulus, and bulk modulus. Attenuation coefficient spectra were also recorded about their center points. A table containing the point measurements of sonic velocities and elastic moduli for the Mullite Series samples along with the 100% standard Al_2O_3 sample, for comparison, is given below. The labeling of these samples is changed from what was used in Experimental Procedure to reflect the volume percent of mullite present in each sample calculated via XRD analyses. The XRD analysis is shown in section 5.2.3.

Table XI. A-Scan point measurements of elastic properties for Mullite Series samples.

Sample	CL (m/s)	CS (m/s)	ν	E (GPa)	G (GPa)	K (GPa)
100% Al2O3	10576	6229	0.234	378	153	237
Mullite 2.1vol%	10524	6197	0.242	374	151	242
Mullite 5.6vol%	10414	6040	0.247	349	140	230
Mullite 16.3vol%	10310	6056	0.237	347	140	220
Mullite 20.6vol%	10212	6028	0.233	338	137	210
Mullite 26.9vol%	9908	5945	0.219	324	133	192

With the exception of shear velocity and Poisson ratio, each property measured through ultrasonic means show a one-to-one correspondence with the concentration of mullite present in each alumina-based sample. Aluminum oxide has higher theoretical sonic velocities and elastic moduli compared to mullite, which is reflected in the measurements shown in table XI; as mullite concentration increases in these alumina-based samples, mostly all properties decrease in a linear fashion. It appears that a linear rule of mixtures for each property does not result in the exact volume percent of each phase. This may be due to poor mixing where mullite tended to agglomerate nonuniformly throughout the samples, the inherent error associated with each test (ultrasound and XRD) is causing the slight deviation, or a linear rule of mixtures does not apply to this specific material system. The expected correlation does exist providing a sample set which is well defined.

The measured attenuation coefficient spectra about the center of each sample show a one-to-one correspondence with the concentration of mullite present in each sample. This is reflected as the general increase in attenuation coefficient from sample to sample. The increase in attenuation from the 100% alumina standard sample, not containing any mullite, is expected to be solely caused by the increase in volume percent

of the mullite phase per sample. The non uniform increase across the frequency range of 12-30MHz implies that the size distribution of the mullite grains varies among samples. These spectra are later corrected for the contribution of intraparticle thermoelastic absorptive attenuation from the alumina grains and used to create ultrasound predicted grain size distributions of the mullite phase present in each (shown in section 5.6.1.1.)

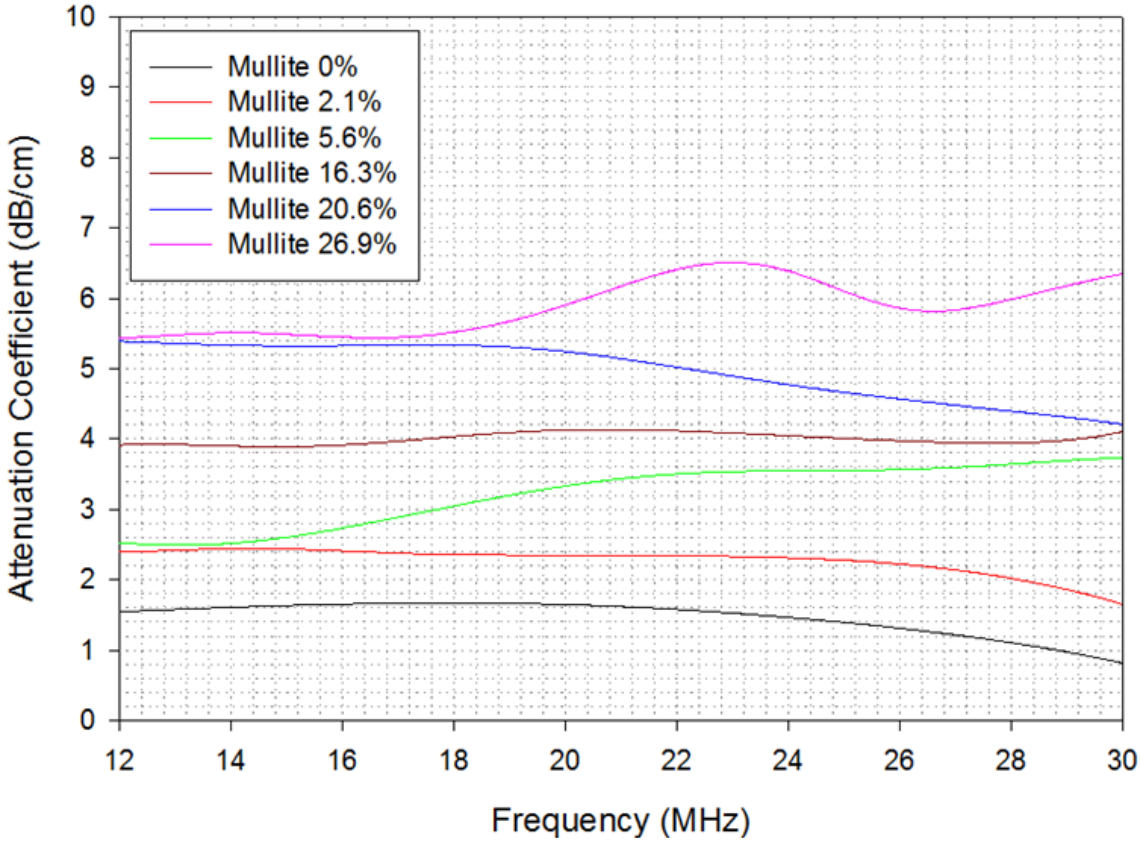

Figure 84. Measured attenuation coefficient spectra about the centers of each sample in the Mullite Series. 20MHz Olympus transducer used with a frequency bandwidth of 12-30MHz.

5.2.2. Mullite Series FESEM Results

Multiple efforts were given to properly etch the grain boundaries between the mullite-phase grains in each sample to reveal the fine grained mullite microstructure. Figure 85 shows representative micrograph images taken from the Mullite 26.9vol%

sample. These micrographs show the mullite phase being uniformly mixed and demonstrate an interconnected pattern. The other samples in the Mullite Series show similar behavior. As magnification is increased from the micrographs seen in Figure 85 to the micrographs in Figure 87 it becomes clear that the interconnected-like pattern of the mullite phase within the alumina is in fact composed of separate smaller mullite grains. EDS spectra revealed the presence of silicon in the darker regions shown in the micrographs of Figure 86. These darker regions are taken to be the mullite phase (highlighted in blue), which is later corroborated through XRD testing.

The images in Figure 87 show the best attempts at etching this microstructure. As can be seen from Figure 87, the average size for the mullite grains from each sample are all submicron, being on the order of a few hundred nanometers. Determination of grain size distributions was performed using four FESEM images taken from each sample. A source of error, which is discussed in section 5.6.3., arises from the quality of the etching as well as the quality of the FESEM images used to measure grain size from. Careful consideration was taken while manually measuring the size of each grain to distinguish between scratches and partially connected grain growth.

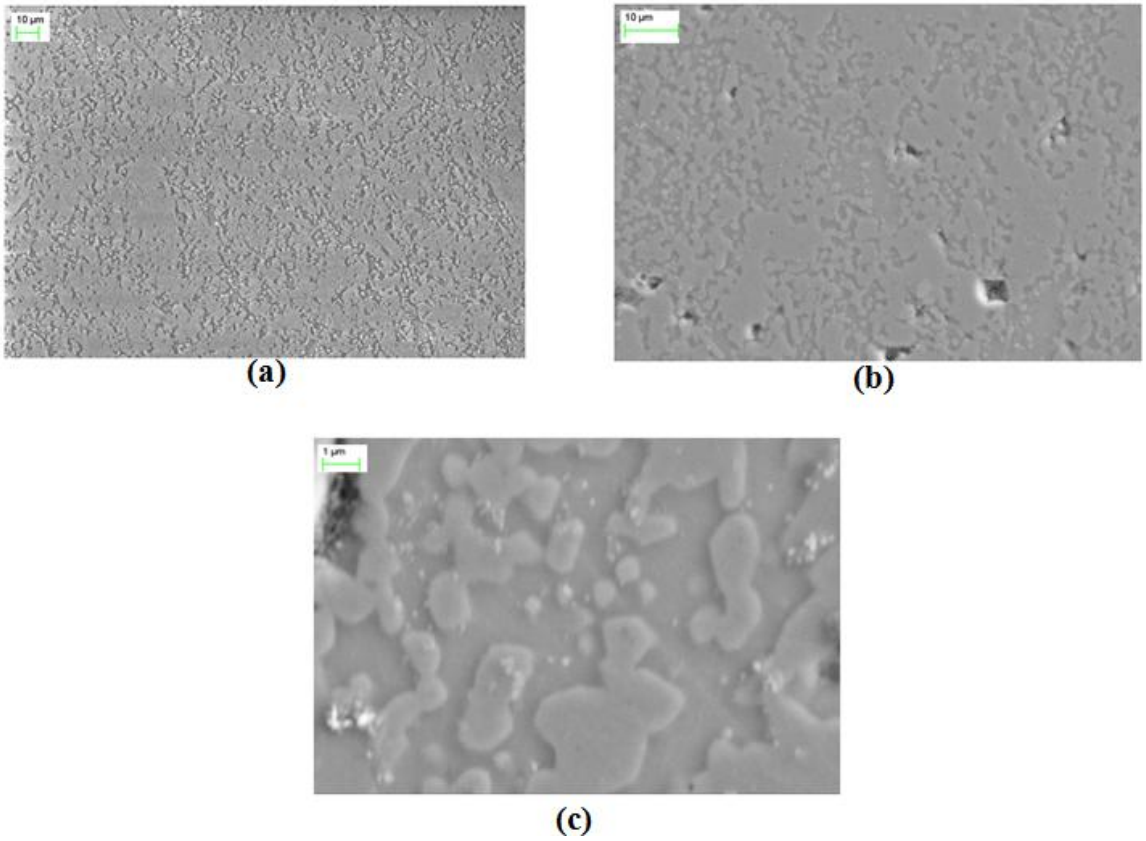

Figure 85. FESEM images showing interconnected-like pattern of mullite phase in Al_2O_3. (a) 1.3kX; (b) 3kX; (c) 20kX magnifications. Images taken from mullite 26.9vol% sample.

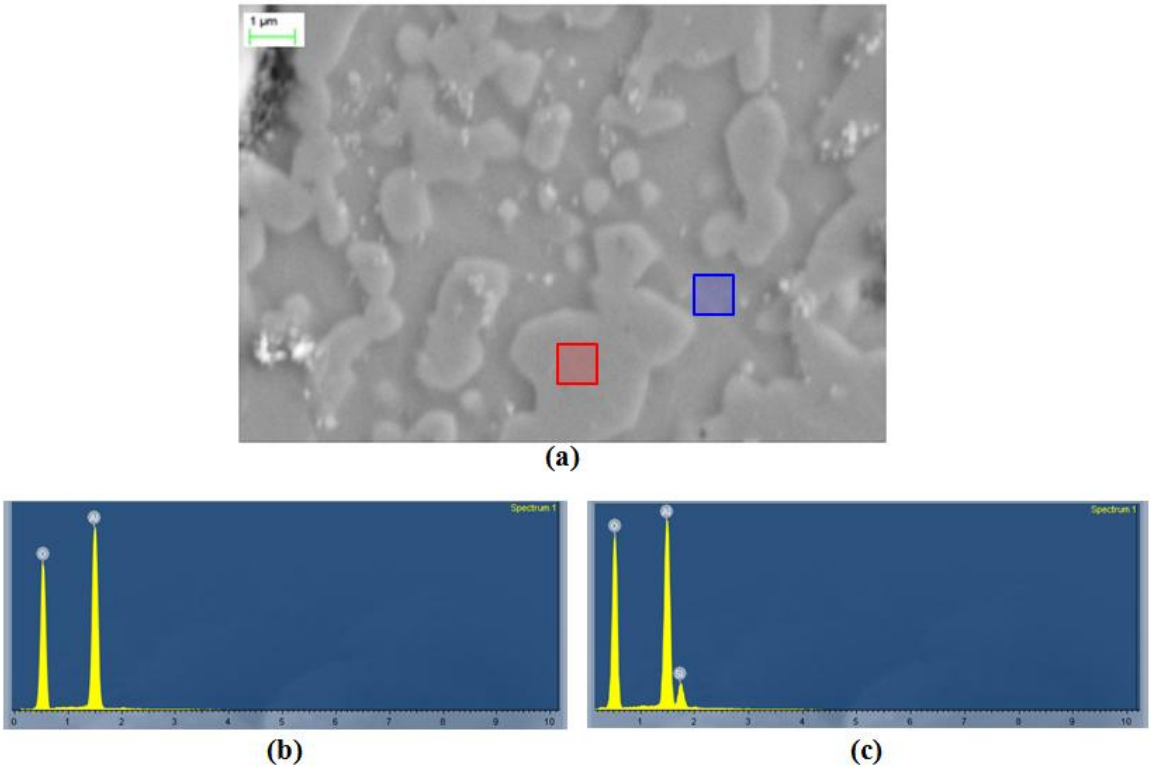

Figure 86. (a) Micrograph image showing distinct regions of alumina and mullite. (b) EDS point analysis of region consisting of Al_2O_3 (red) and (c) region consisting of mullite (blue).

Grain size distributions were measured for the mullite phase present in each sample using the method highlighted in Experimental Procedure. Four micrograph images from each sample were used to accomplish this. The micrographs shown in Figure 87 are representative of the images used to collect a large count of grain sizes. Grain size distribution histograms were created from the measured sizes and fit to Gaussian curves using MATLAB for easier comparison to their ultrasound predicted size distribution counterparts. The measured size distributions for the mullite phase in each sample can be seen in Figure 88. These distributions were normalized to a value of unity for direct comparison. Figure 88, (a)-(d), show a decrease in measured mean grain size which would indicate that as the volume percent of the mullite phase increases, the concentration of smaller mullite grains also increases. The grain size distribution for

Mullite 26.9vol% shows bimodal behavior and an increase in its concentration of larger grains when compared to the other four Mullite Series samples.

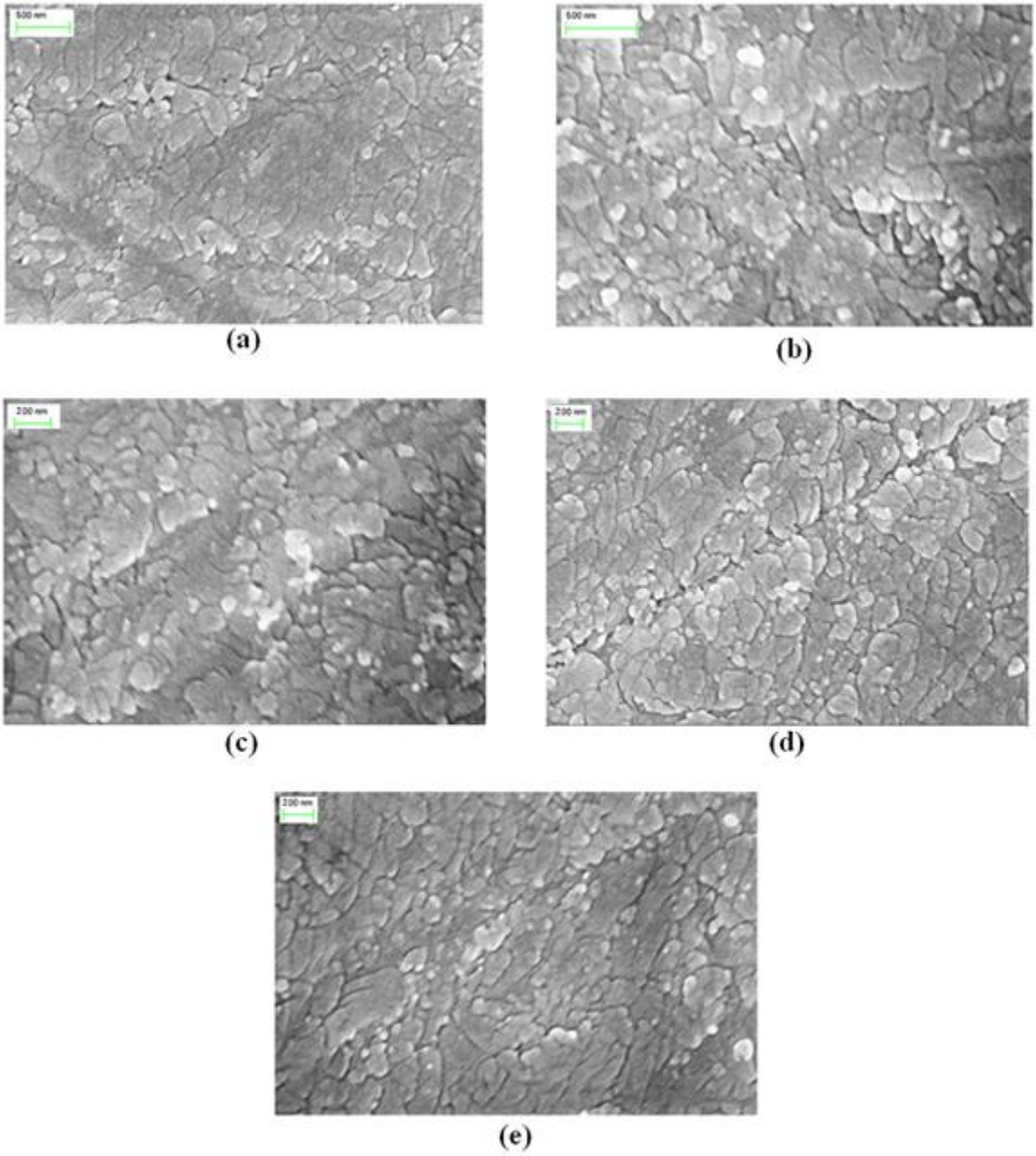

Figure 87. FESEM images showing mullite grains. (a) Mullite 2.1vol%, (b) Mullite 5.6vol%, (c) Mullite 16.3vol%, (d) Mullite 20.6vol%, (e) Mullite 26.9vol%.

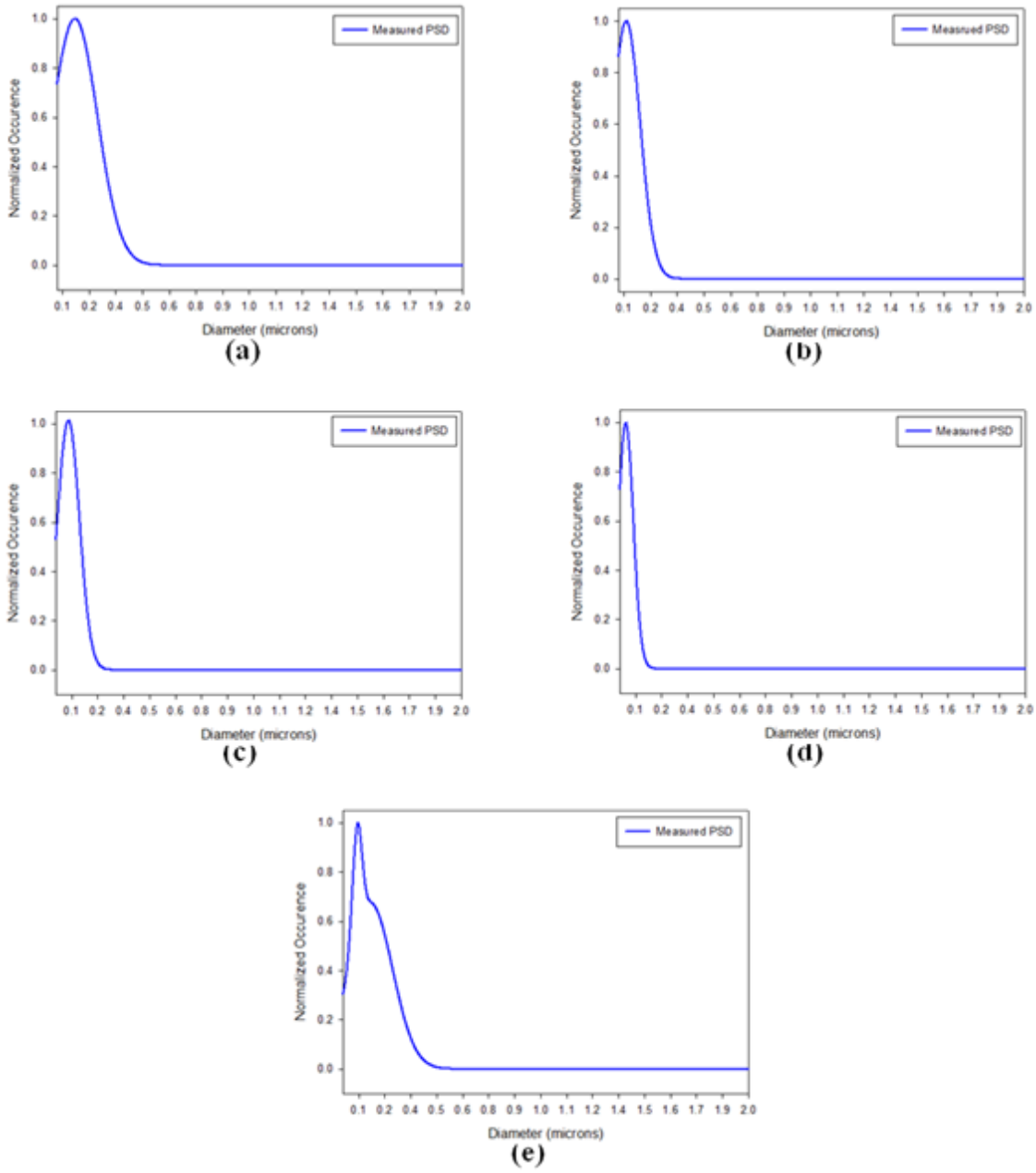

Figure 88. Measured mullite grain size distributions. (a) Mullite 2.1vol%, (b) Mullite 5.6vol%, (c) Mullite 16.3vol%, (d) Mullite 20.6vol%, (e) Mullite 26.9vol%.

5.2.3. Mullite Series XRD Results

X-ray diffraction results of the Mullite Series samples are shown in this section. Quantitative information regarding the calculated volume percent of mullite present in each sample was necessary to obtain such that the measured acoustic attenuation

coefficient spectra could be scaled appropriately. The measured density values for each sample are compared to the theoretical densities calculated by knowing the volume percent of both the alumina and mullite phases present in each sample. The labeling of each sample changed from reflecting the weight percent of SiO_2 added to each base alumina powder to reflect the volume percent of mullite within each sample after XRD quantitative analyses were performed.

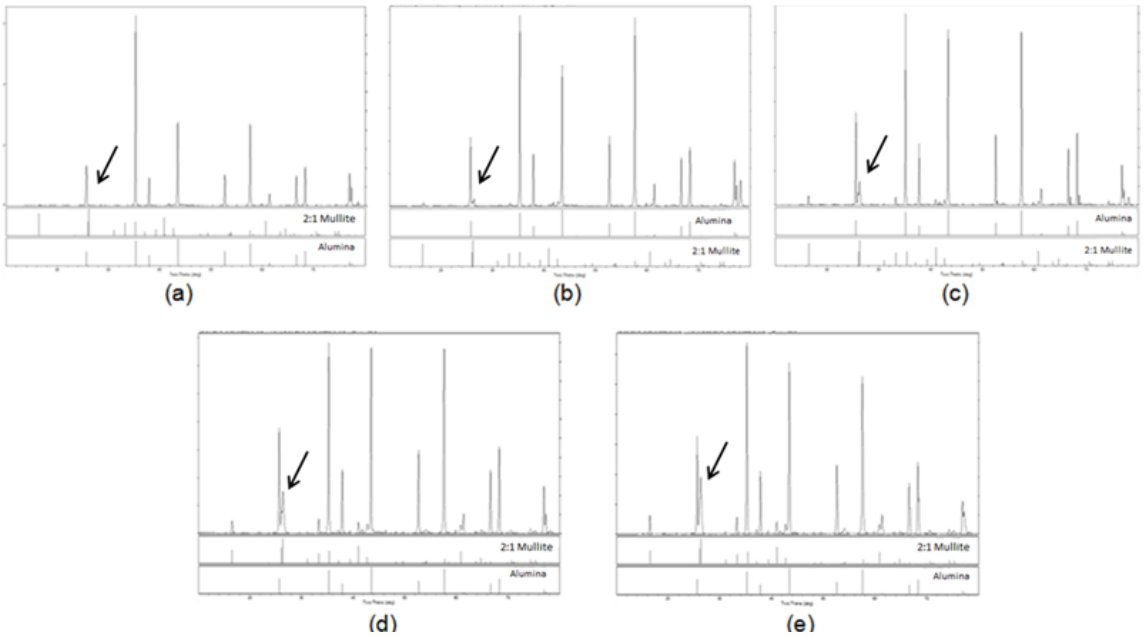

Figure 89. X-ray diffraction spectra. (a) Mullite 2.1vol%, (b) Mullite 5.6vol%, (c) Mullite 16.3vol%, (d) Mullite 20.6vol%, (e) Mullite 26.9vol%. Arrows indicate major peak of 2:1 mullite.

Figure 89 shows the measured XRD spectra for each sample in the Mullite Series. The arrows in each spectrum indicate the major peak of 2:1 mullite. Obtaining a mullite phase with a stoichiometric composition of $2Al_2O_3 \cdot SiO_2$ is considered to be a somewhat rare occurrence which is usually obtained by rapidly cooling from a melt or by direct solidification [236]. The effects of spark plasma sintering on alumina-silica systems is

not fully understood and the 2:1 mullite phase which formed may have formed by the fast cooling of an aluminosilicate melt during SPS treatment.

Quantitative analyses to determine the volume percent of the 2:1 mullite present in the alumina matrix was performed on each sample spectra according to method highlighted in section 4.8. Analysis of the major 2:1 mullite peak for the sample containing the least amount of mullite, Mullite 2.1vol%, required an XRD scan about a shortened two-theta range with a longer dwell time such that the major 2:1 mullite peak would be quantifiable. This separate XRD spectrum for Mullite 2.1vol% is shown in Figure 90.

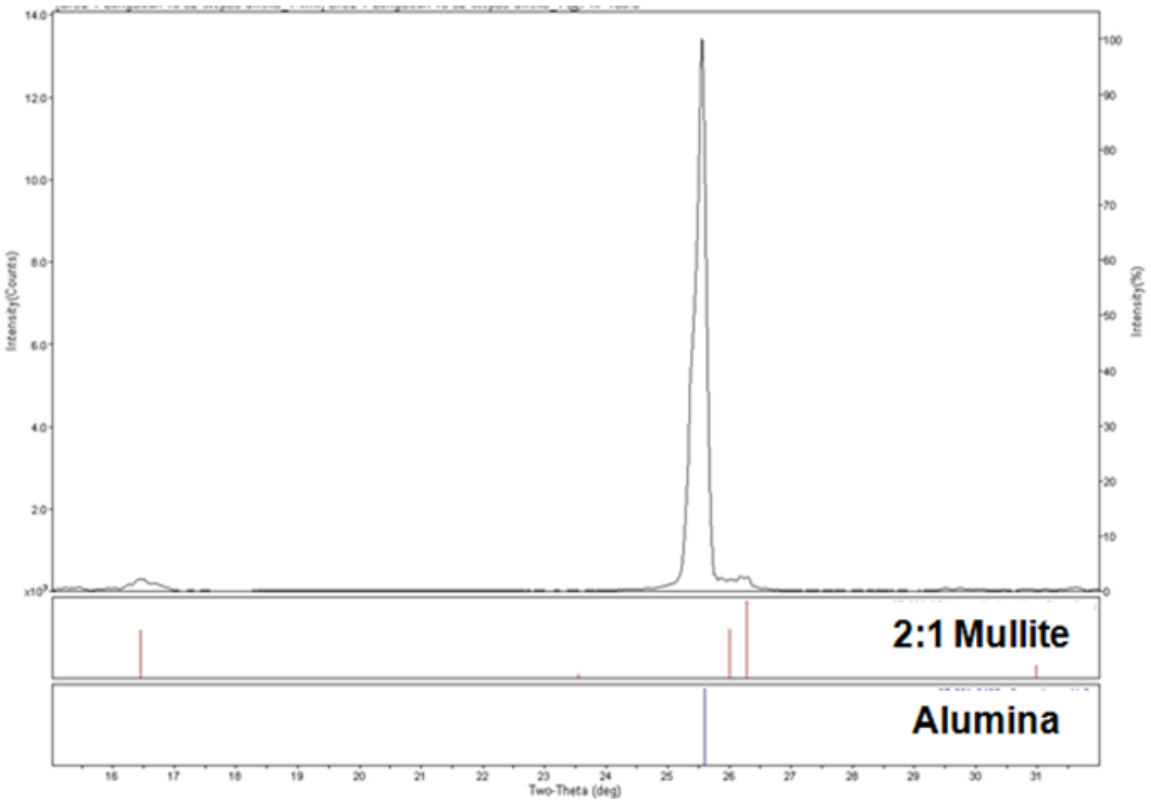

Figure 90. X-ray diffraction spectra. (a) Mullite 2.1vol%, (b) Mullite 5.6vol%, (c) Mullite 16.3vol%, (d) Mullite 20.6vol%, (e) Mullite 26.9vol%. Arrows indicate major peak of 2:1 mullite.

Calculations for the volume percents of mullite present in each sample reveal that an increase in the secondary mullite phase formed during sintering between samples. A histogram plot showing the volume percents of both the alumina and 2:1 mullite in each sample can be seen in Figure 91. According to these XRD calculated volume percents, a simple linear rule of mixtures was applied to obtain theoretical densities which are compared to measured densities for each sample (table XII). It should be noted that the Mullite Series samples containing 16.3 and 26.9 volume percent of mullite resulted in having calculated, theoretical densities which were lower than what was measured. This may be due to agglomeration of the mullite phase over different parts of the sample, which would go unmeasured through an XRD scan of a single surface.

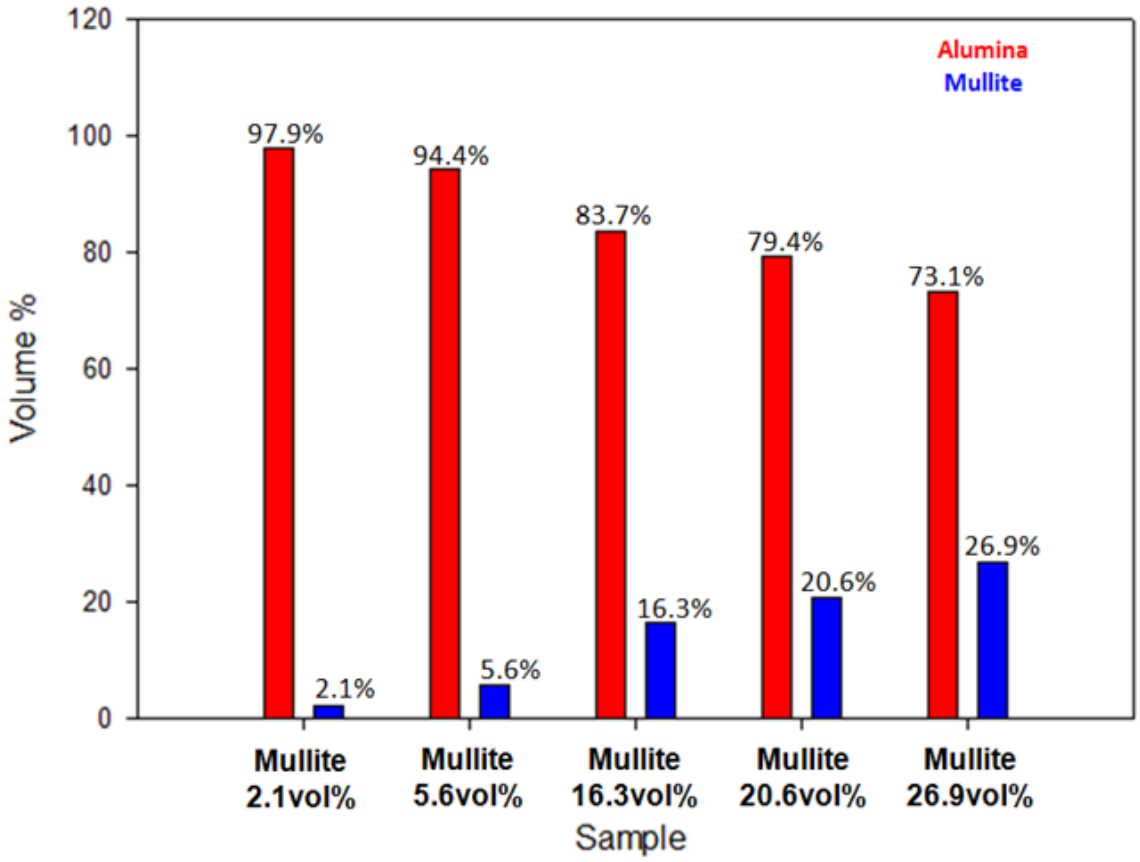

Figure 91. X-ray diffraction quantitative analysis of Mullite Series samples. Volume percent of 2:1 mullite present in each sample.

Table XII. Comparison of theoretical calculated densities based on volume percent of mullite in each Mullite Series samples to measured densities.

wt% SiO_2 added	vol% mullite formed	Measured Density (g/cm^3)	Theoretical Calculated Density (g/cm^3)
1	2.1	3.84	3.95
2	5.6	3.84	3.91
3	16.3	3.83	3.82
4	20.6	3.77	3.78
5	26.9	3.76	3.72

5.3. Characterization of Titanium Carbide Series

The characterization results with respect to ultrasound testing, FESEM imaging, EDS analysis, micrograph analysis, and XRD testing for the Titanium Carbide Series sample set are given in this section. A discussion of the results is given to highlight specific trends or irregularities. Analysis of acoustic spectra are given in this section while the conclusions regarding measured acoustic spectra, theory of intraparticle thermoelastic absorption, use of derived equations for predicting grain size, and comparison to measured grain sizes are drawn in section 5.6.1.2.

5.3.1. Titanium Carbide Series Ultrasound Testing Results

Ultrasonic C-Scan images for each sample from the Titanium Carbide Series are shown in Figures 92-96. The acoustic data collected gave full area property maps of attenuation coefficient, sonic velocities, Poisson ratio, and all elastic properties. These images were used to determine variations in bulk uniformity and the spatial location of anomalous defects. Table XIII gives statistical information for each sample regarding mean values, standard deviations, and the range for each property measured. Slight pressing patterns can be seen in the attenuation coefficient and longitudinal speed of sound C-Scan images for TiC-5vol% and TiC-25vol% samples. These patterns present

as diagonal striations where the property values vary slightly showing alternating behavior between low and high values (colors alternate between yellow and orange). Sample TiC-15vol% shows large pressing patterns on the left and upper right edges of the sample. The manufacturer noted these pressing defects to be caused by incongruence with the die face. The section from this sample was taken in a region which was uniform and away from these pressing defects. The variation of acoustically measured properties across the total area of each sample is minimal. The scales for each C-Scan image may vary between samples to draw attention to this minimal variation. The standard deviation of values over the entire sample areas is relatively low implying their microstructures are uniform and excellent mixing of the TiC particles occurred.

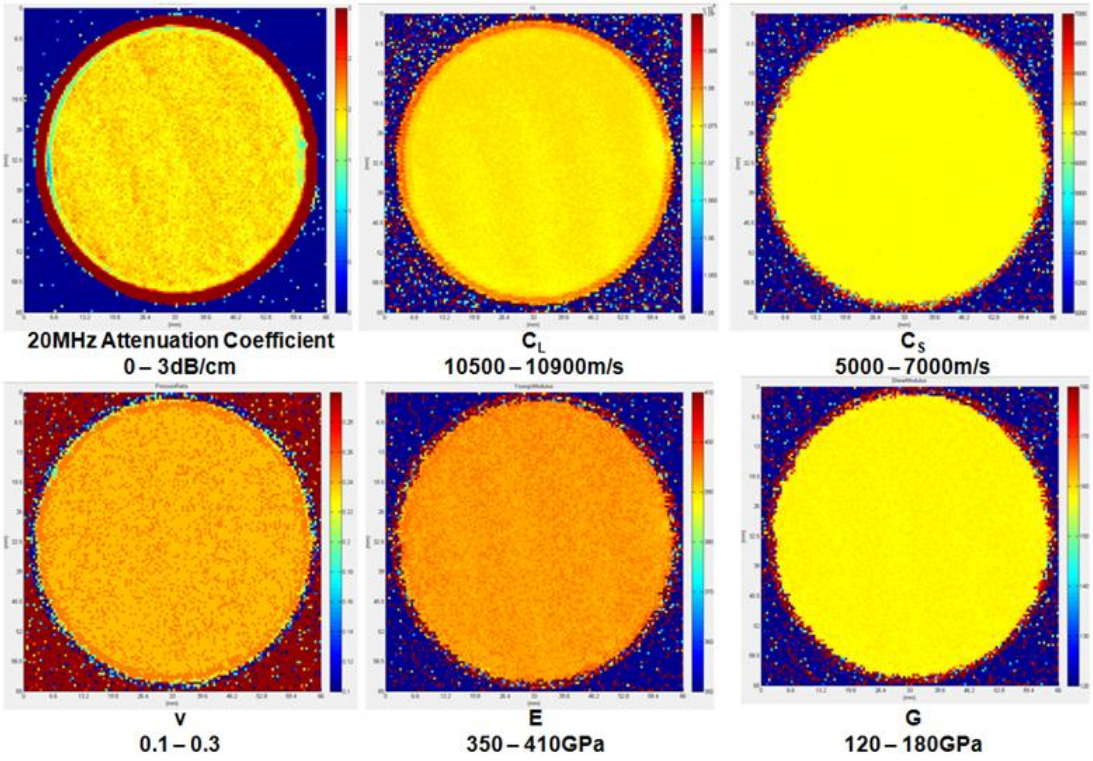

Figure 92. Ultrasonic C-Scan images of measured properties for Titanium Carbide Series sample TiC-5vol%.

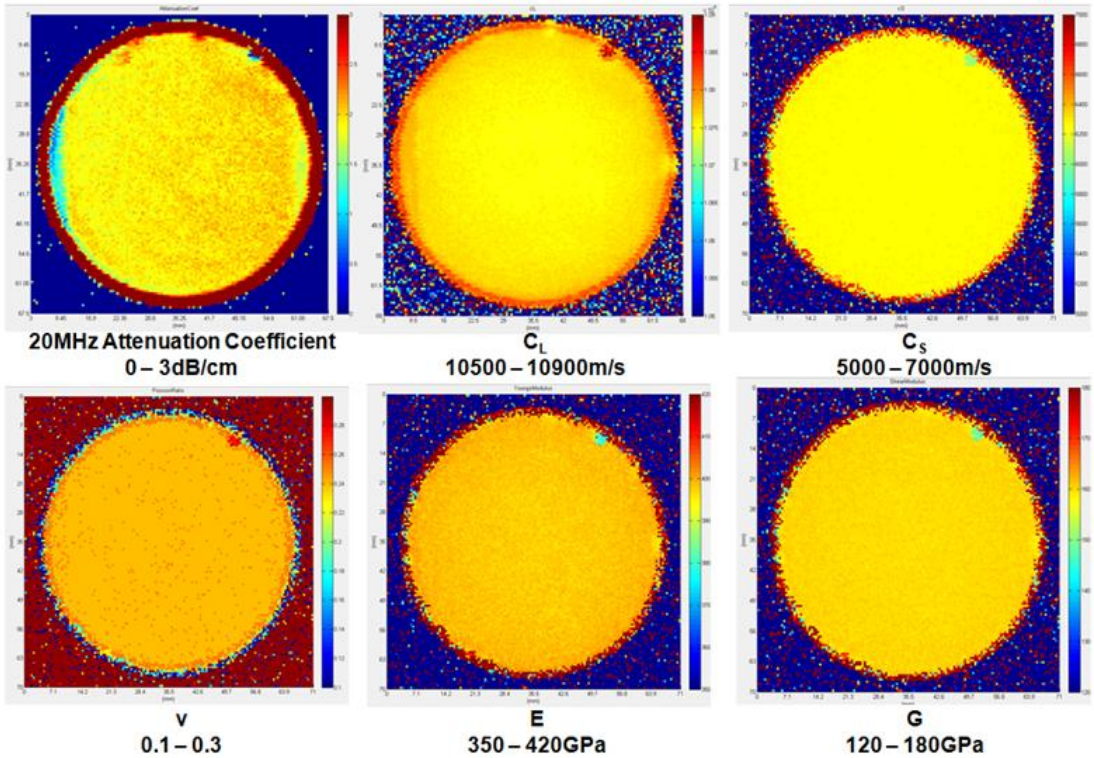

Figure 93. Ultrasonic C-Scan images of measured properties for Titanium Carbide Series sample TiC-10vol%.

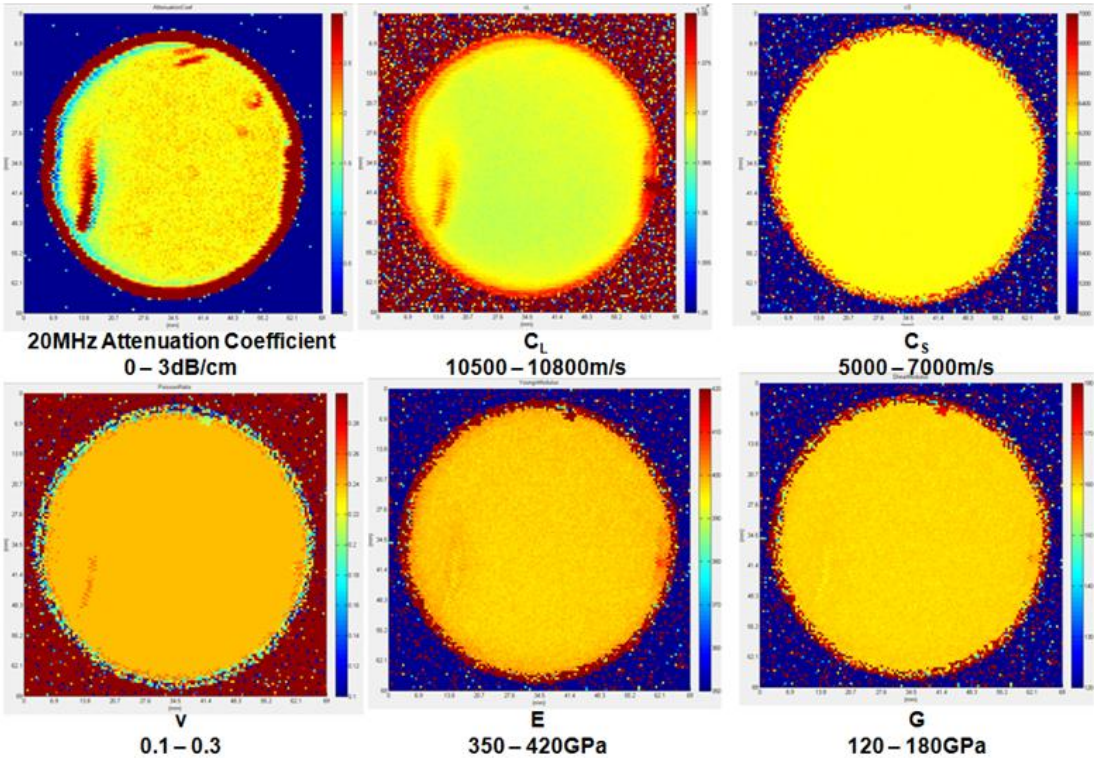

Figure 94. Ultrasonic C-Scan images of measured properties for Titanium Carbide Series sample TiC-15vol%.

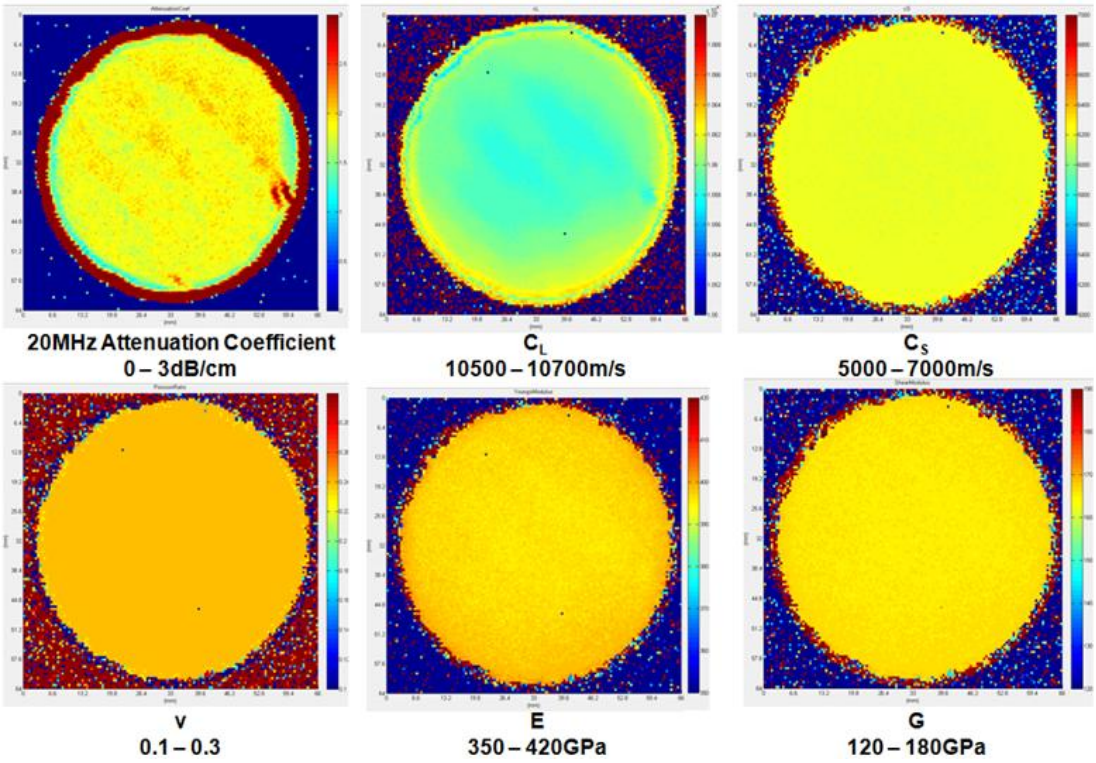

Figure 95. Ultrasonic C-Scan images of measured properties for Titanium Carbide Series sample TiC-25vol%.

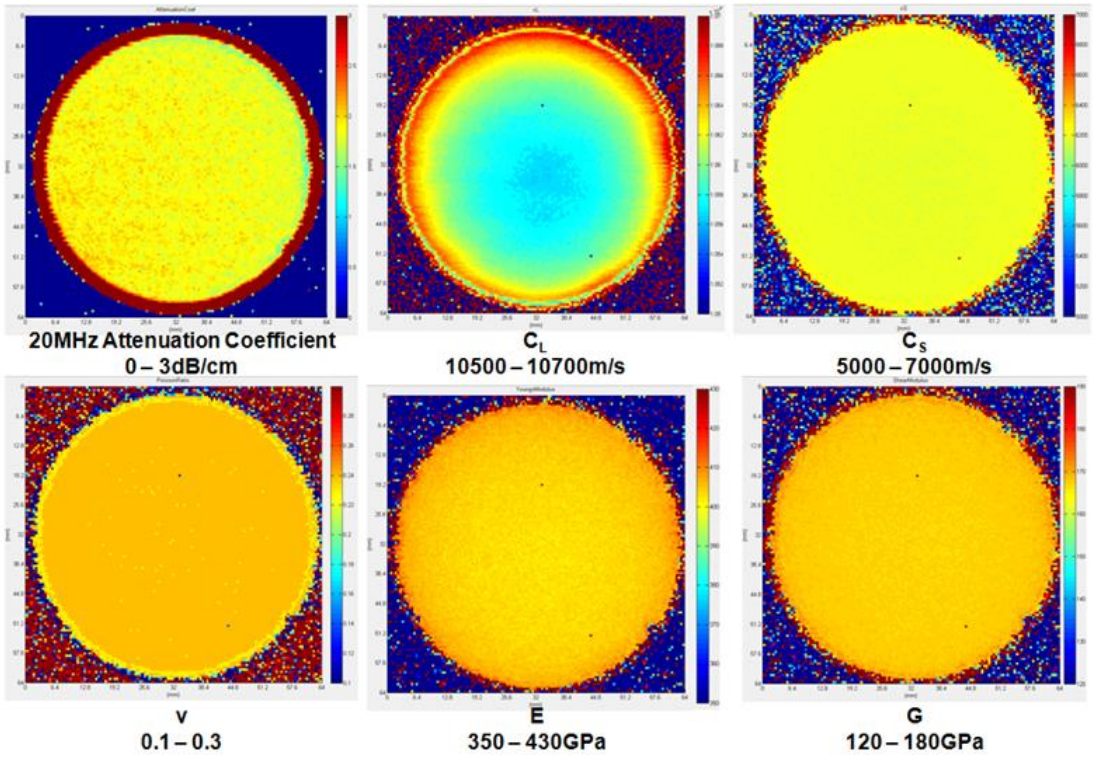

Figure 96. Ultrasonic C-Scan images of measured properties for Titanium Carbide Series sample TiC-35vol%.

Table XIII. Statistical information taken over all points from Titanium Carbide Series sample C-Scan images.

	20MHz α (dB/cm)	C_L (m/s)	C_S (m/s)	ν	E (Gpa)	G (Gpa)
TiC-5vol%						
Mean	1.99	10761	6260	0.24	394	158
StDev	0.12	3.32	8.21	0	0.76	0.52
Min	1.6	10749	6231	0.24	391	157
Max	2.43	10806	6286	0.24	396	160
TiC-10vol%						
Mean	1.96	10756	6267	0.24	398	160
StDev	0.09	5.89	12.6	0	1.15	0.71
Min	1.57	10740	6235	0.24	396	159
Max	2.31	10822	6760	0.24	440	186
TiC-15vol%						
Mean	1.93	10673	6236	0.24	398	160
StDev	0.08	3.65	7.97	0	0.76	0.52
Min	1.68	10661	6203	0.24	395	159
Max	2.26	10684	6260	0.24	400	161
TiC-25vol%						
Mean	1.86	10590	6192	0.24	410	165
StDev	0.09	4.72	6054	0	0.69	0.45
Min	1.5	10582	6164	0.24	407	164
Max	2.26	10606	6212	0.24	412	166
TiC-35vol%						
Mean	1.87	10595	6193	0.24	412	170
StDev	0.08	7.84	19.16	0	0.76	0.45
Min	1.59	10563	6167	0.24	408	169
Max	2.24	10660	7392	0.24	416	171

The average values for longitudinal velocity decrease as the concentration of titanium carbide increases from 5-35 volume percent. This is not reflected in the increase in Young's and shear moduli; it is more likely that this increase in elastic properties is

occurring due to each sample's overall increase in density with higher concentrations of TiC. The average values for 20MHz overall attenuation coefficient show a decrease with increasing TiC concentration. The standard deviation and range for 20MHz overall attenuation coefficient values for each sample decrease accordingly with increasing amounts of TiC in each sample. Viewing the full bandwidth of attenuation coefficient spectra taken about the central points of each sample gives a clearer understanding of the frequency dependent nature of acoustic loss and explanations regarding the size and concentration of the TiC particles actively causing thermoelastic absorption. The attenuation coefficient spectra from each sample in the Titanium Carbide Series on a frequency range of 12-30MHz can be seen in Figure 97.

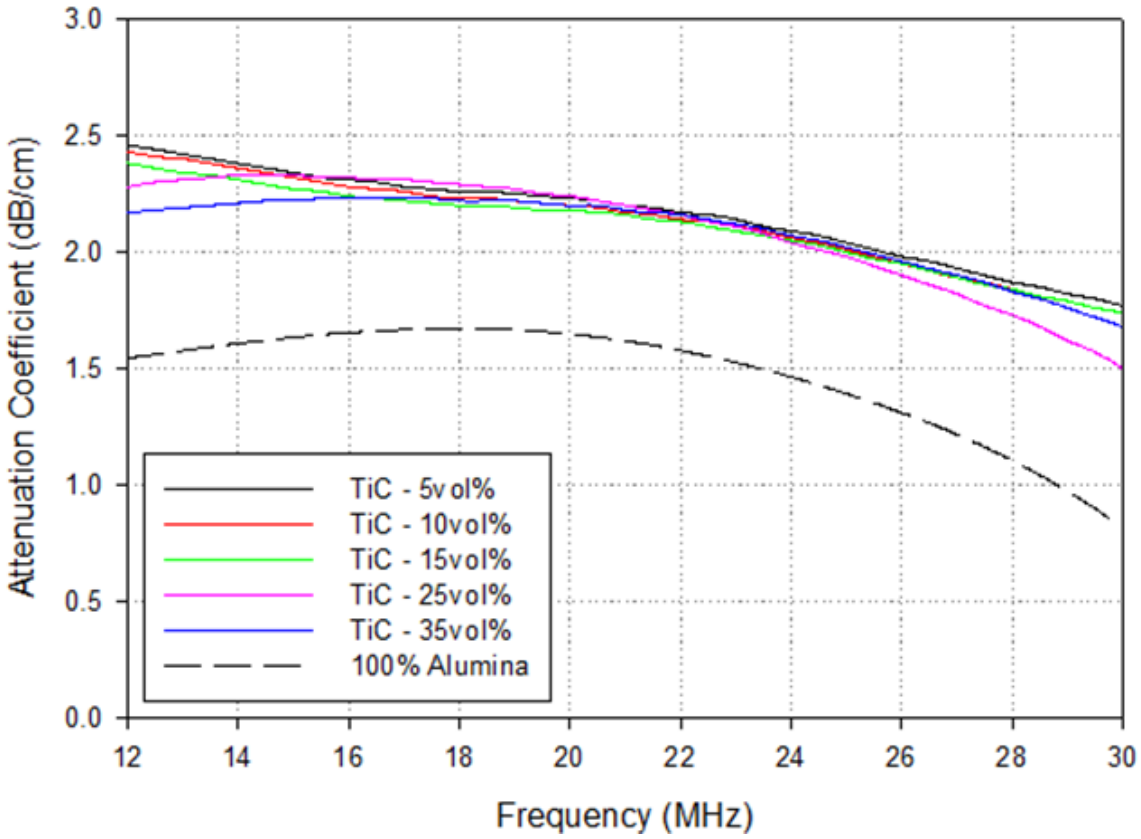

Figure 97. Ultrasonic C-Scan images of measured properties for Titanium Carbide Series sample TiC-35vol%.

The attenuation coefficient spectra seen in Figure 97 all show similar behavior between approximately 18-24MHz. Slight deviation of each spectrum can be seen at the lowest and highest frequencies. The similar behavior of each spectrum does not imply that the sample microstructures which the ultrasonic waves interacted with are similar. Assuming that the magnitude of each spectrum indicates the total thermoelastic attenuation caused by the alumina and TiC grains, once the relative contribution of attenuation from the alumina is subtracted, the attenuation coefficient spectra will spread apart revealing the frequency dependent attenuation coefficient caused solely by the TiC. The corrected spectra for the attenuation caused by the alumina grains can be seen in section 5.6.1.2.

5.3.2. Titanium Carbide Series FESEM Results

The Titanium Carbide Series samples presented with a relatively simpler ceramographic preparation compared to the Mullite Series samples. The TiC grains within the alumina host were significantly larger than the mullite grains in the Mullite Series samples. This made the etching process easier to control as the extent of TiC erosion could be viewed in an optical microscope before using the FESEM. Charging issues which typically occur while performing scanning electron microscopy on alumina-based materials at high magnifications were alleviated due to the relatively lower magnifications that were used on the Alumina-TiC samples. The magnification used for the Titanium Carbide Series samples was 20,000 times. Micrograph images, representative of each of the five samples in the Titanium Carbide Series, are shown in Figure 98. Opposed to the Mullite Series samples where the mullite grains tended to

cluster uniformly over the entire samples, the titanium carbide grains presented as distinct homogeneously spaced grains throughout the alumina-TiC samples.

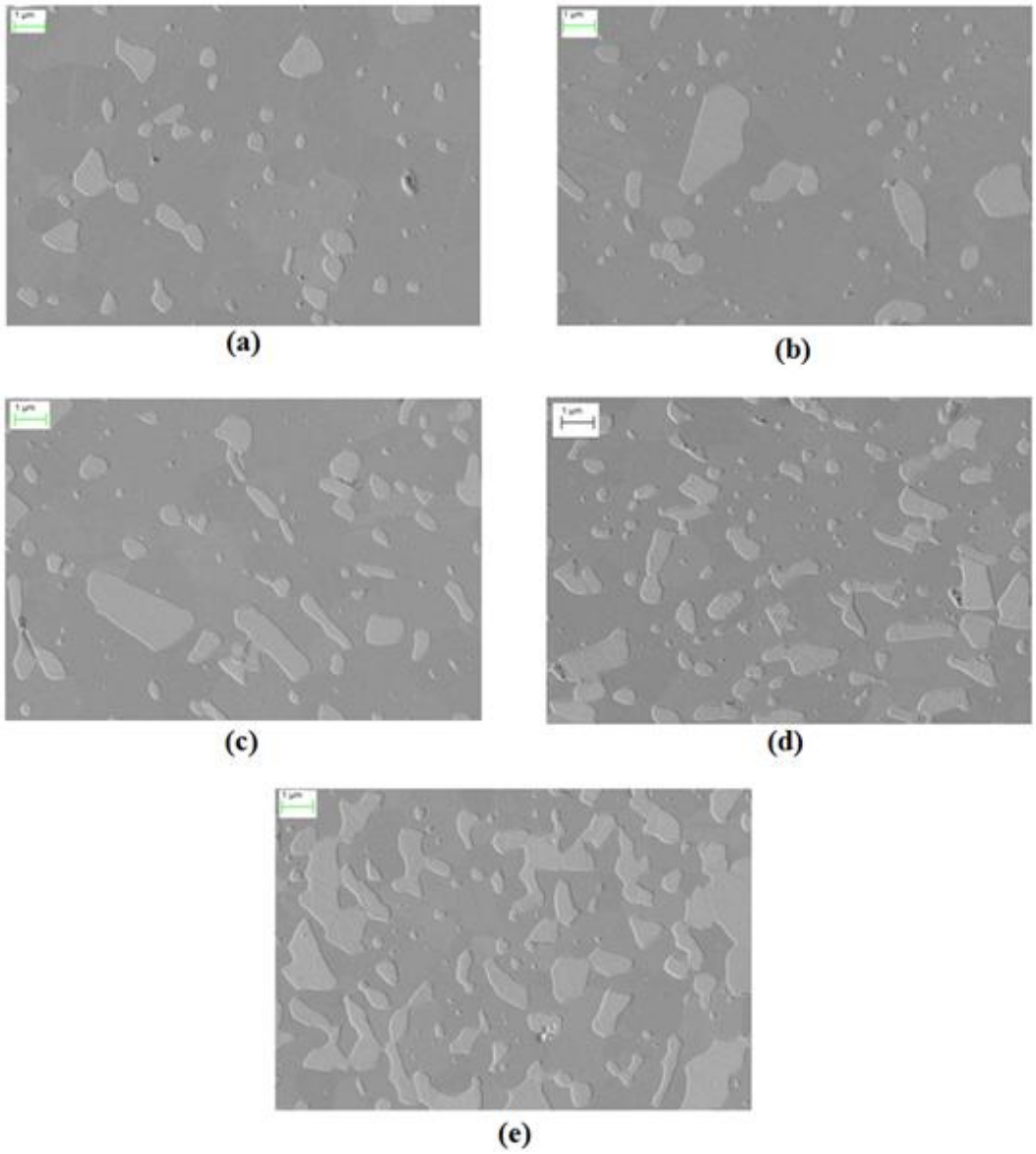

Figure 98. FESEM images showing titanium carbide grains. (a) TiC-5vol%, (b) TiC-10vol%, (c) TiC-15vol%, (d) TiC-25vol%, (e) TiC-35vol%.

The light grey phase seen in the micrograph images of Figure 98 are the titanium carbide grains. This was verified through EDS while FESEM imaging was being performed. EDS spectra showing the difference between the TiC and alumina phases can be seen in Figure 99. Small carbon and titanium peaks can be seen in the spectra which

were taken about alumina grains. The same can be seen for the presence of aluminum in the spectra taken about TiC grains. This is caused by multiple reflections of the electron beam and scattered X-rays impinging on the surrounding material. The dominant peaks seen in the spectra of Figure 99 represent the phases which were present about the labeled areas.

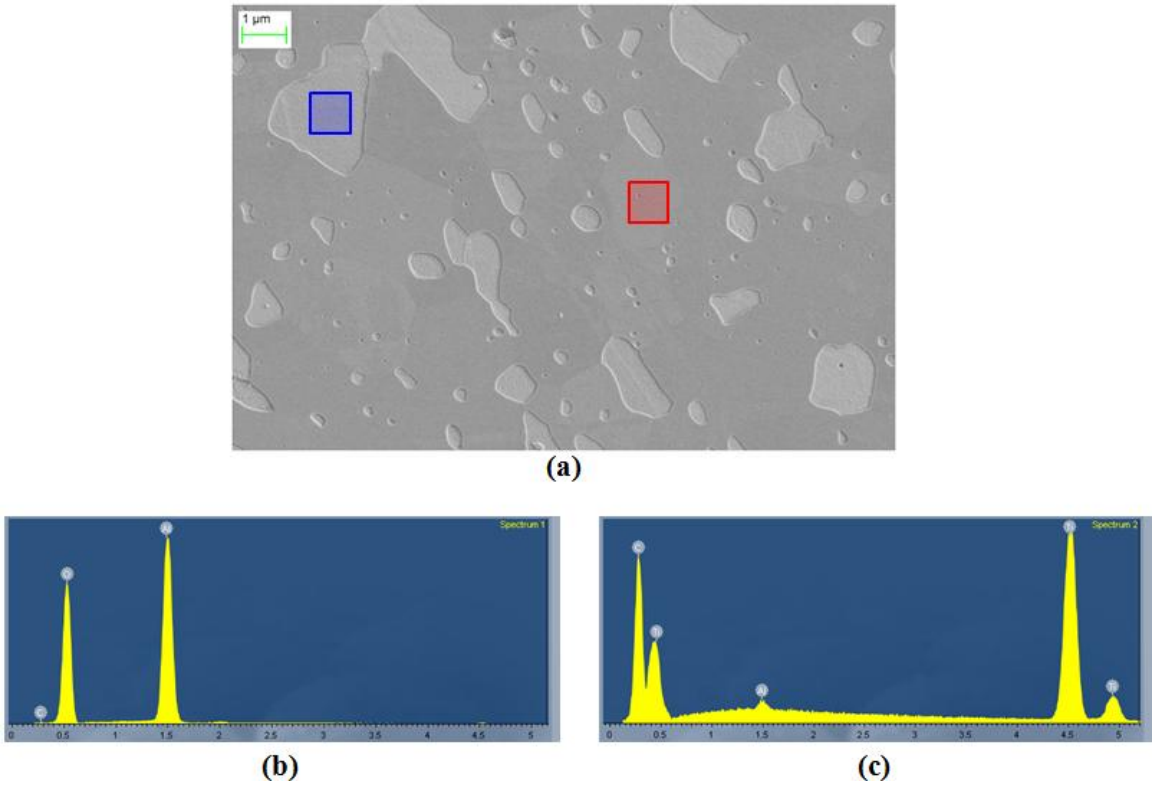

Figure 99. (a) Micrograph image showing distinct regions of alumina and titanium carbide. (b) EDS point analysis of region consisting of Al_2O_3 (red) and (c) region consisting of titanium carbide (blue).

Analysis of the micrograph images provided grain size distributions for each sample in the Titanium Carbide Series. The measured grain size distribution histograms were curve fit to Gaussian distributions such that they could be easily viewed and compared. The curve fit and normalized TiC size distributions can be seen in Figure 100. The grain size domains for each of the measured distributions in Figure 100 are on

different scales as the average grain size tended to increase as the volume percent of titanium carbide increases. Figure 101 shows each grain size distribution from the Titanium Carbide Series on the same plot using the same scaling to show the relative increase in TiC grain size as the volume percent in each sample is increased. The arithmetic mean for TiC grain size from each sample in the Titanium Carbide Series increases accordingly as 0.76, 1.00, 1.17, 1.40, and 1.59 microns as the volume percent of TiC is increased across samples.

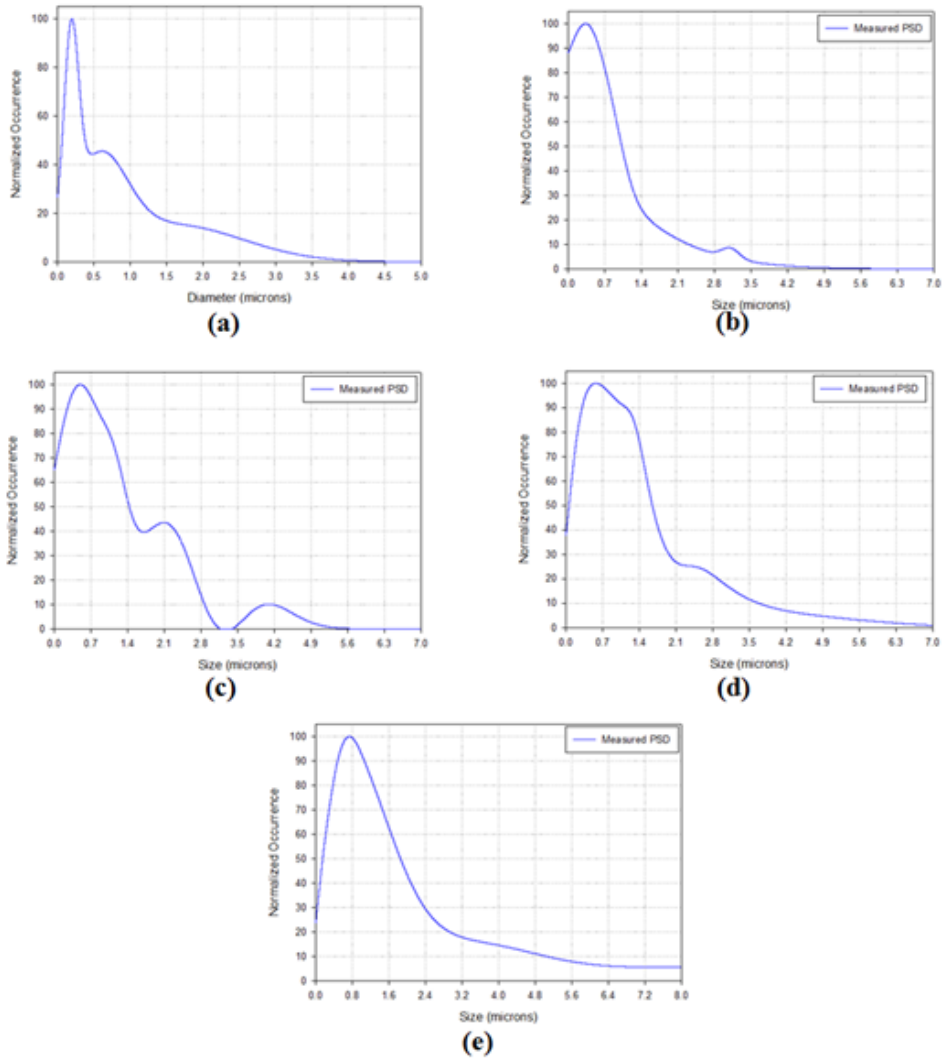

Figure 100. Measured titanium carbide grain size distributions. (a) TiC-5vol%, (b) TiC-10vol%, (c) TiC-15vol%, (d) TiC-25vol%, (e) TiC-35vol%.

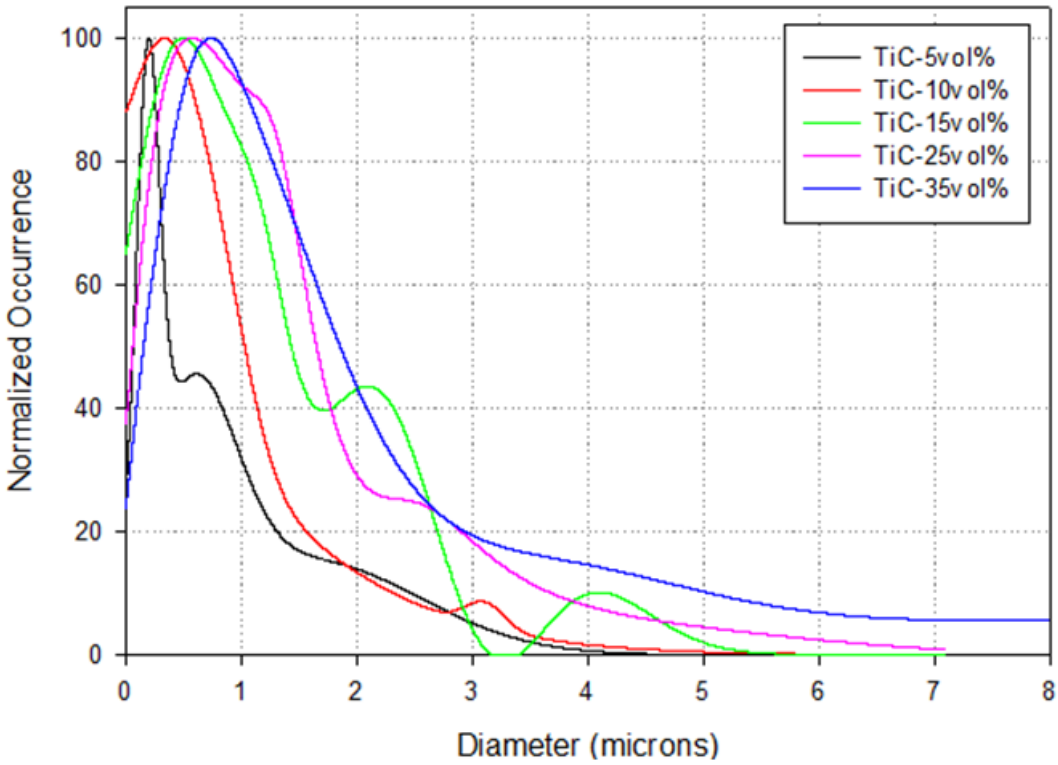

Figure 101. Measured titanium carbide grain size distributions. The domain for the size range is held constant to show the minute increase in measured grain size.

The occurrence of each measured grain size distribution was normalized to 100. Measuring grain size distributions according to a linear intercept method gives no information regarding the relative concentration of phases present within a material. The method developed as part of this thesis attempts to account for this by giving grain size distributions with an absolute scale of occurrence. Comparisons of measured TiC grain size distributions to TiC grain size distributions predicted through ultrasonic means can be seen in section 5.6.1.2.

5.3.3. Titanium Carbide Series XRD Results

Quantifying the volume percent of TiC present within each of the Titanium Carbide Series samples was necessary in creating ultrasound predicted grain size distributions. XRD results showing the increase of titanium carbide for each of these alumina-based materials are shown in Figure 102. The arrows highlight the major peak

of titanium carbide. X-ray diffraction revealed that the volume percent of TiC within the alumina host was almost exactly what the manufacturer claimed them to be. Figure 103 shows the XRD calculated volume percents of the two phases present in each of the Titanium Carbide Series samples. These results indicate that the attenuation coefficient spectra seen in Figure 97 will show a one-to-one correspondence between magnitude of attenuation and concentration of TiC once they are corrected for the absolute concentration of alumina present within each sample.

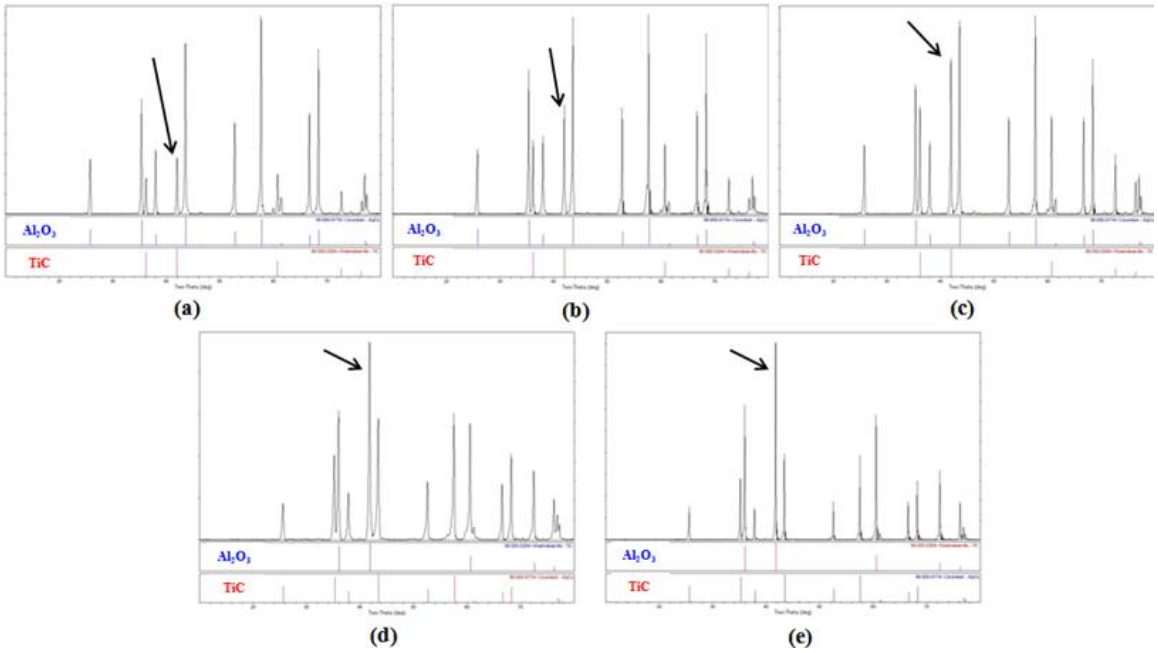

Figure 102. X-ray diffraction spectra. (a) TiC-5vol%, (b) TiC-10vol%, (c) TiC-15vol%, (d) TiC-25vol%, (e) TiC-35vol%.

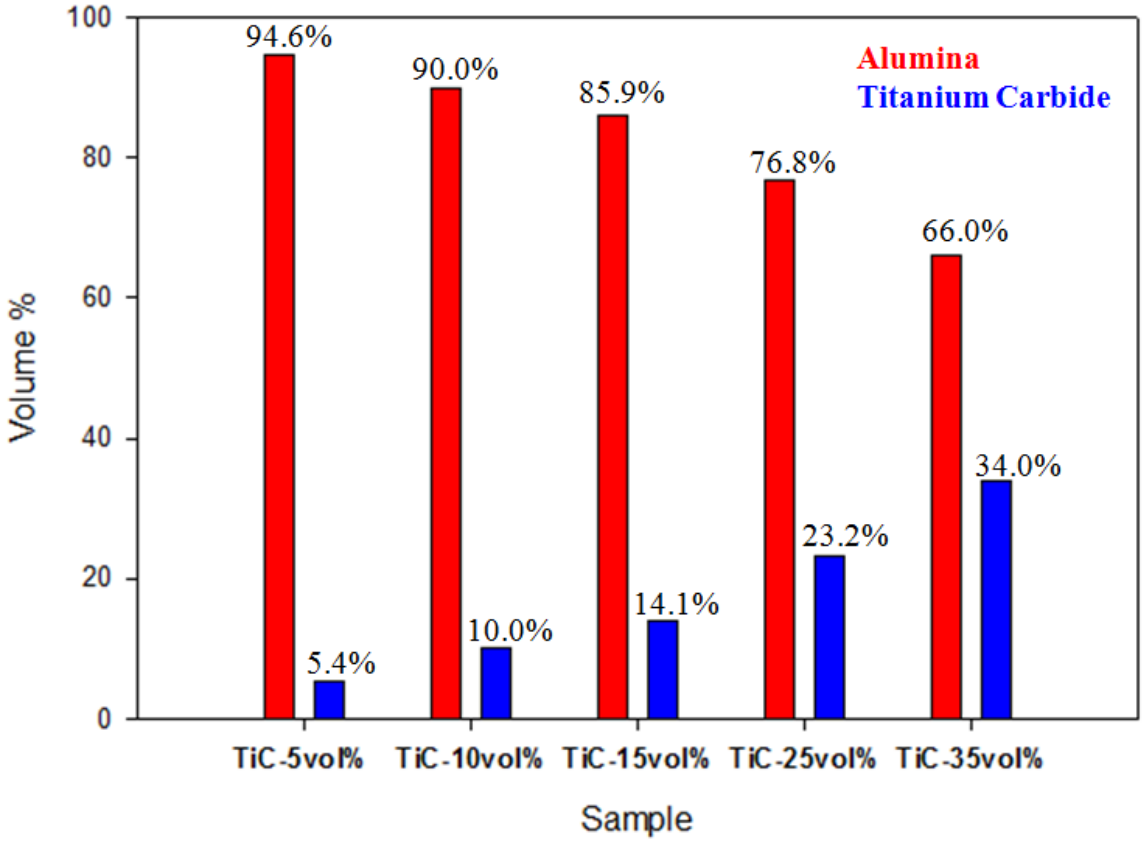

Figure 103. X-ray diffraction quantitative analysis of Titanium Carbide Series samples. Volume percent of TiC present in each sample.

5.4. Characterization of Microstructural Evolution Alumina Series

The characterization results with respect to ultrasound testing, FESEM imaging, and micrograph analysis for the Microstructural Evolution Alumina Series sample set are given in this section. A discussion of the results is given to highlight specific trends or irregularities for both the ultrasound test results and conventional microstructural testing results. Analysis of acoustic spectra are given in this section while the conclusions regarding measured acoustic spectra, acoustic scattering theory, creation of standard scattering factors for Rayleigh and stochastic scattering, and comparison to measured average grain sizes are drawn in section 5.6.2.1.

5.4.1. Microstructural Evolution Alumina Series Ultrasound Testing Results

This section highlights all of the ultrasonic testing results obtained for the Microstructural Evolution Alumina Series samples. C-Scan images of 20MHz overall attenuation coefficient are used to determine the overall homogeneity of each sample. These images were taken into consideration for where smaller sections were cut out of each sample for conventional microstructural testing. Along with the overall attenuation coefficient C-Scan maps, sonic velocity and elastic moduli C-Scans were measured for each sample. The C-Scan maps containing all information collected with the 20MHz transducer for each sample are shown below.

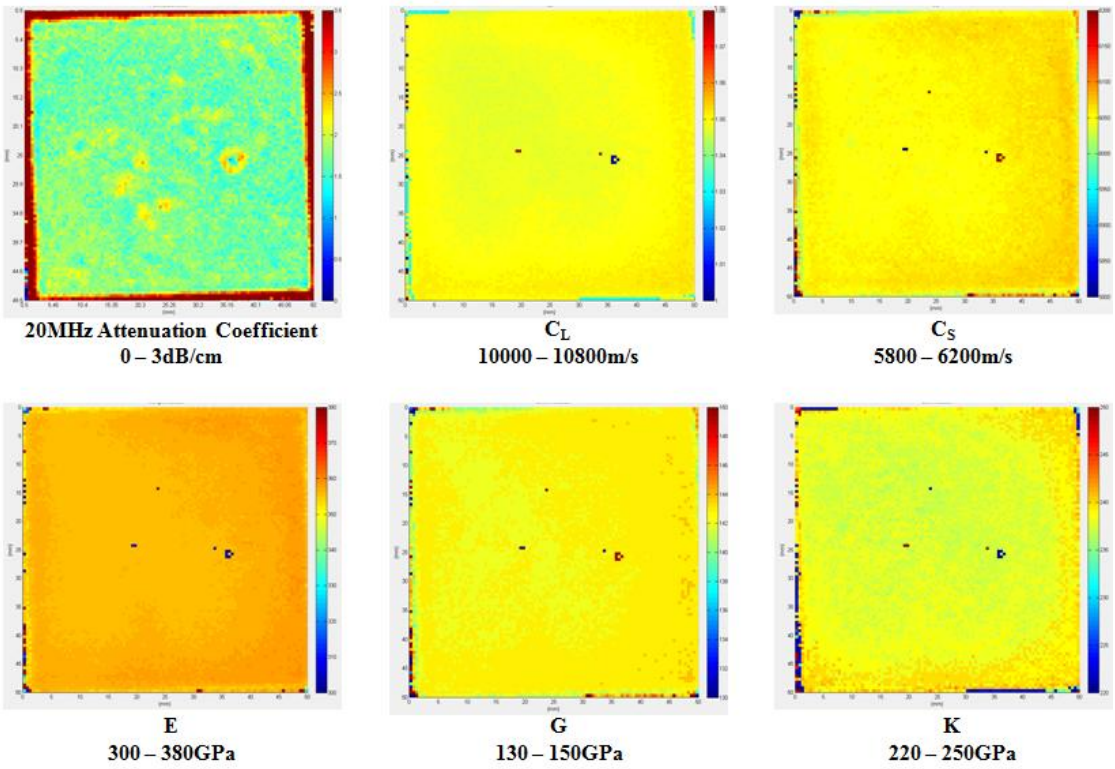

Figure 104. Ultrasonic C-Scan images of measured properties for Microstructural Evolution Alumina Series sample (T0, D0).

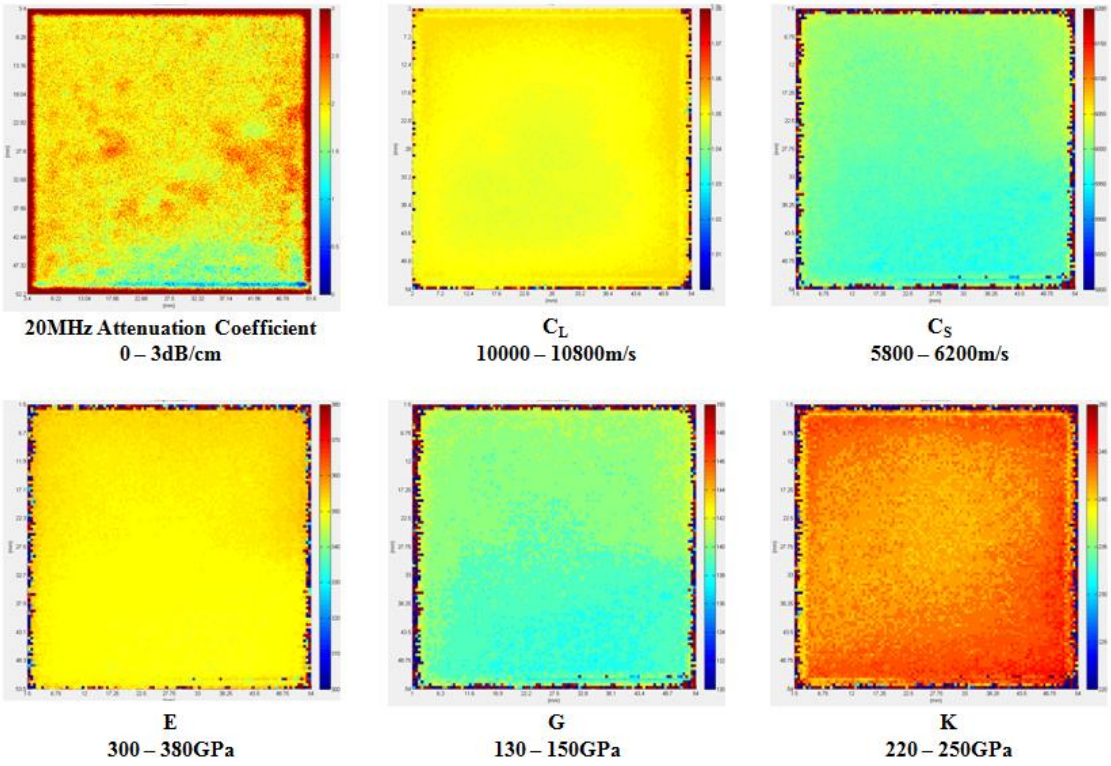

Figure 105. Ultrasonic C-Scan images of measured properties for Microstructural Evolution Alumina Series sample (T0, D0+5).

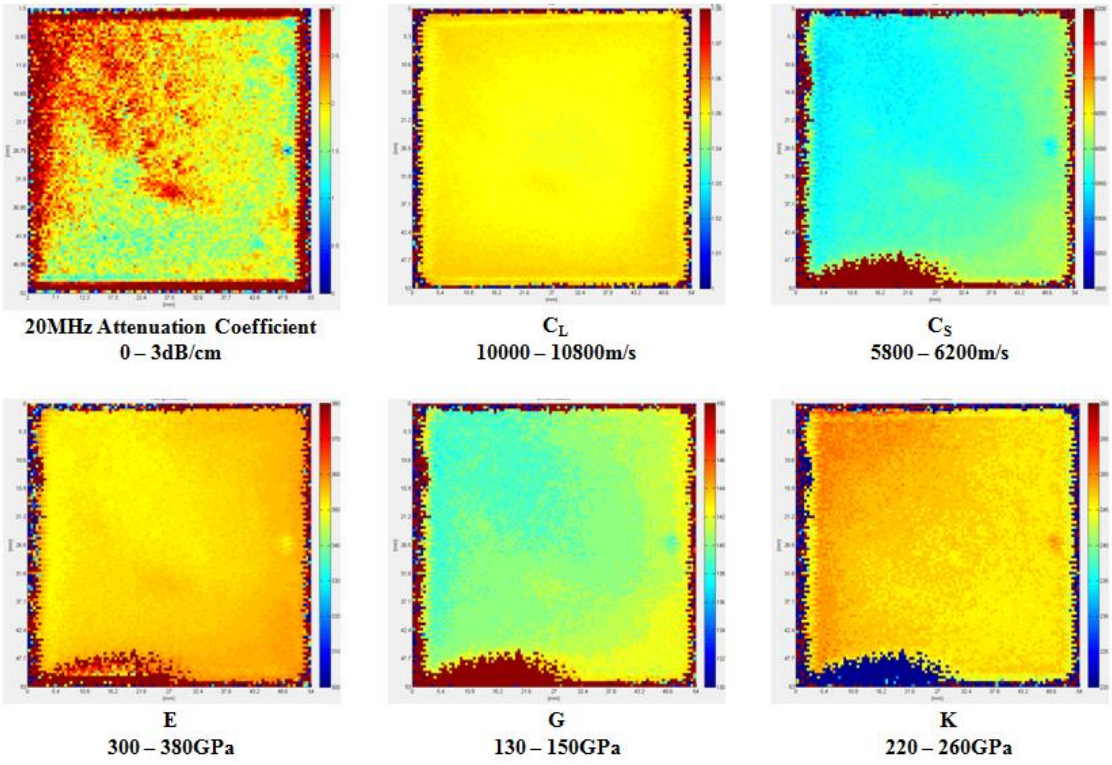

Figure 106. Ultrasonic C-Scan images of measured properties for Microstructural Evolution Alumina Series sample (T0, D0+15).

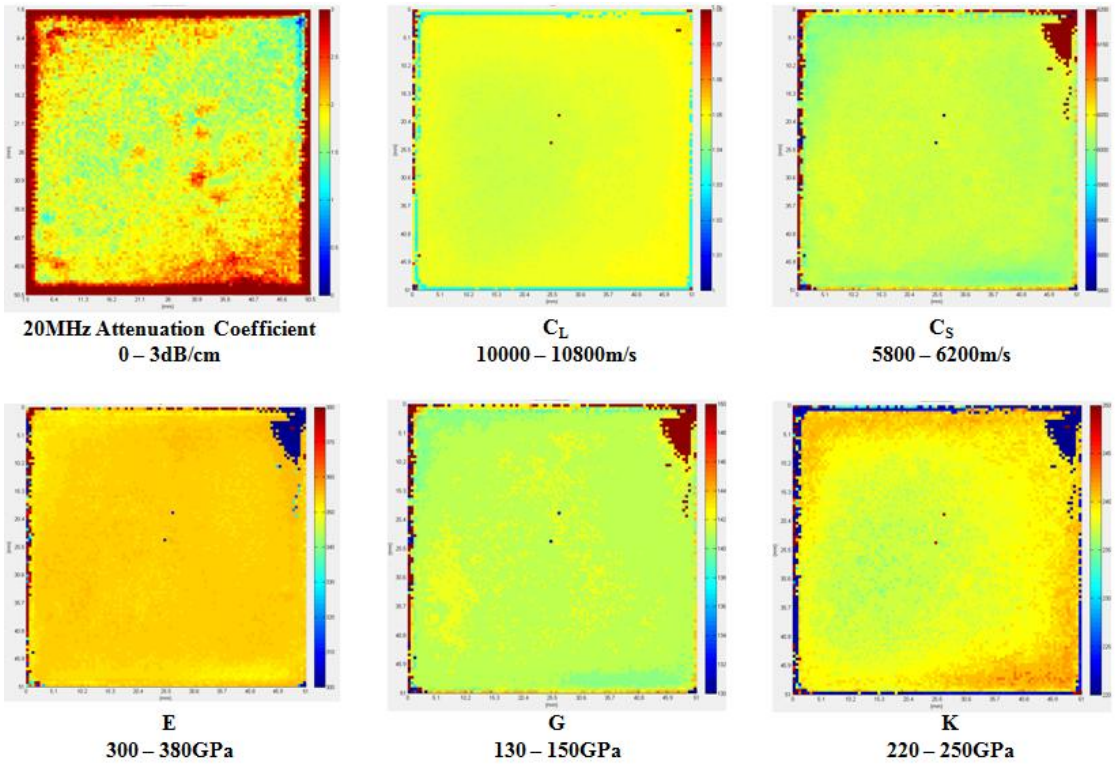

Figure 107. Ultrasonic C-Scan images of measured properties for Microstructural Evolution Alumina Series sample (T0+50, D0).

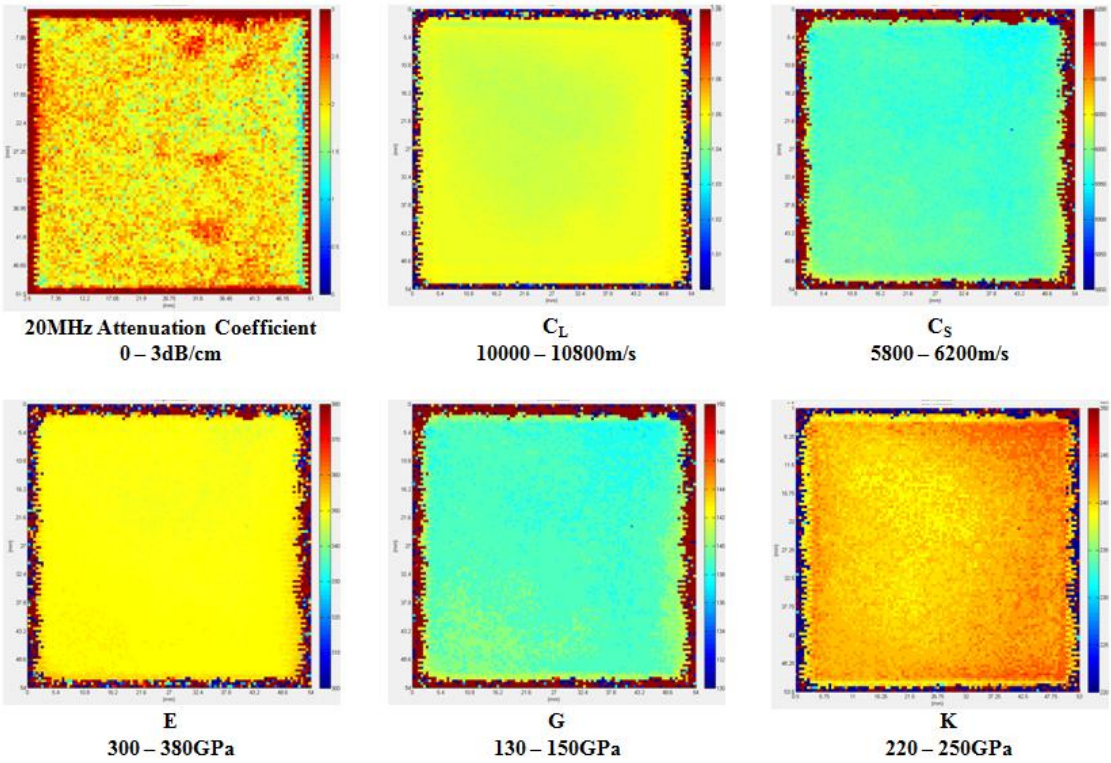

Figure 108. Ultrasonic C-Scan images of measured properties for Microstructural Evolution Alumina Series sample (T0+50, D0+5).

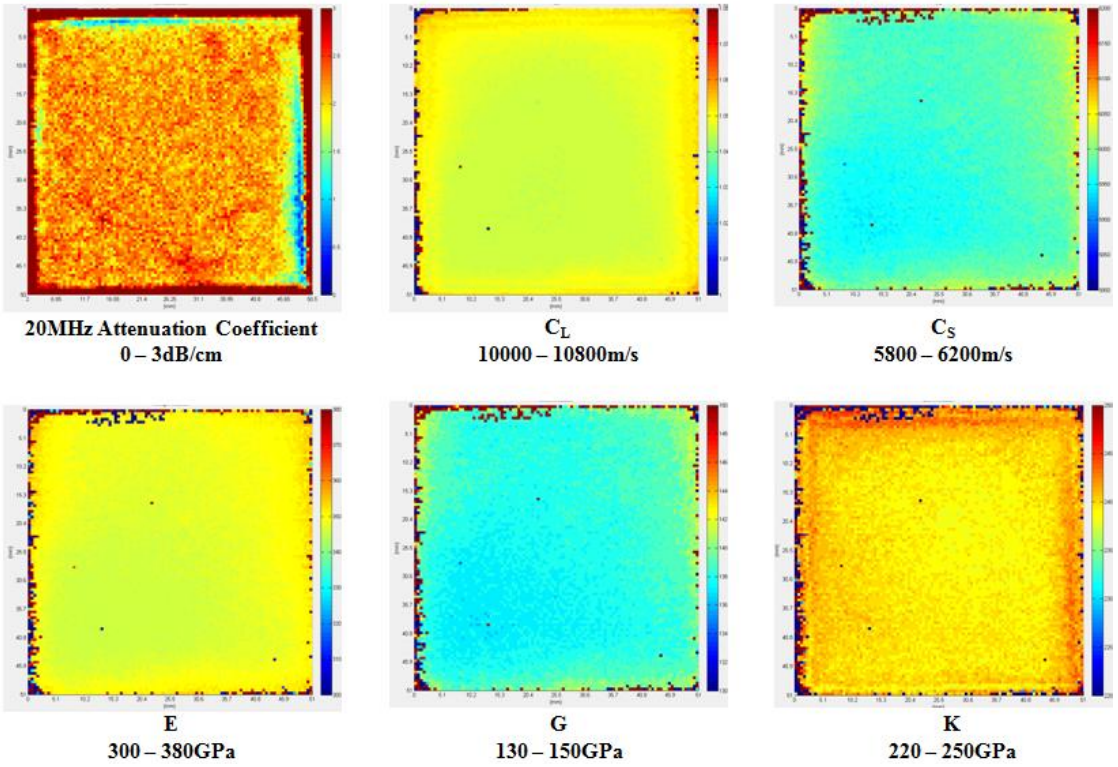

Figure 109. Ultrasonic C-Scan images of measured properties for Microstructural Evolution Alumina Series sample (T0+50, D0+15).

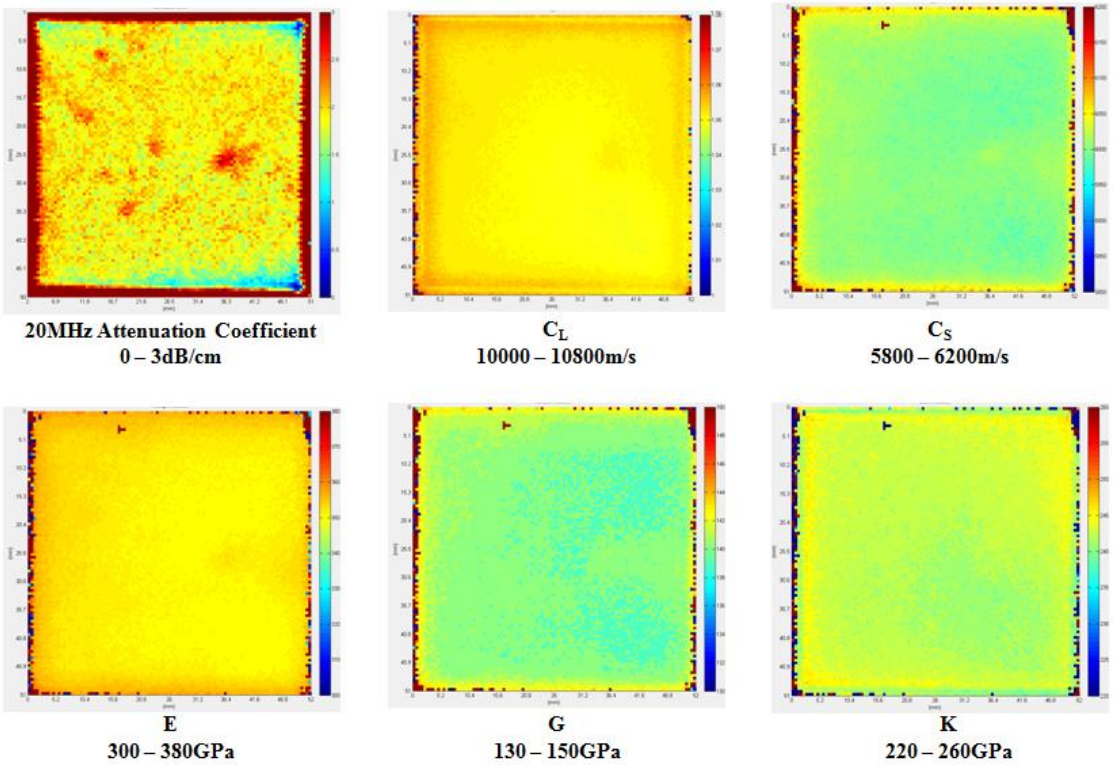

Figure 110. Ultrasonic C-Scan images of measured properties for Microstructural Evolution Alumina Series sample (T0+100, D0).

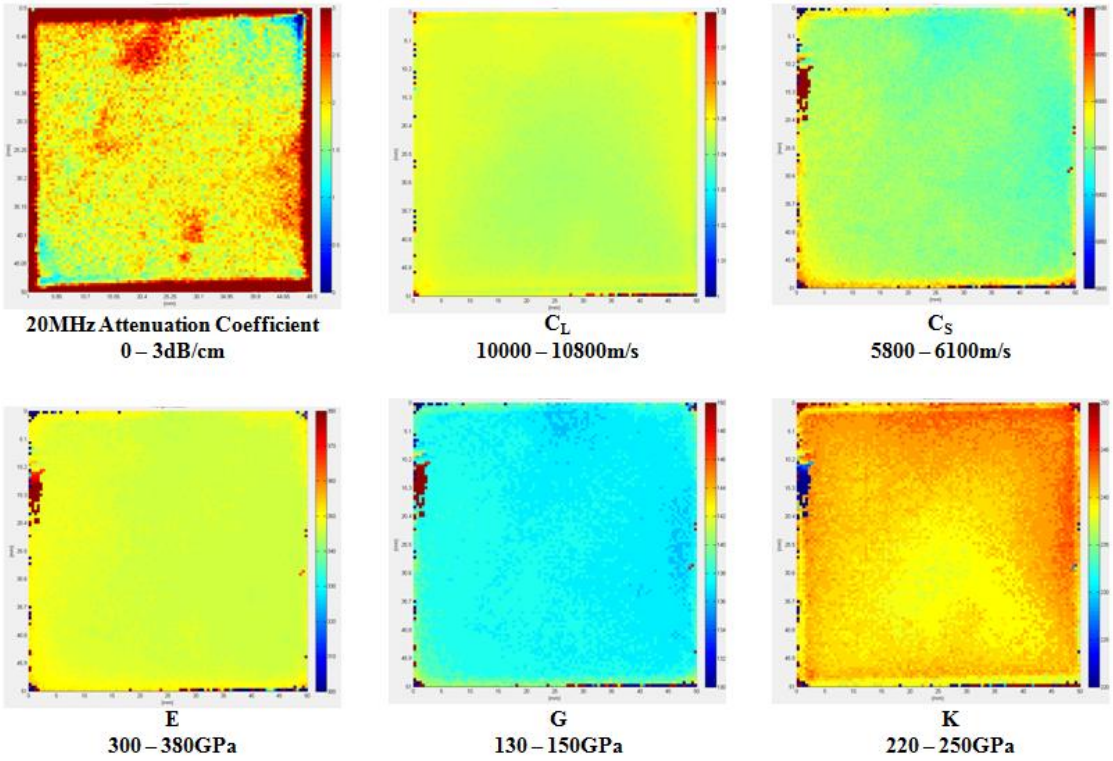

Figure 111. Ultrasonic C-Scan images of measured properties for Microstructural Evolution Alumina Series sample (T0+100, D0+5).

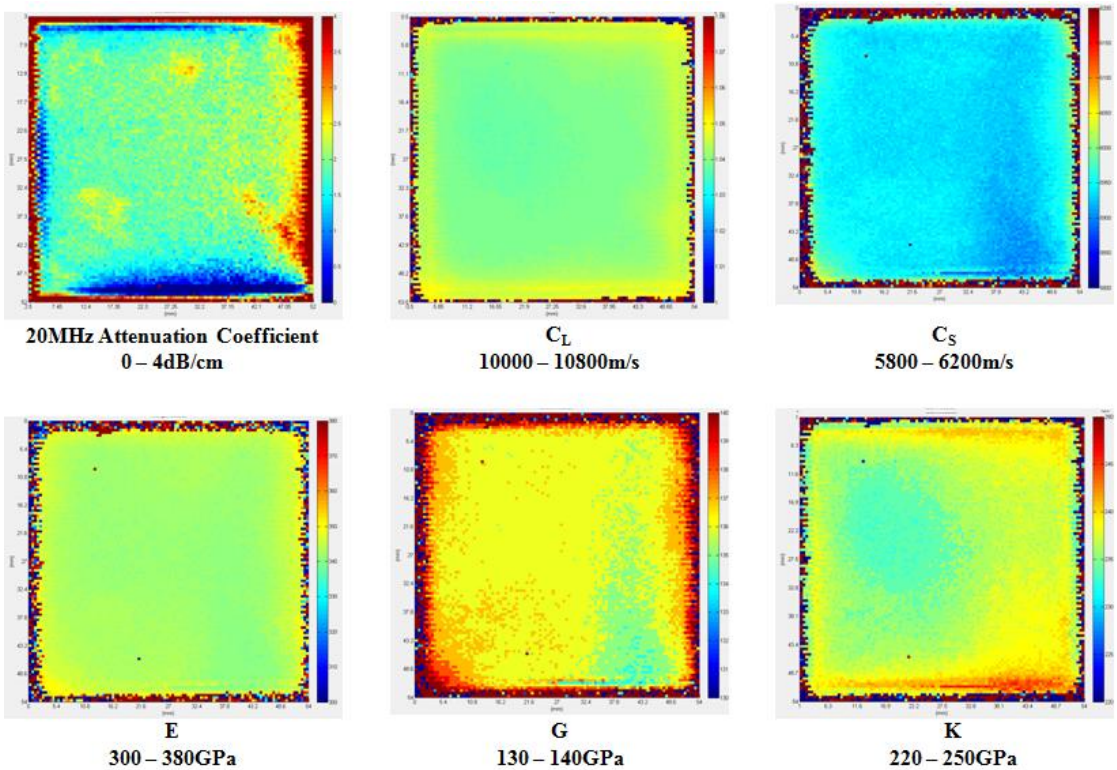

Figure 112. Ultrasonic C-Scan images of measured properties for Microstructural Evolution Alumina Series sample (T0+100, D0+15).

The scaling used for the various C-Scan maps seen in Figures 104-112 was approximately constant between samples with the exception of a few maps where the scales were changed slightly to avoid maxing out the color palette. This occurred notably for the samples listed: (T0, D0+15) bulk modulus map, (T0+100, D0) bulk modulus map, (T0+100, D0+15) 20MHz attenuation coefficient map, and (T0+100, D0+15) shear modulus map. The homogeneity of each sample can be determined by the attenuation coefficient C-Scan images. The samples in the Microstructural Evolution Alumina Series each have some degree of nonuniformity where these nonuniform regions were omitted during microstructural evaluation. Table XIV gives a statistical quantification regarding the variability of each sample property map. The sectioned regions from each sample for conventional microstructural testing were based off of the 20MHz attenuation coefficient C-Scans. The regions from each sample which were sectioned are highlighted in red on the attenuation coefficient C-Scan images, seen in Figure 113.

Almost all samples in this series presented with anomalous features noticeable primarily in the 20MHz attenuation coefficient C-Scan maps. If the features were prominent enough, their effect persisted to the TOF-based measurement; velocities and moduli. This occurred for samples (T0, D0), (T0+50, D0), and (T0+100, D0). All other points within the velocity or elastic properties maps which appear to be erroneous were caused by small fluctuations in the oscilloscope signal which went unmeasured. Each sample had some degree of beveling across its entire area which caused some regions to go unmeasured during acoustic testing. These effects can be seen in samples (T0, D0+15), (T0+50, D0), (T0+100, D0+5), and (T0+100, D0+15). The sample areas where beveling became prominent were excluded from further testing.

Table XIV. Statistical information taken over all points from Microstructural Evolution Alumina Series sample C-Scan images.

	20MHz α (dB/cm)	**C_L (m/s)**	**C_S (m/s)**	**ν**	**E (Gpa)**	**G (Gpa)**	**K (Gpa)**
(T0, D0)							
Mean	1.7	10474	6046	0.25	356	142	237
StDev	0.17	11.88	7.37	0	0.8	0.44	0.98
Min	1.07	10473	6036	0.25	355	142	242
Max	3.37	10526	6078	0.25	359	144	236
(T0, D0+5)							
Mean	1.9	10498	5988	0.26	351	139	243
StDev	0.18	14.82	13.48	0	1.27	0.73	1.04
Min	1.27	10473	5954	0.26	348	137	240
Max	3.57	10547	6028	0.26	355	142	246
(T0, D0+15)							
Mean	1.92	10509	5967	0.26	353	140	247
StDev	0.33	12.64	17.96	0	1.58	0.89	1.24
Min	0.87	10484	5924	0.26	350	138	241
Max	3.7	10559	6030	0.26	358	144	252
(T0+50, D0)							
Mean	1.83	10473	6028	0.25	354	141	238
StDev	0.22	15.08	8.42	0	0.57	0.44	1.48
Min	0.95	10444	5990	0.25	351	140	235
Max	3.11	10518	6046	0.25	355	142	243
(T0+50, D0+5)							
Mean	1.95	10469	5977	0.26	350	139	241
StDev	0.22	15.13	9.92	0	0.93	0.52	0.99
Min	0.83	10444	5884	0.26	342	135	238
Max	2.85	10529	6014	0.26	353	140	244
(T0+50, D0+15)							
Mean	2.17	10460	5978	0.26	348	138	240
StDev	0.19	13.98	15.5	0	1.56	0.75	1.16
Min	1.31	10440	5495	0.26	306	137	237

Max	2.95	10524	6031	0.26	353	142	244
(T0+100, D0)							
Mean	1.9	10512	6003	0.26	352	140	242
StDev	0.18	16.21	8.38	0	0.93	0.51	1.04
Min	0.73	10481	5981	0.26	350	139	239
Max	2.91	10576	6039	0.26	356	142	246
(T0+100, D0+5)							
Mean	1.88	10451	5952	0.26	346	137	240
StDev	0.19	15.25	9.9	0	0.9	0.58	1.33
Min	1.3	10422	5921	0.26	344	136	236
Max	3.03	10517	6171	0.26	364	140	244
(T0+100, D0+15)							
Mean	2.04	10407	5937	0.26	342	136	236
StDev	0.33	25.19	10.95	0	1.21	0.6	1.59
Min	1.22	10337	5899	0.26	339	134	233
Max	4.54	10504	5984	0.26	350	140	241

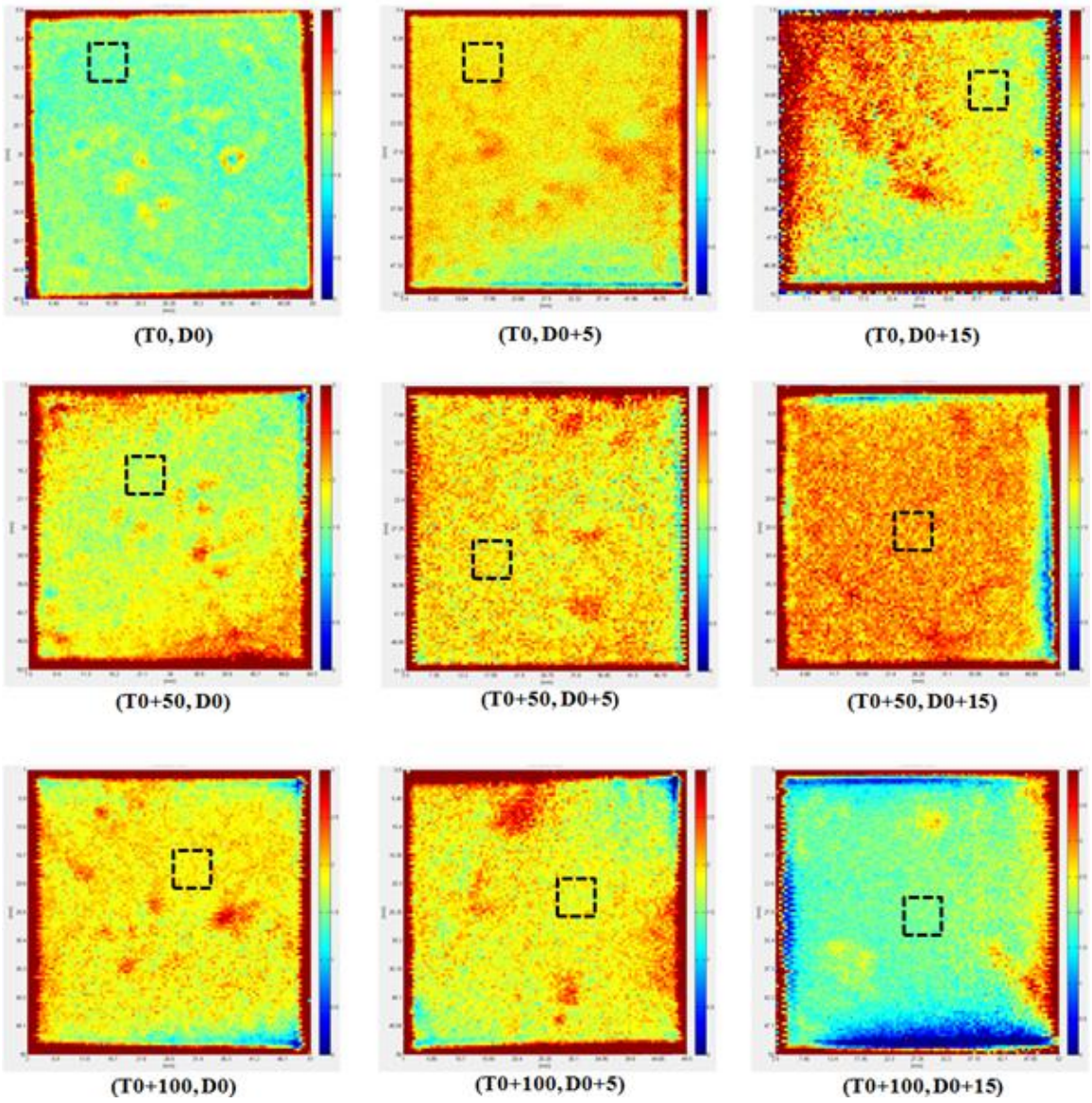

Figure 113. 20MHz overall attenuation coefficient C-Scan maps showing regions which were sectioned for conventional microstructural testing.

The goal of this sample set was to study uniform alumina microstructures and the effect of grain size on acoustic testing. The anomalous regions seen in the 20MHz overall attenuation coefficient C-Scan images were omitted as they were not represented of a uniform alumina microstructure. Due to the inhomogeneity seen in the 20MHz attenuation coefficient maps, slight sample nonuniformity and bevel, full area attenuation

coefficient C-Scan images using the 60MHz or 150MHz transducer could not be obtained. The effects of sample nonuniformity become increasingly noticeable as acoustic frequency was increased. For this reason, single A-Scan point measurements of frequency dependent attenuation coefficient were taken using the 20, 60, and 150MHz transducers about the regions which were deemed acceptable for further testing. The composite graphs of attenuation coefficient using all three transducers can be seen in Figure 114. Again, gaps in the frequency regions of approximately 30-40MHz and 70-80MHz can be seen due to the limited bandwidth of each transducer.

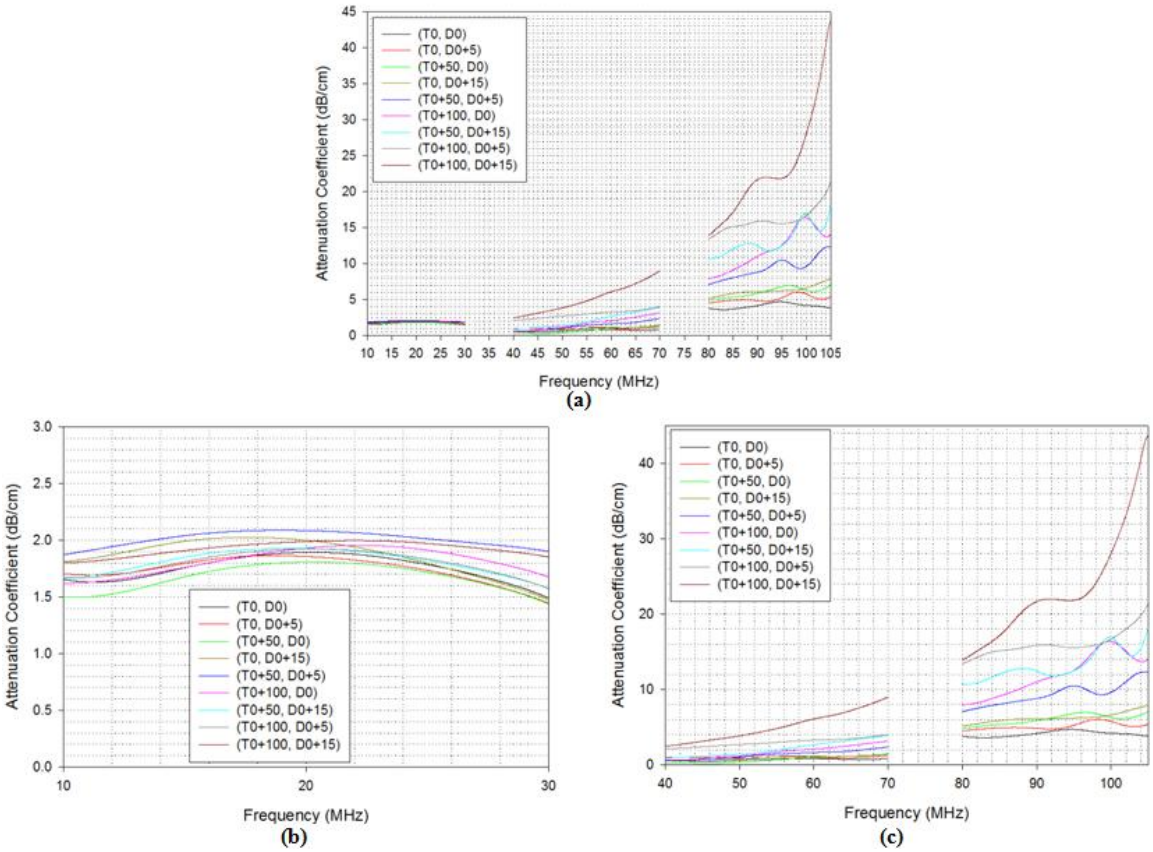

Figure 114. Attenuation coefficient spectra taken about labeled regions in Figure 113. (a) Full scale; (b) Frequency region where absorption dominates; (c) Frequency region where scattering dominates.

The attenuation coefficient spectra measured on the largest frequency bandwidth capable shows both absorption and scattering behavior at different frequencies. Figure 114 (b) shows the peak-like behavior associated with absorptive attenuation. This absorption is most likely caused by the small amount of sintering additives or impurities within the samples. It would be expected that the maxima of these peaks would shift to lower frequencies as alumina grain size increased if the attenuation seen in Figure 114 (b) was controlled by alumina grains. According to the theory of acoustic thermoelastic absorption, alumina grains on the order of 5 microns and greater will actively absorb at much lower frequencies than what was used to measured attenuation coefficient in this thesis.

Figure 114 (c) is the truncated portion of the total measured attenuation coefficient spectra which is controlled by alumina grain scattering. It is this portion of the attenuation coefficient spectrum that is crucial for achieving one of the goals in this thesis. The spectra in the frequency range of 40-105MHz taken from each sample in the Microstructural Evolution Alumina Series shows a strong correlation between the magnitude of attenuation and the increase in dwell time and firing temperature. This indicates that attenuation increased with increasing grain size. The increase in grain size as firing temperature and dwell times increased across samples is verified through microscopy in the next section.

5.4.2. Microstructural Evolution Alumina Series FESEM Results

Each sample in the Microstructural Evolution Alumina series was section about the region labeled in Figure 113. Each of these sections was vertically cut to reveal the inside cross section which the acoustic wave travelled through. These surfaces were those which were examined using the FESEM. Representative micrograph images of each sample are shown in Figures 116-118. The FESEM images are grouped such that temperature is held constant and dwell time varies. Qualitatively, there is a slight increase in grain size between groupings seen in Figures 116-118. As the firing temperature increases the grain size increases as well. Quantitative assessments of sample grain size can be seen in Figure 115. The plots in Figure 115 represent a top-down view of the size distributions from each sample. The samples have been ordered such that they are on an increasing size scale.

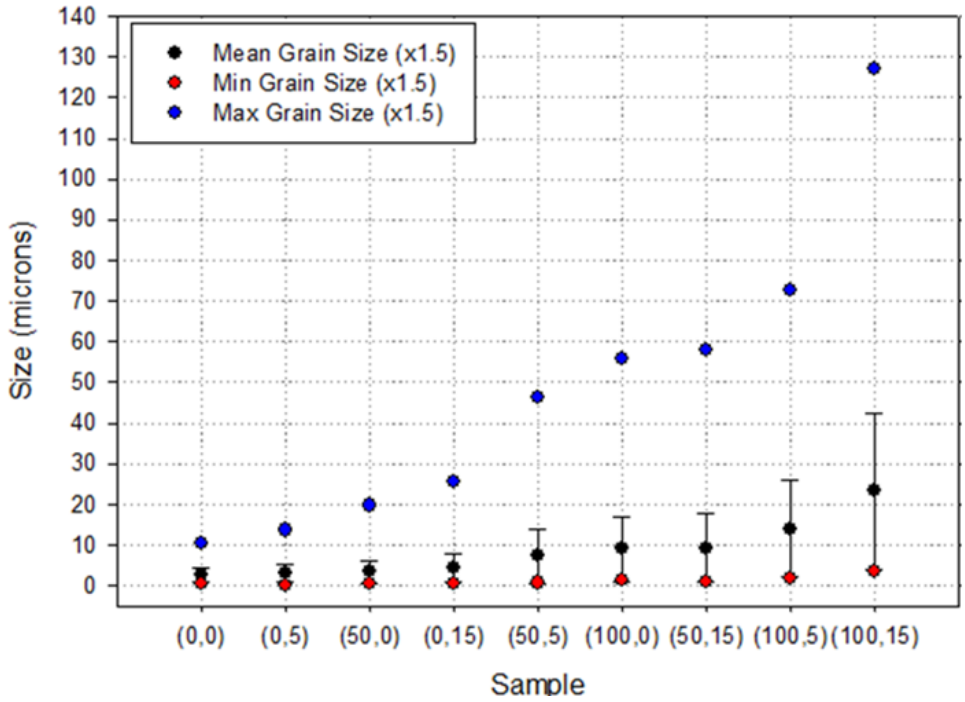

Figure 115. Quantitative evaluation of grain sizes measured from FESEM micrographs. Sizes have been corrected for stereographic effects. Error bars show standard deviation. Ordered pair sample notation is (+increase in temperature, +increase in dwell time).

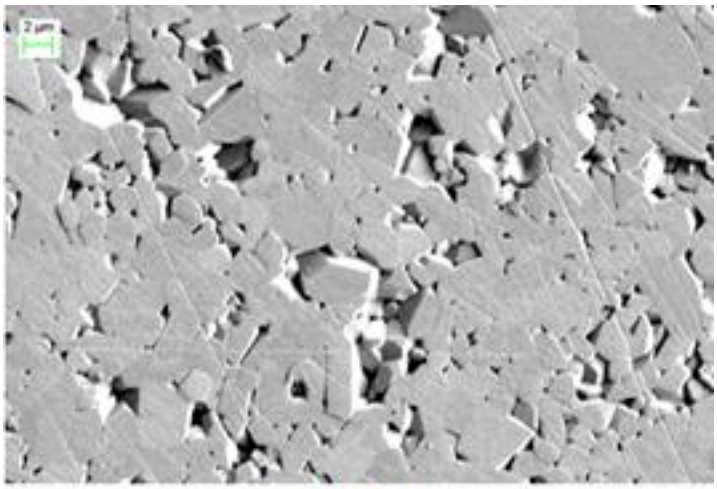

(T0, D0)

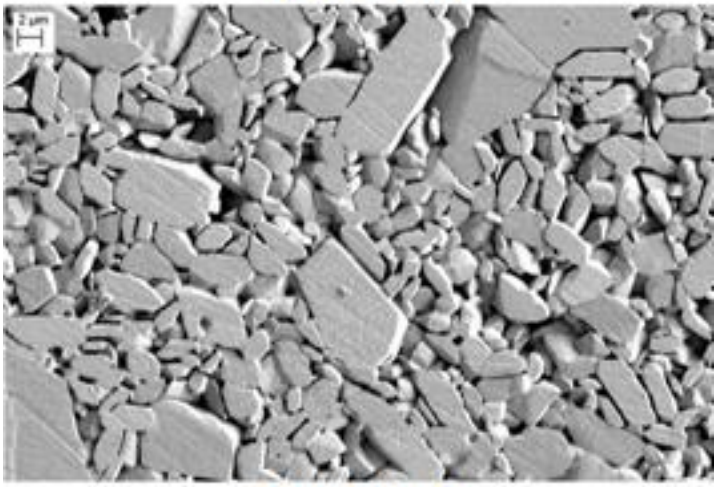

(T0, D0+5)

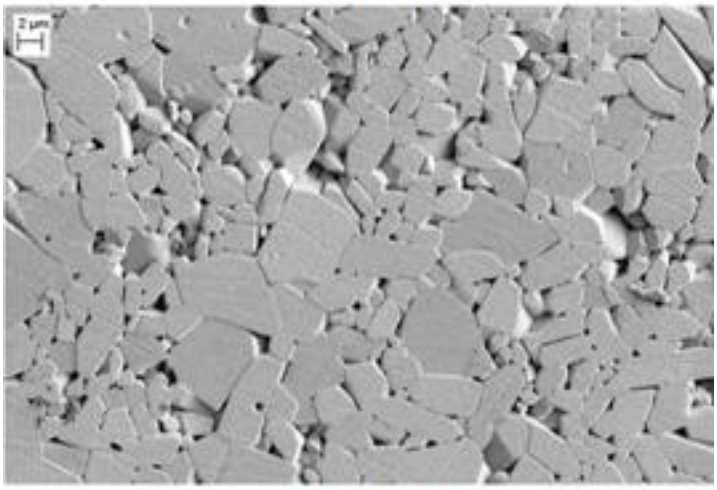

(T0, D0+15)

Figure 116. Representative FESEM micrograph images of Microstructural Evolution Alumina Series samples keeping firing temperature at T0 and varying dwell time.

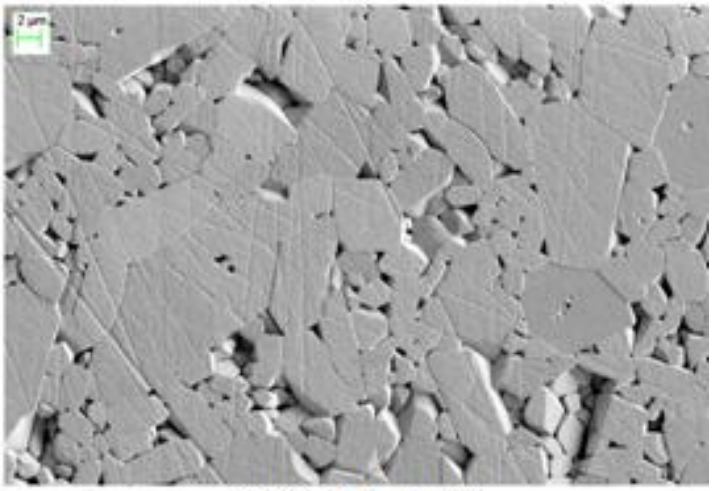

(T0+50, D0)

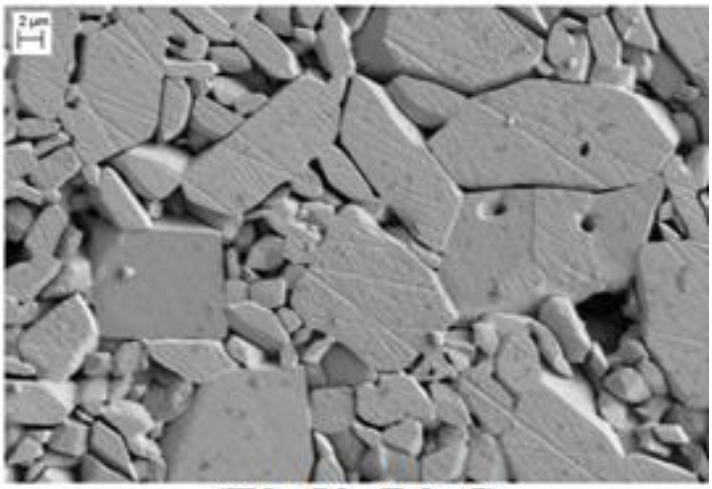

(T0+50, D0+5)

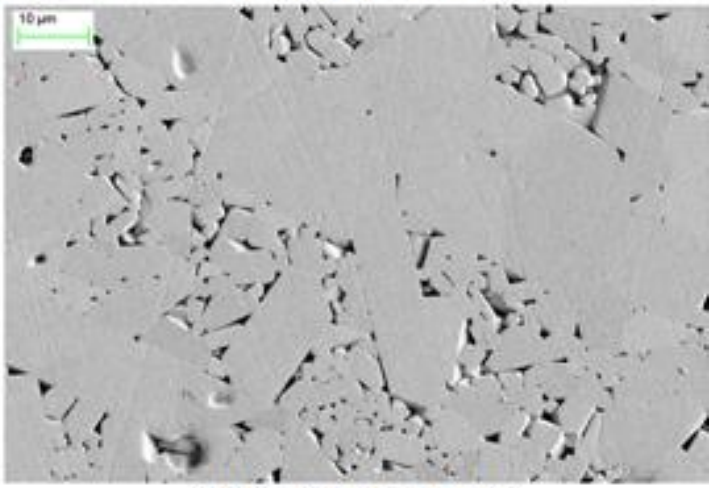

(T0+50, D0+15)

Figure 117. Representative FESEM micrograph images of Microstructural Evolution Alumina Series samples keeping firing temperature at T0+50 and varying dwell time.

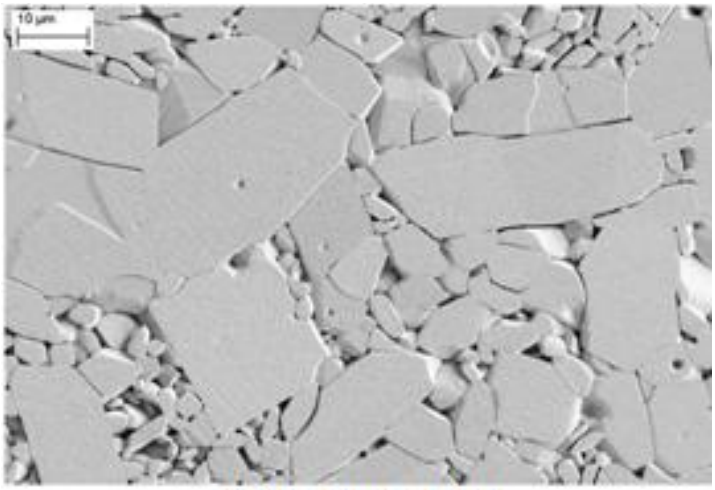

(T0+100, D0)

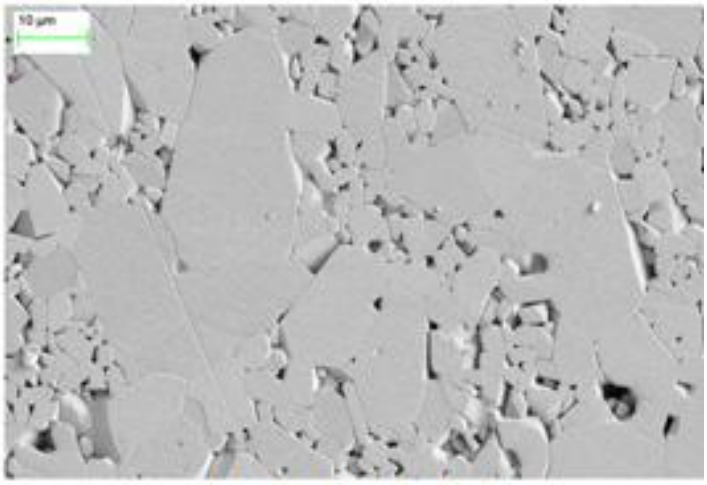

(T0+100, D0+5)

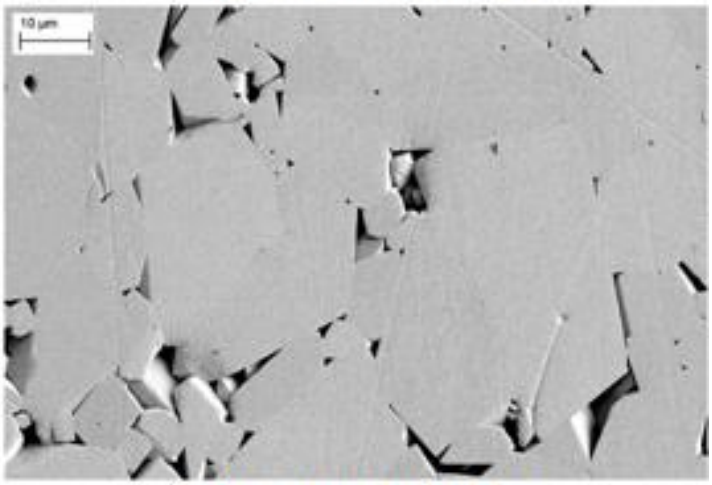

(T0+100, D0+15)

Figure 118. Representative FESEM micrograph images of Microstructural Evolution Alumina Series samples keeping firing temperature at T0+100 and varying dwell time.

5.5. Characterization of Unknown Grain Size Alumina Series

The characterization results with respect to ultrasound testing, FESEM imaging, EDS analysis, and micrograph analysis for the Unknown Grain Size Alumina Series sample set are given in this section. A discussion of the results is given to highlight specific trends or irregularities for both the ultrasound test results and conventional microstructural testing results. Analysis of acoustic spectra are given in this section while the conclusions regarding measured acoustic spectra, acoustic scattering theory, creation of standard scattering factors for Rayleigh and stochastic scattering, and comparison to measured average grain sizes are drawn in section 5.6.2.2.

5.5.1. Unknown Grain Size Alumina Series Ultrasound Testing Results

The purpose of the Unknown Grain Size Alumina Series is to validate the results and standard scattering prefactors, C_R and C_S, obtained from the Microstructural Evolution Alumina Series. Elastic moduli C-Scans from three different alumina samples are given in this section along with attenuation-based measurements. Figures 119-121 show these elastic property maps for each sample in this set. Table XV gives statistical information obtained from each property map for each sample.

More importantly are the attenuation coefficient spectra obtained over portions of the sample areas at frequencies where scattering is dominant. Overall attenuation coefficient C-Scan images were created for each sample to determine the presence of any large anomalous features present at 20MHz in the bulk microstructure. Figure 122 shows these C-Scan images which verify that these samples have rather uniform microstructures at 20MHz.

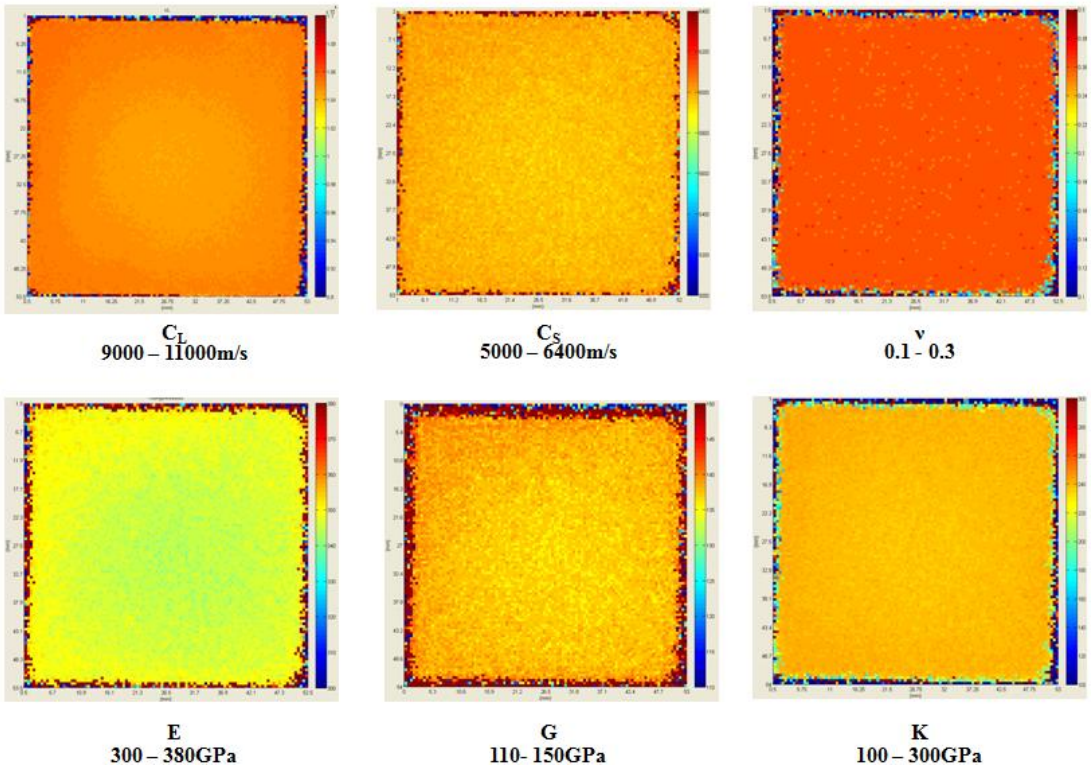

Figure 119. Ultrasonic C-Scan images of measured elastic properties for Unknown Grain Size Alumina Series sample Small.

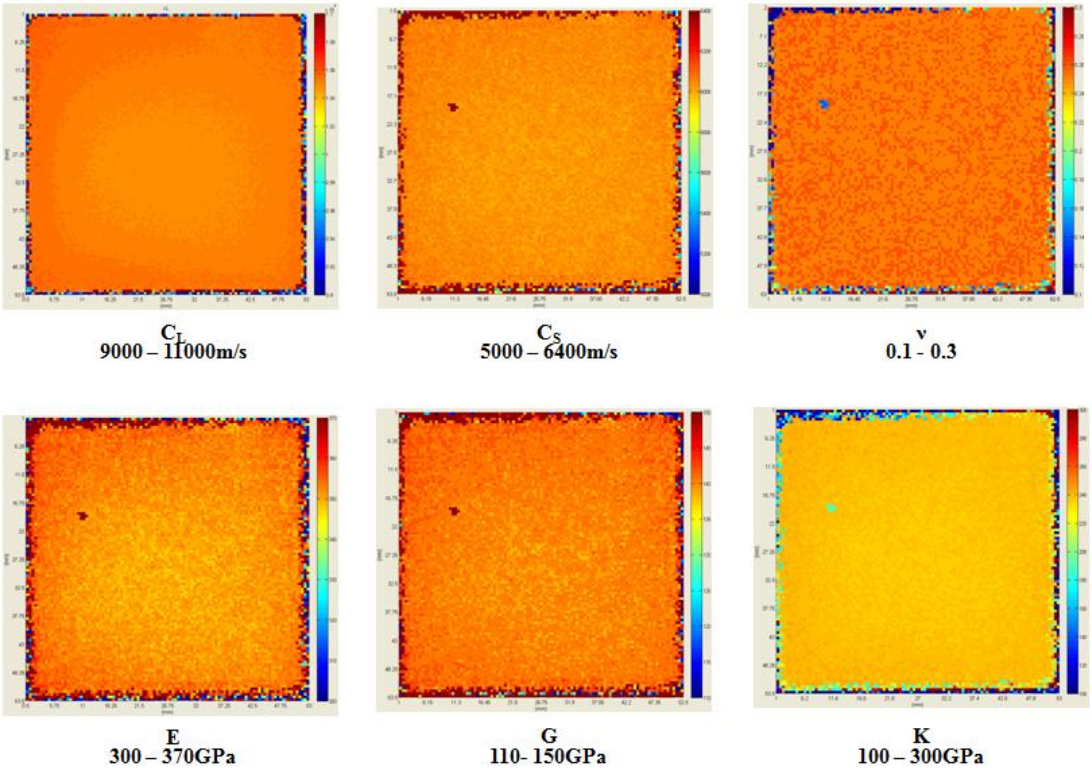

Figure 120. Ultrasonic C-Scan images of measured elastic properties for Unknown Grain Size Alumina Series sample Medium.

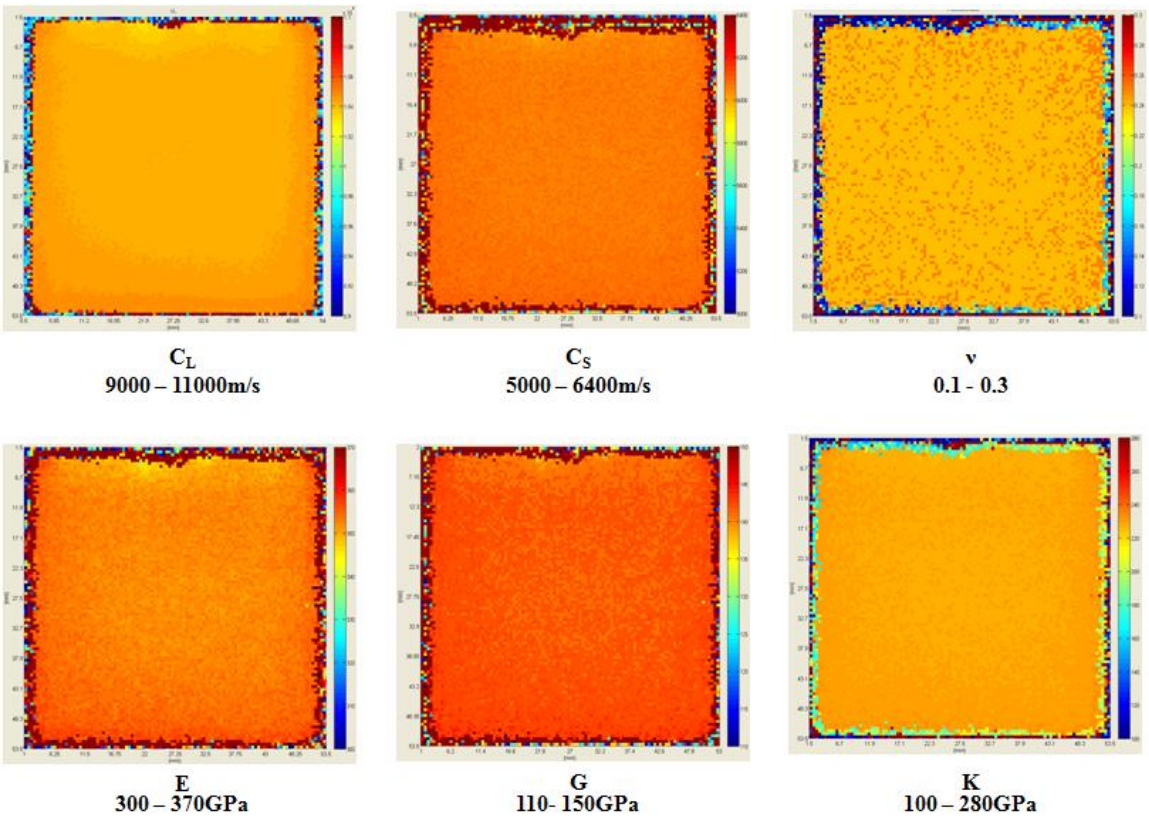

Figure 121. Ultrasonic C-Scan images of measured elastic properties for Unknown Grain Size Alumina Series sample Large.

Table XV. Statistical information taken over all points from Unknown Grain Size Alumina Series sample C-Scan images.

	C_L (m/s)	C_S (m/s)	ν	E (Gpa)	G (Gpa)	K (Gpa)
SMALL						
Mean	10486	5979	0.26	346	137	238
StDev	26.2	23.71	0	1.94	1	1.49
Min	10426	5901	0.26	340	134	234
Max	10570	6503	0.26	353	141	244
MEDIUM						
Mean	10507	6028	0.25	351	139	237
StDev	17.08	16.48	0	1.53	0.84	1.3
Min	10468	5974	0.25	346	137	233
Max	10564	6078	0.25	356	142	242
LARGE						
Mean	10426	6066	0.24	352	141	229
StDev	12	9.65	0	0.89	0.58	0.99
Min	10400	6037	0.24	350	140	227
Max	10471	6096	0.24	355	143	234

These samples had significant sample bevel which made them not perfectly parallel. Most high hardness, high density, ceramic tiles have some form of beveling over their entire areas. The slight beveling in each sample makes it such that the top and bottom of each surface are not even with each other. High frequency C-Scans obtained with ultrasound greater than 30MHz have the tendency of containing erroneous information as the acoustic wave gets redirected away from the transducer due to the sample bevel. This can be seen in Figure 123 which show attempts to obtain 60MHz overall signal attenuation C-Scan images.

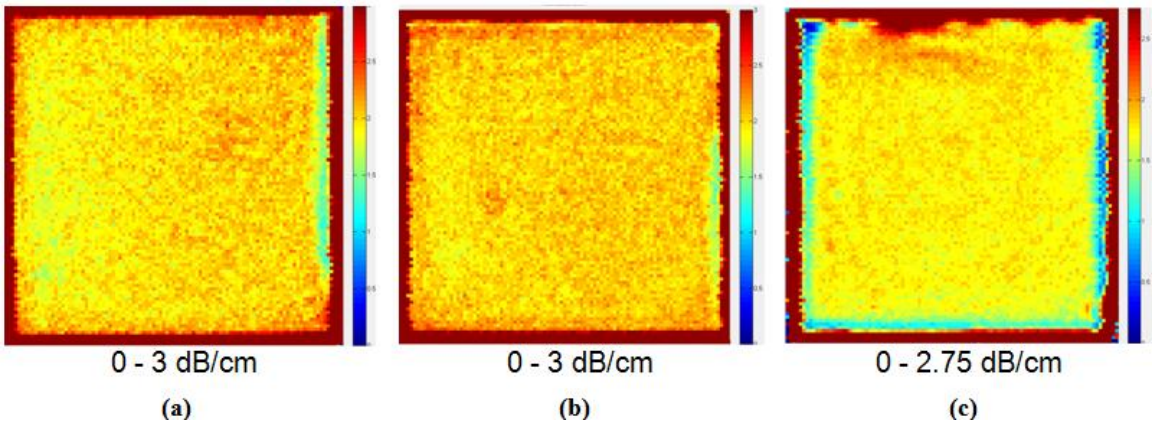

Figure 122. 20MHz overall attenuation coefficient C-Scan maps of (a) Small, (b) Medium, and (c) Large samples from the Unknown Grain Size Alumina Series.

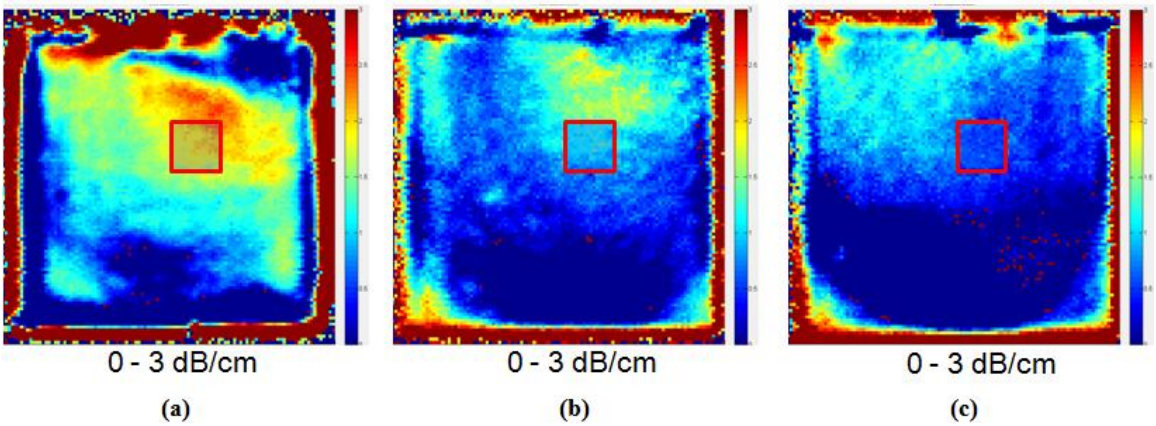

Figure 123. 60MHz overall attenuation coefficient C-Scan maps of (a) Small, (b) Medium, and (c) Large samples from the Unknown Grain Size Alumina Series. Highlighted regions represent areas scanned to alleviate sample bevel effects.

The red highlighted areas seen in the 60MHz overall attenuation coefficient C-Scan maps in Figure 123 represent smaller sections which were rescanned to alleviate issues due to sample bevel. It was necessary to obtain frequency-based attenuation coefficient information over the area of these samples such that maps of mean grain size could be created. The rescans of the smaller sections shown in Figure 123 are shown in Figure 124.

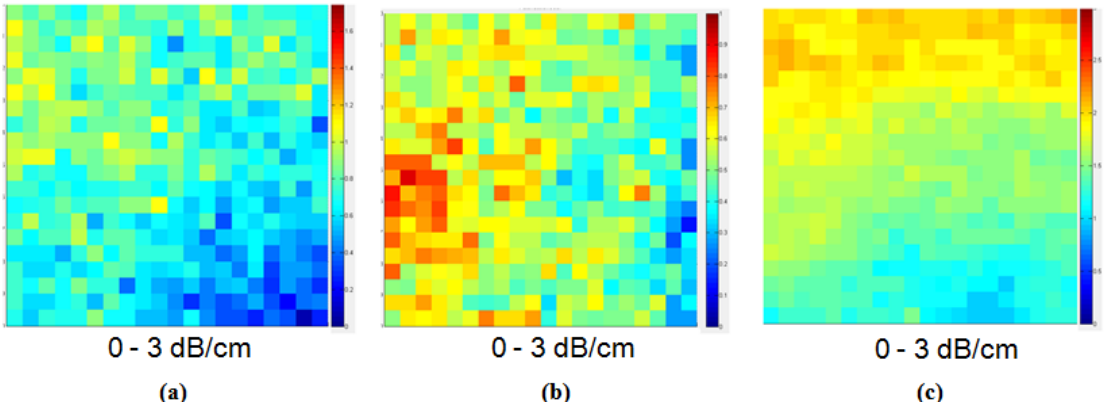

Figure 124. Selected regions from 60MHz overall attenuation coefficient C-Scan maps of (a) Small, (b) Medium, and (c) Large samples from the Unknown Grain Size Alumina Series.

The frequency bandwidth which was used to create these images was on a range of 40-70MHz. Average frequency-based attenuation coefficient spectra were created using the individual spectra from each point in each sample. These average spectra show if absorption, scattering, or both types of loss mechanisms are occurring about the selected region of each sample. These average spectra can be seen in Figure 125. Figure 125 (a) reveals that there is peak-like behavior indicative of an absorption mechanism up to approximately 62MHz. This part of the attenuation coefficient spectrum is believed to be caused by absorption where scattering does not become dominant until approximately 64MHz. All transformations using the attenuation coefficient spectra about the selected area in this sample will omit the portion of the spectra which shows absorptive behavior.

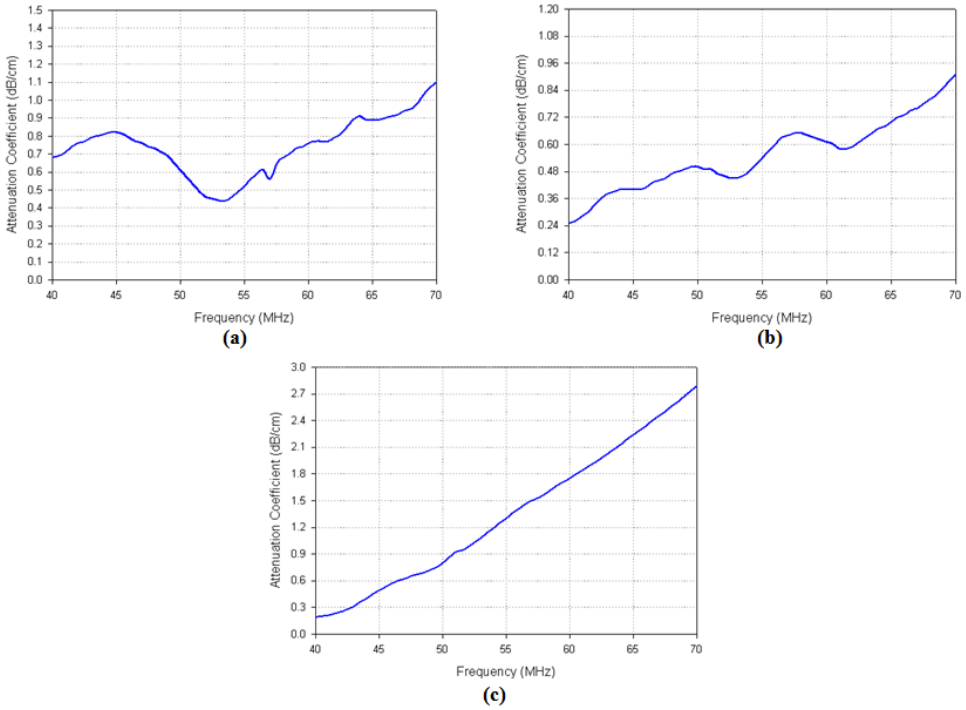

Figure 125. Average attenuation coefficient spectra taken from multiple points in samples (a) Small, (b) Medium, (c) Large.

The average spectrum from the medium sample in this set shows some peak-like behavior which is superimposed on the increasing attenuation coefficient spectrum at approximately 57MHz. Qualitatively, the overall trend of this spectrum can be seen to be power-law in nature. The peak which appears at 57MHz for this spectrum is more likely to be convolution with some small degree of diffuse scattering than an absorptive loss mechanism. This is believed to be the case as a significant concentration of alumina grains of approximately 550nm would need to be present to cause intraparticle thermoelastic absorption at such high frequencies. The entire measured bandwidth (40-70MHz) will be used in transforming the spectra from the medium and large samples into average grain size maps.

Frequency dependent attenuation coefficient spectra maps are typically shown in a slideshow format which cannot be presented as part of this thesis. Figures 126-128

show these data as separate images as attenuation coefficient C-Scan maps using a frequency interval of 1MHz starting from 40MHz. As frequency increases, the magnitude of attenuation is monotonically increasing on average. This is a tell-tale feature of scattering loss behavior.

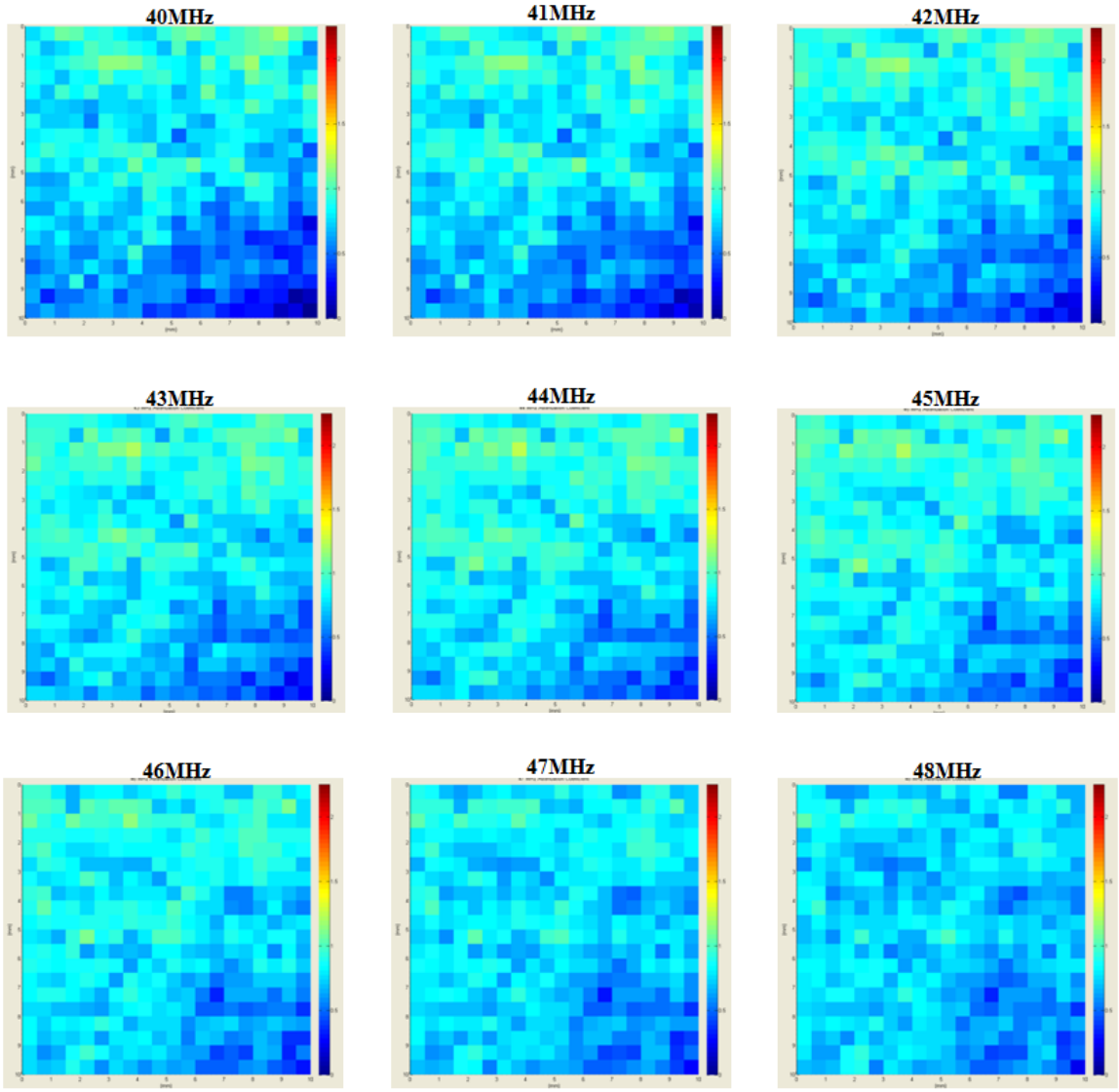

Figure 126a. Attenuation coefficient spectra maps for Unknown Grain Size Alumina Series sample Small. Color palette range: 0-2.25dB/cm. Frequency range: 61-70MHz with an interval of 1MHz.

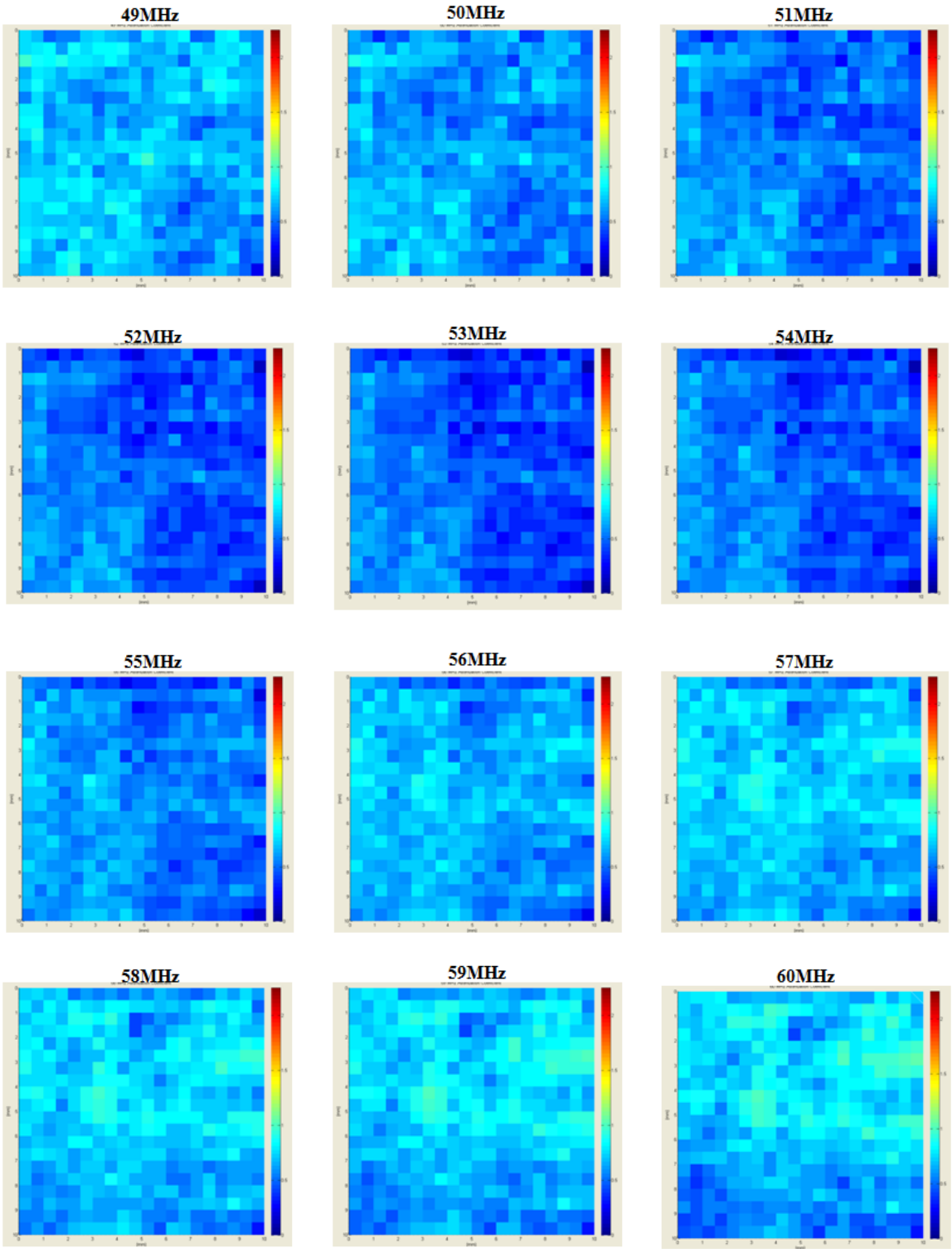

Figure 126b. Attenuation coefficient spectra maps for Unknown Grain Size Alumina Series sample Small. Color palette range: 0-2.25dB/cm. Frequency range: 61-70MHz with an interval of 1MHz.

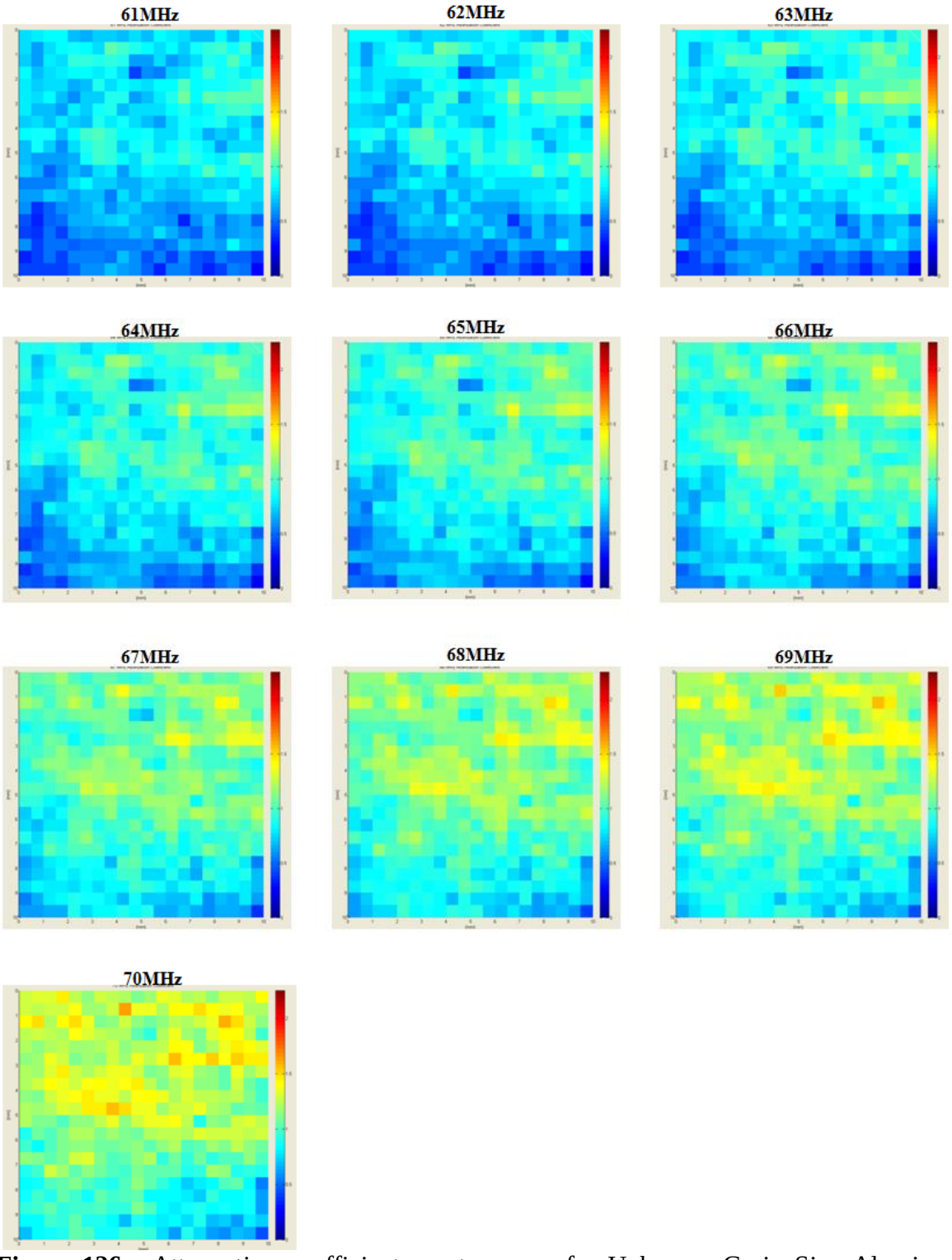

Figure 126c. Attenuation coefficient spectra maps for Unknown Grain Size Alumina Series sample Small. Color palette range: 0-2.25dB/cm. Frequency range: 61-70MHz with an interval of 1MHz.

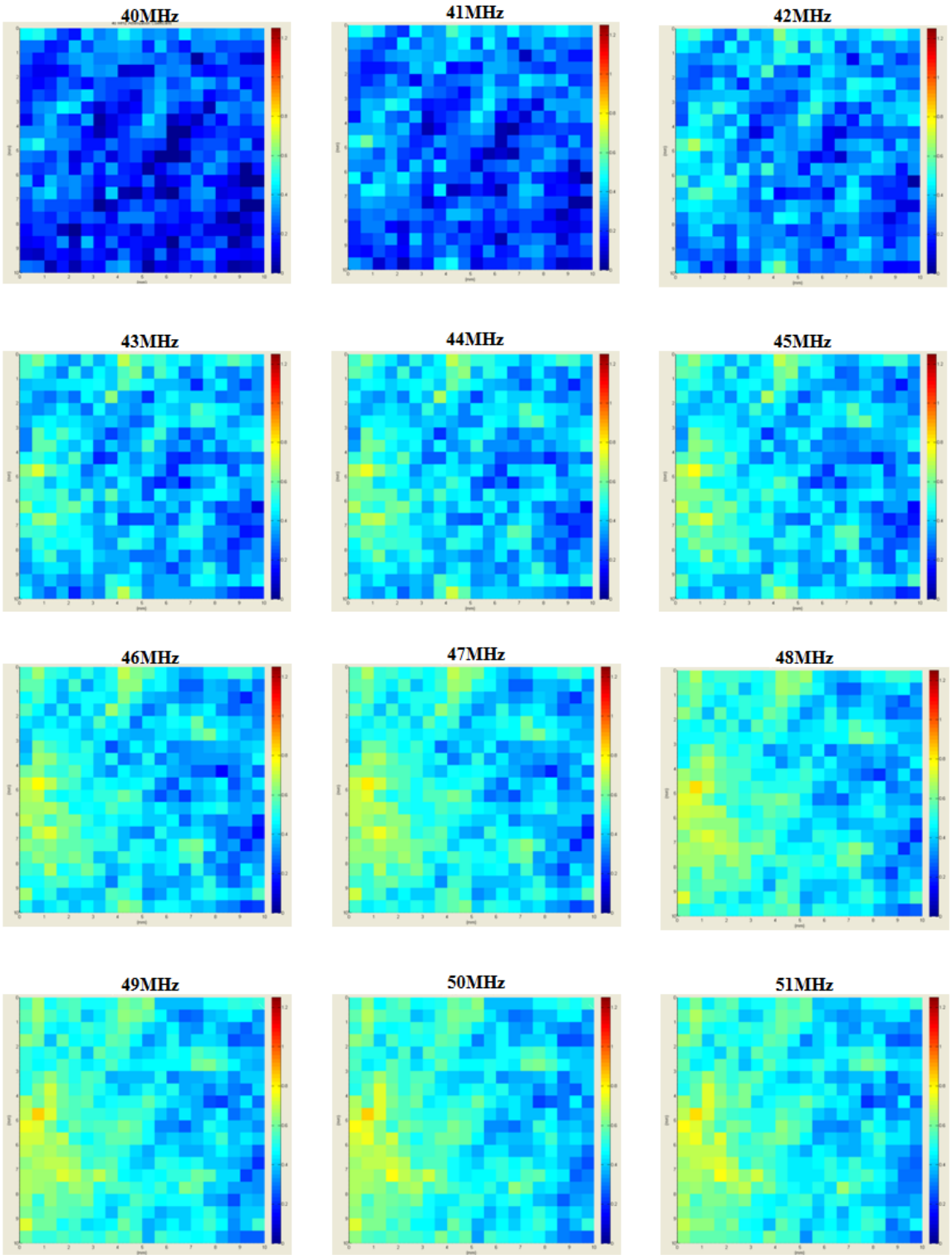

Figure 127a. Attenuation coefficient spectra maps for Unknown Grain Size Alumina Series sample Medium. Color palette range: 0-1.25dB/cm. Frequency range: 64-70MHz with an interval of 1MHz.

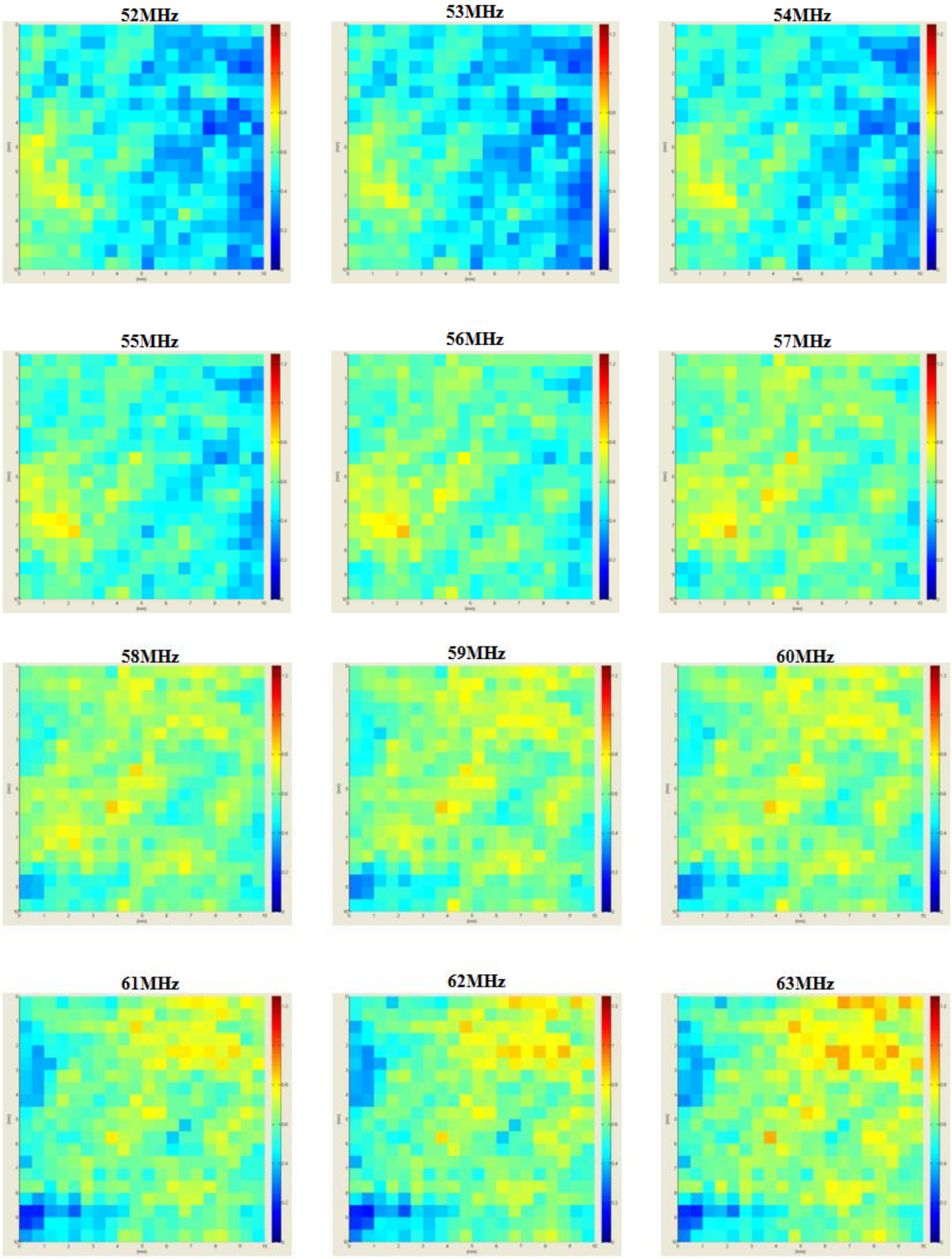

Figure 127b. Attenuation coefficient spectra maps for Unknown Grain Size Alumina Series sample Medium. Color palette range: 0-1.25dB/cm. Frequency range: 64-70MHz with an interval of 1MHz.

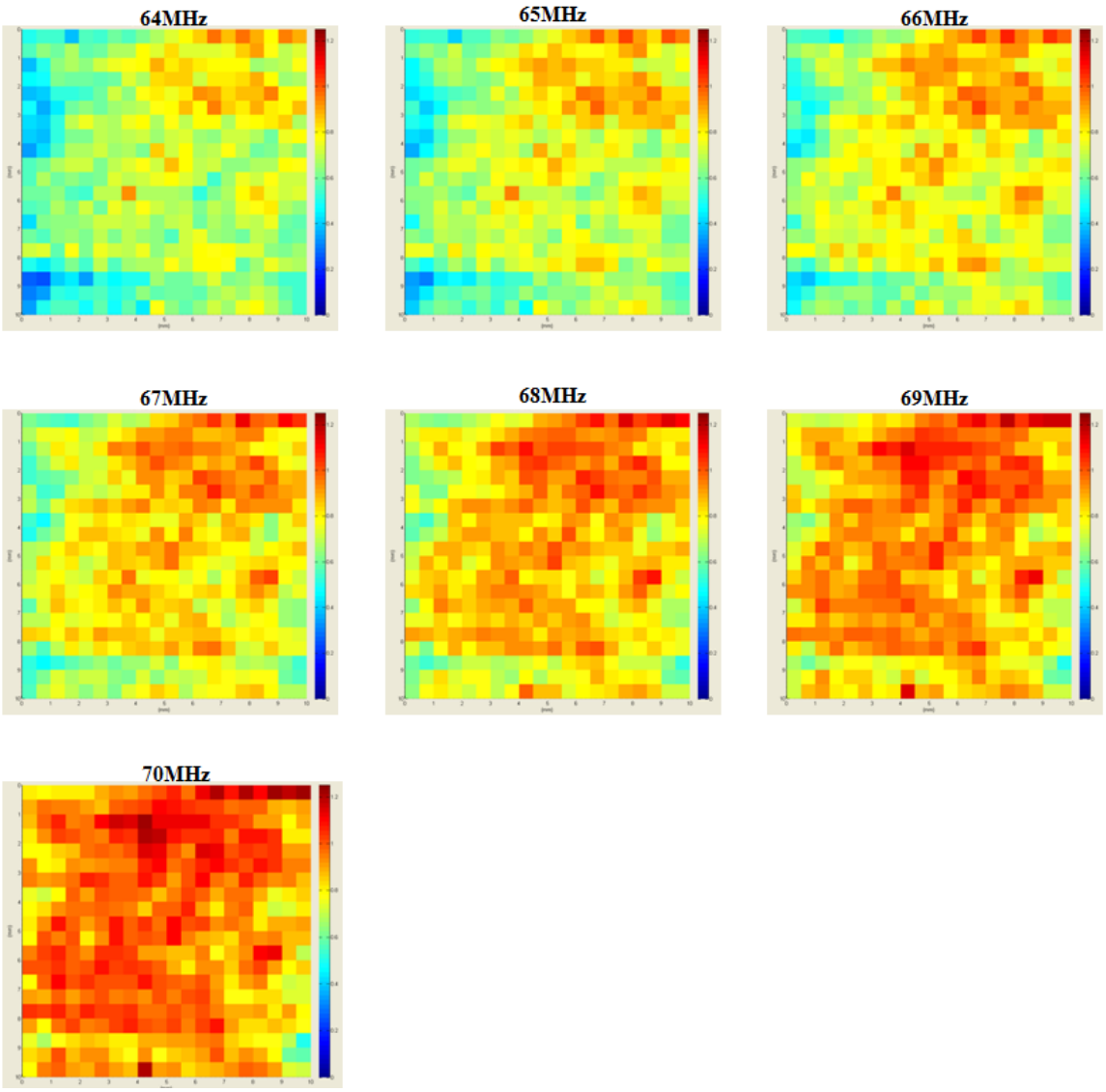

Figure 127c. Attenuation coefficient spectra maps for Unknown Grain Size Alumina Series sample Medium. Color palette range: 0-1.25dB/cm. Frequency range: 64-70MHz with an interval of 1MHz.

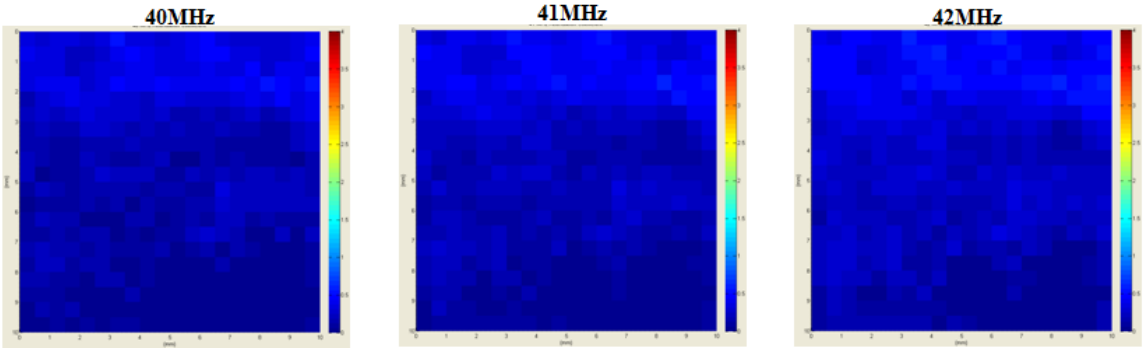

Figure 128a. Attenuation coefficient spectra maps for Unknown Grain Size Alumina Series sample Large. Color palette range: 0-4dB/cm. Frequency range: 55-66MHz with an interval of 1MHz.

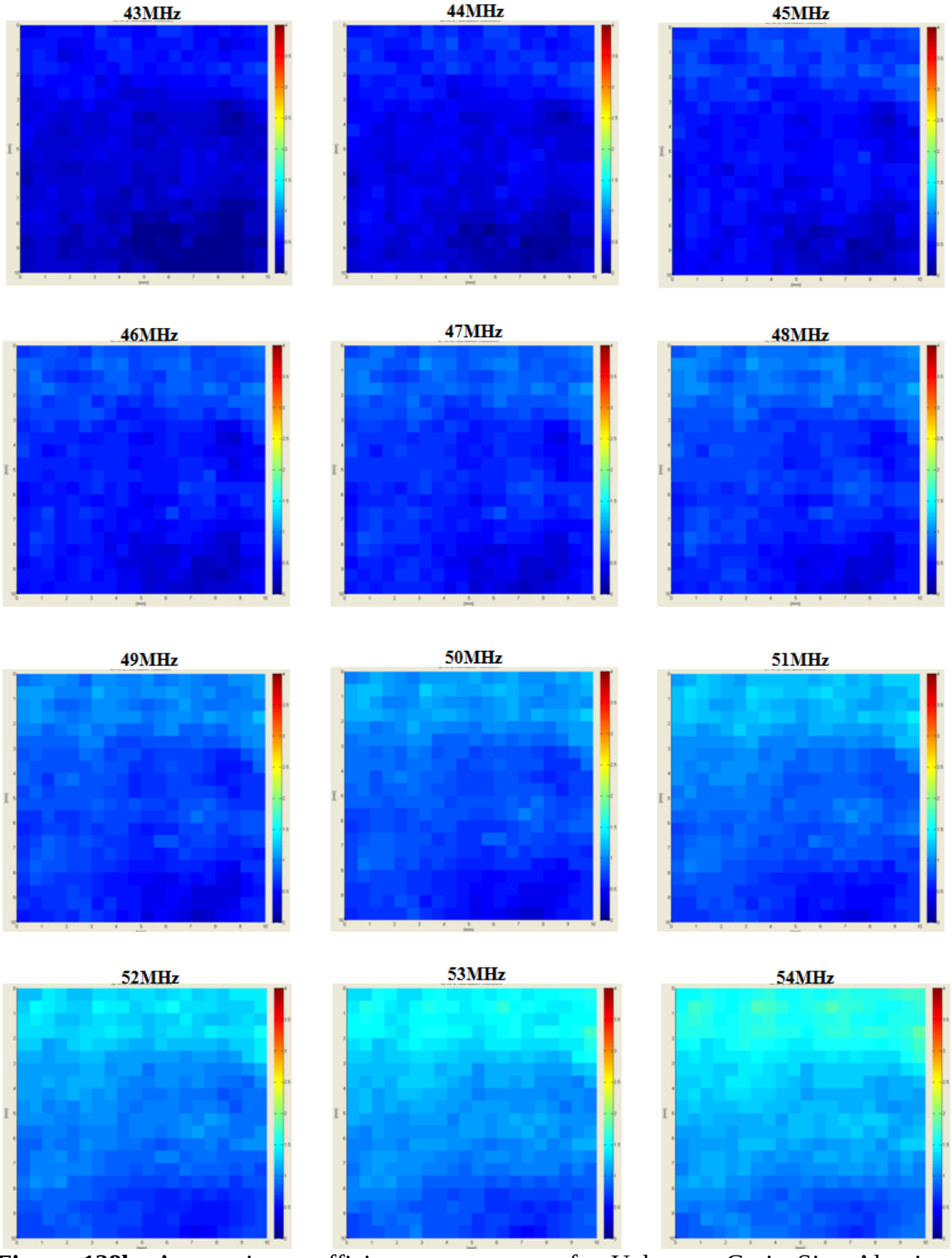

Figure 128b. Attenuation coefficient spectra maps for Unknown Grain Size Alumina Series sample Large. Color palette range: 0-4dB/cm. Frequency range: 55-66MHz with an interval of 1MHz.

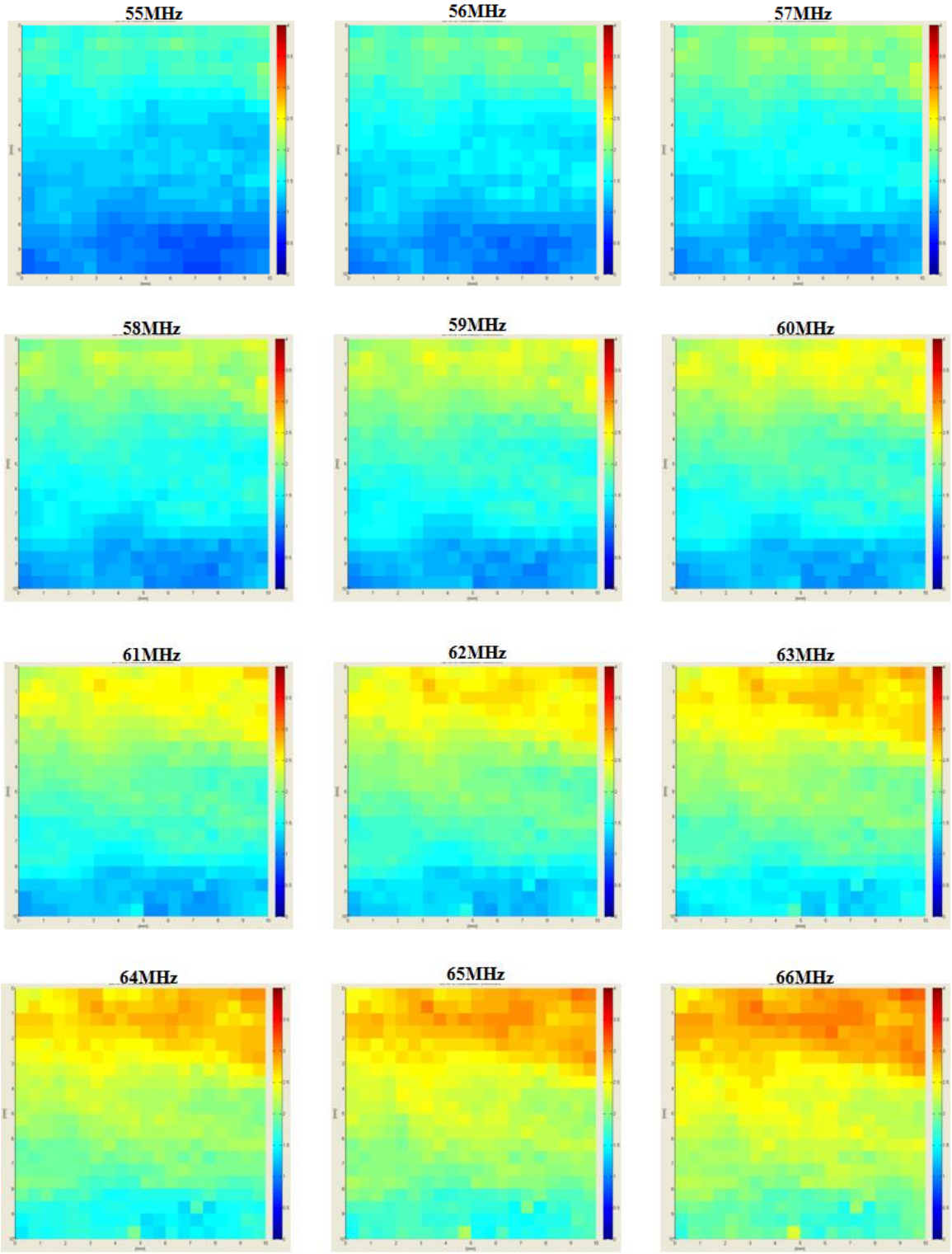

Figure 128c. Attenuation coefficient spectra maps for Unknown Grain Size Alumina Series sample Large. Color palette range: 0-4dB/cm. Frequency range: 55-66MHz with an interval of 1MHz.

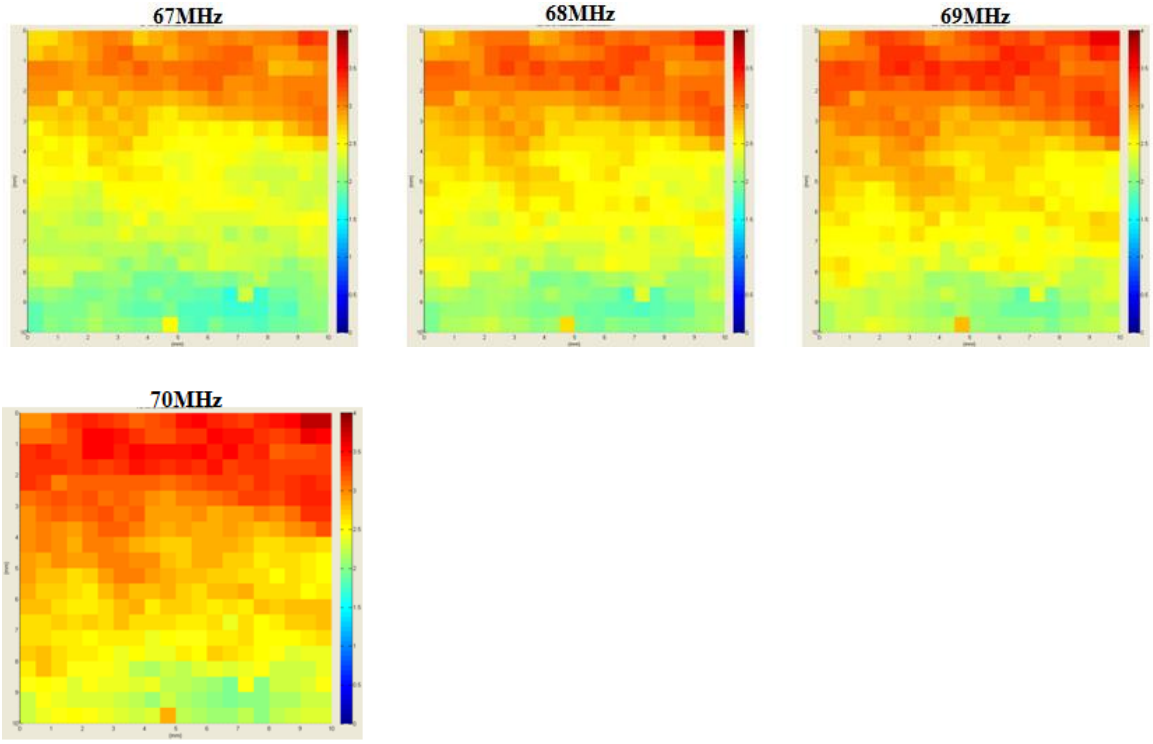

Figure 128d. Attenuation coefficient spectra maps for Unknown Grain Size Alumina Series sample Large. Color palette range: 0-4dB/cm. Frequency range: 55-66MHz with an interval of 1MHz.

The attenuation coefficient spectra maps show little variation between individual frequencies. Looking on a larger frequency scale, the true nature of how these spectra maps change can be understood. It was shown by Portune that for high hardness, dense, polycrystalline ceramics, a change in attenuation coefficient at ultra high frequencies where scattering dominates is caused primarily by fluctuations in grain size [20]. The patterns seen in the spectra maps from Figures 126-128 are believed to be caused by exactly this and will be verified in section 5.6.2.2.

5.5.2. Unknown Grain Size Alumina Series FESEM Results

Five micrograph images taken about horizontal sections through the center of the regions labeled in Figure 123 were used to create measured grain size distributions for each of the three samples in the Unknown Alumina Grain Size Series. A considerable

degree of charging occurred while performing FESEM analysis on these samples; however, using the inlens detector allowed for imaging at low voltages and high magnifications acceptable to be read into the Lince© software for grain size measurements. Representative micrograph images from each sample, Small, Medium, and Large, are shown in Figure 129.

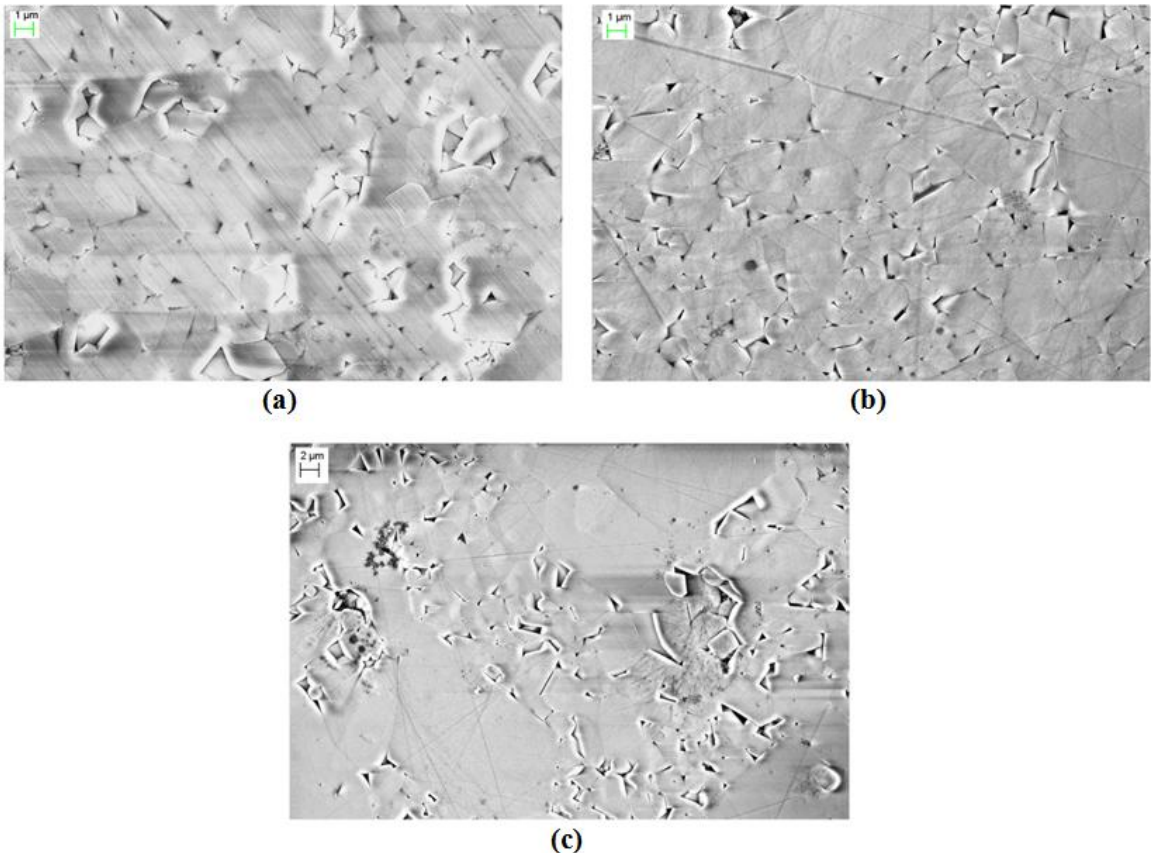

Figure 129. Micrograph images samples (a) Small, (b) Medium, and (c) Large from the Unknown Grain Size Alumina Series.

Measured grain size distributions for each sample show size variations between sections. Table XVI gives the mean, standard deviation, minimum, and maximum values for measured grain sizes. Figure 130 shows normalized grain size distributions fit to Weibull functions for simple comparisons. The size scale for each plot is different

between samples. Comparison of these measured grain size distributions are made with what is predicted through acoustic spectroscopy in section 5.6.2.2.

Table XVI. Statistical information taken from grain size measurements of Unknown Alumina Grain Size Series samples. Units are in microns.

	SMALL	MEDIUM	LARGE
Mean	1.94	1.58	3.90
StDev	1.47	1.15	3.40
Min	0.21	0.25	0.42
Max	13.26	8.62	21.68

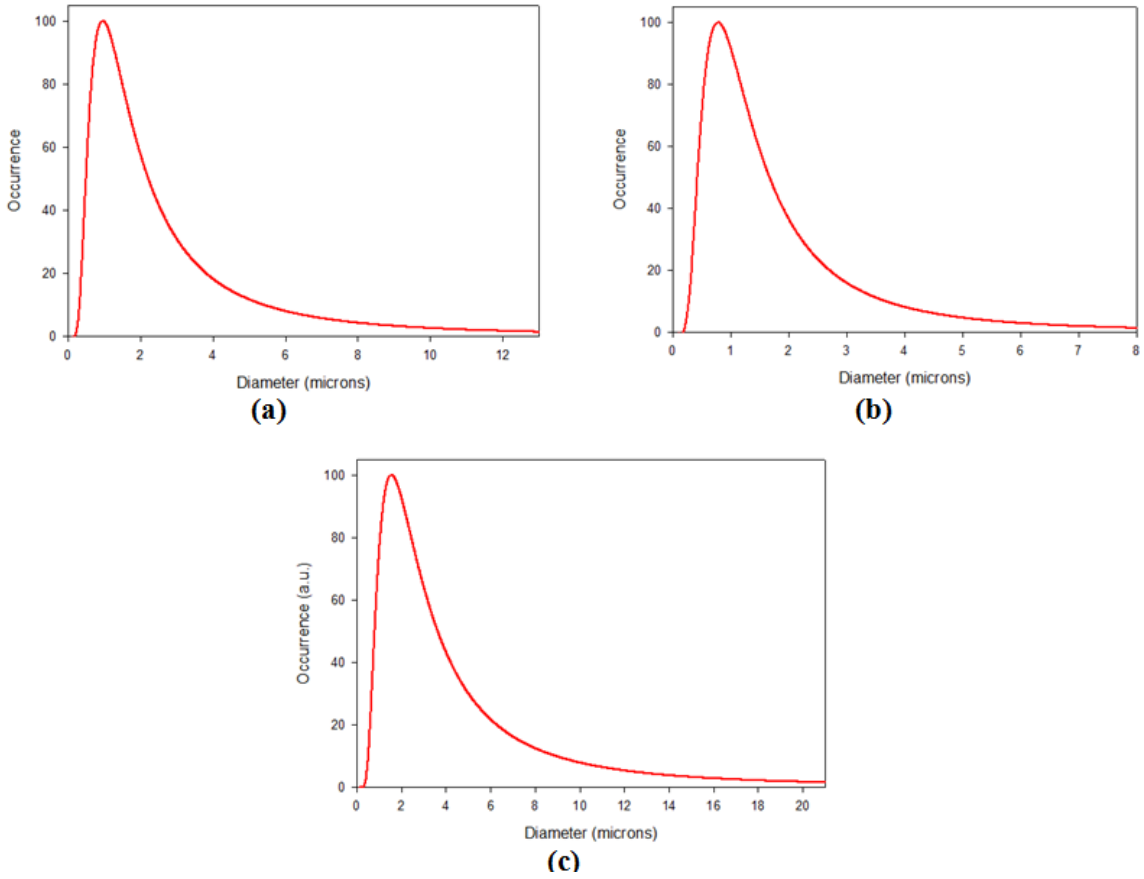

Figure 130. Measured Unknown Grain Size Alumina Series size distributions. (a) Small, (b) Medium, (c) Large.

5.6. Analysis of Acoustic Spectroscopy Results

This section examines correlations between acoustic spectroscopy results and microstructural analyses for each of the four alumina-based sample sets studied in this thesis. Discussions of these results are broken into two sections: samples relating to absorption-based attenuation and those relating to scattering-based attenuation. Possible sources of error which would cause ultrasound predicted grain sizes to differ from conventionally measured grain sizes are explored at the end of this section.

5.6.1. Absorption-Based Acoustic Spectroscopy

The following results involve the transformations of the attenuation coefficient spectra collected from the Mullite Series and Titanium Carbide Series samples to give absolute grain size distributions. The process involving correction for the contribution of thermoelastic absorption by alumina grains is explained. The curve fitting parameters along with how well each fit matched measured acoustic predicted grain size data are given.

5.6.1.1. Analysis of Mullite Series

The attenuation coefficient spectra measured for the Mullite series is used in conjunction with equation 78, the initial energy output of the 20MHz transducer, force output of the 20MHz transducer, and the thermal properties of mullite to obtain mullite grain size distributions. The contribution of the alumina grains present in the path of the ultrasound beam which would also cause intraparticle thermoelastic absorption must be taken into account. The attenuation coefficient spectra obtained from the 100% alumina standard sample is multiplied by the volume percent of alumina measured through X-ray diffraction for each sample. The volume percent of Al_2O_3 in each sample of the Mullite

Series is less than 100%, so this gives a decrease in the 100% alumina attenuation coefficient spectra. These spectra are then subtracted from their associated spectra for each sample containing different amounts of mullite. The final result gives the attenuation coefficient spectra caused solely by the mullite grains in each sample which would be of the appropriate size to cause thermoelastic absorption in the frequency range of 12-30MHz. Figure 131 gives these attenuation coefficient spectra.

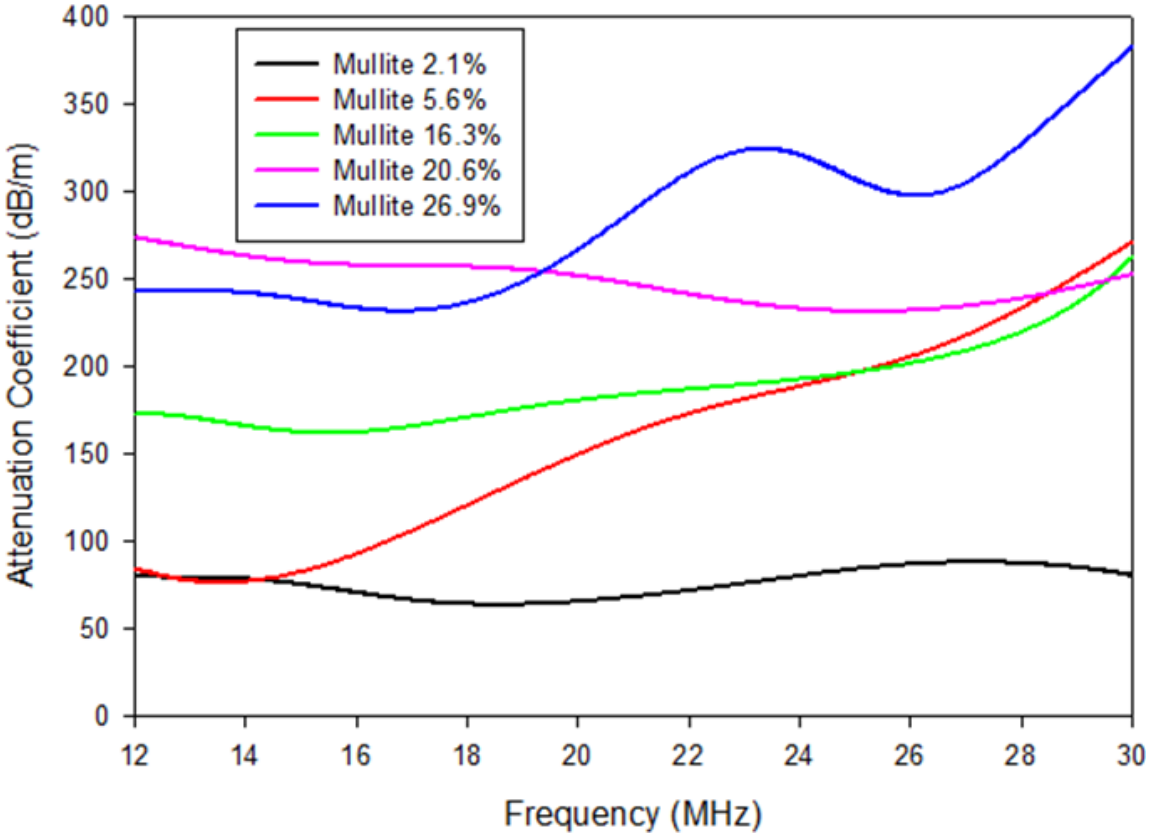

Figure 131. Mullite Series attenuation coefficient spectra corrected for thermoelastic absorption contribution of alumina grains. Gives attenuation spectra solely caused by mullite in each sample.

Using the spectra in Figure 131 along with the other necessary components listed above, grain size distributions in the size range of 0.25-0.40µm for each mullite sample were created. The range of 0.25-0.40µm is dictated by the Zener relationship (equation

30) used in equation 78. Figure 132 shows the mullite grain size distributions in this narrow range for each sample in the Mullite Series.

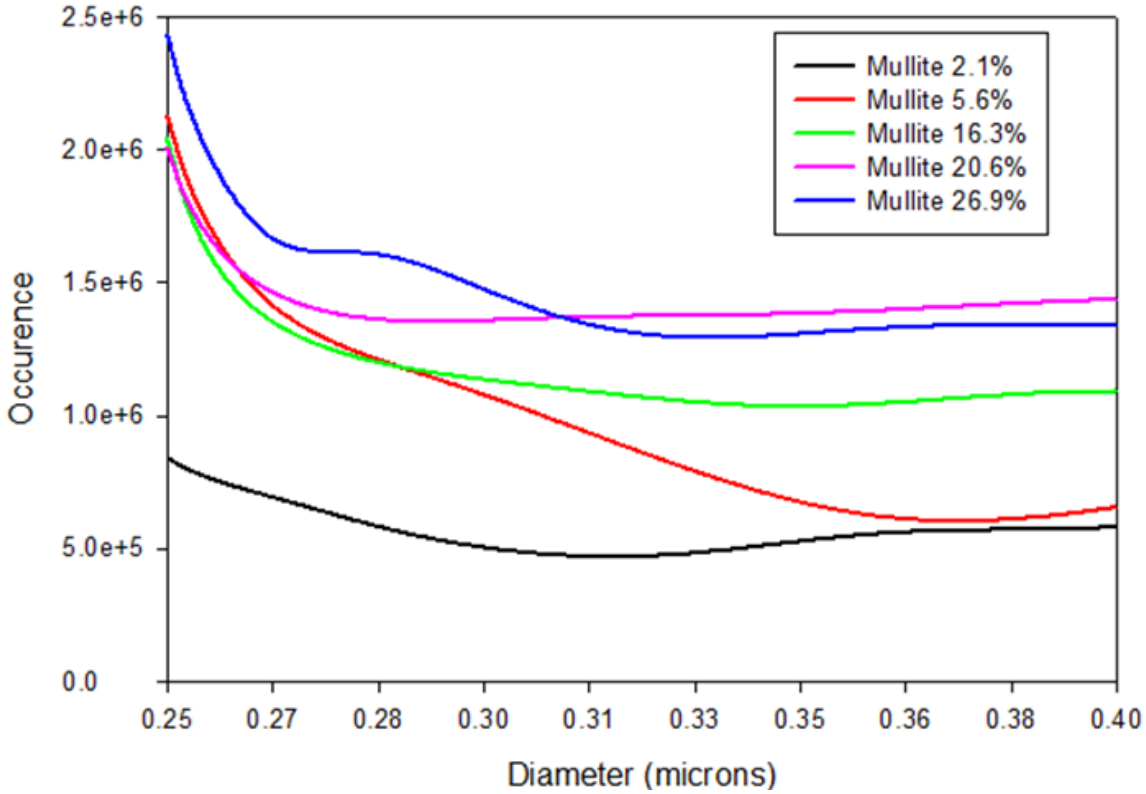

Figure 132. Ultrasound predicted Mullite Series grain size distributions on size range of 0.25-0.40μm corresponding to frequency range of 12-30MHz.

The ultrasound predicted grain size distributions given in Figure 132 show only a portion of the full mullite grain size distributions present in each sample. It was grains of the sizes shown above which contributed to intraparticle thermoelastic absorption. These curves were fit to Gaussian functions using the curve fitting tool in MATLAB. Figure 133 shows the fully Gaussian reconstructed mullite grain size distributions for each sample in the Mullite Series. Table XVII gives information relating to the parameters of each curve fit. Each Gaussian curve fit was allowed to take multiple modes if it provided the best fit.

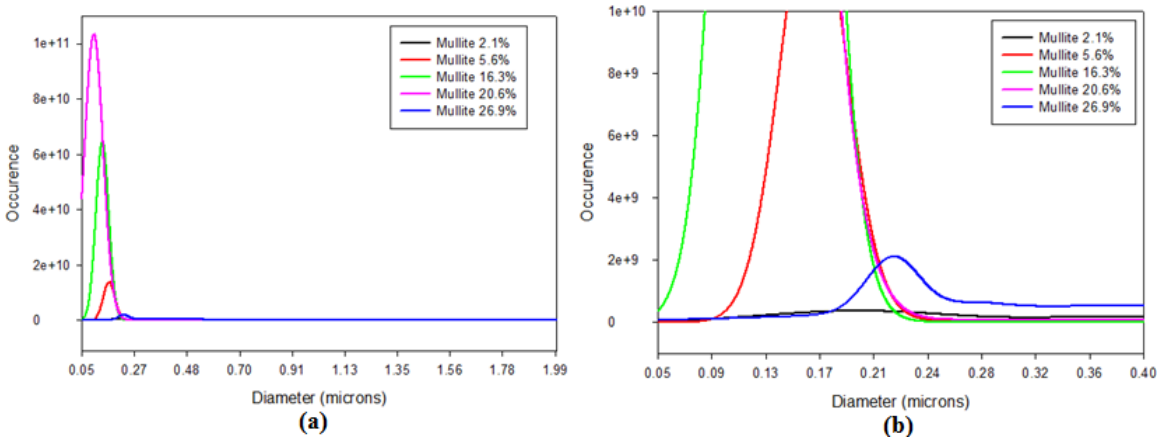

Figure 133. Ultrasound predicted Mullite Series grain size distributions on (a) full range of 0.05-2.00µm and (b) shortened range of 0.05-0.40µm.

Table XVII. Goodness of fit parameters for Gaussian reconstruction curve fits to ultrasound predicted mullite grain size distributions.

	# Modes	R^2	Adjusted R^2	SSE	RMSE
Mullite 2.1vol%	2	0.9973	0.9968	1.13E+09	6047
Mullite 5.6vol%	4	0.9986	0.9982	8.62E+09	17540
Mullite 16.3vol%	4	1.0000	1.0000	2.04E+07	904
Mullite 20.6vol%	4	1.0000	1.0000	1.05E+07	647
Mullite 26.9vol%	3	0.9999	0.9998	3.98E+08	3989

Table XVII gives the number of Gaussian modes used for each curve fit along with the goodness of fit parameters. The R-squared parameter gives a measure of how well a regression line approximates real data points. An R-squared of 1 indicates a perfect fit. Adjusted R-squared is a modification of R-squared which also measures how well the regression fit models the data, but takes into account the number of degrees of freedom associated with the system. Again, an adjusted R-squared value of 1 indicates the best fit. SSE is the sum of squared errors which gives a measure of the discrepancy between the data and the regression model. A smaller SSE value indicates a tighter fit to the model. The RMSE is the root-mean square error which gives a good measure relating to the precision of the fit. A RMSE value which is small indicates a better curve fit. The

R^2 and adjusted-R^2 values for each curve fit illustrates that these fits matched the data fairly well. The SSE and RMSE values appear to be somewhat large; however, with comparison to the occurrence scale in Figure 133, these values are less than 1% of the total which also indicate that the curve fits match experimental data quite well.

Comparing the reconstructed ultrasound grain size distributions to the experimental grain size distributions using FESEM imaging reveals a strong correlation. Figures 134-138 show both the measured mullite grain size distributions along with the mullite size distributions predicted by acoustic spectroscopy. The occurrence scales for each figure was normalized to a value of unity for direct comparison of each distribution.

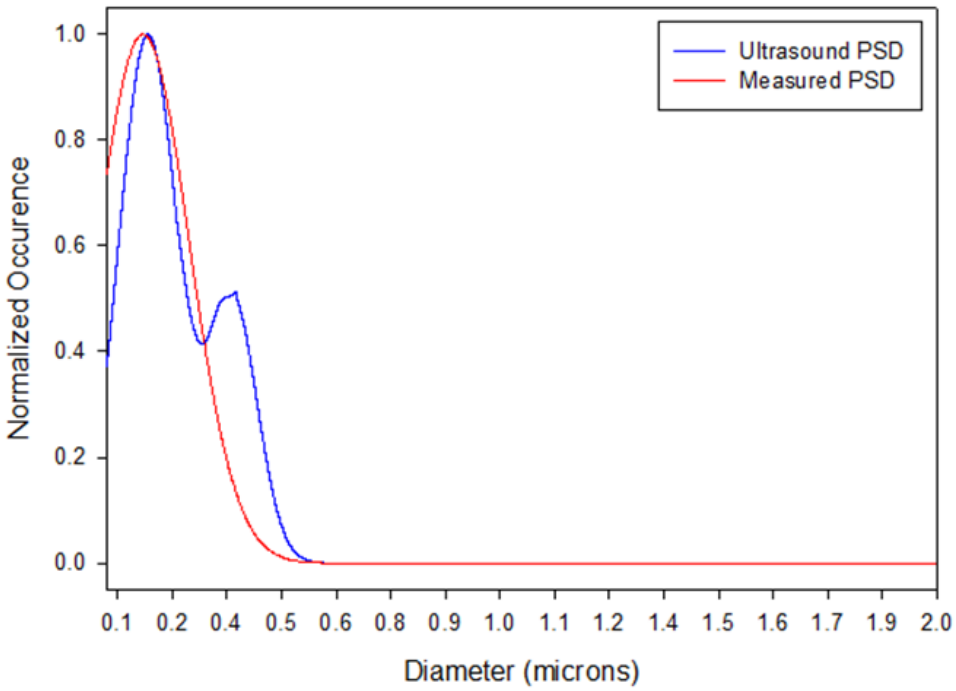

Figure 134. Comparison of ultrasound predicted and measured mullite grain size distributions for Mullite Series sample Mullite 2.1vol%.

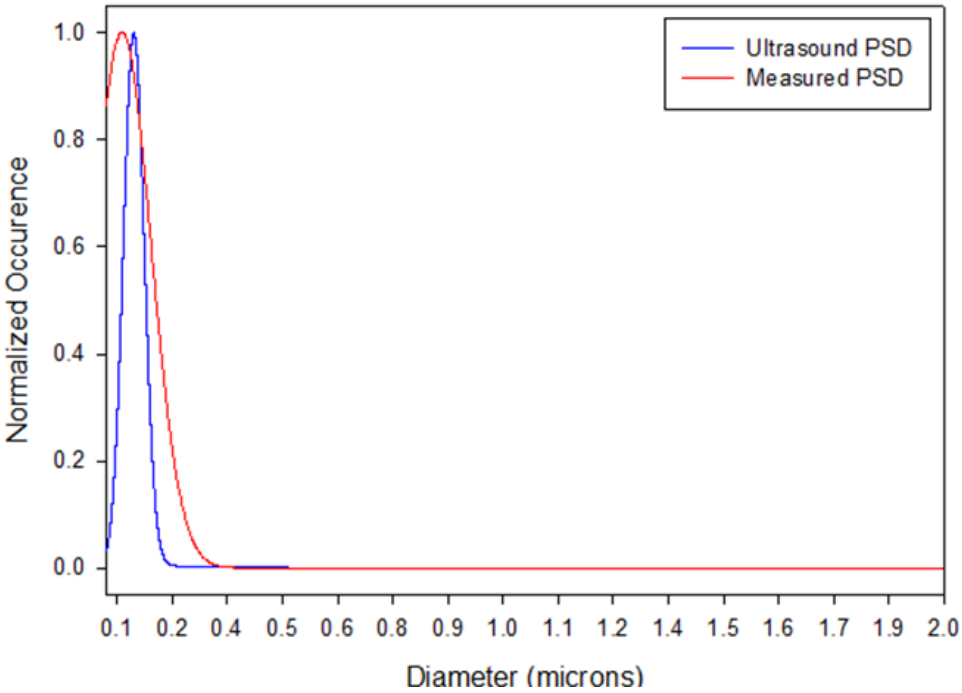

Figure 135. Comparison of ultrasound predicted and measured mullite grain size distributions for Mullite Series sample Mullite 5.6vol%.

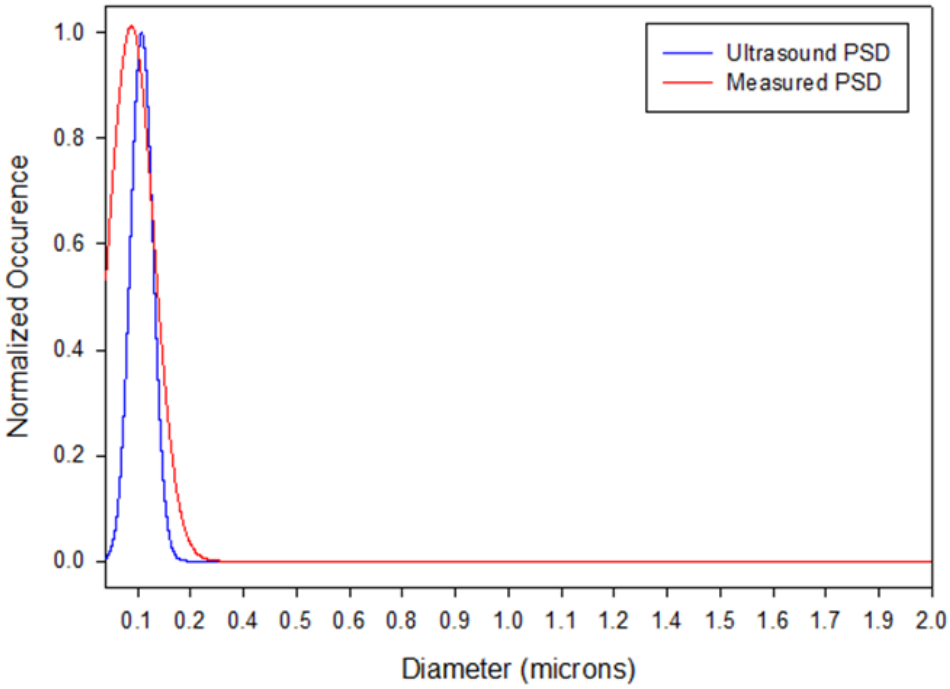

Figure 136. Comparison of ultrasound predicted and measured mullite grain size distributions for Mullite Series sample Mullite 16.3vol%.

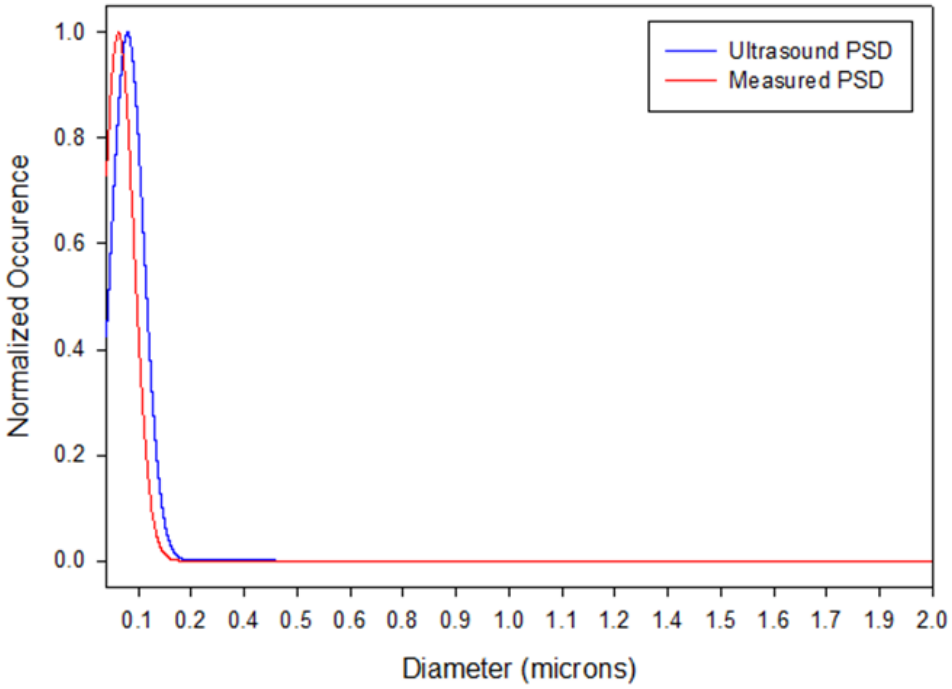

Figure 137. Comparison of ultrasound predicted and measured mullite grain size distributions for Mullite Series sample Mullite 20.6vol%.

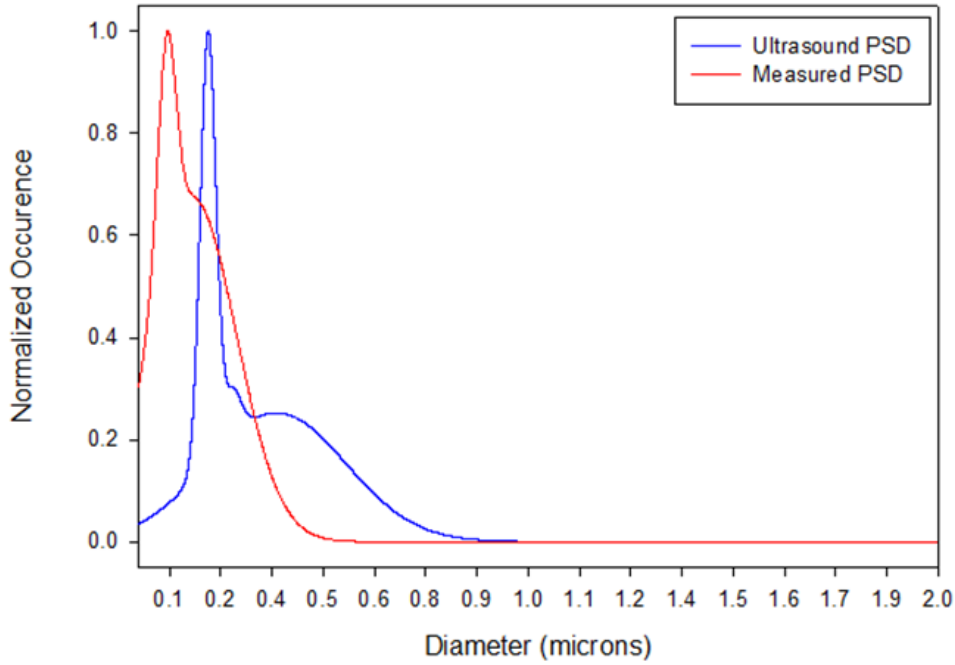

Figure 138. Comparison of ultrasound predicted and measured mullite grain size distributions for Mullite Series sample Mullite 26.9vol%.

The modes of ultrasound predicted grain size distributions match almost perfectly with the conventionally measured grain size distributions. In each case it can be seen that

the ultrasound grain size distributions show an increase in mode of mullite grain size along with a decrease in standard deviation when compared to the FESEM measured grain size distributions. Figure 138 shows interesting behavior for the sample labeled Mullite 26.9vol%: the modes of each type of distribution differ significantly but the ultrasound grain size distribution attempts to mimic the behavior seen with the FESEM measured grain size distribution.

5.6.1.2. Analysis of Titanium Carbide Series

As with the Mullite Series sample spectra, the attenuation coefficient spectra taken about the sample regions in the Titanium Carbide Series were corrected for the intraparticle thermoelastic absorption caused by the alumina grains also present in the path of the ultrasound beam. X-ray diffraction results giving the volume percent of titanium carbide and aluminum oxide in each sample were used to determine the relative increase in attenuation in each spectra, seen in Figure 97, shows due to the contribution of the alumina. The spectra representing 100% alumina shown in Figure 97 was multiplied by the percentage of alumina in each sample. These values were then subtracted from each respective attenuation coefficient spectra relating to each sample in the Titanium Carbide Series. The corrected attenuation coefficient spectra, representing only the attenuation caused by the titanium carbide grains, can be seen in Figure 139. These corrected spectra were used in conjunction with equation 78 along with the energy and force output profiles of the 20MHz transducer to obtain titanium carbide grain size distributions in the range of 0.50-0.80μm. These ultrasound predicted size distributions for TiC grains can be seen in Figure 140.

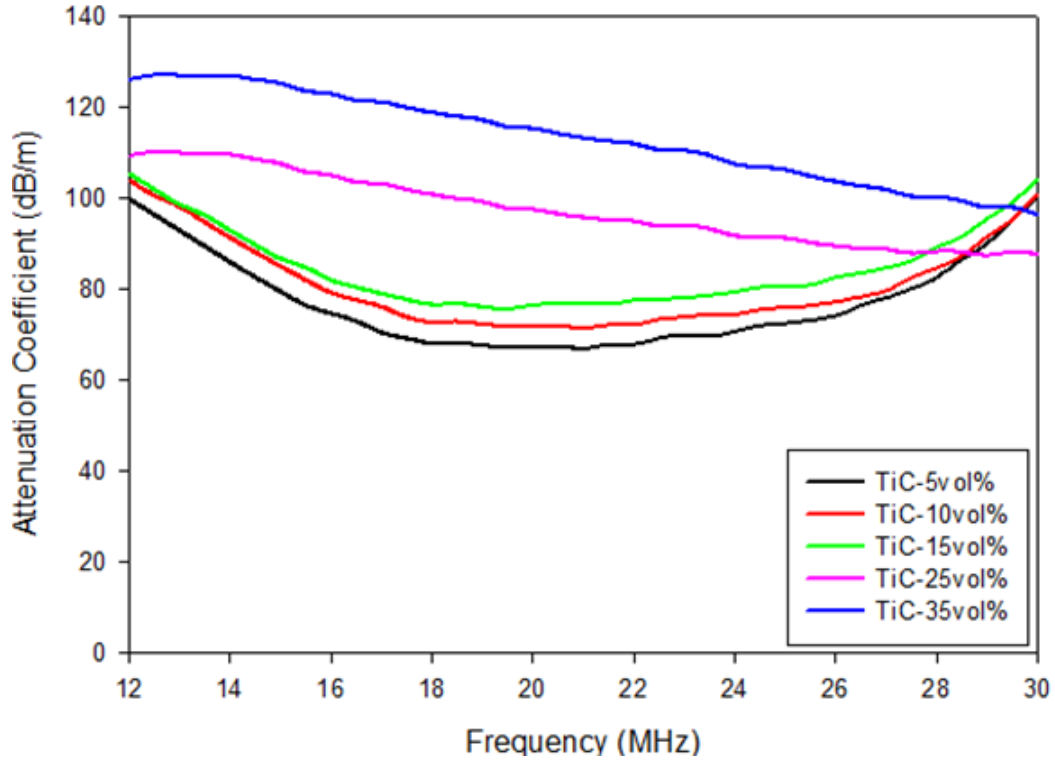

Figure 139. Titanium Carbide Series attenuation coefficient spectra corrected for thermoelastic absorption contribution of alumina grains. Gives attenuation spectra solely caused by TiC in each sample.

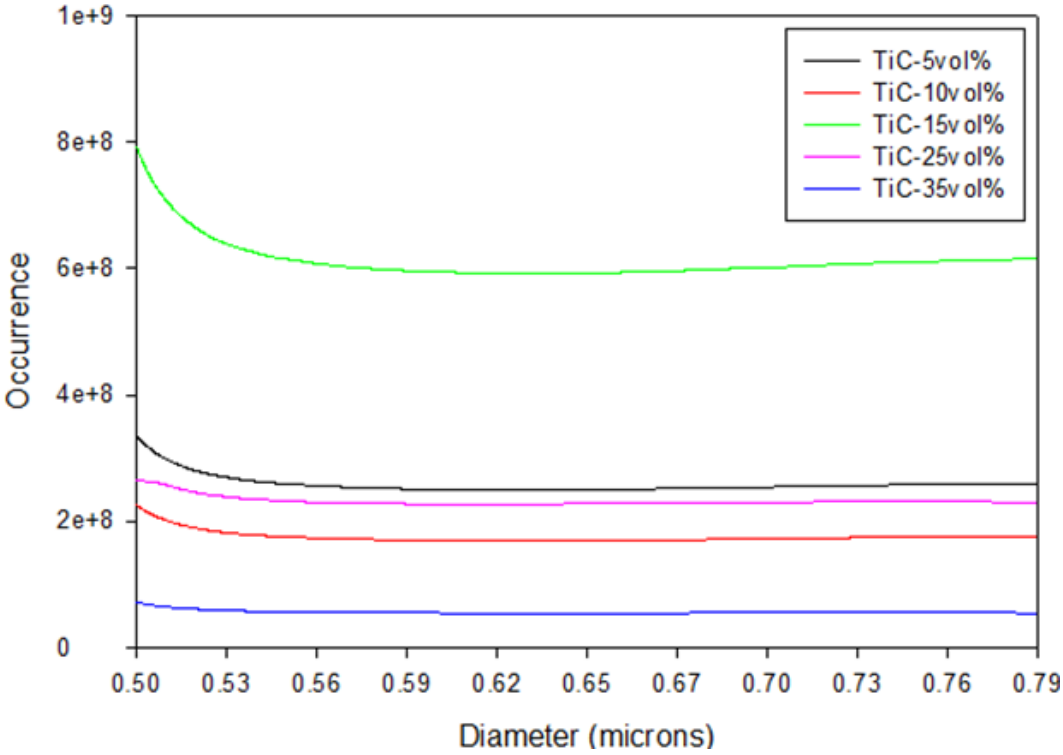

Figure 140. Ultrasound predicted Titanium Carbide Series grain size distributions on size range of 0.50-0.80µm corresponding to frequency range of 12-30MHz.

The ultrasound predicted grain size distributions given in Figure 140 show only a portion of the full titanium carbide grain size distributions present in each sample. It was grains of the sizes shown above which contributed to intraparticle thermoelastic absorption. It should be noted that the absolute occurrence for grains in this size distribution does not scale linearly with the concentration of TiC present in each sample. This implies that the widths of each TiC grain size distribution vary significantly. For instance, there must be many larger TiC grains for sample TiC-35vol% compared to sample TiC-5vol% such that the total volume of the TiC in each sample can be accounted for as the area under the distributions. These curves were fit to Gaussian functions using the curve fitting tool in MATLAB. Figure 141 shows the fully Gaussian reconstructed titanium carbide grain size distributions for each sample in the Titanium Carbide Series. Table XVIII gives information relating to the parameters of each curve fit. Each Gaussian curve fit was allowed to take multiple modes if it provided the best fit.

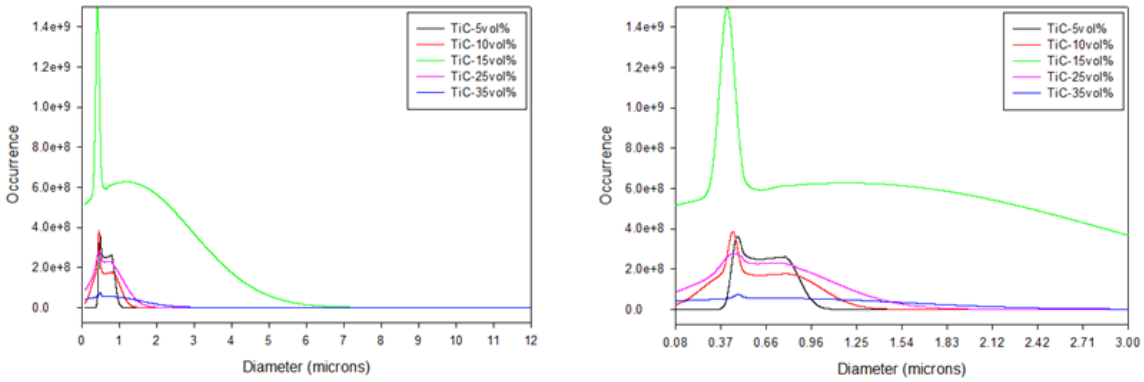

Figure 141. Ultrasound predicted Titanium Carbide Series grain size distributions on (a) full range of 0.08-12.00µm and (b) shortened range of 0.08-3.00µm.

The scale on which the reconstructed TiC grain size distributions are on, greatly influence their size and shape. For example, TiC-15vol% appears to contain significantly more titanium carbide when compared to every other sample. However, it only reaches

up to approximately 6 microns, where samples TiC-25vol% and TiC-35vol% extend to 10 and 12 microns, respectively. For these two samples containing the most amount of TiC, there exist considerably more large TiC grains than small ones when compared to the samples containing less titanium carbide. TiC-15vol% appears to be somewhat anomalous as it didn't follow the same trend as the other samples. It appears that as TiC concentration increases to 15 volume percent, the distribution did not extend to appreciable sizes greater than about 6 microns causing the lower end of the distribution to rise dramatically. For the samples containing 25 and 35 volume percents of titanium carbide, it appears that there was enough of this secondary phase such that it was able to coalesce with surrounding TiC grains and form many more large grains. The commonality that each of these distributions has is the large spike in occurrence at approximately 0.5 microns. Looking at the micrograph images for each sample in Figure 98 it can be seen that there are many TiC grains in each sample that are approximately this size. Qualitatively, it appears that one would expect bimodal (or multimodal) distributions due to the large occurrence of TiC grains at approximately 0.5 microns.

Table XVIII. Goodness of fit parameters for Gaussian reconstruction curve fits to ultrasound predicted titanium carbide grain size distributions.

	# Modes	**R^2**	**Adjusted R^2**	**SSE**	**RMSE**
TiC-5vol%	4	0.9873	0.9862	1.12E+06	183.9
TiC-10vol%	3	0.9987	0.9974	3.19E+08	10140
TiC-15vol%	2	0.9828	0.9807	2.76E+09	29390
TiC-25vol%	2	0.9912	0.9901	8.24E+08	16040
TiC-35vol%	2	0.9950	0.9944	1.04E+09	18010

Considering the high number of TiC grain occurrences, the goodness of fit parameters indicate that each reconstructed ultrasound TiC grain size distributions fits well with each respective Gaussian function.

Comparing the reconstructed ultrasound grain size distributions to the experimental grain size distributions using FESEM imaging reveals a strong correlation. Figures 142-146 show both the measured titanium carbide grain size distributions along with the titanium carbide size distributions predicted by acoustic spectroscopy. The occurrence scales for each figure were normalized to a value of unity for direct comparison of each distribution.

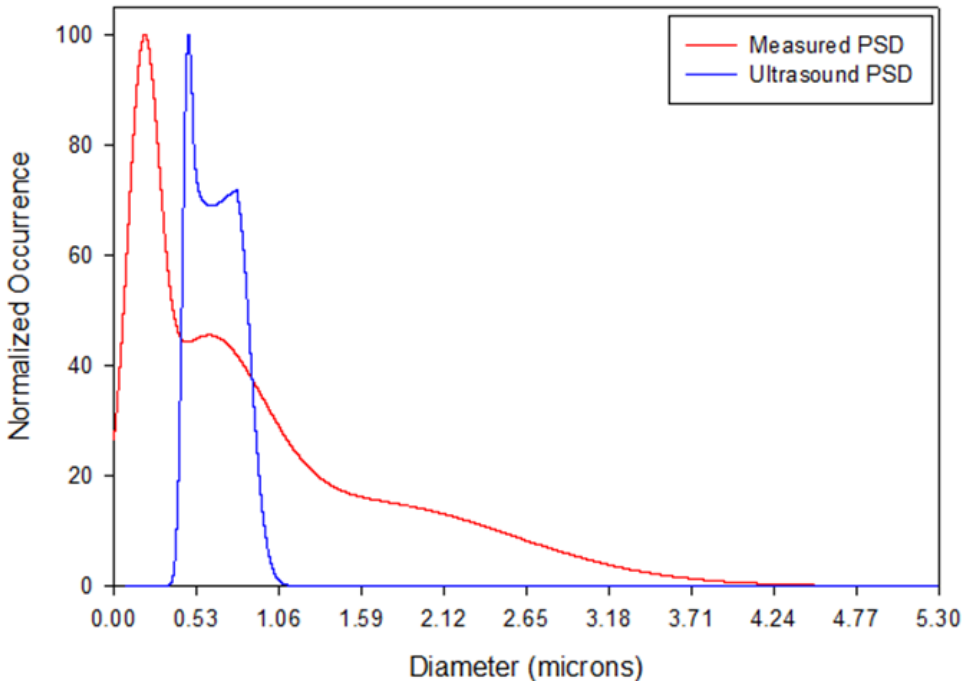

Figure 142. Comparison of ultrasound predicted and measured TiC grain size distributions for Titanium Carbide Series sample TiC-5vol%.

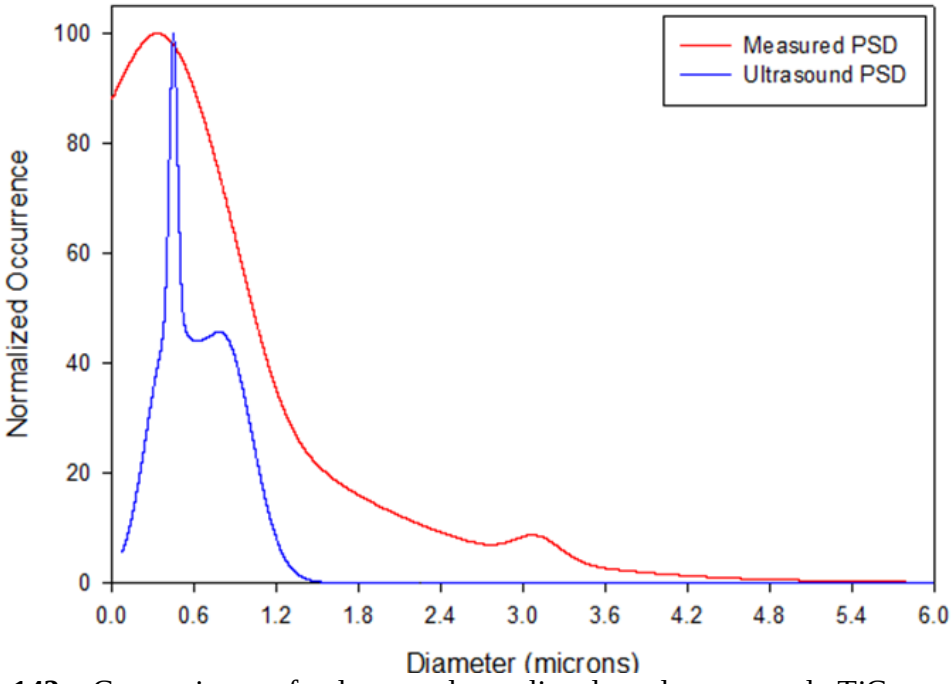

Figure 143. Comparison of ultrasound predicted and measured TiC grain size distributions for Titanium Carbide Series sample TiC-10vol%.

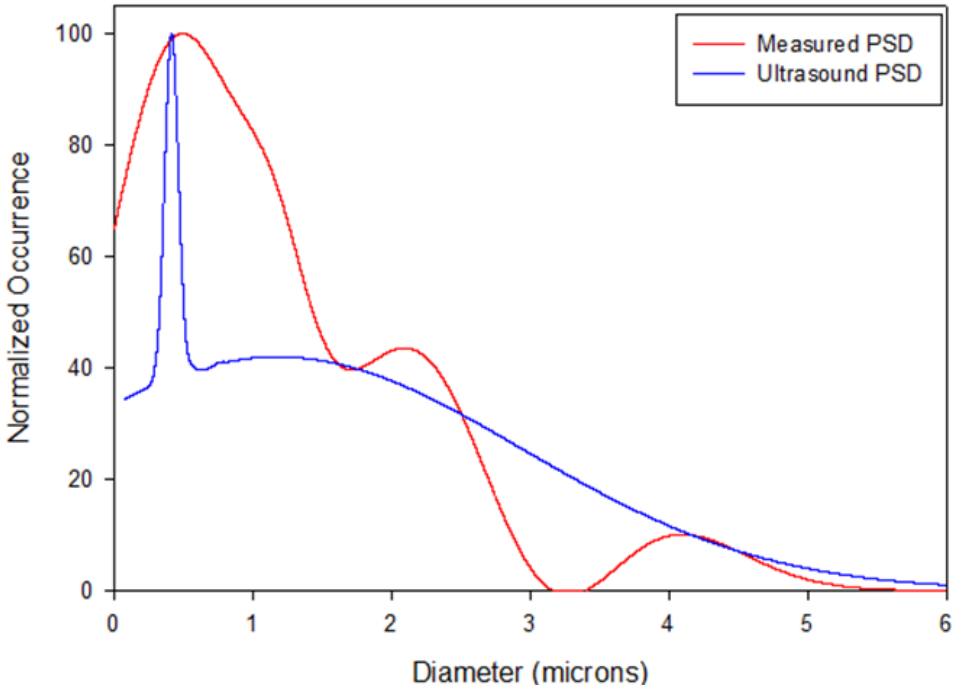

Figure 144. Comparison of ultrasound predicted and measured TiC grain size distributions for Titanium Carbide Series sample TiC-15vol%.

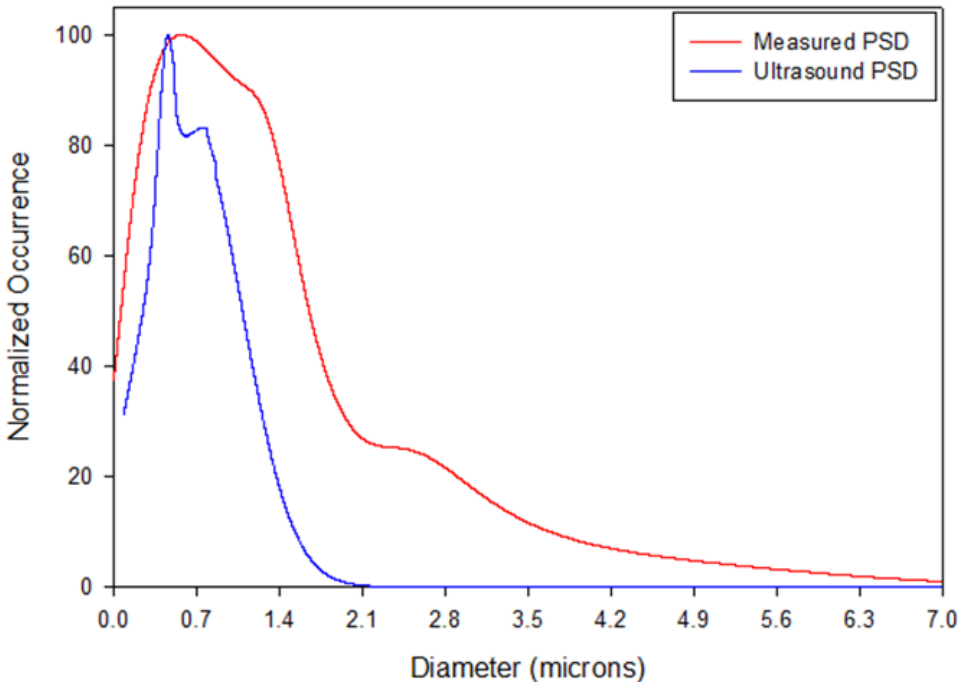

Figure 145. Comparison of ultrasound predicted and measured TiC grain size distributions for Titanium Carbide Series sample TiC-25vol%.

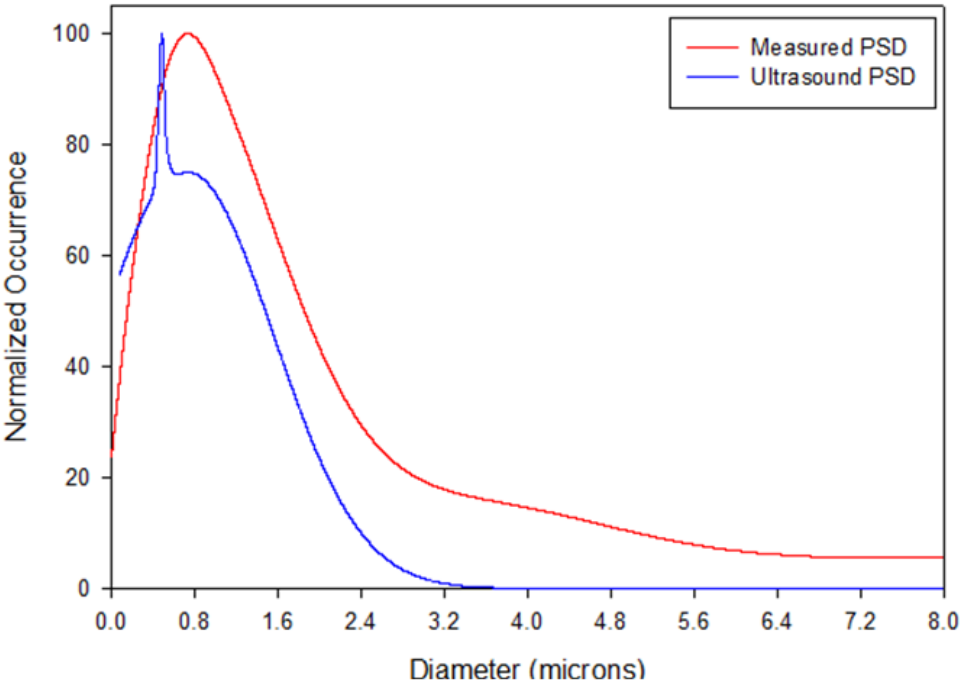

Figure 146. Comparison of ultrasound predicted and measured TiC grain size distributions for Titanium Carbide Series sample TiC-35vol%.

The modes of ultrasound predicted grain size distributions match quite well with the conventionally measured grain size distributions. In each case it can be seen that the ultrasound grain size distributions show an increase in mode of titanium carbide grain size along with a decrease in standard deviation when compared to the FESEM measured grain size distributions. Figure 142 shows a significant deviation between the measured size distribution and ultrasound predicted size distribution. It appears that the ultrasound predicted size distribution for TiC-5vol% is matching with the second mode seen in the measured size distribution at approximately 0.5 microns. The FESEM images show the presence of many really small TiC grains which were almost incapable of being measured using the ASTM approved method. Qualitatively these small grains range in size from approximately 70-150nm.

5.6.2. Scattering-Based Acoustic Spectroscopy

The following results are based on the Microstructural Evolution Alumina Series and Unknown Grain Size Alumina Series samples. The method of determining the Rayleigh and stochastic scattering prefactors, C_R and C_S, based on the Microstructural Evolution Alumina Series is outlined. Validation of these prefactors is given through the correlation of acoustic predicted average grain size versus measured average grain size of the Unknown Grain Size Alumina Series samples.

5.6.2.1. Analysis of Microstructural Evolution Alumina Series

The method used to determine the Rayleigh and stochastic scattering prefactors, C_R and C_S, is described in this section. Comparison of acoustic predicted average grain with measured average grain size for each sample in the Microstructural Evolution Alumina Series using the determined C_R and C_S prefactors is given. An outcome of these

results validates the concept that losses due to stochastic scattering by a few large grains outweigh Rayleigh scattering losses caused by many smaller grains.

Figure 115 gave the mean, minimum, maximum, and standard deviations of the measured grain size distributions for each sample in the Microstructural Evolution Alumina Series. By knowing the sonic velocities and wavelength of sound in these materials distinctions for where Rayleigh, stochastic, or both types of scatter occur according to alumina grain size could be made. Figure 147 highlights where the different types of scattering would occur due to the measured grain sizes. Each sample has the lower end of their grain size distributions falling in the range where Rayleigh scattering is operable. With the exception of sample (T0, D0) and possibly (T0, D0+5) it was expected that stochastic scattering would influence the attenuation behavior seen in these samples due to the large grains in the tail ends of each distribution falling in the range where stochastic scattering occurs.

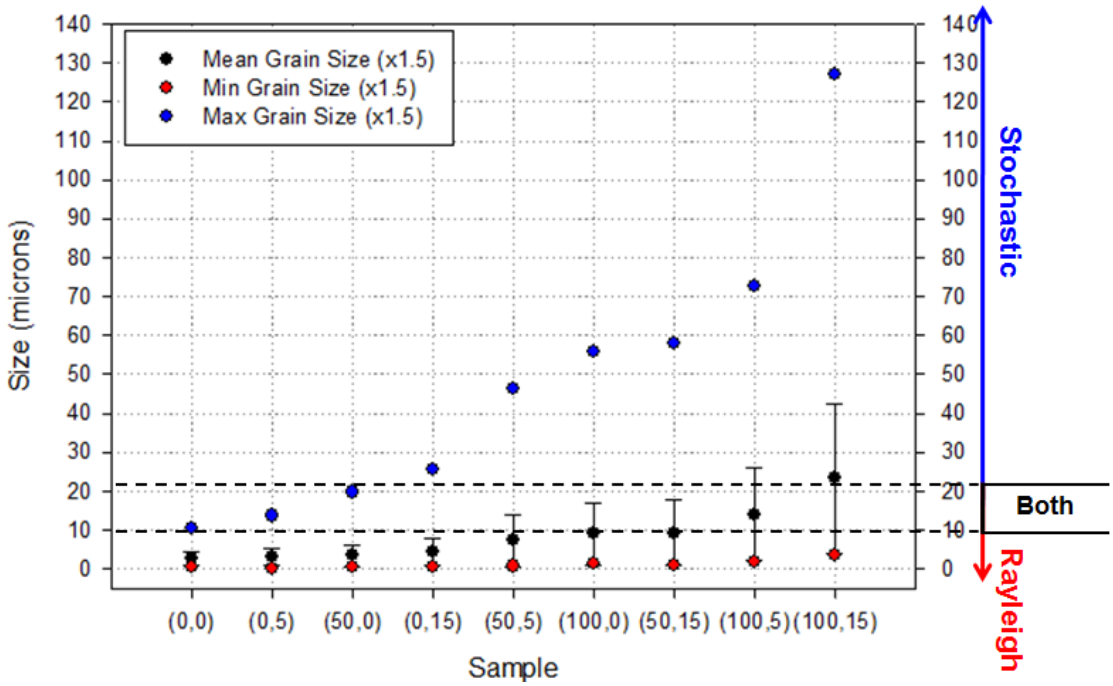

Figure 147. Measured grain sizes for Microstructural Evolution Alumina Series. Size ranges where Rayleigh, stochastic, or both types of scattering labeled.

Using the measured average grain sizes for each sample along with the measured average attenuation coefficient values taken from the spectra seen in Figure 114 (c) values for C_R and C_S were found for each sample by inverting equations 38 and 39. These C_R and C_S values are expected to be constant between each sample as they are dependent on the material providing their grain sizes allow for either Rayleigh or stochastic scattering. Figure 148 shows the scattering prefactor values as a function of each sample. The sample (T0, D0) is a complete outlier in both cases indicating that its scattering behavior varies dramatically compared to what occurs in the other 8 samples. Due to the exceptionally small grain sizes seen in sample (T0, D0) and the grain size range where Rayleigh scattering dominates, the value of C_R from sample (T0, D0) is taken to be accurate.

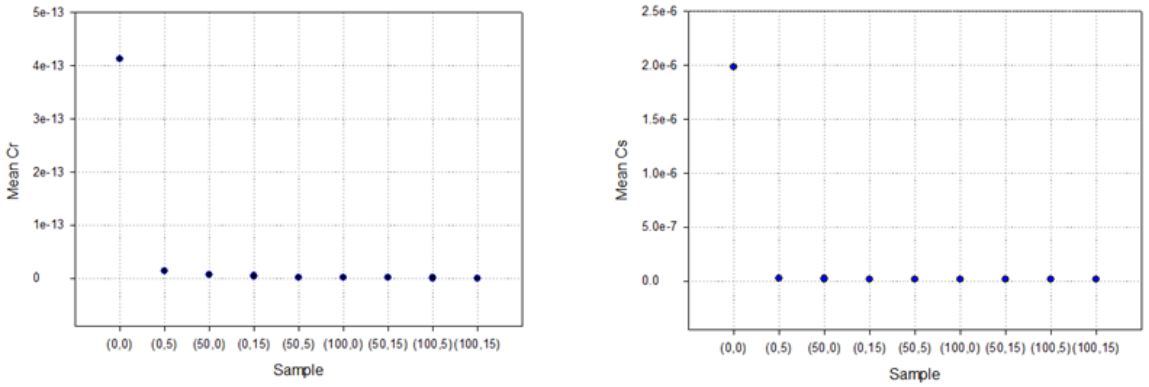

Figure 148. Computed (a) C_R and (b) C_S values for each sample assuming either Rayleigh or stochastic scattering.

Sample (T0, D0+5) shows behavior akin to the samples with larger grain sizes for its values of C_R and C_S with a slight deviation towards the Rayleigh behavior sample (T0, D0) indicates. Although sample (T0, D0+5) has a grain size distribution somewhat similar to sample (T0, D0), its slight increase in grain size distribution allows for stochastic scattering to prevail. The sample containing the largest grains and largest

distribution, (T0+100, D0+15), has the majority of its grains in a region where stochastic scattering certainly dominates. The C_S value given by sample (T0+100, D0+15) is taken to be correct for this type of alumina with grains of the appropriate size to cause stochastic scattering. The deviation of sample (T0, D0) for both C_R and C_S compared to every other sample indicates the size range where there is a strong disconnect between Rayleigh and stochastic scattering.

Omitting sample (T0, D0), the averages and standard deviations for the C_R and C_S values, seen in Figure 148, were computed using the values from the rest of the samples. The average and standard deviation for the C_R prefactor are $3.36*10^{-15}$ and $4.66*10^{-15}$, respectively. The fact that the standard deviation is greater than the mean creates the case where C_R could possibly be a negative value which has no physical interpretation. For this reason it is believed that all samples, except for (T0, D0), do not exhibit Rayleigh scattering behavior. Using all samples containing grains larger than those seen in sample (T0, D0), the average and standard deviation for the C_S prefactor are $1.27*10^{-8}$ and $3.28*10^{-9}$, respectively. The values for C_R and C_S which are accepted to be valid for dense, polycrystalline, alumina are $4.12*10^{-13}$ and $8.45*10^{-9}$, respectively. Empirically, C_R and C_S must have units of $(\text{seconds/meter})^4$ and $(\text{seconds/meter})^2$, respectively; although, analytical forms for each are not understood.

These values were tested by back-predicting the average grain size of the Microstructural Evolution Alumina Series. The C_R and C_S values, measured attenuation coefficient spectra, and known frequency were used according to equations 38 and 39 to solve for acoustic predicted mean grain size. These acoustic predicted average grain size values were compared with measured data. Linear curve fits were performed for each set

of data where the slope of the line indicates how well the predicted data matches with experimental. Figures 149 and 150 show the results of these tests.

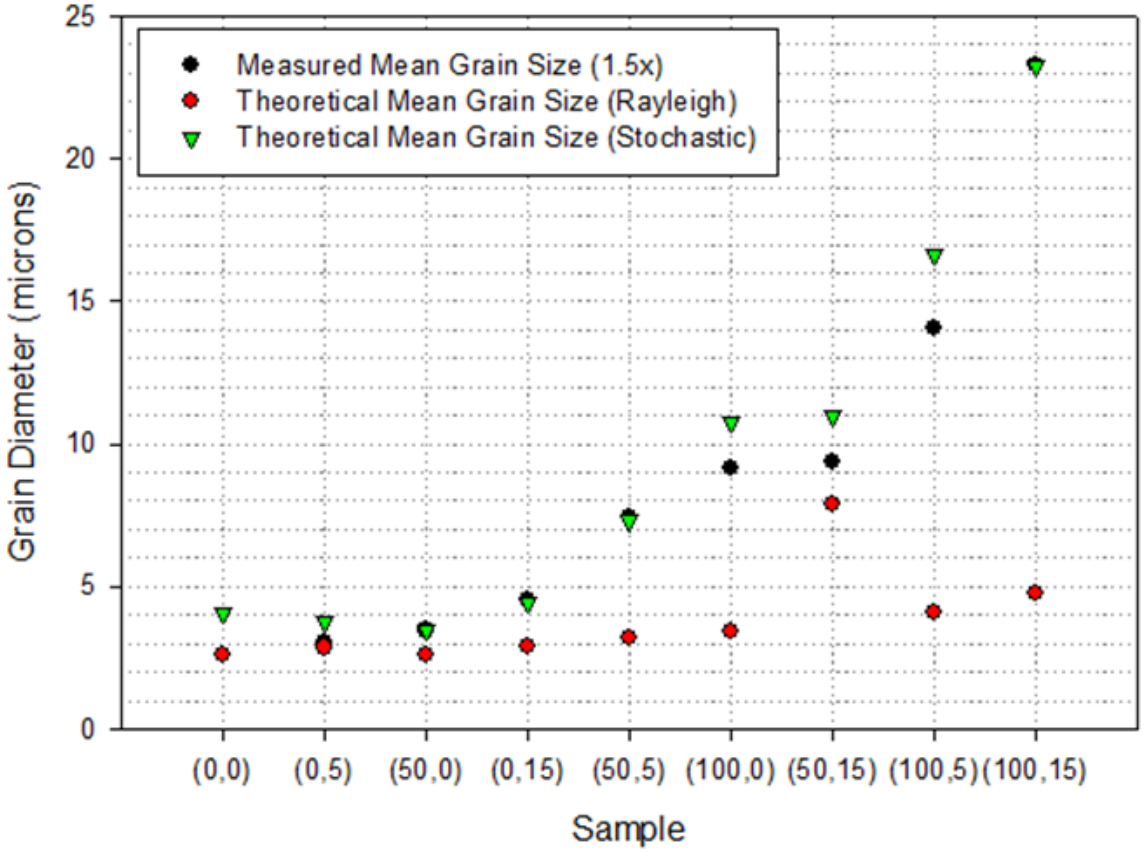

Figure 149. Measured vs. Rayleigh predicted vs. stochastic predicted average grain sizes for each sample in the Microstructural Evolution Alumina Series.

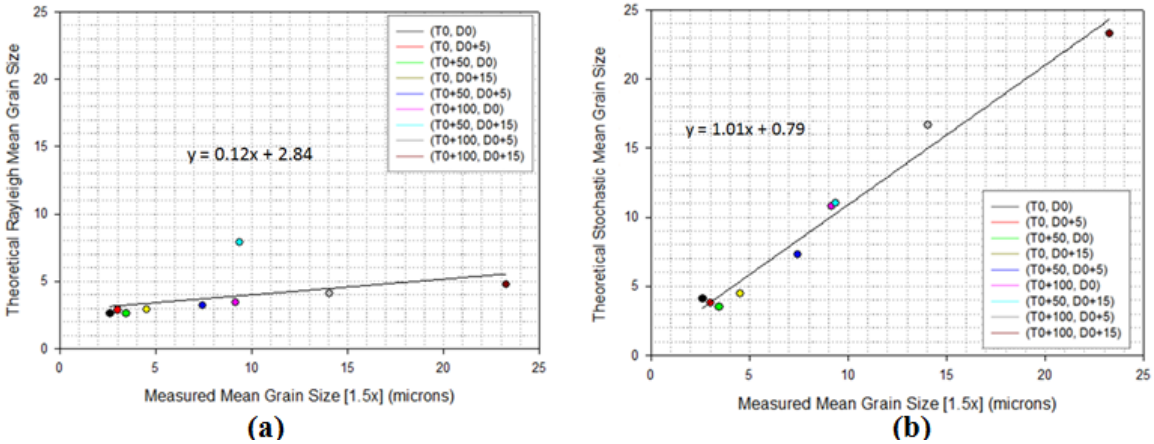

Figure 150. Linear fits with regression equation for (a) Rayleigh predicted vs. measured average grain sizes and (b) stochastic predicted vs. measured average grain sizes.

The slope of a linear curve fit indicates how well two sets of data are correlated, where a slope of '0' indicates there is no correlation and a slope of '1' indicates a strong correlation. The slope of the linear regression line seen in Figure 150 (a) reveals that a strong correlation between Rayleigh predicted mean grain size and measured mean grain size does not exist. This regression line has a slope of 0.12. The linear curve fit for the plot seen in Figure 150 (b) show that the acoustic stochastic mean grain sizes correlate almost perfectly with the measured mean grain sizes for each sample, having a slope 1.01. Figures 149 and 150 give strong validation to the concept that a few large grains causing stochastic scattering result in more acoustic energy loss than many small grains causing Rayleigh scattering. Although the modes of each measured grain size distribution for this sample set lie in a range where Rayleigh scattering can occur, it is the larger grains in the tail-ends of each distribution which cause stochastic scattering to completely dominate the attenuation seen at ultra high frequencies.

5.6.2.2. Analysis of Unknown Grain Size Alumina Series

Testing of the C_R and C_S prefactors was done on three alumina samples known to have the same composition as the samples in the Microstructural Evolution Alumina Series. For this, the Rayleigh and stochastic scattering prefactors, measured attenuation coefficient spectra at each point, frequencies of 40-70MHz, and equations 38 and 39 were used to solve for average grain size at each point. As each attenuation coefficient spectra map, seen in Figures 126-128, consists of multiple points at multiple frequencies, equations 38 and 39 were used to calculate the average grain size at each frequency per point in each sample. The calculated grain sizes, per point, were then averaged to obtain mean grain size at each point. This was done assuming either Rayleigh or stochastic

scattering. When performing this type of analysis it would be unknown whether a sample has grains small enough to cause predominantly Rayleigh scattering, large grains to cause stochastic scattering, or a distribution of both. Therefore, it is assumed that the grain size distributions of each sample are wide enough to cause both types of scattering.

The following results show the acoustic predicted mean grain size maps created for the smaller area scans of the Unknown Grain Size Alumina Series samples. The mean, standard deviation, minimum, and maximum values of each map are shown in Table XIV. These statistical data were overlaid on the measured grain size distributions from each sample as a measure of how well the acoustic predicted average grain size matched with the measured.

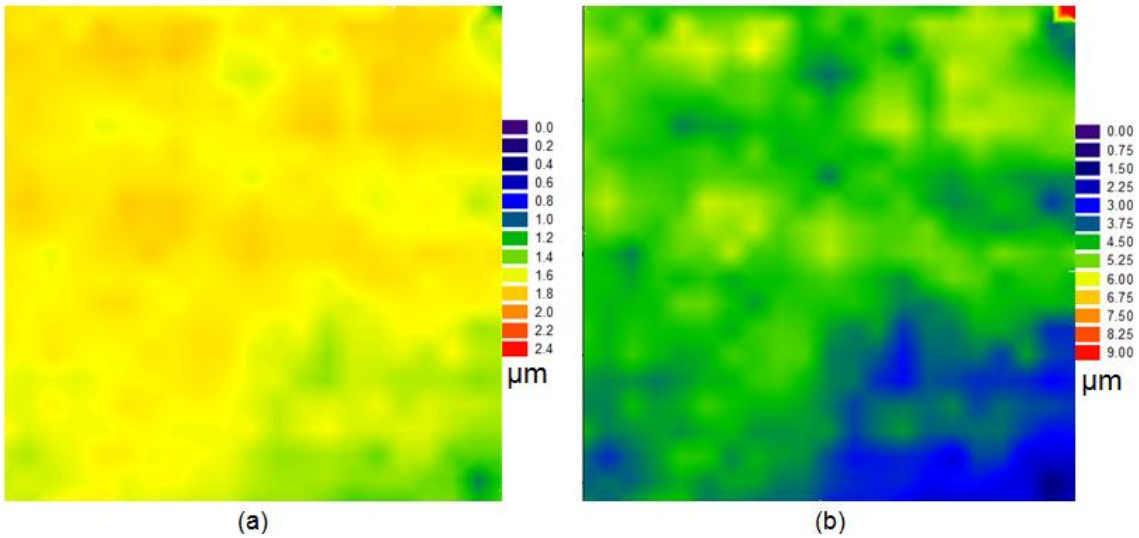

Figure 151. Acoustic predicted mean grain size maps of Unknown Grain Size Alumina sample Small. (a) Assuming Rayleigh scattering and (b) assuming stochastic scattering.

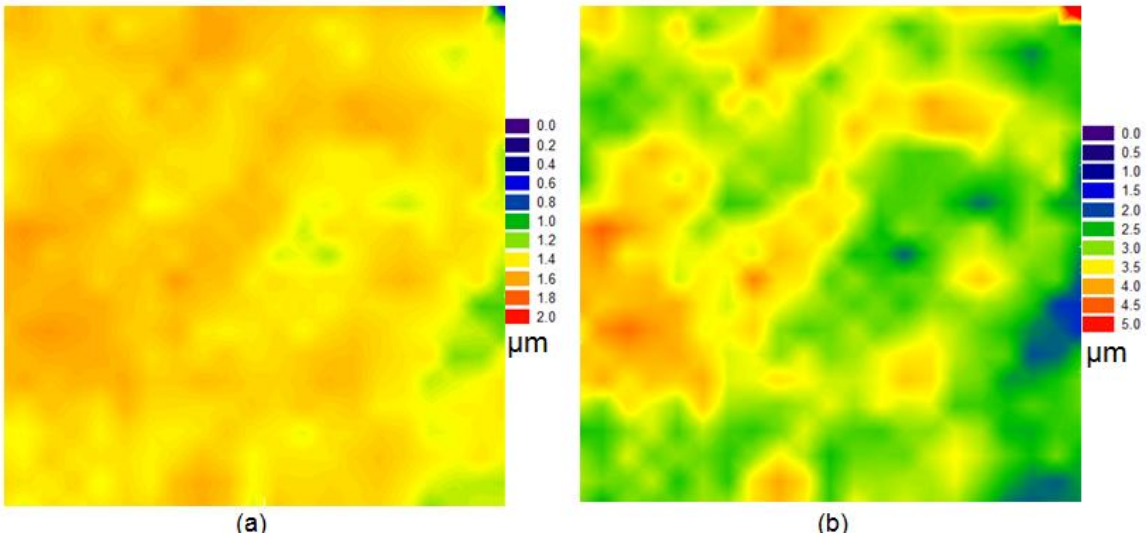

Figure 152. Acoustic predicted mean grain size maps of Unknown Grain Size Alumina sample Medium. (a) Assuming Rayleigh scattering and (b) assuming stochastic scattering.

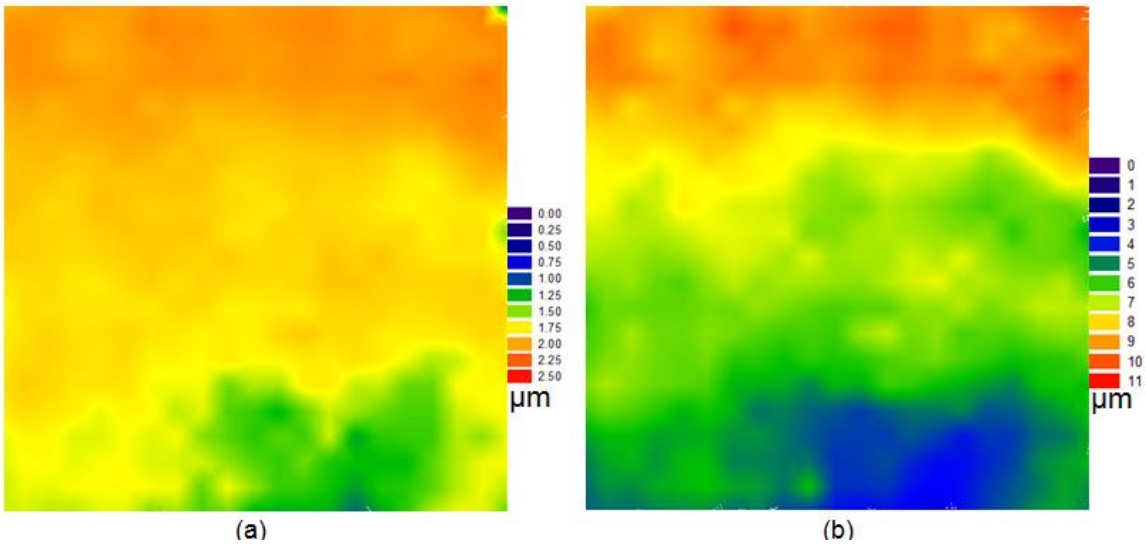

Figure 153. Acoustic predicted mean grain size maps of Unknown Grain Size Alumina sample Large. (a) Assuming Rayleigh scattering and (b) assuming stochastic scattering.

Each of the acoustic predicted grain size maps seen in Figures 151-153 mimic the behavior of the overall attenuation coefficient maps seen in Figure 124. This is consistent with the belief that acoustic attenuative losses at high frequencies are controlled by scattering by the grains of the primary phase of the material in scrutiny. It

would be a misconception to claim that the assumed Rayleigh or assumed stochastic mean grain size maps represent the actual values of the grains at each point. These maps appear to show the mode and breadth of the grain size distributions where any variation seen across the spatial dimension of each sample would represent a change in the width of the samples grain size distribution.

Table XIV. Statistical information taken from Rayleigh and stochastic predicted mean grain size maps.

	SMALL	**MEDIUM**	**LARGE**
Rayleigh			
Mean	1.61	1.43	1.77
St .Dev.	0.10	0.10	0.21
Min	0.96	0.29	0.76
Max	1.79	1.62	2.11
Stochastic			
Mean	4.47	3.12	6.74
St .Dev.	1.20	0.56	1.58
Min	1.41	1.82	3.15
Max	6.01	10.15	10.07

It would be impossible to completely verify the validity of these acoustic predicted grain size maps as one would have to measure the actual grain sizes of every grain the in the bulk of the material through some serial sectioning process. The amount of time necessary to count each grain through micrograph images for these samples would take an estimated ten thousand years, assuming one could measure a single grain every second. Upon matching the statistical data of each map with the measured grain size distribution from each sample, a strong correlation can be seen between acoustic predicted and micrograph measured sizes.

Figures 154-156 give the measured grain size distributions with the acoustic predicted statistical data assuming Rayleigh and stochastic scattering. Statistical Rayleigh data are shown in shades of green while statistical stochastic data are shown in shades of blue. The dotted vertical lines within the green or blue shades represent the average predicted grain sizes assuming Rayleigh and stochastic. The darker green and darker blue shaded boxes about the dotted vertical lines represent the standard deviation for each type of predicted grain size and the lighter green and blue boxes represent the minimum and maximum for Rayleigh and stochastic grain sizes, respectively.

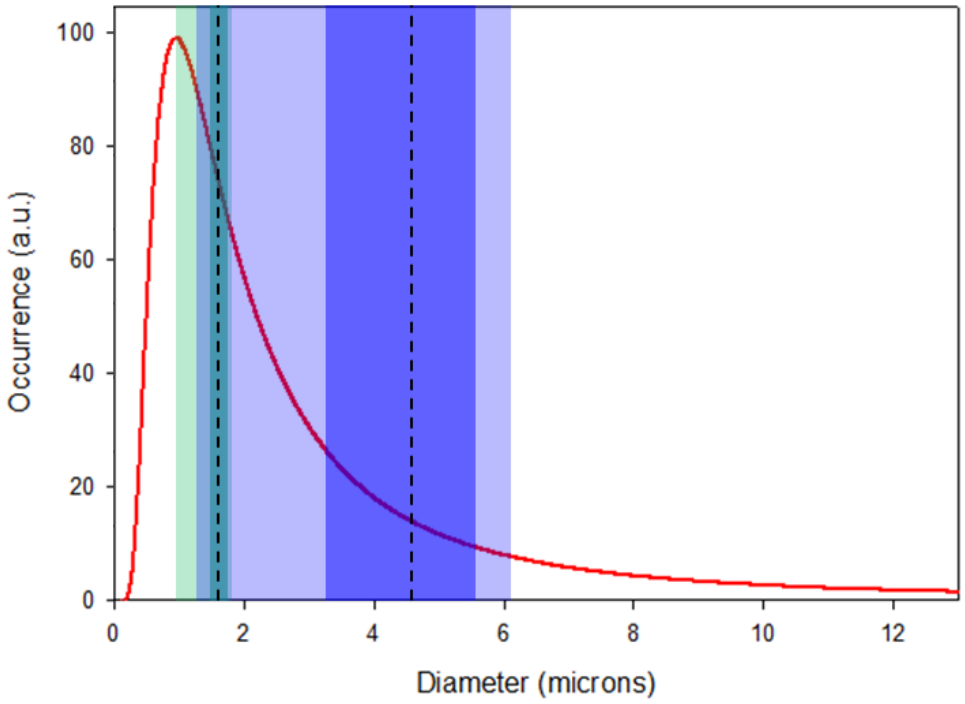

Figure 154. Overlay of predicted statistical information seen in Table XIV on measured grain size distribution of Unknown Alumina Grain Size Series sample Small.

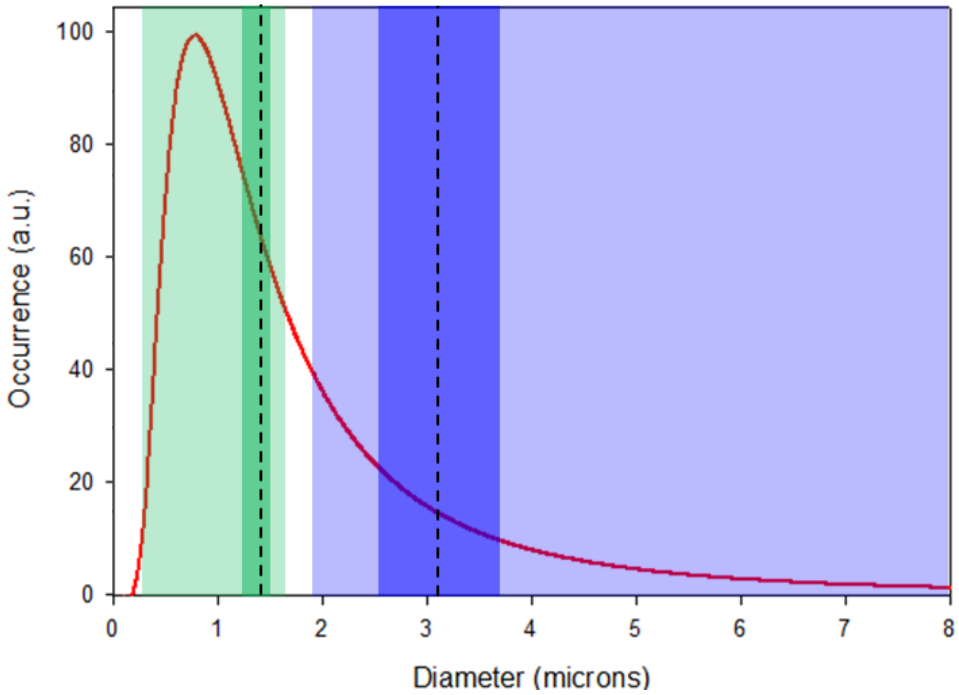

Figure 155. Overlay of predicted statistical information seen in Table XIV on measured grain size distribution of Unknown Alumina Grain Size Series sample Medium.

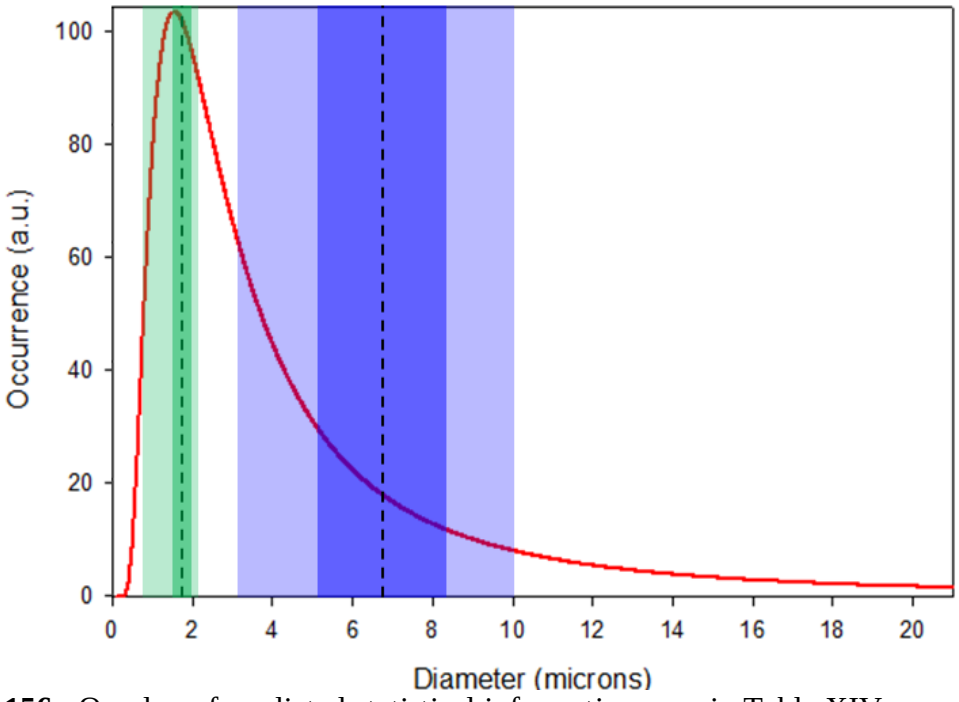

Figure 156. Overlay of predicted statistical information seen in Table XIV on measured grain size distribution of Unknown Alumina Grain Size Series sample Large.

The information shown in Figures 154-156 comparing the measured grain size distributions with the acoustic predicted data show a strong correlation for using Rayleigh scattering to predict the modes of these distributions. Assumptions regarding stochastic scattering predict how skewed each distribution is. The difference between the sheer numbers of grains an acoustic wave interacts with compared to the amount of grains that can be measured using an ASTM standard using micrograph images is a strong factor as to why predicted and measured grain sizes do not match perfectly. This is discussed further as a source of error in the next section.

5.6.3. Sources of Error

Each test performed on the four sample sets discussed in this thesis has some error associated with it. This can be caused by initial assumptions, experimental error due to the user, or experimental error due to the measurement technique and equipment resolution. Possible sources of error are discussed regarding the results seen for each sample set.

5.6.3.1. Attenuation Coefficient Spectra-Ultrasound Test Setup Accuracy

The prediction of microstructural feature sizes using an acoustic amplitude attenuation based technique has accuracy commensurate with the voltage resolution of the oscilloscope. Due to the finite voltage step created by the analog-to-digital converter card for the oscilloscope display, amplitude based measurements have some standard deviation associated with them. Again, the voltage resolution for the ultrasound test equipment used in this thesis is 7.1825mV. This amounts to an average standard deviation in attenuation coefficient spectra of 0.054dB/cm when using the 20MHz transducer. Use of the 60MHz transducer gives an average standard deviation in

attenuation coefficient of 0.079dB/cm. Comparing these standard deviation values for each transducer with the measured attenuation coefficient spectra for all sample sets used in this thesis, the absolute occurrence of grain sizes can have as much as approximately 5% error.

The relation of the attenuation coefficient spectra to microstructural feature size is not dependent on the voltage resolution but rather the time resolution and the ability to obtain accurate power spectral densities through the use of fast Fourier Transforms. As mentioned in section 2.5.3., the necessary time resolution of an oscilloscope to perform FFT's is dictated by how high of a frequency transducer is being used. A Fourier transform requires at least 5 data points to accurately define a sine wave. Therefore at the highest frequencies used in this thesis a time resolution of 2ns is necessary to obtain all frequency components of signals containing as much as 110MHz. The time resolution which is achieved by the ultrasound test equipment used in this thesis is approximately 0.3ns which is far greater than the necessary 2ns at the highest frequencies. Therefore, there is no significant error introduced due to the time resolution of the ultrasound test equipment.

5.6.3.2. Derived Equations-Analytical Equation of Acoustic Grain Size Distribution

The derived equation used to determine ultrasound predicted grain size distributions, (equation 78) for the Mullite Series and Titanium Carbide Series made use of an assumption which may introduce some error into the final results. This assumption is that the microstructural features which the acoustic wave interacts with have spherical morphologies. The derivation of the 'S' parameter made use of a standard 100% alumina sample whose grain size distribution was measured and used as an input to determine the

force output of the 20MHz transducer. All parts of this derivation which involved length, area, or volume terms assumed those for perfect spheres. It is not known how much error this assumption may impart as the features within the alumina-based microstructures have morphologies which are not perfect spheres; they can all be approximated as different forms of spheroids. It appears, however, that this assumption still allows for predicted grain sizes which show strong correlations with measured data. This may be due to the fact that grain size measurements based off of micrograph images also assume that measurements of the grains great diameter are being performed and thereby also assume spherical or circular grains.

5.6.3.3. Material Properties-Assumption of Thermal Properties

The Zener equation uses frequency, density, thermal conductivity, and specific heat as its inputs. Frequency and density are measured, known terms; however, the thermal conductivity and specific heat are taken from various sources (JANAF tables, Engineered Materials Handbook, or literature). The error introduced in assuming the referenced literature for these values if correct affects the size of the grains predicted through acoustic means. An increase in thermal conductivity causes an increase in predicted grain size where an increase in specific heat will cause a decrease. Due to the fact that the inverted Zener equation is dependent on exceptionally high frequencies, small variations in referenced values for the thermal conductivity or specific heat will not create large variation in the predicted grain sizes.

5.6.3.4. Measurement of Secondary Phase Concentration-X-ray Diffraction

The absolute occurrence of the grain size distribution predicted for the Mullite Series and Titanium Carbide Series is directly dependent on the quantitative results obtain via XRD. The error given to the occurrence of acoustic predicted grain size distributions from XRD results scales proportionally with the error associated with the RIR method for determining relative concentrations of different phases within a material. All quantification-based XRD results had less than 5% error, which is considered acceptable for accurate concentration measurements using the RIR method.

5.6.3.5. Measured Number of Grains-Micrograph versus Ultrasound

It is unclear which type of measurement technique for these grain size distributions is more valid; ultrasound predicted or micrograph measured. The micrograph measured grain size distributions were created from a single sectioned surface using between 300-500 grains, whereas the ultrasound predicted size distributions contain information from billions of grains contained within the entire volume of the sample. As a standard model for measuring grain size distributions using acoustic spectroscopy in dense polycrystalline ceramics does not exist, it is assumed that the micrograph measured distributions, based on Heyn's lineal intercept model, is more accurate [233]. A complete comparison of this would involve serial sectioning and measurement of an inordinate amount of grains which would require a tremendous amount of time.

Variability in a grain size distribution will become extremely sensitive to acoustic based measurements, whereas it may not be easily detected through the use of micrograph measurements. Statistically, a sample population consisting of 300 or more

elements is considered to be representative of the entire population according to specific distribution models (such as the Student t distribution). The measured grain size distributions would therefore be valid for the sample surface interrogated using a microscope, and it is assumed that those single surfaces are representative of entire bulk grain size populations which the ultrasound beam interacted with. Therefore, it is expected that the acoustic predicted and micrograph measured grain size distributions or average grain sizes will vary from one another.

5.6.3.6. Measured Number of Grains-Stereographic Correction

The main source of measurement error for determining grain size distributions from micrograph images lies with the assumption that the grains are spherical. Stereographic inconsistencies account for the measurement of features to be under by 1.5 times of what is seen in micrographs. However, this is valid for perfect spheres which would be an upper limit of this source of error. The lower limit would assume the features are approximated as cubes, in which case the measurement of features based off of micrograph images would be exact. For the grains measured in the sample series for this thesis (alumina, mullite, and titanium carbide), they tend to approximate oblate spheroids which are closer in shape to spheres than cubes. The correction for each measured grain size distribution by multiplying each size by 1.5 times is possibly a slight overestimate. Comparisons of the measured grain size distributions with those of the acoustic predicted distributions show strong correlations which validates that a stereographic correction of 1.5 times is accurate.

6. Conclusions

This thesis demonstrated the veracity of using high frequency acoustic spectroscopy as a feasible characterization technique for nondestructively predicting microstructural variability and size parameters. The goal of this thesis, to develop an ultrasound nondestructive measurement technique which provides a method to predict grain sizes of alumina-based materials, was achieved. The physics relating to the phenomena of acoustic loss mechanisms in dense, polycrystalline aluminum oxide was both expounded upon and developed to suit the needs of this thesis. Average values of primary phase alumina grains were found over large sample areas as well as predictions for secondary phase grain size distributions. These results correlate strongly with measured microscopy results.

Several important results from the work performed in this thesis are discussed below. Generally, these results can be described as the expansion of acoustic attenuation theory in dense, polycrystalline alumina and the characterization of aluminum oxide-based materials. The development of intraparticle thermoelastic absorption mathematics for alumina-based materials allowed for the testing performed on two of the sample sets studied in this thesis. The extension of acoustic scattering theory to account for grain sizes commonly associated with alumina used for structural applications gave merit to the testing performed on half of the samples used in this thesis.

6.1. Innovative Enhancements and Upgrades to Ultrasound System

To provide the ability to use acoustic spectroscopy as a method of characterizing alumina microstructure an analog-to-digital converter card with a 3GHz sampling rate was acquired through Gage Electronics. It was determined that a sampling rate of 3GHz

would provide sufficient temporal resolution such that fast Fourier transforms up to approximately 150MHz could be taken. The necessity of having this capability was paramount to measuring ultra high frequency attenuation coefficient spectra which exhibited predominantly scattering behavior. Two tasks involved in meeting the goal of extending the measureable frequency range was to integrate a high-sampling rate A/D card and acquiring an ultrasound transducer capable of ultra high frequencies. The integration of such an A/D card required reprogramming of the Legacy© software code used to transform the sample reflections to give power spectral densities. A custom made 150MHz longitudinal, planar transducer was acquired through Imaginant. Testing of this transducer with the ultrasound equipment used in this thesis revealed it had a useable bandwidth of approximately 80-110MHz.

6.2. Development of Analytical Equations

As stated in an earlier chapter, equations which describe the amount of energy lost due to intraparticle thermoelastic absorption as well as the size and number of grains causing such absorption did not exist. This thesis developed equations for both where the latter provides the means of determining grain size distributions of secondary phases within aluminum oxide. Scattering attenuation coefficient is proportional to average grain size, frequency, and constant factors (depending on which scattering regime is applicable). These scattering factors are material constants and must be determined before using acoustic scattering attenuation coefficient spectra as a means of determining average grain size. This thesis provides a basis on the process of obtaining such factors for aluminum oxide which can be applied to other dense, polycrystalline ceramics.

6.2.1. Intraparticle Thermoelastic Energy Loss Equation

Knowledge of acoustic intraparticle thermoelastic absorption was furthered through this work. A derivation which gave an analytical solution for the amount of energy which is lost due to this type of attenuation mechanism was developed.

$$E_{\alpha TE}(f) = \frac{2}{3} \cdot F_T(f) \cdot a(f) \cdot N_G(f)$$

6.2.2. Intraparticle Thermoelastic Energy Loss Equation

The creation of an analytical equation to predict grain size distributions of secondary phases within dense aluminum oxide was achieved. This equation shows the strong dependency of measured attenuation coefficient on the concentration of secondary phases present within a bulk material microstructure.

$$N_G(f) = \frac{3 \cdot E_i(f) \cdot (1 - e^{-\alpha(f) \cdot d})}{2 F_T(f) \cdot a(f)}$$

6.2.3. Foundation of Determining Scattering Prefactors

The extension of acoustic scattering theory to include the predictability of average aluminum oxide grain size over large sample areas was demonstrated in. This included empirically obtaining the Rayleigh and stochastic scattering prefactors, C_R and C_S, respectively. Knowing these two prefactors is the foundation of utilizing ultra high frequency attenuation coefficient data in predicting average grain sizes of alumina-based materials. The methodology behind obtaining these prefactors can be applied to other dense, polycrystalline materials whose scattering behavior is strongly dictated by primary phase grains.

6.3. Acquisition and Creation of Custom Engineered Alumina Sample Sets

The transformation of acoustic attenuation coefficient spectra to provide microstructural information was facilitated by gaining an understanding of the acoustic loss mechanisms operable in these samples. Understanding why the material causes such losses is critical for any application. The frequency range in which acoustic losses could be measured was dictated by the output profile of each transducer. It is understood that the microstructure for each material system inspected using an acoustic spectroscopy method must considered accounting for different loss mechanisms dominating in different frequency regimes.

As a result alumina sample sets where created or acquired to have microstructures that would cause strong absorptive or scattering acoustic losses. Four alumina sample sets were used in this thesis; two for testing absorption-based loss mechanisms and two for testing scattering-based loss mechanisms. The two alumina-based sets used for testing absorption-based loss mechanisms contained incremental amounts of either mullite or titanium carbide. The two sample sets which were used to test scattering attenuation as a method of determining microstructure systematically varied the alumina grain size and contained unknown alumina grain sizes.

6.4. Ultrasonic, FESEM Imaging, Grain Size Analysis, and XRD

Alumina-based materials were characterized both ultrasonically and through conventional microstructural testing methods include FESEM analysis and XRD quantification. Ultrasonic testing provided material properties such as sonic velocities and elastic moduli. The ultrasound NDE also gave C-Scan attenuation coefficient images for each sample set not produced via SPS. These C-Scan images showed the

homogeneity and variability of each sample which allowed for the determination of smaller sections to be studied further.

These chosen sections from each sample were ceramographically prepared for FESEM imaging, and several micrographs were taken for each sample. Each micrograph was analyzed using a semi-automated process to determine grain size distributions. Each measured distribution took into account for stereographic effects. X-ray diffraction was used to determine the volume percent of the secondary phases present within the two sample sets containing either mullite or TiC. XRD revealed that each sample set was well defined, containing an incremental amount of different secondary phases.

6.5. Correlation of Predicted and Measured Data

Before preparation for conventional microstructural testing, acoustic attenuation coefficient spectra were obtained about the region of interest in each sample. The attenuation coefficient spectrum from each sample was transformed using the techniques developed and highlighted in this thesis to output grain size information on either the primary alumina phase or the secondary phases present. Determination of average alumina grain sizes about large sample areas showed strong correlations with conventionally measured distributions. Average grain size maps of aluminum oxide were proportional to the overall attenuation coefficient C-Scan maps using a 60MHz transducer. This further validates that scattering attenuation is dominated by the grains of the primary phase within dense, polycrystalline ceramics. Quantitative predictions of mullite and titanium carbide grain size distributions in two of the sample sets studied in this thesis showed good agreement with their associated micrograph measured grain size distributions. Possible sources of error, including assumptions, equipment resolution, and

that introduced by a user were discussed as potential causes of variability seen between acoustic predicted grain size and micrograph measured grain size.

7. Future Work

The techniques outlined in this thesis used to perform acoustic spectroscopy on dense, polycrystalline alumina have the potential of becoming commonplace testing methods. This is true for not just alumina-based materials, but all types of high hardness, dense structural ceramics. Expanding the use of acoustic spectroscopy as a nondestructive microstructural characterization technique to other types of materials will require a jump in the understanding of acoustic-based physics, specifically the physics involved with acoustic attenuation mechanisms. This thesis laid a foundation for using two types of loss mechanisms in specific frequencies regimes such that valuable microstructural information could be gleaned.

Extending this concept to a wider variety of materials will require completing certain tasks. In general these tasks can be listed as followed:

1.) The understanding of different types of absorption mechanisms applicable on frequency ranges and size scales different than what was used in this thesis. The theory of acoustic scattering is understood, where the concept of using attenuation spectra to predict average grain sizes outlined in this thesis is robust enough to easily transfer to different types of dense ceramic or metallic materials. Creation of standard sample sets to do this is outlined below.

Many acoustic absorption mechanisms exist. Intraparticle thermoelastic absorption was the specific kind of absorption that occurs in the frequency range used for the samples in this thesis. There is a wealth of information which can be extracted from lower frequencies pertaining to materials with feature sizes larger than what was seen in the samples studied. Covering a larger frequency range will allow for the extension of

using acoustic spectroscopy not only in dense ceramics but also different types of materials to include plastics, glasses, glass ceramics, and metals. Each of these materials has microstructures which cause fundamentally different absorptive losses at frequencies lower than the megahertz regime. Gaining an understanding on the specifics of these different loss mechanisms will allow for the interpretation of microstructural information from attenuation spectra.

2.) To study attenuation spectra taken from lower frequencies it is crucial to obtain transducers, pulser-receivers, and remote-pulsers which are capable of emitting and receiving ultrasonic pulses in the kHz regime. This equipment is readily available and less expensive than their higher frequency counterparts. Having a pulser-receiver which is rated to go as low as a tenth of a megahertz should be sufficient for the acoustic testing performed on dense solid materials such as ceramics, glasses, glass ceramics, plastics, and metals. Ultrasonic transducers in this frequency range are easier to manufacturer with a more reliable and repeatable signal output.

It has been a misconception that using higher frequencies is always better. Higher frequency ultrasonic testing is useful when performing C-Scan imaging to locate smaller features; however, there is a realistic upper limit to how high a frequency can be used before diffraction becomes an issue. The wealth of information able to be obtained through acoustic spectroscopy contained at lower frequencies has yet to be exploited.

3.) Software which can accommodate the manipulation of large data sets and expedite the process of transforming acoustic spectra into microstructural information is needed. This should be done to account for as many loss mechanisms which can be understood at any given time. This software can possibly be an add-on to the Rutgers CCR developed

program Hermes© where a new function sorts attenuation coefficient spectra over large sample areas such that the same manipulations used in this thesis are automatically performed.

Depending on the type of loss mechanism being exploited, user-defined inputs for different parameters will be necessary. For example, if one is performing acoustic spectroscopy using spectra which exhibit strong intraparticle thermoelastic absorption behavior, inputs for the materials thermal conductivity, specific heat, and volume concentration (via XRD) will be necessary. If spectra are taken from where scattering dominates, one will need to input the Rayleigh (C_R) and stochastic (C_S) scattering prefactors.

Once all of the appropriate data can be read into such a program, it will need the capability of being displayed and exported as a file type able to be opened with other graphical analysis software. Data display of grain size distributions may take the form of .avi files which can easily show four dimensional datasets as a type of movie. The four dimensions of such datasets include the x and y spatial dimensions, a color scale representing occurrence, and the size changing as a function of time as the movie is playing. The user should have the option of easily obtaining singular grain size distributions from each point in this four dimensional dataset and creating an average grain size distribution from multiple points.

4.) Software in the form of a database that allows for the creation of a library of materials, their parameters, active acoustic loss mechanisms across different frequencies, acoustic scattering parameters, attenuation coefficient spectra, etc. This database should allow the user to easily input new materials or change parameters of old ones as it is

developed. Recording all information from multiple materials collected with the methods highlighted in this thesis is essential in progressing acoustic spectroscopy as a useful characterization technique. Users need the capability of easily comparing acoustic data such that a stronger understanding of acoustic spectroscopy can be obtained.

5.) To confirm the trends presented in this thesis, different types of dense, polycrystalline ceramics must be tested. This should take the form of using custom engineered samples which vary one aspect of their microstructures at a time. The common structural ceramic materials which could be examined at the Rutgers CCR include silicon carbide, boron carbide, and magnesium aluminate spinel. Each of these materials has a wide host of processing procedures including different methods of densification and use of additives. Ideally, each custom engineered sample set should maintain a constant densification method using as little additives as possible or using a single type of additive at a time. Each type of custom engineered sample set should also include a sample which contains no additives. This sample is necessary to be used as a baseline standard to which all other samples containing additives will be compared against. This will simplify studying measured attenuation coefficient spectra as a start of confirming the trends seen with the alumina-based materials in this thesis.

Starting possible custom engineered silicon carbide sets should include those which vary the grain size, boron carbide additive concentration, carbon additive concentration, and alumina additive concentration. These additives are those which may be considered to be common within SiC used for structural applications. Hot pressing of SiC will ensure that near full densities can be reached without the use of sintering aids. A method of varying the SiC grain size is to systematically change firing temperatures,

pressing pressures, and dwell times at such temperatures and pressures. Starting powders should be as fine as possible such that samples containing submicron grain sizes can be achieved. The size range between samples in this SiC set should range from submicron to hundreds of microns. Having a SiC sample set which systematically varies grain size will allow for the determination of the Rayleigh and stochastic scattering prefactors. These prefactors can then later be used with attenuation spectra taken from silicon carbide with unknown grain size such that average of SiC grain size can be predicted.

Once lower frequency acoustic capabilities are obtained through the acquisition of low frequency pulser-receivers, additives of specific size ranges no longer have to be targeted (as was done with the Mullite and Titanium Carbide Series in this thesis). The size of additives such as boron carbide, carbon, and alumina can be allowed to vary without consequence being incapable of measuring their thermoelastic absorption behavior (both intra and inter particle). These three samples sets should independently contain incremental concentrations of B_4C, Carbon, and Al_2O_3 spanning several samples within each set. Covering a wide range of additive concentration may be difficult but it is necessary in being able to accurately use acoustic spectroscopy to predict the concentration of these additives in future SiC samples. These custom engineered samples should contain between 0.5-30vol% of the different additives. If other methods are necessary (HIP, CIP, etc.) to fully densify these materials with such high and low additive concentrations, then the entire sample set should be produced using such methods.

As with the proposed custom engineered silicon carbide sample sets, the boron carbide sample sets should be tailored in similar fashions. These B_4C samples should

also have systematically varied grain size through the same method of varying firing temperatures, pressing pressures, and dwell times. The use of additives such as carbon and silicon carbide should be varied in a controlled approach. Varying the boron carbide grain size will allow for a better understanding of acoustic scattering behavior while varying additive concentration will lend to acoustic absorption knowledge. Boron carbide has a tremendous degree of elastic anisotropy between its a and c crystallographic directions. A sample set which can vary the degree of texturing between samples will provide a standard for predicting possible texturing in future B_4C materials. Scattering behavior will certainly change depending on the crystal orientation in which the acoustic wave is introduced. This can certainly be quantified through the use of empirical observation of a sample set which varies the degree of texturing.

Magnesium aluminate spinel (MAS) is becoming a popular structural material due to its high mechanical properties and transparency across the visible spectrum and into the infrared. As with its mechanical properties, MAS exhibits transparency due to its microstructure. Additive type and concentration, such as lithium fluoride, can create color centers which may degrade the transparency of this material. A custom engineered MAS sample set should vary the concentration of LiF such that this set contains samples with LiF concentrations between 0-30vol%. The goal of this would be to alter the visible transparency. In this sense, acoustic absorption can be correlated with optical density through the use of a visible spectrometer. Creating a MAS sample set which varies grain size by changing the sintering temperatures and dwell times of each sample will promote different degrees of grain growth. This sample set can be used to obtain the Rayleigh and stochastic scattering prefactors, similarly to what was performed in this thesis with the

Microstructural Evolution Alumina Series. These scattering prefactors, specific to MAS, can be used for future prediction of average grain sizes.

The results provided by the work performed in this thesis expanded the knowledge of ultrasound nondestructive testing in ceramic materials. Future work can make acoustic spectroscopy a mainstay and common occurrence for microstructural testing of many types of solid materials. Acoustic nondestructive characterization can provide an inexpensive, safe, and faster alternative to conventional and nondestructive testing techniques for measuring microstructural features throughout large sample areas.

8. References

1. Medvedovski, E., *Alumina Ceramics for Ballistic Protection.* American Ceramic Society Bulletin, 2002. **81**(3): p. 6.
2. Medvedoski, E., *Alumina Ceramics for Ballistic Protection: Part 2.* American Ceramic Society Bulletin, 2002. **81**(4): p. 6.
3. Terpstra, R.A., P.P.A.C. Pex, and A.H. de Vries, *Ceramic Processing*. 1995, Chapman Hall: New York.
4. Aalund, R. *Spark Plasma Sintering*. 2008 [cited 2011 3-28]; Available from: www.thermaltechnology.com/pdf/SPS%20Reprint%20may08.pdf.
5. Xie, Z., J. Yang, and Y. Huang, *Densification and grain growth of alumina by microwave processing.* Materials Letters, 1998. **37**: p. 215-220.
6. Bottiglieri, S. and R.A. Haber, *High Frequency Ultrasound of Alumina for High Strain-Rate Applications*. Advances in Ceramic Armor V, ed. J. Swab. 2009, Hoboken, NJ: John Wiley and Sons Inc.
7. Witek, S.R. and D. Butler, *Grain-boundary microstructure of a commerial 97% alumina and the effect of ZrO_2/Y_2O_3 additions.* Journal of the Mechanics and Physics of Solids, 1985. **56**: p. 896-923.
8. Karandikar, P.G., et al. *A REVIEW OF CERAMICS FOR ARMOR APPLICATIONS*. in *International Conference on Advanced Ceramics and Composites*. 2008. Daytona Beach, Fl: Rev. 3 Ceramic Engineering and Science Proceedings.
9. Schmerr, L.W., *Fundamentals of Ultrasonic Nondestructive Evaluation A Modeling Approach*. 1998, Plenum Press: New York.
10. Reed, J.S., *Principle of Ceramics Processing 2nd edition*. 1995, John Wiley & Sons Inc.: Alfred,NY.
11. Cheung, N.W. and M.A. Nicolet, *Materials Characterization*. Materials Research Society Symposia Proceedings. Vol. 69. 1986, Pittsburgh, Pennsylvania: Materials Research Society.
12. Holbrook, J. and J. Bussiere, *Nondestructive Monitoring of Materials Properties*. Materials Research Society Symposium Proceedings. Vol. 142. 1988, Pittsburgh,Pennsylvania: Materials Research Society.
13. Ritter, J.E., et al., *Proof testing of ceramics.* Journal of Materials Science, 1980. **15**: p. 2275-2281.
14. Brennan, R.E., *Ultrasonic Nondestructive Evaluation of Armor Ceramics*, in *Materials Science and Engineering*. 2007, Rutgers the State Univ. of New Jersey: Piscataway, NJ. p. 521.
15. Kim, J. and P.K. Liaw, *The Nondestructive Evaluation of Advanced Ceramics and Ceramic-Matrix Composites.* Journal of Materials Science, 1998. **50**(11).
16. Bray, D.E. and R.K. Stanley, *Nondestructive Evaluation A Tool in Design, Manufacturing, and Service*. 1997, CRC Press: New York.
17. Datta, S.K., J.D. Achenbach, and Y.S. Rajapakse, *Elastic Waves and Ultrasonic Nondestructive Evaluation*, in *Proceedings of the IUTAM Symposium*. 1989, Elsevier: Amsterdam, Netherlands.

18. Dukhin, A.S. and P.J. Goetz, *Ultrasound for Characterizing Colloids: Particle Sizing, Zeta Potential Rheology*. 2002, Amsterdam, Netherlands: Elsevier Science B.V.
19. Vary, A., *Materials Analysis by Ultrasonics Metals, Ceramics, Composites*. 1987, Noyes Data Corporation: New Jersey.
20. Portune, A.R., *NONDESTRUCTIVE ULTRASONIC CHARACTERIZATION OF ARMOR GRADE SILICON CARBIDE*, in *Materials Science and Engineering*. 2010, Rutgers the State University of New Jersey: Piscataway, NJ. p. 489.
21. Bhatia, A.B., *Ultrasonic Absorption*. 1967, Oxford: Clarendon Press.
22. Fitting, D.W. and L. Adler, *Ultrasonic Spectral Analysis for Nondestructive Evaluation*. 1981, Plenum Press: New York.
23. Vargas, M. and N. Kioussis. *An ab-initio Examination of the Surface Electronic Structure*. Alumina α-Al2O3 (ī10): [cited 2011 3-9-11]; Available from: www.csun.edu/~mmv71887/Aluminareport1.
24. Vodenitcharova, T., et al., *The effect of anisotropy on the deformation and fracture of sapphire wafers subjected to thermal shocks.* Materials Processing Technology, 2007. **194**: p. 11.
25. Paglia, G., *Determination of the structure of y-alumina using empirical and first principle calculations combined with supporting experiments*, in *Applied Physics Applied Chemistry*. 2004, Curtin University of Technology.
26. Committee, A.I., *Engineered Materials Handbook*. 1991, ASM International: USA.
27. Levin, I. and D. Brandon, *Metastable Alumina Polymorphs: Crystal Structures and Transition Sequences.* J. Am. Ceram. Soc., 1998. **81**: p. 1995-2012.
28. Habashi, F., *A Hundred Years of the Bayer Process for Alumina Production.* Can. Min. Metall. Bull., 1988. **81**(909): p. 70-76.
29. CoorsTek, *CeraShield Armor Ceramics*, C. Tek, Editor. 2006: Golden, Co.
30. AZOM_Materials. *Alumina*. 2001 [cited 2011 3-9]; Available from: http: //www.azom.com/Details.asp?ArticleID=52.
31. NDT_Resource_Center. *Electrical Conductivity and Resistivity*. 2011 [cited 2011 3-10]; Available from: http: //www.ndt-ed.org/EducationResources/CommunityCollege/Materials/Physical_Chemical/Electrical.htm.
32. Touzin, M., et al., *Relationships between dielectric breakdown resistance and charge transport in alumina materials—Effects of the microstructure.* Journal of the European Ceramic Society, 2007. **27**: p. 1193-1197.
33. Serway, R.A. and R.J. Beichner, *Physics for Scientists and Engineers, Fifth Edition*. 2000: USA.
34. Swalin, R., *Thermodynamics of Solids, 2nd edition*. 1972, Wiley-Interscience NY.
35. Somiya, S., *Advanced Technical Ceramics*. 1984, Academic Press Japan, Inc.: Japan.
36. Wachtman, J.B., *Mechanical Properties of Ceramics*. 1996, New York: Wiley - Interscience.
37. Callister, W., *Materials Science and Engineering: an Introduction.4th Edition*. 1997, John Wiley and Sons Inc.: USA.

38. Callister, W., *Materials Science and Engineering: an Introduction 7th Edition*. 2007, John Woley and Sons Inc.
39. NDT_Resource_Center. *Tensile*. 2011 [cited 2011 3-10]; Available from: http: //www.ndt-ed.org/EducationResources/CommunityCollege/Materials/Mechanical/Tensile.htm.
40. Kaufman, C., *Influence of material properties on the ballistic performance of ceramics for personal body armour.* Shock Vibration, 2003. **10**(1): p. 51-58.
41. Beer, F.P. and E.R. Johnston, *Mechanics of Materials, 3rd edition.* 2001, McGraw-Hill.
42. Lawn, B., *Fracture of Brittle Solids - Second Edition*. 1993, Cambridge University Press: Cambridge.
43. Griffith, A.A., *The Phenomena of Rupture and Flow in Solids.* Philosophical Transactions of the Royal Society of London, 1921. **221**(A): p. 163-198.
44. Swab, J.J., *Recommendations for Determining the Hardness of Armor Ceramics.* International Journal of Applied Ceramic Technology, 2004. **1**(3): p. 7.
45. Amethyst Galleries, I. *The Mineral Corundum*. 2011 [cited 2011 3-29]; Available from: www.galleries.com/minerals/oxides/corundum/corundum.htm.
46. Simunek, A., *Anisotropy of hardness from first principles: The cases of ReB2 and OsB2.* Physical Review B, 2009. **80**: p. 4.
47. ASTM, *Standard Practice for Fabricating Ceramic Reference Specimens Containing Seeded Voids.* ASTM International, 2004.
48. ASTM, *ASTM Standard C 1326 - 03 Standard Test Method for Knoop Indentation Hardness of Advanced Ceramics*, ASTM International.
49. Quinn, G.D., P. Green, and K. Xu, *Cracking and the Indentation Size Effect for Knoop Hardness of Glasses.* J. Am. Ceram. Soc., 2003. **86**(3): p. 441-448.
50. Krell, A., *A New Look at Grain Size and Load Effects in the Hardness of Ceramics.* Material Science Engineering, 1998. **A245**: p. 277-284.
51. McColm, I.J., *Ceramic Hardness*. 1990, Plenum Press: New York, NY.
52. Li, H. and R.C. Bradt, *The Indentation Load/Size Effect and the Measurement of the Hardness of Vitreous Silica.* J. Non-Crystal. Sol., 1992. **146**: p. 197-212.
53. *NIST Property Data Summaries: Alumina*. [cited 2011 3-14]; Available from: http: //www.ceramics.nist.gov/srd/summary/ftgal2o3.htm.
54. Bitossi. *Products - Dry Grinding*. [cited 2011 3-17]; Available from: http: //www.industriebitossi.com/lang1/dry_grinding.html.
55. Belen'kaya, I.B., et al., *Ceramic for Spark-Plug Insulators.* Steklo i Keramika, 1981. **5**: p. 19-20.
56. Richerson, D.W., *Modern Ceramic Engineering: 3rd edition. Properties, Processing and Use in Design*. 2006, Taylor and Francis Group, LLC.: Boca Raton, Fl. p. 18-20.
57. IXYS. 2007 [cited 2011 3-11]; Available from: http: //www.j-rep.com/download/ixys-appli-book/S29_30.pdf.
58. Xiao, Z.L., et al., *Nickel antidot arrays on anodic alumina substrates.* Applied Physics Letters, 2002. **81**: p. 2869-2871.

59. Bradley, L., L. Li, and F.H. Stott, *Characteristics of the microstructures of alumina-based refractory materials treated with CO and diode lasers.* Applied Surface Science, 1999. **138-139**: p. 233-239.
60. Cerglass, N. *High Purity Al2O3 Crucibles and Furnace Ware*. 2004 [cited 2011 3-10].
61. Robertshaw_Industrial. *High Temperature/Pressure Alumina Insulated probe Model 738A.* [cited 2011 3-10]; Available from: http: //www.robertshawindustrial.com/images/pdf/110_738A.pdf.
62. Gobain, S. *Saint Gobain Abrasive Materials - Aluminum Oxide*. [cited 2011 3-17]; Available from: http: //www.abrasivematerials.saint-gobain.com/aluminium-oxide.aspx.
63. Metallographic. *Alumina Polishing Abrasives*. 2006 [cited 2011 3-17]; Available from: http: //www.metallographic.com/Industrial%20Products/Alumina.htm.
64. Smile, S.Y. *Everything You Wanted to Know About Toothpaste Toothpaste - What's In It?* 2007 [cited 2011 3-17]; Available from: http: //www.saveyoursmile.com/toothpaste/toothpaste-c.html.
65. Corporation, M. *Sectioning, Mounting, Grinding, Polishing*. [cited 2011 3-17]; Available from: www. metallographicsupplies.com.
66. Normandia, J., *Ceramics Research Leads to Improved Armor Performance.* AMPTIAC, 2004. **8**(4): p. 9.
67. Glicksman, M.E., *Diffusion in Solids. Field Theory, Solid-State Principles, and Applications.* 2000, New York: Wiley-Interscience.
68. German, R.M., *Liquid Phase Sintering* 1985, Plenum Press: New York.
69. KOSMOS, A.S., L.I. BELIC, and D. SUSNIK, *ADDITIVES IN COARSE GRAIN ALUMINA CERAMICS FOR METALLIZATION.* Fizika A, 1996. **5**(2): p. 85 - 90.
70. Ferguson, J.B. and H.E. Merwin, *The Ternary System CaO-MgO-SiO_2.* Proceedings of the National Academy of Sciences, 1918. **5**(1): p. 16 - 18.
71. Orange, G., et al., *High temperature mechanical properties of reaction-sintered mullite/zirconia and mullite/alumina/zirconia composites.* Journal of Materials Science, 1985. **20**: p. 8.
72. Williams, T. *What is a ceramic?* [cited 2011 3-21]; Available from: http://webpages.charter.net/dawill/tmoranwms/Cer_Sinter.html.
73. Medvedoski, E., *Alumina–mullite ceramics for structural applications.* Ceramics International, 2006. **32**: p. 369-375.
74. Kim, H.-E., A.J. Moorhead, and S.-H. Kim, *Strengthening of Alumina by Formation of a Mullite/Glass Layer on the Surface*. Journal of the American Ceramic Society. Vol. 80. 1997: American Ceramic Society. 4.
75. Kostyukov, N.S., E.Y. Medvedovski, and F.Y. Kharitonov, *Electroinsulating Corundum-Mullite Ceramics.* Acadademy of Science USSR, 1988.
76. Venkatesh, V.C., Z.A. Ahmad, and M. Konneh, *Performance Studies of Alumina TiC-based Ceramic Tool Insters when Turning Tool Steels*: University Teknologi Malaysia.
77. Kitiwan, M. and D. Atong, *Pressureless Sintered Al_2O_3 - TiC Composites Prepared from Microwave and Conventional Synthesized Powders*: National Metal and Materials Technology Center.

78. Nikolic, M., *A Phenomenological Analysis of Sintering Kinetics of Alumina*. Material Science Forum, 2004. **453-454**: p. 441-446.
79. Stobierski, L. and A. Gubernat, *Sintering of Silicon Carbide I: Effect of Carbon.* Ceramics International, 2003. **29**: p. 287-292.
80. Dillon, S.J. and M.P. Harmer, *Intrinsic Grain Boundary Mobility in Alumina.* J. Am. Ceram. Soc., 2006. **89**: p. 3885-3887s.
81. Alliegro, R.A., *Pressure-Sintered Silicon Carbide*. American Ceramic Society, 1956. **39**(11): p. 386 - 389.
82. Peelen, J.G., *Alumina: Sintering and Optical Properties*, in *Technical Science*. 1977, University College London: London.
83. Isobe, T., et al., *Spark plasma sintering technique for reaction sintering of Al_2O_3/Ni nanocomposite and its mechanical properties.* Ceramics International, 2008. **34**: p. 213-217.
84. Kopeliovich, D. *Spark Plasma Sintering*. 2010 [cited 2011 3-28]; Available from: http://www.substech.com/dokuwiki/doku.php?id=spark_plasma_sintering&DokuWiki=e579a03e5...
85. Shen, Z., et al., *Spark Plasma Sintering of Alumina.* Journal of the American Ceramic Society, 2002. **85**(8): p. 1921-1927.
86. Risbud, S., C. Shan, and A. Mukherjee, *Retention of nanostructure in aluminum oxide by very rapid sintering at 1150C.* Journal of Materials Research, 1996. **10**(2): p. 237.
87. Wang, S.W., L.D. Chen, and T. Hirai, *Densification of Al2O3 powder using spark plasma sintering.* J. Mater. Res., 2000. **4**: p. 982-987.
88. Papadakis, E.P., *Ultrasonic Instruments and Devices Reference for Modern Instrumentation, Techniques, and Technology*. 1999, USA: Academic Press.
89. Krautkramer, J. and H. Krautkramer, *Ultrasonic Testing of Materials*. 4th Fully Revised ed. 1990, Berlin: Springer-Verlag.
90. Rossing, T., *The Science of Sound*. 1990, Reading, MA: Addison-Wesley.
91. Finch, R.D., *Introduction to Acoustics* 2005, Upper Saddle River, NJ: Pearson Education 653.
92. Kuttruff, H., *Ultrasonics Fundamentals and Applications*. 1991, Elsevier Applied Science: New York.
93. Bhardwaj, M.C. and A.S. Bhalla, *Non Destructive Characterization of Superconductors*. 1991, Chapman and Hall. p. 210-213.
94. Bhardwaj, M.C., *Evolution, Practical Concepts and Examples of Ultrasonic NDC.* Ceramic Monographs, 1992: p. 7.
95. Brown, A.E., *RATIONALE AND SUMMARY OF METHODS FOR DETERMINING ULTRASONIC PROPERTIES OF MATERIALS AT LAWRENCE LIVERMORE NATIONAL LABORATORY*. 1997, Lawrence Livermore National Laboratory.
96. Zhang, C. and D. Gross, *On Wave Propagation in Elastic Solids with Cracks*. 1998, Computational Mechanics Publications: Boston, USA.
97. Charlesworth, J.P. and T. J.A.G., *Engineering Applications of Ultrasonic Time-of-Flight Diffraction*. 1989, John Wiley & Sons INC.: New York.

98. NDT_Resource_Center. *Acoustic Impedance*. [cited 2011 3-29]; Available from: www.ndt-ed.org/EducationResources/CommunityCollege/Ultrasonics/Physics/acousticimpedance.htm.
99. Flanders, P.B., *A method of Measuring Acoustic Impedance.* Bell System Technical Journal, 1932: p. 402-410.
100. Kennelly, A.E. and R.P. Siskind, *The Acoustic Impedance of Straight Cylindrical Air Columns in Brass Tubes.* Proceedings of the American Philosophical Society, 1927. **66**: p. 89.
101. Zwislocki, J.J. and A.S. Feldman, *Acoustic Impedance of Pahtological Ears.* ASHA Monographs, 1970(15): p. 1-41.
102. Aleman, P.B., *Acoustic Impedance Inversion of Lower Permian Carbonate Buildups in the Permian Basin, Texas*, in *Geophysics*. 2004, Texas A&M University.
103. Clawson, S. and H. Meng. *Seismic Acoustic Impedance Inversion in Reservoir Characterization Utlizing gOcad*. 2000 [cited 2011 3-29]; Available from: www.oilit.com/2journal/2article/0004/0005.pdf.
104. Francis, A.M. and F.H. Syed, *Application of Relative Acoustic Impedance Inversion to Constrain Extent of E Sand Reservoir on Kadanwari Field*. 2001, SPE and PAPG Annual Technical Conference: Islamabad.
105. *Density and Acoustic Impedance Values*. 2011 [cited 2011 3-29]; Available from: www.inficonthinfilmdeposition.com/en/densityandacousticvalues.html.
106. NDT_Resource_Center. *Acoustic Properties for Metals in Solid Form*. 2011 [cited 2011 3-29]; Available from: www.ndt-ed.org/GeneralResources/MaterialProperties/UT/ut_matlprop_metals.htm.
107. *NDT Resource Center: Collaboration for NDT Education*. [cited 2011 3-30]; Available from: www.ndt-ed.org/.
108. Chiffoleau, G.J.A., T.A. Steinberg, and M. Veidt, *Reflection of structural waves at a solid/liquid interface.* Ultrasonics, 2003. **41**: p. 347-356.
109. *American Society of Nondestructive Testing.* [cited 2011 3-30]; Available from: www.asnt.org/.
110. Lynnworth, L.C., *Industrial Applications of Ultrasound -A Review II. Measurements, Tests, and Process Control Using Low-Intensity Ultrasound.* IEEE Transactions on sonics and ultrasonics, 1975. **22**(2): p. 31.
111. Bottiglieri, S. and R.A. Haber, *Corrective Techniques for Ultrasonic Nondestructive Evaluation.* Proceedings of the 34th ICACC, 2010.
112. Uberall, H., et al., *Dynamics of acoustic resonance scattering from spherical targets: Application to gas bubbles in fluids.* J. Acoust. Soc. Am., 1979. **66**(4): p. 12.
113. Flax, L. and H. Uberall, *Resonant scattering of elastic waves from spherical solid inclusions.* J. Acoust. Soc. Am., 1980. **67**: p. 1432-1442.
114. Bottiglieri, S., et al. *Non-Destructive Ultrasound Characterization (NDC) of High-Density, High-Hardness Ceramics*. in *Ceramic, Composites, and Optical Materials Center Meetings*. 2010. Rutgers University.
115. Evans, A.G., et al., *Ultrasonic attentuation in ceramics.* J. Appl. Phys., 1978. **49**(5): p. 11.

116. Auckland, D.W., C.D. Smith, and B.R. Varlow, *Application of ultrasound to the NDT of solid insulation.* IEEE Proc.-Sci. Meas. Technol., 1994. **141**: p. 20-24.
117. Bouda, A.B., S. Lebaili, and A. Benchaala, *Grain size influence on ultrasonic velocities and attenuation.* NDT&E International, 2003. **36**: p. 1-5.
118. Papadakis, E.P., *Grain-Size Distribution in Metals and Its Influence on Ultrasonic Attenuation Measurements.* The Journal of the Acoustical Society of America, 1961. **33**: p. 1616-1621.
119. Baaklini, G.Y., E.R. Generazio, and J.D. Kiser, *High-Frequency Ultrasonic Characterization of Sintered Silicon Carbide.* J. Am. Ceram. Soc., 1989. **72**: p. 383-387.
120. Adler, L., J.H. Rose, and C. Mobley, *Ultrasonic method to determine gas porosity in aluminum alloy castings: Theory and experiment.* J. Appl. Phys., 1986. **59**(2): p. 12.
121. Dukhin, A.S., et al., *Acoustic and electroacoustic spectroscopy.* Colloids and Surfaces A: Physicochemical and Engineering Aspects, 2000. **173**: p. 127-158.
122. Thompson, B.R., *Elastic-Wave Propagation in Random Polycrystals: Fundamentals and Application to Nondestructive Evaluation.* Topics Appl. Phys., 2002. **84**: p. 24.
123. Hirsekorn, S., *The scattering of ultrasonic waves by polycrystals.* J. Acoust. Soc. Am., 1982. **72**: p. 1021-1031.
124. Mason, W.P. and H.J. McSkimin, *Attenuation and Scattering of High Frequency Sound Waves in Metals and Glasses.* The Journal of the Acoustical Society of America, 1947. **19**: p. 464-473.
125. Ishimaru, A., *Theory and Application of Wave Propagation and Scattering in Random Media.* Proceedings of the IEEE, 1977. **65**(7): p. 32.
126. Beyer, R.T. and S.V. Letcher, *Physical Ultrasonics*. 1969, Academic Press: New York.
127. Seaholtz, R.G. and J. Panda, *Rayleigh Scattering Diagnostic for Dynamic Measurement of Velocity and Temperature*. 2001, NASA. p. 17.
128. Ying, C.F. and R. Truell, *Scattering of a Plane Longitudinal Wave by a Spherical Obstacle in an Isotropically Elastic Solid.* Journal of Applied Physics, 1956. **27**(6): p. 12.
129. Mason, W.P. and H.J. McSkimin, *Energy losses of sound waves in metals due to scattering and diffusion.* Journal of Applied Physics, 1948. **19**(10): p. 940-946.
130. Hulst, H.C.v.d., *Light scattering by small particles*. 1957, New York: Wiley. 470.
131. Nicoletti, D.W., N. Bilgutay, and B. Onaral, *SCALING PROPERTIES OF ATTENUATION AND GRAIN SIZE.* ULTRASONICS SYMPOSIUM, 1990: p. 1119-1122.
132. Lifshitz, R. and Parkhomovoski, *Theory of propagation of supersonic waves in polycrystals.* Zhurnal Eksperimentalnoi i Teoreticheskoi Fizika, 1950. **20**: p. 175-182.
133. Merkulov, L., *Investigation of Ultrasonic Scattering in Metals.* Soviet Physical Technical Letters, 1957. **1**(1): p. 59-69.
134. Dukhin, A.S. and P.J. Goetz, *New developments in acoustic and electroacoustic spectroscopy for characterizing concentrated dispersions.* Colloids and Surfaces A: Physicochemical and Engineering Aspects, 2001. **192**: p. 267-306.

135. Papadakis, E.P., *Ultrasonic Attenuation Caused by Scattering in Polycrystalline Metals.* The Journal of the Acoustical Society of America, 1965. **37**: p. 711-717.
136. Strutt, J.W., *The Theory of Sound*. Vol. I. 1945, New York: Dover Publications.
137. Smith, R.L., *The Effecto f Grain Size Distribution on the Frequency Dependence of Ultrasonic Attenuation in Polycrystalline Materials.* The Journal of Ultrasonics, 1982. **20**(5): p. 211-214.
138. Maisel, J., *Preliminary investigation of an electrical network model for ultrasonic scattering*, in *NASA CR-3770*. 1984.
139. Strutt, J.W., *The Theory of Sound*. Vol. II. 1945, New York: Dover Publications.
140. Mie, G., *Beitrage zur Optik truber Medien, speziell kolloidaler Metallosungen.* Ann. Phys., 1908(330): p. 377-445.
141. Cox, A.J., *An experiment to measure Mie and Rayleigh total scattering cross sections*, A.J. DeWeerd, Editor. 2002, American Association of Physics Teachers: American Journal of Physics. p. 620-625.
142. Bottiglieri, S., V.A. DeLucca, and R.A. Haber, *Non-Destructive Ultrasound Characterization (NDC) of High-Density, High-Hardness Ceramics*. 2011, Rutgers University: Piscataway. p. 1-46.
143. Blitz, J. and G. Simpson, *Ultrasonic Methods of Non-destructive Testing*. 1996, London: Chapman and Hall.
144. Sewell, C.J., *On the Extinction of Sound inf a Viscous Atmosphere by Small Obstacles of Cylindrical and Sperhical Form.* Philosophical Transactions of the Royal Society of London, 1910. **A210**: p. 239.
145. Epstein, P.S. and R.R. Carhart, *The Absorption of Sound in Suspensions and Emulsions.*I. Water Fog in Air.* J. Acoust. Soc. Am., 1953. **25**(3): p. 13.
146. Urick, R.J., *The Absorptiono f Soundi n Suspensionso f Irregular Particles.* THE JOURNAL OF THE ACOUSTICAL SOCIETY OF AMERICA, 1948. **20**: p. 283-289.
147. Allegra, J.R. and S.A. Hawley, *Attenuation of Sound in Suspensions and Emulsions: Theory and Experiments.* J. Acoust. Soc. Am., 1971. **51**(5): p. 20.
148. Dhadwal, H.S., K. R.R., and K. Suh, *Integrated fiber optic probe for dynamic light scattering.* Applied Optics, 1993. **32**(21): p. 3901-3904.
149. Dukhin, A.S., *Acoustic spectroscopy for concentrated polydispersed colloids with high density contrast.* Langmuir, 1996. **12**(21): p. 4987-4997.
150. Barrett, H.H. and M.G. Holland, *Critique of Current Theories of Akhieser Damping in Solids.* Physical Review, 1969. **1**(6): p. 2538-2544.
151. Hartmann, B. and J. Jarzynski, *Ultrasonic Hysteresis Absoprtion in Polymers.* Journal of Applied Physics, 1972. **43**(11): p. 9.
152. Ferry, J.D., *Viscoelastic Properties of Polymers*. 2nd ed. 1970, New York: Wiley.
153. Burlak, G.N. and V. Ostrovskii, *Acoustic hysteresis phenomena due to the dislocation nonlinearity in crystals.* Technical Physics Letters, 1997. **23**(9): p. 725-726.
154. Lucke, K., *Ultrasonic Attenuation Caused by Thermoelastic Heat Flow.* Journal of Applied Physics, 1956. **27**: p. 1433-1438.
155. Nava, R., et al., *Akheizer damping and the thermal conductivity of pure and impure dielectrics.* Physical Review 1975. **14**(2): p. 800-807.

156. Luo, L., et al., *Ultrasound absorption and entropy production in biological tissue: a novel approach to anticancer therapy.* Diagnostic Central, 2006. **1**(35): p. 6.
157. Verma, G.S., *Ultrasonic Absorption due to Chemical Relaxation in Electrolytes.* Reviews of Modern Physics, 1959. **31**(4): p. 1052-1071.
158. Bauer, H.J., *Physical Acoustics*. W.P. Mason ed. Vol. IIA. 1965, New York: Academic Press.
159. Sehgal, C.M., *Ultrasonic Absorption and Dispersion in Biological Media: A postulated Model.* Journal of the Acoustical Society of America, 1982. **72**(6): p. 1711-1718.
160. Zener, C., *Internal Friction in Solids I. General Theory of Thermoelastic Internal Friction.* Physical Review, 1940. **52**(152): p. 15.
161. Zener, C., *Internal Friction in Solids II. General Theory of Thermoelastic Internal Friction.* Physical Review, 1938. **53**: p. 10.
162. Herzfeld, K. and T.A. Litovitz, *Absorption and Dispersion of Ultrasonic Waves*. 1959, New York: Academic Press.
163. Lessen, M., *Thermoelastic Damping at the Boundary Between Dissimilar Solids*.* Journal of Applied Physics, 1956. **28**(3): p. 364-366.
164. Zener, C., *Internal Friction in Solids.* Physical Review, 1937. **52**: p. 6.
165. Kamel, R., *Measurement of the Internal Friction of Solids.* Physical Review, 1949. **75**: p. 1606.
166. Greene, G.A., Y.I. Cho, and A. Bar-Cohen, *Advances in Heat Transfer*. Vol. 41. 2009, San Diego: Academic Press.
167. Arcaro, A., *Grain Sizes of Polycrystalline Aluminum Oxide*, S. Bottiglieri, Editor. 2009: Piscataway.
168. Vary, A., *Nondestructive Testing Handbook, Ultrasonic Testing*. 2nd ed. Vol. 7. 1991, Columbus.
169. Babick, F., F. Hinze, and S. Ripperger, *Dependence of ultrasonic attenuation on the material properties.* Colloids and Surfaces A: Physicochemical and Engineering Aspects, 2000. **172**: p. 33-46.
170. Goodenough, T.I.J., et al., *Detection and quantification of insoluble particles by ultrasound spectroscopy.* Ultrasonics, 2005. **43**: p. 5.
171. Meyer, S., et al., *A comparative study of ultrasound and laser light diffraction techniques for particle size determination in dairy beverages.* MEASUREMENT SCIENCE AND TECHNOLOGY, Jan. 2006. **17**: p. 9.
172. Haines, N.F., *Ultrasonic Spectroscopy.* Physics in Technology, 1976: p. 8.
173. Papadakis, E.P., *From Micrograph to Grain-Size Distribution with Ultrasonic Applications.* Journal of Applied Physics, 1964. **35**: p. 1586-1594.
174. Thompson, R.B., *Ultrasonic Measurement of Mechanical Properties.* IEEE Ultrasonics Symposium, 1996: p. 735-744.
175. Roderick, R.L. and R. Truell, *The Measurement of Ultrasonic Attentuation in Solids by the Pulse Technique and Some Results in Steel.* Journal of Applied Physics, 1952. **23**(2): p. 13.
176. Vary, A., *FEASIBILITY OF RANKING FRACTURE TOUGHNESS BY ULTRASONIC MEASUREMENTS.* Ultrasonics Symposium Proceedings, 1975: p. 588-590.

177. Klima, S.J. and H.E. Kautz, *Nondestructive Evaluation of Advanced Ceramics*. 1988, NASA: Cleveland. p. 11.
178. Nicoletti, D.W., *Scaling Properties of Ultrasonic Attenuation and Grain Size in Metals*. 1991, Drexel University: Ph.D. Thesis.
179. Roney, R.K., *The Influence of Metal Grain Size on the Attenuation of an Ultrasonic Wave*. 1950, California Insitute of Technology: Ph.D. Thesis.
180. Kulkarni, N., B. Moudgil, and M. Bhardwaj, *Ultrasonic Characterization of Green and Sintered Ceramics: I, Time Domain.* American Ceramic Society Bulletin, 1993. **73**(6): p. 8.
181. Kulkarni, N., B. Moudgil, and M. Bhardwaj, *Ultrasonic Characterization of Green and Sintered Ceramics: II, Frequency Domain.* R&D Review, 1994. **73**: p. 83-85.
182. Roth, D.J., et al., *Quantitative Mapping of Pore Fraction Variations in Silicon Nitride Using an Ultrasonic Contact Scan Technique*. 1993, NASA Cleveland
183. Portune, A.R., S. Bottiglieri, and R.A. Haber, *Non-Destructive Evaluation (NDE) of Ceramics*. 2010, Rutgers University: Ceramics, Composites, and Optical Materials Center: Piscataway.
184. *Ultrasonic Testing of Aerospace Materials*. Preferred Reliability Practices [cited 2011 4-21]; Available from: http://klabs.org/DEI/References/design_guidelines/test_series/1422msfc.pdf.
185. *Non-Contact Ultrasound: Concrete, Highway, Bridges, Air Strips, Analysis*. [cited 2011 4-25]; Available from: http://www.ultrangroup.com/Applications/PDF/Concrete.pdf.
186. International, N.E. *Tube Views*. 2009 [cited 2011 4-25]; Available from: http://www.neimagazine.com/story.asp?sc=2053969.
187. *Introduction to Nondestructive Testing*. [cited 2011 4-26]; Available from: www.ndt.net/article/icem2004/papers/193/193.htm.
188. Roth, D.J., et al., *COMMERCIAL IMPLEMENTATION OF ULTRASONIC VELOCITY IMAGING METHODS VIA COOPERATIVE AGREEMENT BETWEEN NASA LEWIS RESEARCH CENTER AND SONIX, INC.*, NASA, Editor. 1996, Nasa: Cleveland, OH. p. 37.
189. Mix, P.E., *Introduction to Nondestructive Testing*. 1987, New York: John Wiley & Sons.
190. *Wave Propagation*. [cited 2011 4-27]; Available from: http://www.ndt-ed.org/EducationResources/CommunityCollege/Ultrasonics/Physics/wavepropagation.htm.
191. *Fundamentals of Ultrasonic Imaging and Flaw Detection*. 2010 [cited 2011 4-27]; Available from: http://zone.ni.com/devzone/cda/tut/p/id/3368.
192. Serbian, S., *Ultrasonic Material Property Determinations*. Materials Analysis by Ultrasonics - Metals, Ceramics, Composites. 1987, Park Ridge: Noyes Data Corporation.
193. Olympus, *OmniScan MXU Software: User's Manual*. 2007.
194. *Gage High Speed Digitizers for PCI Bus*. [cited 2011; Available from: http://www.gage-applied.com/products/pci_family.htm.
195. Papadakis, E.P., *Physical Acoustics, Principles and Methods*. Vol. 4. 1968: Academic Press.

196. *Basic Principles of Ultrasonic Testing*. [cited 2010 4-28]; Available from: http://www.ndt-ed.org.
197. Hamilton, M.F. and D.T. Blackstock, *Nonlinear Acoustics*. 1998, Academic Press: New York.
198. Handley, M. *Fourier Transforms*. [cited 2011 4-28]; Available from: http://www.cs.columbia.edu/~hgs/teaching/ais/slides/03-fourier.pdf.
199. Cooley, J.W. and J.W. Tukey, *An algorithm for the machine calculation of complex Fourier series.* Mathematics of Computation, 1965. **19**: p. 297-301.
200. Smith, J.O. *Mathematics of of the Discrete Fourier Transform (DFT) with Audio Applications, Second Edition.* 2007 [cited 2011 4-28]; Available from: http://ccrma.stanford.edu/~jos/mdft/.
201. Oppenheim, A.V. and R.W. Schafer, *Discrete-Time Signal Processing*. 1999: Prentice Hall Signal Processing Series.
202. *Mathematical Definition of the STFT*. [cited 2011 4-28]; Available from: https://ccrma.stanford.edu/~jos/sasp/Mathematical_Definition_STFT.html.
203. Harris, F.J., *On the Use of Windows for Harmonic Analysis with the Discrete Fourier Transform.* Proceedings of the IEEE, 1978. **66**: p. 51-84.
204. Selesnick, I. *Short Time Fourier Transform.* 2005 [cited 2011 4-29]; Available from: http://cnx.org/content/m10570/latest/.
205. Roberts, M.J. *Correlation, Energy Spectral Density and Power Spectral Density*. 2005 [cited 2011 4-29]; Available from: http://www.cse.unt.edu/~rakl/class3020/Chapter8.pdf.
206. *JSR Ultrasonic Pulser-Receivers.* [cited 2011; Available from: http://www.jsrultrasonics.com/pulsereceivers.html.
207. Leveque, G., E. Rosenkrantz, and D. Laux, *Correction of diffraction effects in sound velocity and absorption measurements.* MEASUREMENT SCIENCE AND TECHNOLOGY, 2007. **18**: p. 3458-3462.
208. Xu, W. and J.J. Kaufman, *Diffraction Correction Methods for Insertion Ultrasound Attenuation Estimation.* IEEE transactions on Biomedical Engineering, 1993. **40**: p. 563-570.
209. Woo, J. *A Short History of the Development of Ultrasound in Obsterics and Gynecology*. [cited 2011 5-2]; Available from: http://www.ob-ultrasound.net/history1.html.
210. Gericke, O.R., *Spectrum and Contour Analysis of Ultrasonic Pulses for the Determination of Microstructure in Metals.* Journal of the Acoustical Society of America, 1960. **32**.
211. *Pizoelectric Transducers*. [cited 2011 5-4]; Available from: http://www.ndt-ed.org/EducationResources/CommunityCollege/Ultrasonics/EquipmentTrans/piezotransducers.htm.
212. Luo, L., et al., *Effects of Mn doping on dielectric and piezoelectric properties of 0.71Pb($Mg_{1/3}Nb_{1/3}$)O_3-0.29PbTiO_3 single crystals.* Applied Physics Letters, 2007. **90**.
213. *Piezoelectric Ceramic Products*. [cited 2011 5-4]; Available from: http://www.piceramic.de/pdf/KATALOG_english.pdf.

214. *Ultrasonic Flaw Detection*. 2010 [cited 2011 5-4]; Available from: http://www.olympus-ims.com/en/applications-and-solutions/introductory-ultrasonics/introduction-flaw-detection/.
215. *Characterisitics of Piezoelectric Transducers*. 2010 [cited 2011 5-4]; Available from: http://www.ndt-ed.org/EducationResources/CommunityCollege/Ultrasonics/EquipmentTrans/characteristicspt.htm.
216. *Flaw Detectors: High Frequency*. 2011 [cited 2011 5-4]; Available from: http://www.olympus-ims.com/en/ultrasonic-transducers/highfrequency/.
217. *Olympus - Ultrasonic Transducers Technical Notes*. 2010 [cited 2011 5-5]; Available from: www.olympusNDT.com.
218. *Radiated Fields of Ultrasonic Transducers*. [cited 2011 5-5]; Available from: http://www.ndt-ed.org/EducationResources/CommunityCollege/Ultrasonics/EquipmentTrans/radiatedfields.htm.
219. *Transducer Beam Spread*. 2010 [cited 2011 5-5]; Available from: http://www.ndt-ed.org/EducationResources/CommunityCollege/Ultrasonics/EquipmentTrans/beamspread.htm.
220. Bhardwaj, M.C., *High-Resolution Ultrasonic Nondestructive Characterization.* Ceramic Bulletin, 1990. **69**(9): p. 1490-1496.
221. *Basic Principles of Ultrasound*. 2004 [cited 2011 5-6]; Available from: http://www.echo-web.com/html/echo-202-free/echo202-4-body.asp?code=free.
222. *Transducer Types*. [cited 2011 5-9]; Available from: http://www.ndt-ed.org/EducationResources/CommunityCollege/Ultrasonics/EquipmentTrans/transducertypes.htm.
223. *Inside a Phased Array Transducer*. [cited 2011 5-9]; Available from: http://www.olympus-ims.com/en/ndt-tutorials/transducers/inside/.
224. *Pulser-Receivers*. [cited 2011 5-10]; Available from: http://www.ndt-ed.org/EducationResources/CommunityCollege/Ultrasonics/EquipmentTrans/pulserreceivers.htm.
225. *Gage - High Speed PCI Digitizers*. [cited 2011 5-11]; Available from: http://www.gage-applied.com/Products/pci_digitizers.htm.
226. Kuffel, E., W.S. Zaengl, and J. Kuffel, *High Voltage Engineering: Fundamentals*. 1984, Burlington, MA: Pergamon Press.
227. *Techno Inc. CNC Routers. Linear Motion. Grippers*. [cited; Available from: http://www.techno-isel.com/.
228. *Measurement Computing. PCI and PCIe Data Acquisition*. [cited; Available from: http://www.mccdaq.com/solutions/PCI-Data-Acquisition.aspx.
229. *The Ultran Group. Ultrasound Redefined.* [cited 2011 5-11]; Available from: http://www.ultrangroup.com/.
230. *Mistras Group, Inc.* [cited; Available from: http://www.mistrasgroup.com/.
231. *Olympus. OmniScan MX*. [cited 2011 5-11]; Available from: http://www.olympus-ims.com/en/omniscan-mx/.
232. *Ferro Ceramic Grinding, Inc.: Ceramic Properties Table*. 2010 [cited 2011 5-25]; Available from: http://www.ferroceramic.com/mullite_table.htm.

233. *ASTM E1382-97: Standard Test Methods for Determining Average Grain Size Using Semiautomatic and Automatic Image Analysis.* ASTM International, 2010.
234. Luis, S., *Lince Linear Intercept*: Darmstadt, Germany.
235. *Semi-Quantitative Analysis by XRD*. [cited 2011 6-1]; Available from: http://www.h-and-m-analytical.com/pdfs/semi-quant.pdf.
236. Soares, R.M., A.C.S. Sabioni, and e. al., *Structural Characterization of Mullites Synthesized by Thermal Decomposition of Topaz.* Materials Research, 2007. **10**(1): p. 4.